

AD/A-000 942

SOLAR COLLECTOR THERMAL POWER SYSTEM.
VOLUME III. BASIC STUDY AND EXPERIMENTAL
EVALUATION OF THERMAL TRAIN COMPONENTS

Robert Richter

Xerox Corporation/Electro-Optical Systems

Prepared for:

Air Force Aero Propulsion Laboratory

November 1974

DISTRIBUTED BY:

NTIS

National Technical Information Service
U. S. DEPARTMENT OF COMMERCE

UNCLASSIFIED

SECURITY CLASSIFICATION OF THIS PAGE (When Data Entered)

REPORT DOCUMENTATION PAGE		READ INSTRUCTIONS BEFORE COMPLETING FORM
1. REPORT NUMBER AFAPL-TR-74-89-3	2. GOVT ACCESSION NO.	3. RECIPIENT'S CATALOG NUMBER ADA-000 942
4. TITLE (and Subtitle) SOLAR COLLECTOR THERMAL POWER SYSTEM Volume III - Basic Study and Experimental Evaluation of Thermal Train Components		5. TYPE OF REPORT & PERIOD COVERED Final 16 Aug 1971 to 28 Jun 1974
7. AUTHOR(s) Robert Richter Xerox Corporation Electro-Optical Systems		6. PERFORMING ORG. REPORT NUMBER 4074-Final
9. PERFORMING ORGANIZATION NAME AND ADDRESS Xerox Corporation/Electro-Optical Systems 300 North Halstead Street Pasadena, California 91107		8. CONTRACT OR GRANT NUMBER(s) F33615-72-C-1092
11. CONTROLLING OFFICE NAME AND ADDRESS Air Force Aero Propulsion Laboratory/POE Wright-Patterson Air Force Base, Ohio 45433		10. PROGRAM ELEMENT, PROJECT, TASK AREA & WORK UNIT NUMBERS PE62203F Project 3145 Task 314519 Work Unit 31451940
14. MONITORING AGENCY NAME & ADDRESS (if different from Controlling Office) Air Force Aero Propulsion Laboratory Wright-Patterson Air Force Base, Ohio 45433		12. REPORT DATE November 1974
		13. NUMBER OF PAGES 284
		15. SECURITY CLASS. (of this report) Unclassified
16. DISTRIBUTION STATEMENT (of this Report) Approved for public release; distribution unlimited		15a. DECLASSIFICATION/DOWNGRADING SCHEDULE
17. DISTRIBUTION STATEMENT (of the abstract entered in Block 20, if different from Report)		
18. SUPPLEMENTARY NOTES Reproduced by NATIONAL TECHNICAL INFORMATION SERVICE U S Department of Commerce Springfield VA 22161		
19. KEY WORDS (Continue on reverse side if necessary and identify by block number) Thermal Space Power Heat Pipe Energy Transport Space Power System Study		
20. ABSTRACT (Continue on reverse side if necessary and identify by block number) The final Technical Report presents the work performed on the Solar Collector Thermal Power System (SCTPS) Program from 16 August 1971 to 28 June 1974. The report covers Phase I (Preliminary Technology and System Design Analysis) and Phase II (Experimental Evaluation of Component Performance) and is issued in three volumes. Volume I contains the system analysis for a solar collector thermal power system supplying thermal energy to a Vuilleumier cooler that is carried on a BMS type satellite. The analysis also investigates specific		

DD FORM 1 JAN 73 1473

EDITION OF 1 NOV 65 IS OBSOLETE

UNCLASSIFIED

SECURITY CLASSIFICATION OF THIS PAGE (When Data Entered)

UNCLASSIFIED

SECURITY CLASSIFICATION OF THIS PAGE(When Data Entered)

requirements of individual components of the power system, including the solar collector, heat pipes, and the thermal energy storage system. An extensive bibliography of pertinent heat transfer, solar collectors, and space power system reports is a part of this volume. Volume II presents the technical effort in the development of a 15-foot long primary heat pipe capable of transferring 6 kW of thermal power and its integration with the remaining components of a complete thermal train. The effort comprised the design, fabrication, and testing of the heat pipe as an individual component and the integration and testing with the secondary heat pipe, the thermal energy storage unit, and a radiation heat transfer joint. In Volume III, the basic studies and the experimental evaluation of thermal train components are collected. This includes the tests of subscale thermal energy storage capsules, the design, fabrication, and testing of the secondary heat pipe with its full scale thermal energy storage unit; the design, fabrication, and testing of subscale heat pipes for the evaluation of material compatibility; the design, fabrication, and testing of a subscale heat pipe with a cavity receiver; and a heat pipe wick study performed in support of the design of a second primary heat pipe and the subscale cavity heat pipe.

UNCLASSIFIED

SECURITY CLASSIFICATION OF THIS PAGE(When Data Entered)

FOREWORD

Volume III of this report, "Basic Studies and Experimental Evaluation of Thermal Train Components," comprises the effort of a number of individual contributors who are members of the staff of the Xerox Corporation, TRW, and the General Electric Company. The entire technical effort was under the direction of R. Richter of the Xerox Corporation. The basic input of Section III was submitted by O. O. Haroldson and E. S. Kovalcyk of TRW. The data of Section IV were provided by R. L. Hammel and R. Mendelsohn of TRW. The technical work reported in subsections 5.1 through 5.3 and subsections 7.1 through 7.4 were performed under the technical direction of T. F. Lyon of the General Electric Company. Subsections 5.4 through 5.5, Section VI, subsections 7.5 and 7.6, Section VIII, and Section IX are the technical contributions of the author.

The author acknowledges with thanks the support of the above-mentioned contributors for working as a team toward the success of the overall program.

CONTENTS

I	INTRODUCTION	1
II	TECHNICAL BACKGROUND	3
	2.1 Introduction	3
	2.2 Material Compatibility	3
	2.3 Component Operation	4
III	THERMAL TRAIN SUBSYSTEM PRELIMINARY STUDY	7
	3.1 Thermal Train Subsystem Function and Description	7
	3.2 Preliminary Thermal Train Subsystem Analysis	8
	3.2.1 Mechanical Design Analysis	8
	3.2.2 Preliminary Thermal Analysis of TTS	11
	3.3 Rotary Heat Pipe Joints	13
	3.3.1 Two Axis Gimbale Joint	13
	3.3.2 Single Axis Radiation Joint	20
	3.3.3 Radiation Joint Test	20
	3.4 Variable Conductance Heat Pipe Test	25
	3.5 High Emittance Coatings	25
	3.6 Thermal Insulation	27
	3.6.1 Material Description	29
	3.6.2 Performance of Insulation Systems	31
	3.7 Conclusions and Recommendations	36
IV	SUBSCALE HEAT PIPE DESIGN AND MANUFACTURING	39
	4.1 Introduction	39
	4.2 Hardware Description	40
	4.3 Preliminary Endurance Test Evaluation and Processing	45
	4.4 Endurance Testing	49
	4.5 Metallurgical Investigation of Localized Tube Wall Penetration	66
	4.6 Microprobe Analysis Report	78
	4.6.1 Background	78
	4.6.2 Analysis Performed	78
	4.6.3 Results Obtained	78
	4.7 Conclusions	80
V	THERMAL ENERGY STORAGE CAPSULE EVALUATION	89
	5.1 Introduction	89
	5.2 Test Series TTIV	90
	5.2.1 Test System - Test TTIV	90
	5.2.2 Test Conditions	92
	5.2.3 Test System Cyclic Operation	94
	5.2.4 Start-up Tests	103
	5.3 Cartridge Geometry Optimization Tests	103
	5.3.1 Test System - Tests TT2V and TT3V	105
	5.3.2 Thermal Cycle Tests	109
	5.3.3 First Endurance Test	119
	5.3.4 Analysis of Thermal Behavior During LiF Freezing	119
	5.3.5 Comparison of Calculated and Measured Cooling Curves	129

CONTENTS (Contd)

5.3.6	Thermal Behavior During LiF Melting	133
5.4	Extended Thermal Cycling of Subscale Thermal Storage Units	137
5.4.1	Thermal Behavior of Thermal Energy Storage Material	141
5.4.2	Long Duration Testing	151
5.5	Summary and Conclusion	153
VI	FULL SCALE ROTARY HEAT TRANSFER JOINT	161
6.1	Introduction	161
6.2	Design	161
6.3	Fabrication	161
6.4	Operation	169
6.5	Conclusion	175
VII	FULL SCALE SECONDARY HEAT PIPE WITH THERMAL ENERGY STORAGE UNIT	177
7.1	Introduction	177
7.2	Secondary Heat Pipe and Thermal Energy Storage Design	177
7.3	Fabrication	180
7.3.1	Cartridge Fabrication	180
7.3.2	Final Assembly of the Secondary Heat Pipe	183
7.3.3	Total System Weight	189
7.4	Test Setup	189
7.5	Testing	190
7.5.1	Steady State Power Losses	190
7.5.2	Transient Operation	195
7.6	Conclusions	213
VIII	SUBSCALE CAVITY RECEIVER AND HEAT PIPE	215
8.1	Introduction	215
8.2	System Evaluation	215
8.3	Design	217
8.4	Fabrication	227
8.5	Filling of Heat Pipe	230
8.6	Test Setup	230
8.7	Testing	238
8.8	Conclusion	249
IX	EXPERIMENTAL WICK STUDY	253
9.1	Introduction	253
9.2	Experimental Setup	253
9.3	Conclusion	268
REFERENCES		271

ILLUSTRATIONS

1	Typical BMS Type Solar Collector Thermal Power System	9
2	A Conceptual Thermal Train Subsystem	10
3	A Conceptual TTS Thermal Model	12
4	Conceptual Gimbaleed Radiative Joint Design	17
5	Conceptual Gimbaleed Radiative Heat Pipe Joint	19
6	Single Axis Rotary Radiative Joint - Concept 1	21
7	Single Axis Rotary Radiative Joint - Concept 2	21
8	Single Axis Rotary Radiative Joint - Concept 3	21
9	Rotary Joint Test Assembly - Preliminary Concepts	23
10	Stainless Steel/Sodium Variable Conductance Heat Pipe Operation	26
11	Apparent Conductivity of Idealized Test Samples	32
12	Typical Foil/Oxide Deposition Heat Flux	33
13	Effect of Compressor Loading on Insulation Heat Flux; Tantalum/ThO ₂ Particle Deposition	34
14	Corner Configuration Performance, Ta/ThO ₂ Particle Deposition	35
15	Parts for Six Subscale Heat Pipes	42
16	Close-up of Subscale Parts	42
17	Subscale Heat Pipe Assembly	43
18	Fill System	48
19	Filled Endurance Test Heat Pipes	48
20	Location and Extent of Tube Wall Change in Inconel Type SN-1	67
21	View of Tube I.D.	68
22	Damage Revealed as Inner Screen Was Removed	68
23	Wall Damage Seen After Removal of Screen	69
24	Reacted Region Seen on Tube Wall as Screens Were Removed	71
25	Cross Section of Wall Penetration	72
26	Cross Section of Reacted Zone Found 180° from Wall Penetration	72
27	Detail of the Corrosion Attack at the Reacted Region	73
28	Location of Regions Evaluated by Microprobe Analysis	75
29	Location of Failures in Subscale Heat Pipes SN 1 and SN 4	77
30	Photomicrograph Showing the Cross Section of a Failed Area of the Inconel Tube	81
31	Photomicrograph Showing Location No. 1	81
32	Photomicrograph Showing Location No. 2	81
33	Photomicrograph Showing Location No. 3	82
34	Photomicrograph Showing Location	82
35	Ni K α X-Ray Image	82
36	Fe K α X-Ray Image	83
37	Cr K α X-Ray Image	83
38	Cu K α X-Ray Image	83
39	P K α X-Ray Image	83
40	Ni K α X-Ray Image	84
41	Cr K α X-Ray Image	84
42	Na K α X-Ray Image	84

ILLUSTRATIONS (Contd)

43	Fe K α X-Ray Image	84
44	Cu K α X-Ray Image	85
45	Ni K α X-Ray Image	85
46	Fe K α X-Ray Image	85
47	Au M α X-Ray Image	85
48	Cu K α X-Ray Image	86
49	Cr K α X-Ray Image	86
50	Na K α X-Ray Image	86
51	Photomicrograph Showing the Outer Surface of the Inconel Tube Away from the Failed Area	87
52	Au M α X-Ray Image of the Outer Surface of the Inconel Tube Away from the Failed Area	87
53	Heat Pipe - Thermal Storage Unit Before Filling and Sealing	91
54	Heat Pipe - Thermal Storage Unit with heater and Thermocouples Attached	91
55	Test System for Heat Pipe - Thermal Storage Unit Calorimetric Tests	93
56	Steady-State (Isothermal) Heat Loss of HP-TES Unit TTI for Temperatures Near the LiF Melting Point	95
57	Heat Pipe - Thermal Energy Storage Unit Showing Thermocouple Locations	96
58	Temperature Variations of HP-TES Unit During Thermal Cycle #1	98
59	Variation in Temperature (TC #5) During Three Cycles Under Excess Power Conditions for Test Unit TTI	100
60	Temperature Variation (TC #5) of HP-TES Unit TTI During Three Cycles Under Nominal Power Input Conditions	101
61	Temperature Variation of Heat Pipe-Thermal Storage Unit During Startup with Power Input of 360 Watts and No Power Output	104
62	Heat Pipe/Thermal Energy Storage Configurations Investigated in Cartridge Geometry Optimization Tests	106
63	Interior of TT3 Test Unit Showing Three LiF Thermal Storage Cartridges	107
64	Heat Pipe/Thermal Energy Storage Test Setup for Test TT2V Showing Thermocouple Locations	108
65	Steady-State (Isothermal) Heat Loss for HP-TES Test TT2V for Temperatures Near the LiF Melting Point	110
66	Temperature Variation During Two Cycles Under Nominal Power Conditions for Test TT2V	111
67	Temperature Variation of TC #5 During Two Cycles Under 10% Excess Salt Conditions for Test TT2V	113
68	Temperature Variation of TC #5 During Two Cycles Under 20% Excess Salt Conditions for Test TT2V	113
69	Steady-State (Isothermal) Heat Loss for HP-TES Test TT3V (Three Cartridges) for Temperatures Near the LiF Melting Point	115

ILLUSTRATIONS (Contd)

70	Temperature Variation During Two Cycles Under Nominal Power Conditions for Test TT3V	116
71	Temperature Variation During Two Cycles Under 10% Excess Salt Conditions for Test TT3V	118
72	Temperature Variation During Two Cycles Under 20% Excess Salt Conditions for Test TT3V	118
73	Endurance Test Setup	120
74	Schematic of Endurance Test Setup	121
75	Calculated Freezing Pattern for Cylindrical Thermal Storage Cartridge Containing Lithium Fluoride	124
76	Radiographs of LiF Cartridge Inside Test Unit TT2 Following Testing	125
77	Cooling Curve for Test Unit TT2 for Nominal Power Conditions	130
78	Cooling Curve for Test Unit TT2 with 1.3 Times Normal Power	130
79	Cooling Curve for Test Unit TT2 with 1.8 Times Normal Power	131
80	Cooling Curve for Test Unit TT3 for Nominal Power Conditions	131
81	Cooling Curve for Test Unit TT3	132
82	Cooling Curve for Test Unit TT3	132
83	Temperature Variation of Test Unit TT2 During Energy Storage	134
84	Temperature Variation of Test Unit TT2 During Energy Storage	134
85	Temperature Variation of Test Unit TT2 During Energy Storage	135
86	Temperature Variation of Test Unit TT3 During Energy Storage	135
87	Temperature Variation of Test Unit TT3 During Energy Storage	136
88	Temperature Variation of Test Unit TT3 During Energy Storage	136
89	Conceptual LiF Melting Pattern in Cylindrical Cartridge	138
90	Insulation Requirement for Subscale Thermal Energy Storage System	139
91	Subscale Thermal Energy Storage Units TT2 and TT3 with Controls	140
92	Temperature Measuring Equipment for Subscale Thermal Energy Storage Unit Tests	140
93	Power Losses as Function of Operating Temperature of Subscale Thermal Energy Storage Unit TT2	142
94	Power Losses as Function of Operating Temperature of Subscale Thermal Energy Storage Unit TT3	143
95	Presentation of Heating and Cooling Cycle of Subscale Thermal Energy Storage Unit TT2	145
96	Presentation of Heating and Cooling Cycle of Subscale Thermal Energy Storage Unit TT3	146
97	Comparison of Fusion Energy Release Rates for the Two Subscale Thermal Energy Storage Units TT2 and TT3	148
98	Thermal Energy Storage Capsules TT2 and TT3 after Long Duration Endurance Testing	152

ILLUSTRATIONS (Contd)

99	Radiograph of Thermal Energy Storage Unit TT3 after 11 Months Cycling	154
100	Radiograph of Thermal Energy Storage Unit TT3 after 11 Months Cycling	155
101	Radiograph of Thermal Energy Storage Unit TT3 after 11 Months Cycling	156
102	Radiograph of Thermal Energy Storage Unit TT3 after 11 Months Cycling	157
103	Radiograph of Thermal Energy Storage Unit TT3 after 11 Months Cycling	158
104	Full Scale Rotary Heat Transfer Joint	162
105	Design Correlation for Rotary Radiation Heat Transfer Joint	163
106	Design Concept of Full Scale Rotary Radiation Heat Transfer Joint	164
107	Rotary Radiation Heat Transfer Joint	165
108	Rotary Radiation Heat Transfer Joint with Cooling Coils Under Glass Tape	167
109	Rotary Radiation Heat Transfer Joint with Inner Insulation Sleeve Over Cooling Coils	167
110	Rotary Radiation Heat Transfer Joint with Four Layers 3/8-inch Thick Flex Min-K Insulation Over Inner Insulation Sleeve	168
111	Rotary Radiation Heat Transfer Joint with Final Layers of 1/2-inch Thick Cera-Felt Insulation	168
112	Rotary Radiation Heat Transfer Joint with Insulation Shown	170
113	Rotary Radiation Joint	170
114	Rotary Radiation Heat Transfer Joint Fully Assembled	171
115	Rotary Radiation Heat Transfer Joint Installed	171
116	Test Setup of Rotary Radiation Heat Transfer Joint	172
117	Enthalpy Increase of Water Due to Evaporation and Superheating	173
118	Flow Calibration of a Nominal 0.010-inch Orifice	174
119	Completed Assembly Filled with Sodium and Sealed	178
120	Secondary Heat Pipe with 3 kW Thermal Energy Storage Systems	179
121	Thermal Storage Cartridge	181
122	Automatic Welding of Cartridge Tubes	182
123	LiF Filled Cartridge Before and After Wick Application	184
124	Inner Tube Assembly after Welding	186
125	Inner Tube Assembly with One Cluster of Cartridges Attached	187
126	Completed Inner Tube Assembly	188
127	Secondary Heat Pipe Heater	191
128	Insulation Requirement for Full Scale Secondary Heat Pipe with Thermal Energy Storage System	192

ILLUSTRATIONS (Contd)

129	Setup for Testing of Secondary Heat Pipe with Rotary Radiation Heat Transfer Joint	193
130	Secondary Heat Pipe with Insulation, Thermocouples, and Heaters Installed	194
131	Control Stands for Secondary Heat Pipe Test	194
132	Energy Losses from Fully Insulated Secondary Heat Pipe with Rotary Radiation Heat Transfer Joint	196
133	Temperature History of Secondary Heat Pipe and Thermal Energy Storage Unit During One Heating and Cooling Cycle	197
134	Energy Storing and Energy Release History of Thermal Energy Storage Unit and Secondary Heat Pipe	200
135	Temperature History of Secondary Heat Pipe and Thermal Energy Storage Unit During One Heating and Cooling Cycle	202
136	Thermal Energy Release History of Thermal Energy Storage Unit and Secondary Heat Pipe	203
137	Temperature History of Secondary Heat Pipe and Thermal Energy Storage Unit During Energy Release	205
138	Temperature History of Secondary Heat Pipe and Thermal Energy Storage Unit During Energy Release	205
139	Temperature History of Secondary Heat Pipe and Thermal Energy Storage Unit During Energy Release	206
140	Temperature History of Secondary Heat Pipe and Thermal Energy Storage Unit During Energy Release	206
141	Temperature History of Secondary Heat Pipe and Thermal Energy Storage Unit During Energy Release	207
142	Temperature History of Secondary Heat Pipe and Thermal Energy Storage Unit During Energy Release	207
143	Thermal Energy Release History of Thermal Energy Storage Unit and Secondary Heat Pipe	208
144	Thermal Energy Release History of Thermal Energy Storage Unit and Secondary Heat Pipe	208
145	Thermal Energy Release History of Thermal Energy Storage Unit and Secondary Heat Pipe	209
146	Thermal Energy Release History of Thermal Energy Storage Unit and Secondary Heat Pipe	209
147	Thermal Energy Release History of Thermal Energy Storage Unit and Secondary Heat Pipe	210
148	Thermal Energy Release History of Thermal Energy Storage Unit and Secondary Heat Pipe	210
149	Effect of Energy Release Rate on the Final Temperature of the Secondary Heat Pipe after Thermal Energy Extraction	211
150	Optical Dimensions for Receiver and Collector Calculations	216

ILLUSTRATIONS (Contd)

151	Test Setup for Cavity Mechanical/Thermal Integrity Tests	218
152	Condenser Cooling Coil Configuration	219
153	Heat Pipe Dimensions	221
154	Heat Pipe Design Dimensions	222
155	Area Ratio of Wick and Vapor Flow Pass as Function of Angle	223
156	Pressure Drops and Available Pressure for a Heat Pipe Design with a Wick-to-Vapor-Flow Area Ratio of 0.5	225
157	Pressure Drops and Available Pressure for a Heat Pipe Design with a Wick-to-Vapor-Flow Area Ratio of 1	226
158	Receiver	228
159	Insulation Requirement for Spherical Receiver Heat Pipe	229
160	Spherical Receiver/Heat Pipe with Heat Exchanger	231
161	Spherical Receiver	232
162	Thermocouple Arrangement for Cavity/Heat Pipe Interface	233
163	Subscale Cavity Heat Pipe with Auxiliary Heater	234
164	Calibrated Volume and Pressure Gages in Fill Station	235
165	Fill Station	235
166	Fully Insulated and Instrumented Cavity/Heat Pipe	236
167	Cavity with Shield and Insulation	236
168	Cavity Heat Pipe Test Setup	237
169	Temperature Distribution Along Subscale Cavity Heat Pipe	239
170	Temperature Distribution Along Subscale Cavity Heat Pipe	240
171	Temperature Distribution Along Cavity Heat Pipe After Improvement of Insulation	241
172	Temperature Distribution Along Subscale Cavity Heat Pipe	242
173	Temperature Distribution at Steady State for Subscale Cavity Heat Pipe	244
174	Temperature Distribution Along Subscale Cavity Heat Pipe	245
175	Calibration of Orifice for Subsonic Flow	246
176	Experimentally Established Correlation Between Upstream Pressure and Downstream Pressure of Measuring Orifice	247
177	Measured Correlation Between Power Input, Power Losses and Power Extraction at Condenser	248
178	Temperature Distribution Along Cavity Heat Pipe During Radiation Test	250
179	Apparent Radiation Power on the Cavity Receiver as Function of Power Input into the Radiation Source	251
180	Wick Study Fixture (1 of 3)	255
181	Wick Study Fixture (2 of 3)	256
182	Wick Study Fixture (3 of 3)	257
183	Wick Study Test Fixture	258
184	Wick Study Setup Schematic	259
185	Laboratory Setup for Wick Study	260

ILLUSTRATIONS (Contd)

186	Correlations Between Pressure Difference and Flow Rate	261
187	Correlations Between Pressure Difference and Flow Rate	263
188	Correlations Between Pressure Drop and Flow Rate Through Wick Structure	264
189	Correlations Between Pressure Drop and Flow Rate Through Wick Structure	265
190	Pressure Drop Across a Wick Structure	266
191	Permeability K for Standard Bolting Cloth	267
192	The Available Flow Factor $\Delta p x K$ as a Function of the Packing Factor	269

TABLES

I	Analysis Results	14
II	Heat Pipe Design Requirements - Heat Pipe Loads	15
III	Heat Pipe Design Requirements - Heat Pipe Interface Conductances	15
IV	High Temperature, High Emittance Coatings	28
V	Foil Properties	30
VI	Recommended Insulation System Thermal Design Values	37
VII	Solar Collector Primary Heat Pipe - Comparison of Design Parameters	41
VIII	Subscale Heat Pipe - Bill of Materials	44
IX	Subscale Heat Pipe - Comparison of Test with Calculated Design Parameters	46
X	Heat Pipe Life Test (Heat Pipe No. 1)	50
XI	Heat Pipe Life Test (Heat Pipe No. 2)	51
XII	Heat Pipe Life Test (Heat Pipe No. 3)	56
XIII	Heat Pipe Life Test (Heat Pipe No. 4)	59
XIV	Heat Pipe Life Test (Heat Pipe No. 5)	60
XV	Heat Pipe Life Test (Heat Pipe No. 6)	61
XVI	Summary of Integrated Test Times - Subscale Endurance Test	64
XVII	Relative X-Ray Intensity	76
XVIII	Elements Detected in Spectral Scans of Failed Tube	79
XIX	Complete Test Data for Cycle No. 18 (Test TTIV) Under Nominal Power Conditions	102
XX	Comparison of Maximum Temperature Variation of T5 during Cyclic Operation for Test Series TT2V and TT3V	119
XXI	Test Data from 1000-Hour Cycling Test	122
XXII	Fertinent Data for Thermal Energy Storage Units TT2 and TT3	150
XXIII	Materials, Thermophysical Properties for 3 kW HP/TES Design	180
XXIV	Cartridge Weights	185
XXV	Thermal Energy Storage System Weight	189
XXVI	Radiation Heat Transfer Joint and Secondary Heat Pipe with Thermal Energy Storage Unit	212

SECTION I

INTRODUCTION

In Volume I of this report, the Preliminary Technology Systems Study of a solar collector thermal power system was presented. Volume II of this report comprised the effort for the design and testing of a 15-ft long primary heat pipe and its mating with the remaining components of a thermal power train. In this third and last volume of this report, the results of the basic studies and the experimental evaluation of thermal train components except for the primary heat pipe are collected.

A considerable amount of background for the final design and operation of a solar collector thermal power system lies in the area of materials properties and long-time effects of operating conditions on materials and their combinations. This type of background cannot be established by analytical means alone but requires experimental evaluation and verification.

In support of and prior to the experimental effort, a Thermal Train Subsystem Preliminary Study was undertaken by TRW under subcontract to Xerox Corporation. The results of this study are presented in their entirety in Section III of this volume with corrections and editorial modifications by the author. It is quite obvious that some of the approaches presented in Section III of this volume are inconsistent or even in disagreement with the baseline Solar Collector Thermal Power System which is presented in Volume I of this report. However, since the basic findings and conclusions are technically correct and might be of value at a later date for a different system, the study has been included in its entirety and without deletion of concepts which were rejected by the overall systems study presented in Volume I.

Before the start of this program, some experimental work had already been conducted by other investigators and by contributors to this program. For instance, lithium fluoride as thermal energy storage material had been used and experimentally evaluated by the General Electric Company as reported in Section V. The investigation of lithium fluoride as thermal energy storage material was extended under this program and additional experimental and analytical work was carried out in an attempt to understand the behavior of the thermal energy storage material when undergoing a phase change. Because the analysis is very much predicated on the operation in a 1-g gravitational field, the results might not be fully applicable in the zero-g environment encountered in space and must therefore be critically evaluated as was done in Volume I, Subsection 2.1.4.5.

All original contributions to this volume were substantially modified and revised by the author of this report to assure consistency in their presentation and in the content of the material presented in this report.

SECTION II

TECHNICAL BACKGROUND

2.1 INTRODUCTION

In this volume of a three volume report, the basic studies and experimental evaluation of thermal train components are presented. Most of the need and requirements for the experimental effort described are based on the study which is presented in Section III of this volume. The major problems exposed by the study were materials compatibility, behavior of thermal energy storage material, heat transfer across a thermal joint, high power density energy transfer through a heat pipe, and the characteristic of wick material in heat pipes. These problems were investigated under six separate tasks. As each task was only a part of the larger overall effort in establishing the feasibility of a solar collector thermal power system, it is understandable that none of the investigations could solve all technical questions underlying the stated problems. Each investigation had to address itself to a limited aspect pertaining to the need of the overall requirements of the solar collector thermal power system.

2.2 MATERIAL COMPATIBILITY

In the evaluation of safe combinations of materials, sufficient data for reaching conclusive decisions were missing. No tests had been conducted with material combinations over the length of time that were under consideration for the life time of the solar collector thermal power system in space. The most appropriate material for encapsulating the thermal energy storage material which the study suggested, lithium fluoride salt, appeared to be Cb-1% Zr. No failure in the containment of LiF in Cb-Zr. had been recorded. This material appeared also to be compatible with sodium at high temperature which was to be the working fluid for the heat pipe.

For the heat pipe, a high nickel alloy or columbia 1%-zirconium appeared to be appropriate. While Cb-1% Zr seemed to have the strength and the compatibility with sodium at the high operating temperature, it has the disadvantage of oxidizing in air at elevated temperatures. Testing in the laboratory and prelaunch operation would have required a vacuum tight sleeve which would have presented great technical difficulties. Inconel 600, which was the most available structural material, was selected for the heat pipe tube material. A considerable amount of operational time had been accumulated with a similar material, Inconel 800, and sodium, though at operating conditions which were in several aspects quite different from those conditions for which the solar collector thermal power system heat pipes had to be designed. The important additional requirement of a

heat pipe when operating in space is a high creep strength at high temperatures. The internal pressure of the heat pipe is equal to the vapor pressure of the working fluid which is a function of the operating temperature of the heat pipe. Since the study indicated that the operating temperature would be high and the diameter of the heat pipe would be relatively large under conditions of no external pressure, the stresses on the heat pipe were found relatively high compared to the creep strength of compatible material. To minimize the number of materials, Inconel was also selected as the material for the wick of the heat pipe.

With the combination of four materials operating at a relatively high temperature, the uncertainty of chemical interactions is quite high. Since time plays a large factor in many common chemical rate determined reactions, only real time tests could furnish the answers required for building a system that can operate over the intended length of time without failure due to material deterioration. However, evaluation of material compatibility requires not only long duration operation. Testing might have to be repeated with different combinations which will demand long duration testing again. Time for the development of the solar collector thermal power system was and will therefore remain most critically determined by the evaluation of materials and their availability.

For the above stated reasons subscale heat pipe tests were initiated which are presented in Section IV of this volume. It was attempted to simulate as many of the pertinent operating conditions of a full scale heat pipe as possible. Naturally, scaling down of all pertinent parameters at the same time is not possible, but the power transfer density along the heat pipe, the operating temperature, and the materials which the full scale heat pipe would have had to be designed for were scaled. The power density at the evaporator could not be simulated because no electric heater could generate the power densities that are available with a focused radiation energy source. In Section V of this volume, long duration operation experiments with subscale thermal energy storage capsules are described. In these tests, the behavior under repeated cycling of the Cb-1% Zr capsules containing LiF were to be investigated. Such tests were very representative of the actual conditions to be encountered in the final system. While the results of a year long testing were very positive, it would be very dangerous to extrapolate to 5 years operation.

2.3 COMPONENT OPERATION

A considerable amount of work can be performed analytically in predicting the operational behavior of components. However, experimental verification is needed for giving confidence that all known parameters have been fully taken into account in the analysis and that the effects either overlooked or considered minor do not have a larger influence than expected.

The testing of the subscale thermal energy storage units, as described in Section V was designed to generate data to confirm the analytically predicted behavior of the thermal energy storage material.

It was predicted that, during solidification, a considerable temperature drop would occur across the solidified material when conducting the latent heat of fusion from the molten core to the outer surface. Similarly during melting, the temperature of the capsule wall should exceed the melting temperature of the thermal storage material to allow heat transfer through the molten material to the solid material. Furthermore, there were indications that during energy extraction, heat exchange might have to take place in a radiative mode between the thermal energy storage material and its container wall. This could lead to an additional temperature drop because by contraction during freezing, the thermal energy storage material will lose contact with the container wall.

Several methods for improving the design of the thermal energy storage units for minimizing the temperature differentials that are imposing limitations on the overall thermal train design were to be evaluated. Some of the parameters that warranted further experimental investigations were:

- a. Number of capsules
- b. Length of capsules
- c. Configuration of capsules
 - (1) Circular cylinders
 - (2) Elliptic cylinders
- d. Finning of internal capsule surface
- e. Percent of void during fill of capsules
- f. Hollow core design

The trend caused by many of the above-mentioned parameters can fairly easily be evaluated analytically. For confirming, however, the optimum design available for the final application, testing of the new configurations was felt necessary. The tests were also required to prove that capsules can maintain their integrity after many cycles at a high temperature.

The design, manufacturing, and testing of the subscale cavity receiver and heat pipe is presented in Section VIII of this volume. This task falls also into the category of hardware confirmation of analytically predicted operation prior to committing larger resources to the building of full scale components. The wick study which is included in Section IX was a task which should have been part of the initially planned program. When, however, the design and manufacture of the first primary heat pipe was contracted, the impression was given that the characteristic of wick structures made of bolting cloth was fully known and that the effect of the wick construction on the final performance was well understood. The testing of the first primary heat pipe, as described in Section II of the second volume of this report, proved that the internal design of heat pipes needed further background studies. The wick study furnished needed data for the design and building of the second primary heat pipe.

The subscale spherical heat pipe task and the wick study demonstrated very dramatically the value of generating background information prior to designing and operating full scale components. The cost effectiveness can easily be demonstrated when comparing the cost of the supporting tasks with the cost of trial and error solutions with full scale components.

SECTION III

THERMAL TRAIN SUBSYSTEM PRELIMINARY STUDY

Under contract to Xerox Corporation, TRW Systems conducted preliminary studies of certain areas of the Thermal Train Subsystem. The objective of the long range program is to develop, fabricate, and assemble components for a Thermal Train Subsystem (TTS), with which the feasibility and performance of a Solar Collector Thermal Power System can conclusively be demonstrated. The present study was aimed at defining some of the problem areas in the TTS, and suggesting approaches to this solution. Specific areas of investigation included an overall TTS configuration, a rotary thermal joint design, a composite heat pipe design, and materials.

3.1 THERMAL TRAIN SUBSYSTEM FUNCTION AND DESCRIPTION

For the representative satellite system the Solar Collector Thermal Power System has to deliver continuously approximately 3 kW to a Vuilleumier cooler (VM). The purpose of the Thermal Train Subsystem (TTS) is to receive solar radiation from a solar collector and transfer that energy to the VM interface and to a thermal energy storage unit. Since energy is needed at a constant rate during an entire orbit, the TTS functions as a storage system and modulator to accommodate orbit variations and eclipse periods.

The TTS capable of accomplishing these functions in a ground test includes the following basic components:

- a. Cavity solar heat receiver
- b. Heat pipes
- c. Rotary heat pipe joints
- d. Thermal energy storage unit
- e. VM refrigerator interface (simulated)
- f. Insulation and structural supports
- g. Calorimeter for acceptance and ground demonstration testing.

These components must be packaged as a subsystem which will reliably function for a period of three to five years and which will accommodate

the expected mission restraints of a BMS type vehicle. For purposes of this study, it was assumed that a BMS type vehicle will be placed into a 400 n. mi. orbit (100 minute period), inclined 67° . Maximum shade time will be 35 minutes and because of orbital precession, the solar vector relative to the spacecraft is virtually unlimited. The TTS will operate between 1300° and 1700° F with the actual temperature of each component established only after the type of fusible material for the storage unit has been selected and the TTS layout has been made. The VM cooler interface will operate nominally at 1250° F $\pm 20^{\circ}$.

3.2 PRELIMINARY THERMAL TRAIN SUBSYSTEM ANALYSIS

3.2.1 MECHANICAL DESIGN ANALYSIS

The subsystem study efforts initially consisted of defining practical BMS type solar collector thermal power systems for which the TTS could be analyzed and evaluated. Since many spacecraft configurations can satisfy the BMS type mission, a baseline design was defined which included and satisfied all of the known mission requirements. This initial baseline BMS type solar collector thermal power system configuration is shown in Figure 1. It can be seen that this typical system includes the following BMS type mission considerations:

- a. The sensor systems are positioned to meet the mission viewing requirements without blockage from other elements.
- b. Velocity vector stabilized spacecraft body section with proportions typical for equipment and radiator area requirements.
- c. Solar collector/cavity receiver stowed on the launch axis, and having proportions compatible with power requirements.
- d. Gimbaling which provides deployment from the stowed position to the operational sun tracking position, and which allows for continuous unshadowed sun tracking throughout the mission.
- e. The gimbaling and tracking concept can also support the required solar cell electrical power system without blockage of sensor systems viewing requirements.

From this Solar Collector Thermal Power System concept, the initial baseline Thermal Train Subsystem configuration as shown in Figure 2 was derived. This subsystem consists of the following elements:

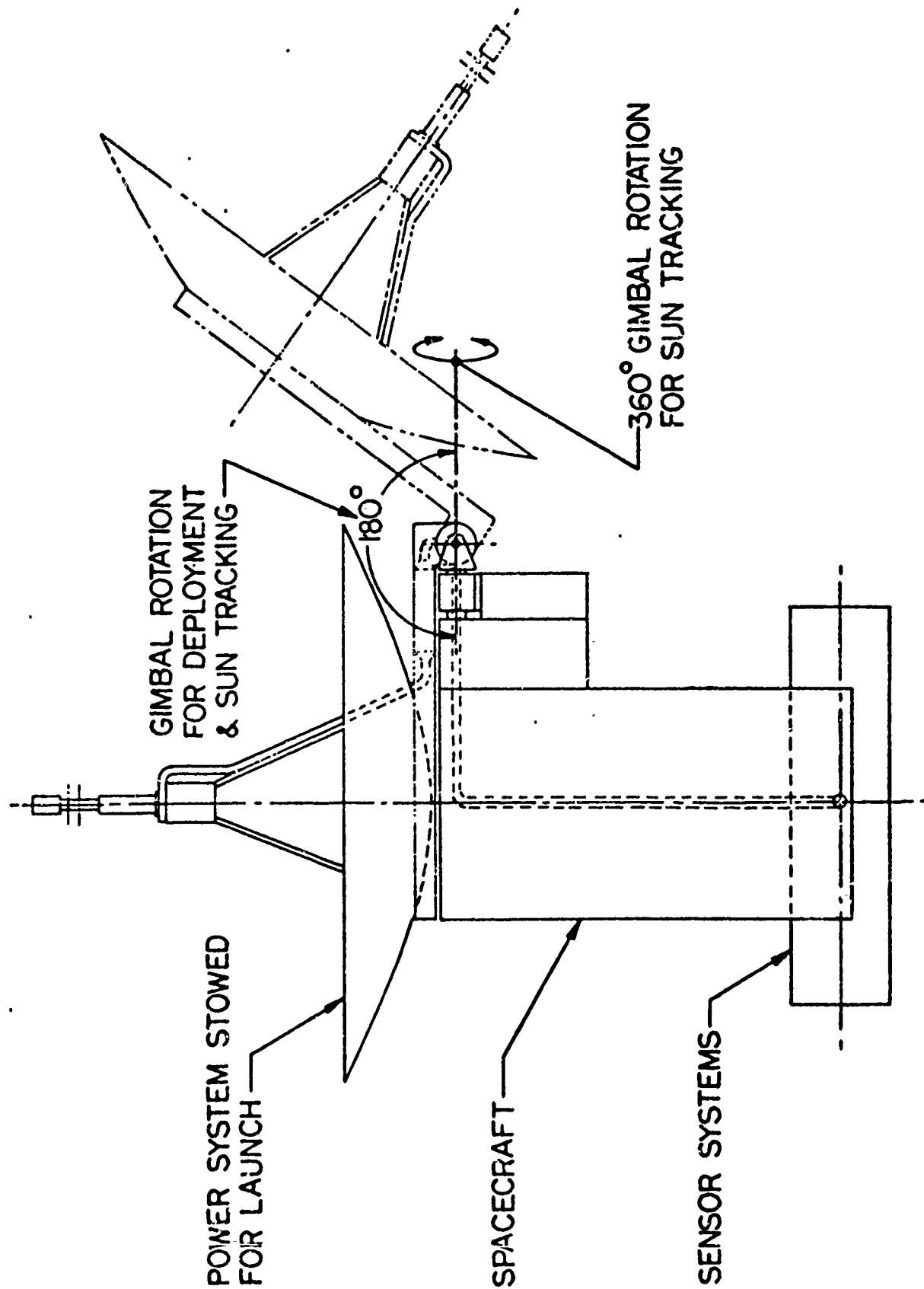


Figure 1. Typical BMS Type Solar Collector Thermal Power System

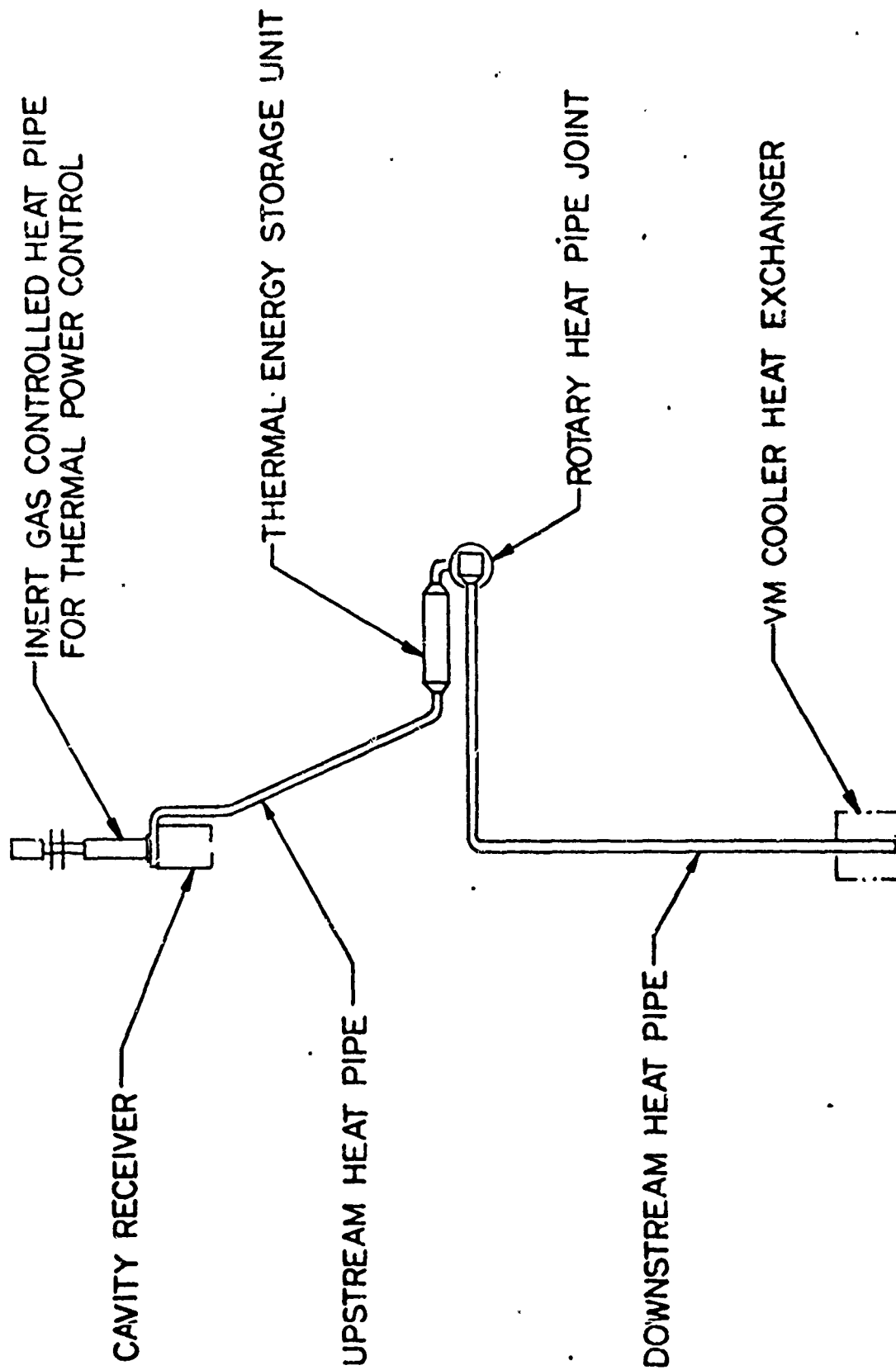


Figure 2. A Conceptual Thermal Train Subsystem

- a. Cavity solar energy receiver
- b. Thermal energy storage unit (TES)
- c. Rotary gimbaled heat pipe joint
- d. Vuilleumier (VM) cooler heat exchanger
- e. Heat pipe systems to absorb, transmit and deliver thermal power to the VM cooler system.
- f. Inert gas controlled heat pipe for rejection of excess power

To allow for sensor scanning motion, a single axis rotating joint was introduced at the VM cooler interface.

Other practical systems and TTS alternatives could be considered as proposed in Reference 1. They include:

- Body mounted sensor systems
- Slotted cavity receivers
- Spherical receiver concepts
- Other TTS control schemes and requirements
- Other locations for TES and control elements
- Other VM cooler heat exchanger concepts

However, in the present study, only the described subsystem was considered from a systems point of view.

3.2.2 PRELIMINARY THERMAL ANALYSIS OF TTS

A simple thermal analysis of the TTS as depicted in Figure 2 was formulated for establishing the general thermal characteristics and isolate any severe errors in the design.

The model used in the thermal analysis is shown in Figure 3. The assumptions underlying the analysis are as follows:

- Melting temperature of thermal energy storage (TES) material is 1560°F (LiF salt)
- VM engine requires 2300 watts

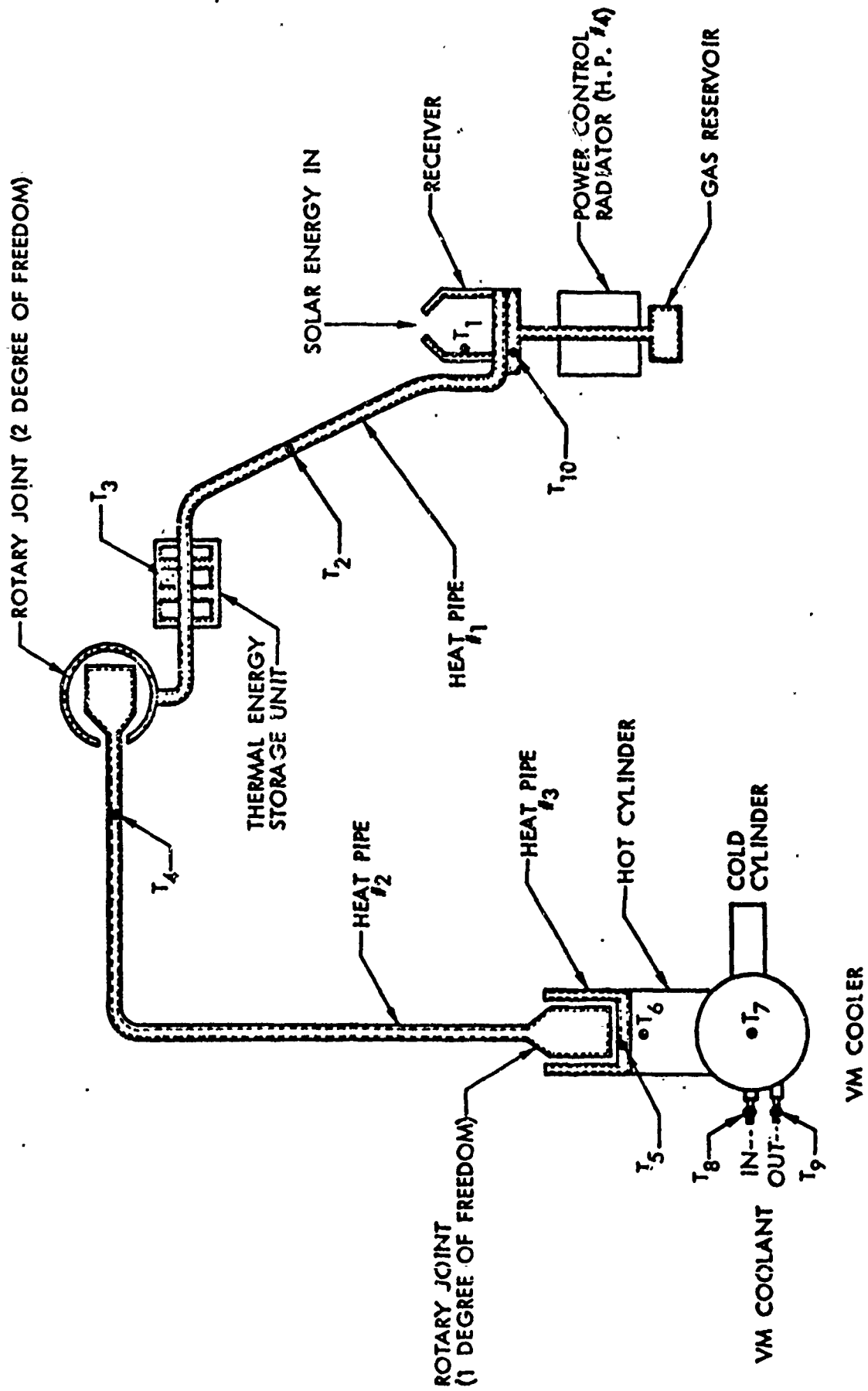


Figure 3. A Conceptual TTS Thermal Model

- No insulation and receiver losses
- Rotary joint area at VM cooler is 4.2 ft^2
- Two-axis rotary joint area is 1.44 ft^2
- Power control radiator temperature differential from full ON to full OFF is 30°F

The analysis was made for three cases

- a. Eclipse
- b. Solar radiation with the TES material in the process of melting
- c. Solar radiation with the TES material completely melted

The results are given in Table I. They indicate that certain severe constraints might exist in the actual subsystem. First, it apparently makes little difference where the gas-loaded heat pipe is placed from a thermal control point of view. Rather, the control of the temperature at the VM interface is closely tied to the joint conductances at the thermal storage connections. The greater the conductances (the larger the temperature differentials), the less temperature control at the VM interface. From this limited analysis, it is not obvious that a gas-loaded heat pipe by itself will be capable of controlling the VM interface temperature adequately.

The most obvious method of overcoming such a shortcoming is to install a variable conductance joint in the system.

From this analysis heat pipe requirements can be established. Tables II and III list this information.

3.3 ROTARY HEAT PIPE JOINTS

In order to support the analytical model presented in Figure 3, both one and two axis radiative heat pipe joints were sized and configured for estimating losses and thermal performance. In addition, consideration was given to methods of testing joint concepts.

3.3.1 TWO AXIS GIMBALED JOINT

The solar collector thermal power system, as presented in Figure 1, requires heat transport across a two-axis gimbal joint. A rotation of 360° is required to accommodate the primary sun tracking motion during orbit operations, and 180° of rotation about a second axis is

TABLE I
ANALYSIS RESULTS*

	<u>Case 1 eclipse</u>	<u>Case 2 solar melting TES</u>	<u>Case 3 solar TES melted</u>
Hot cylinder temperature (°F)	1230	1251	1307
VM engine Q (watts)	2300	2300	2300
Heat loss H.P. No. 4 (watts)	62	65	1765
Thermal storage net Q (watts)	-2362	1700	0.0
Receiver heat input (watts)	0.0	4065	4065

*Insulation and receiver losses not included

TABLE II
HEAT PIPE DESIGN REQUIREMENTS
HEAT PIPE LOADS

	<u>Max Q (watts)</u>	<u>Max operating temp (°F)</u>
Heat pipe No. 1	4065	1605
Heat pipe No. 2	2300	1426
Heat pipe No. 3	2300	1313
Heat pipe No. 4	1765	1590

TABLE III
HEAT PIPE DESIGN REQUIREMENTS
HEAT PIPE INTERFACE CONDUCTANCES

	<u>Conductance Btu/hr-°F</u>
Receiver to H.P. No. 1	430
TES to H.P. No. 1	655
H.P. No. 1 to H.P. No. 4	360
H.P. No. 1 to joint surface	650
H.P. No. 2 to joint surface	650
H.P. No. 2 to H.P. No. 3 interface surface	650
H.P. No. 3 to H.P. No. 2 interface surface	650

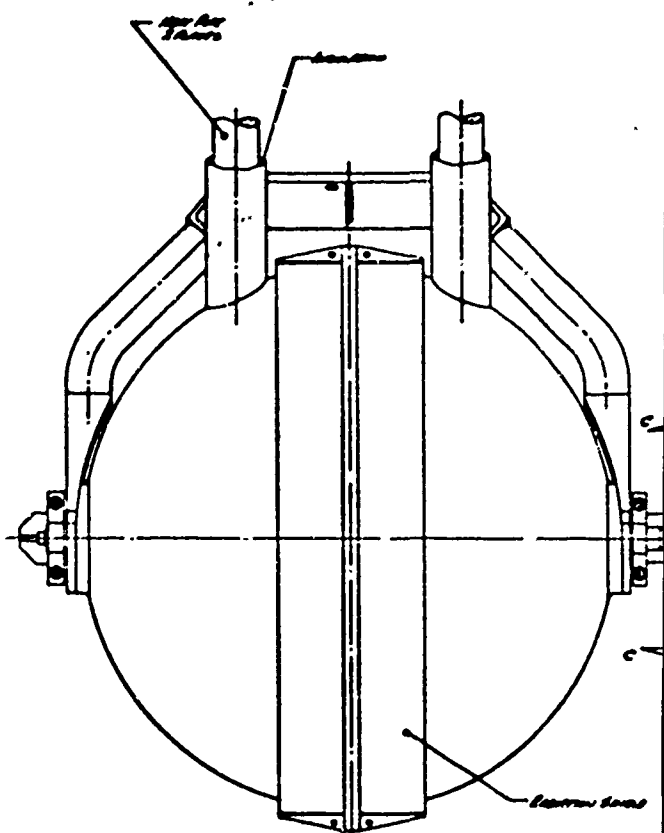
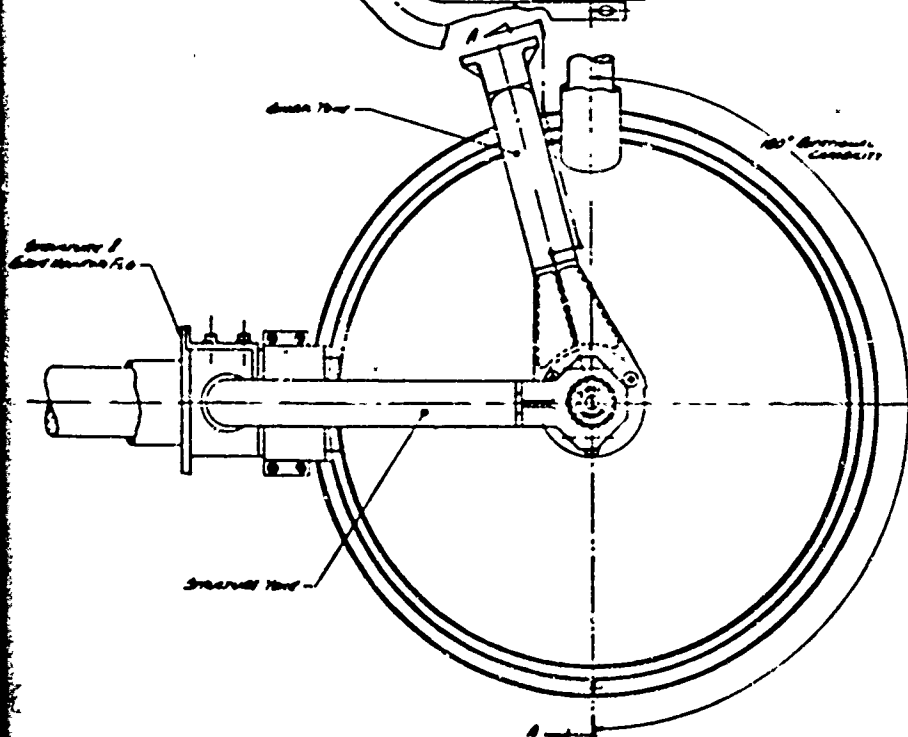
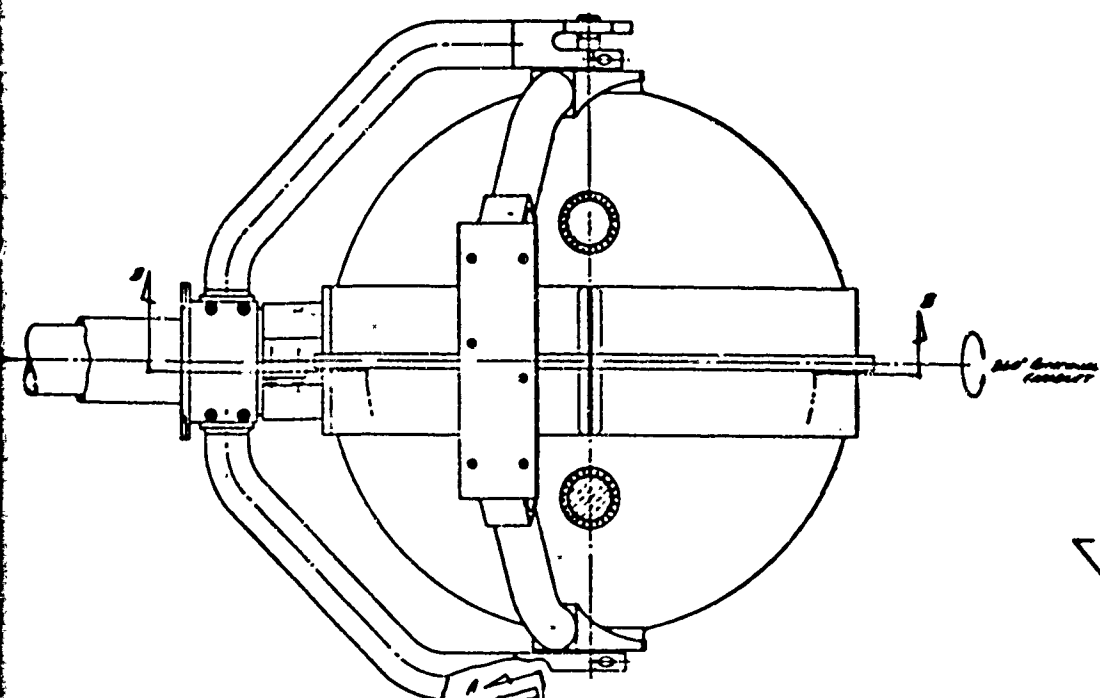
necessary to allow collector deployment and sun tracking in the elevation. Layout L-123437 (Figure 4) and Figure 5 present a concept of a radiative joint which would satisfy these requirements. The joint consists of two upstream heat pipes. Each terminates in a hemispherical chamber for emitting thermal energy to the downstream heat pipe system. The downstream heat pipe has a spherical absorber/evaporator section leading to a small diameter heat pipe. This small diameter heat pipe is stationary with respect to the mechanical gimbaling arrangement. The emitter and absorber radiating surfaces are coated with a high temperature, high emittance material for high heat transfer efficiency.

The emitter side of the joint is designed as two separate heat pipe systems in order to provide better heat pipe wick configurations and a more favorable pressure vessel design as compared to a single slotted spherical emitter. Also, the two separate halves provide a simpler assembly approach.

The two hemispherical halves are joined completely enclosing the spherical absorber, except for a 180° slot which provides for one axis gimbal rotation. For the reduction of losses, a radiation shield is attached to the structural yoke to cover the slot in all gimbal positions. The emitter heat pipe and the radiation shield are insulated by a high temperature multi-layer radiation blanket. Thin-wall pressure vessel and container insulation design is used to minimize weight and losses due to conduction heat transfer. The mechanical portions of the joint are thermally insulated from the heat pipe, and this can be of conventional spacecraft structural design.

Mechanically, the gimbal consists of a structural yoke which rotates the entire emitter portion (including gimbal yoke and attached solar collector) about the stationary absorber heat pipe. The primary sun tracking motion occurs about this axis for which 360° of angular rotation is required. Bearings and drive system would be attached at the mounting flange shown in the layout. The drive mounting flange for the other axis of rotation is shown in View C-C. This drives the upstream portion of the thermal train through the 180° rotation as required for deployment and sun tracking in the elevation angle. Bearings for the elevation axis are located in the insulated low temperature portions of the joint. To minimize friction, operating clearances are maintained for relative motion between the various parts of the gimbal by the low friction bearings supporting each gimbal portion.

The motions of the two-axis gimballed joint described above could also be accomplished by two separate one-axis joints. However, this configuration would require two separate temperature drops in the thermal system. Thus, the combined two-axis gimbal is much more desirable for gimballed sun tracking.



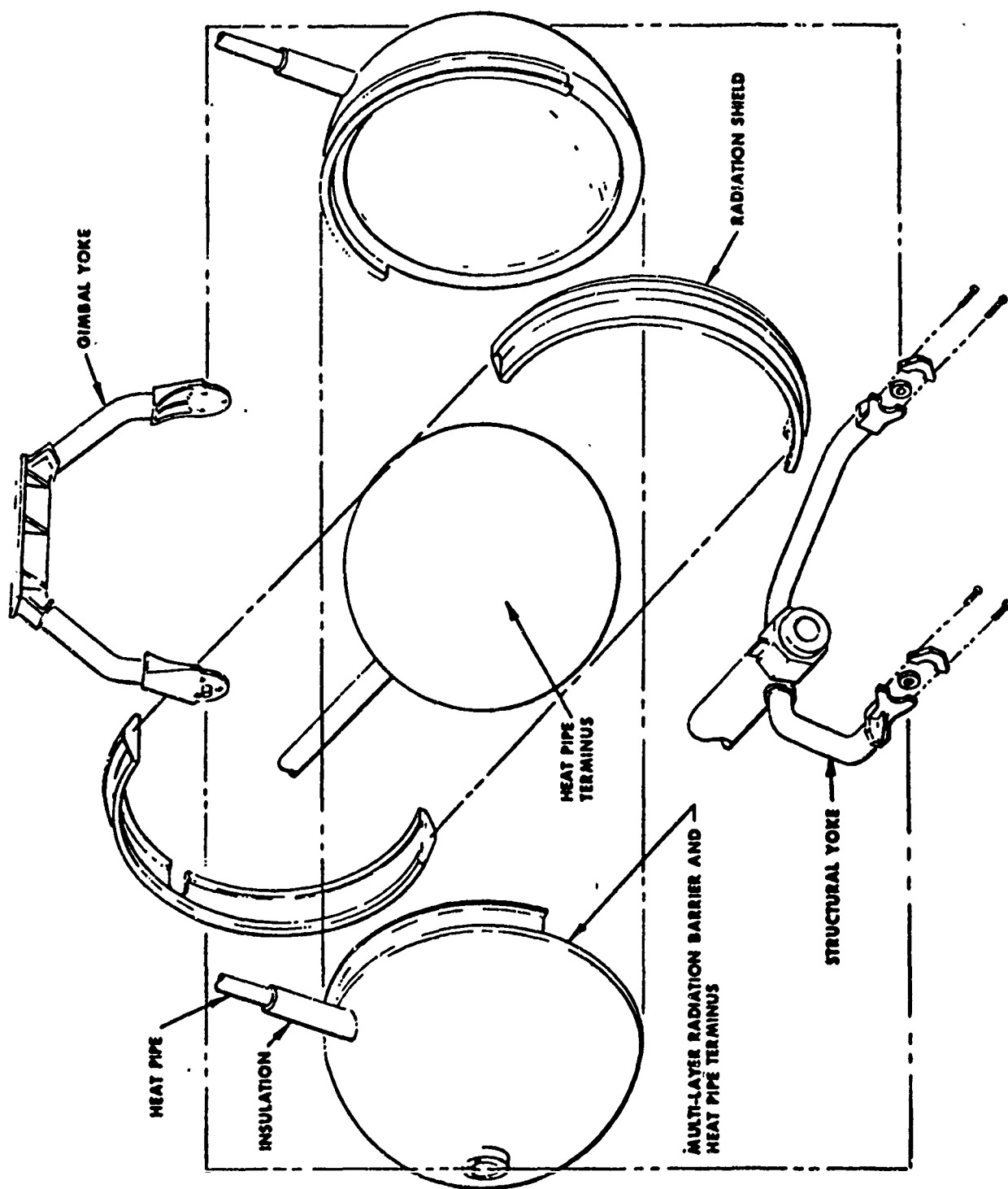


Figure 5. Conceptual Gimballed Radiative Heat Pipe Joint

In any event, the joint described above points out several problems which will be encountered if a double-axis joint must be employed. Most important, such a joint will have to be relatively large, about 1 foot in diameter. This causes weight problems, alignment problems, and of course problems associated with the heat pipe design.

In spite of these problems, a TTS, requiring a double-axis joint, could have advantages. For this design a smaller non-slotted solar collector could be used. It also allows for much greater latitude in vehicle orientation. Only an in-depth systems analysis in which all aspects of the problem are considered could finalize the selection.

3.3.2 SINGLE AXIS RADIATION JOINT

The single axis rotary joint has its best application at the VM cooler interface where the required sensor scanning motions must be considered. Figures 6, 7, and 8 depict concepts of simple joints which could be used in this area. In all cases, the heat pipe arrangement is essentially the same. Only the insulation changes to any appreciable extent. The adequacy of such a joint will hinge largely upon the ability of the insulation to limit thermal losses. It will be necessary to conduct tests for establishing the heat transfer efficiency of a joint.

3.3.3 RADIATION JOINT TEST

A test of a single axis radiation joint is contemplated to establish joint feasibility. For such a joint test to be worthwhile, essentially a full-detail joint has to be tested, which should be at least half-scale and preferably full-scale. Also the joint test should not only establish the feasibility of a joint but should also investigate problems associated with providing a "thermal switch" in the TTS. Starting with a basic configuration suggested by Xerox, the test fixture shown in layout L-123459 (Figure 9) was conceived for this dual purpose.

Basically, it consists of the following major parts:

- a. An emitter heat pipe operating at about 1500⁰F which receives its heat from an electrical heater.
- b. A heat receiver which transfers its heat to a water cooled calorimeter or else is itself an air cooled calorimeter.
- c. A rotating insulation cup which has a section cut out to allow radiation interchange between the receiver and emitter.
- d. A drive assembly for changing the position of the rotating insulation cup.
- e. Exterior multi-foil insulation for prevention of heat loss from the test article.

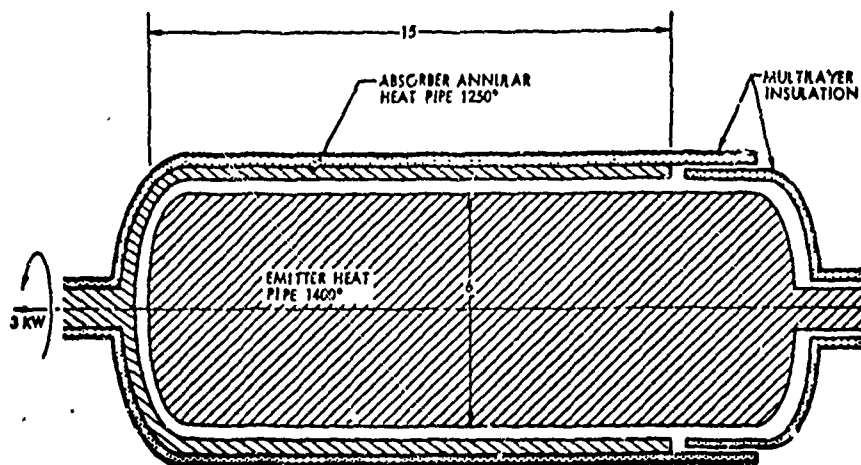


Figure 6. Single Axis Rotary Radiative Joint - Concept 1

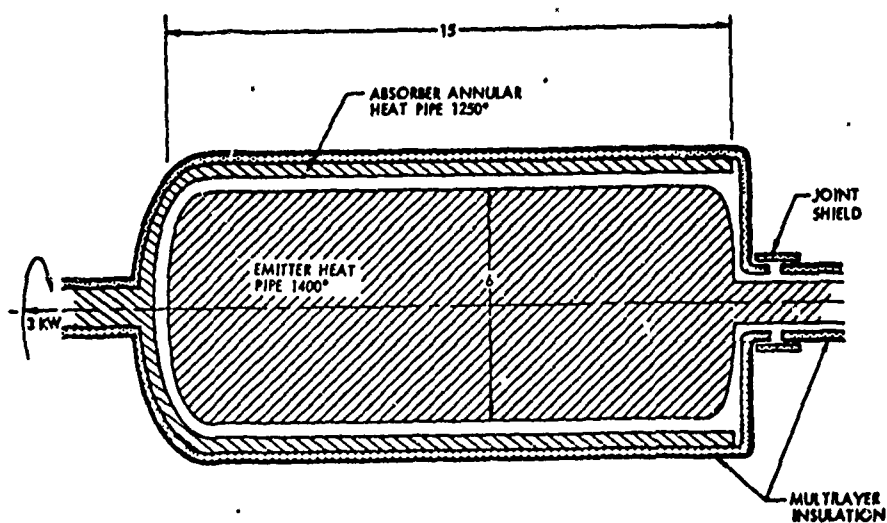


Figure 7. Single Axis Rotary Radiative Joint - Concept 2

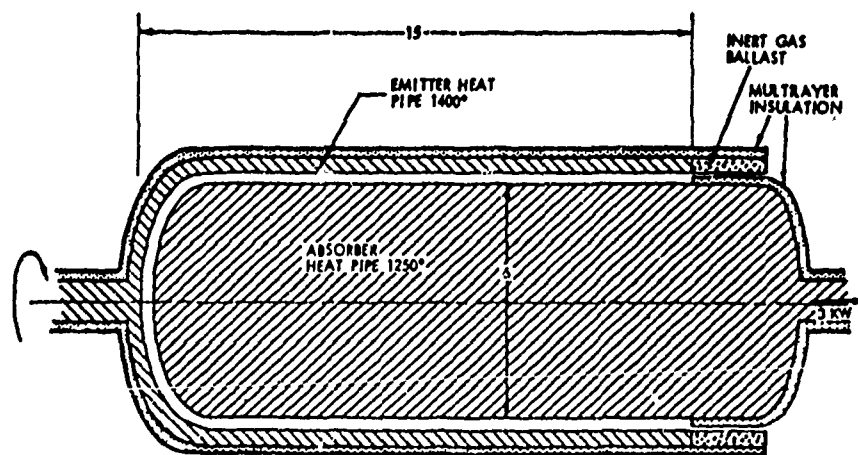
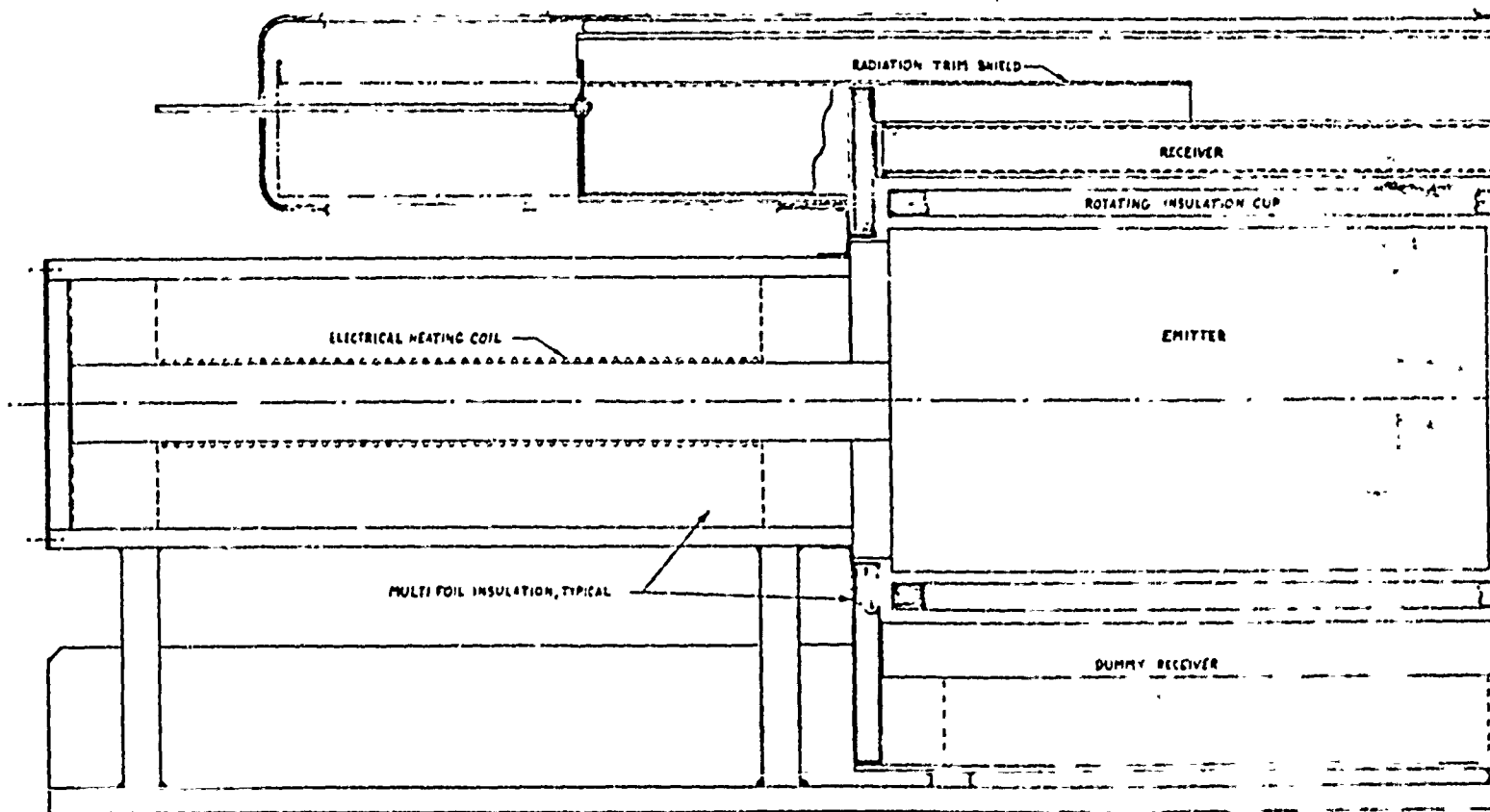
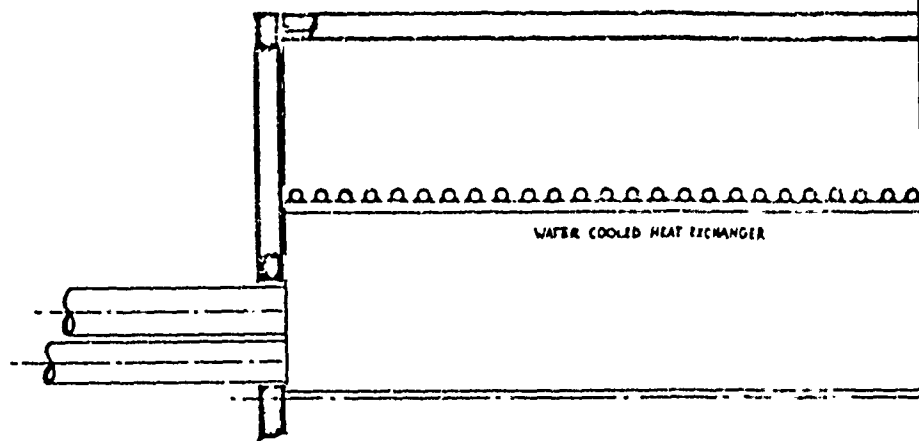


Figure 8. Single Axis Rotary Radiative Joint - Concept 3



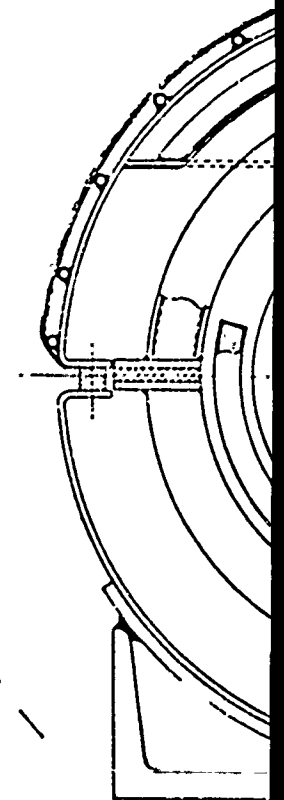
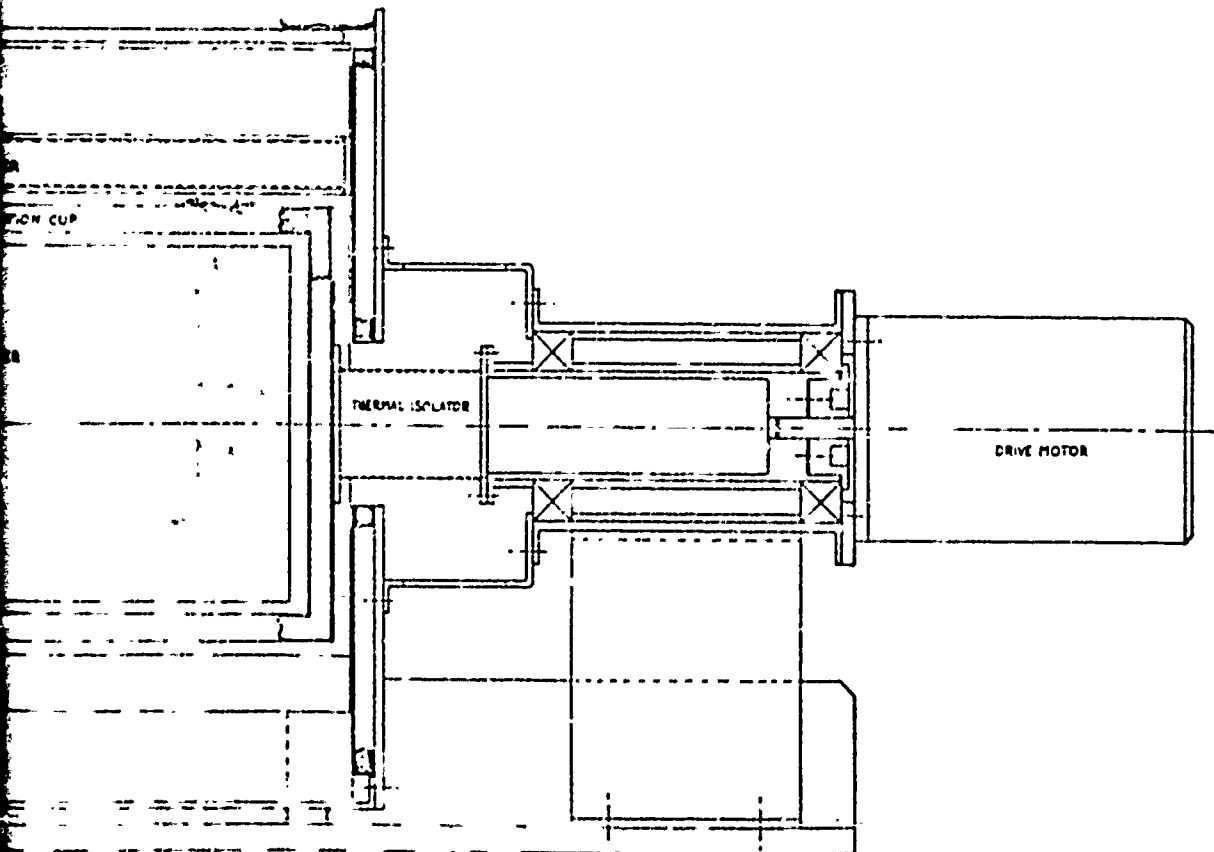
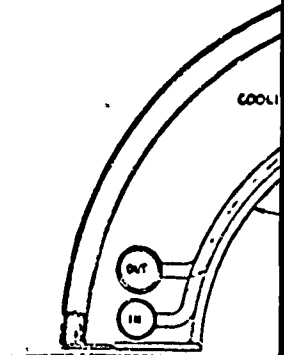
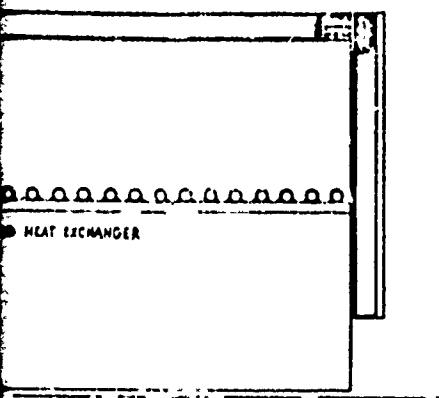
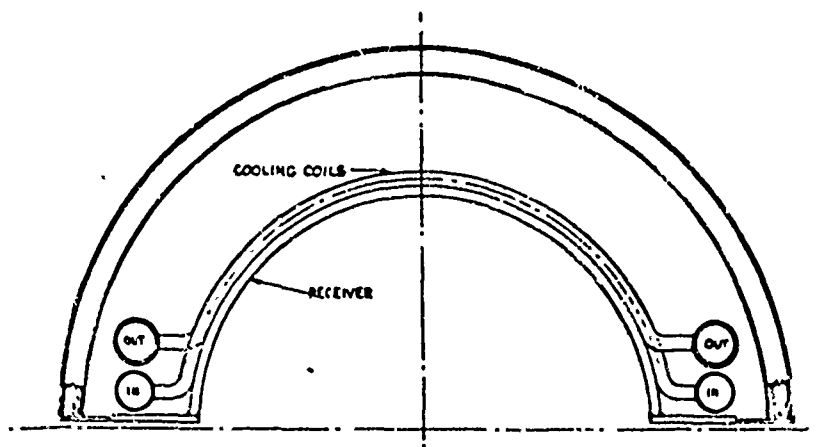
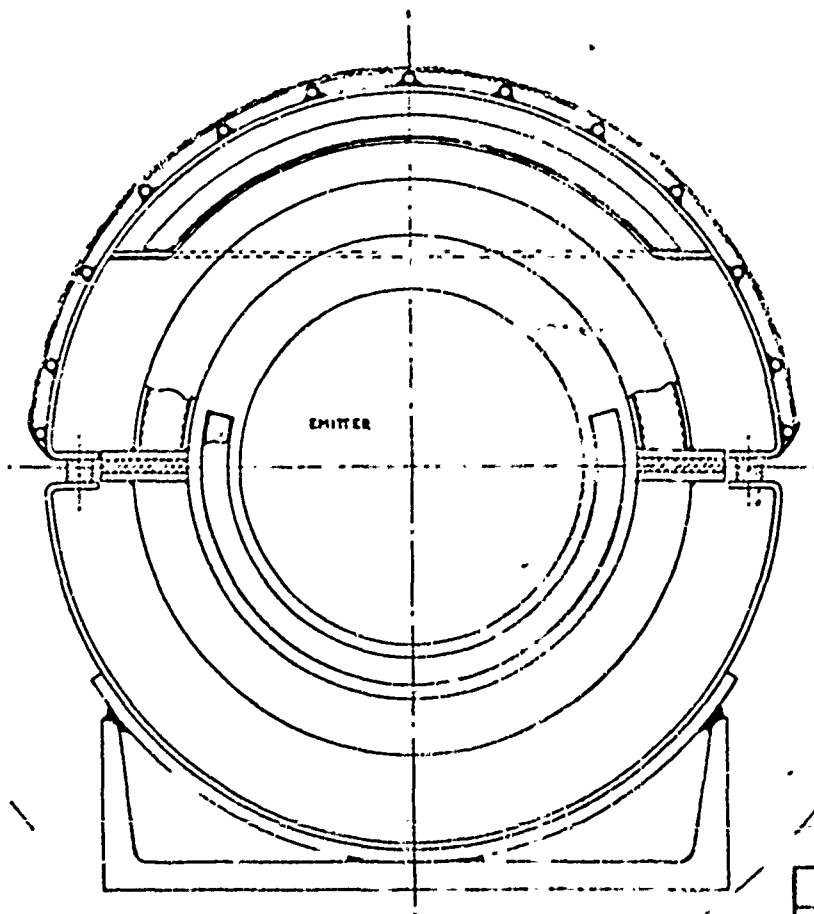
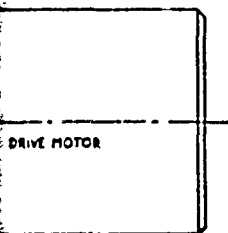


Figure 9. R



AIR COOLED HEAT EXCHANGER
ALTERNATE CONCEPT



TRW	
<small>THE SPACE RACE - EXTENDED DESIGN TECHNOLOGY</small>	
ROTARY JOINT TEST ASSY PRELIMINARY CONCEPTS	29 MAY 71 L123459

Figure 9. Rotary Joint Test Assembly - Preliminary Concepts

Testing on this apparatus must be done in a vacuum (10^{-5} torr or less). By varying the electrical power setting and cup position, the following information can be obtained:

- Efficiency of exterior insulation when applied to a realistic large joint.
- Efficiency of cup insulation when acting as an open switch (preventing flow of heat to receiver).
- Ability of cup insulation to function as a trimming device so that the temperature and/or heat rate at the VM interface may be varied as necessary.
- Effectiveness of radiation interchange surfaces; that is, effective emissivity and view factor.
- General operation of realistically shaped heat pipes.

3.4 VARIABLE CONDUCTANCE HEAT PIPE TEST

From Figures 2 and 3, it is seen that a variable conductance heat pipe (Reference 2) is required in the TTS as a temperature control device. In order to demonstrate the general working characteristics of such a pipe, a simple test was performed using an existing sodium heat pipe.

The pipe was fabricated from 1/2-inch stainless tubing and was 24 inches long. Heat was applied to the evaporator section by an RF coil placed around the evaporator. The input heat was varied by adjusting the RF grid current. The condenser section of the heat pipe lost its heat by radiation and natural convection to the surrounding environment. Thermocouples were attached along the surface of the pipe to aid in ascertaining the pipe operation.

The results of this testing are presented in Figure 10. The pipe was not specifically designed to operate at any given temperature related to the TTS study. Thus, the results are not directly applicable, but show typical operating characteristics of such a pipe. If designed for a specific performance, such a device can control the temperature of the TTS.

3.5 HIGH EMITTANCE COATINGS

Regardless of the final TTS configuration, at least one thermal radiation joint will be included. In order to keep the radiating surface areas at a minimum, these surfaces must exhibit high emittances. Obtaining high emittance surfaces is ordinarily not a difficult task. However, it becomes a serious problem when the operation is in vacuum at temperatures ranging up to 1800°F.

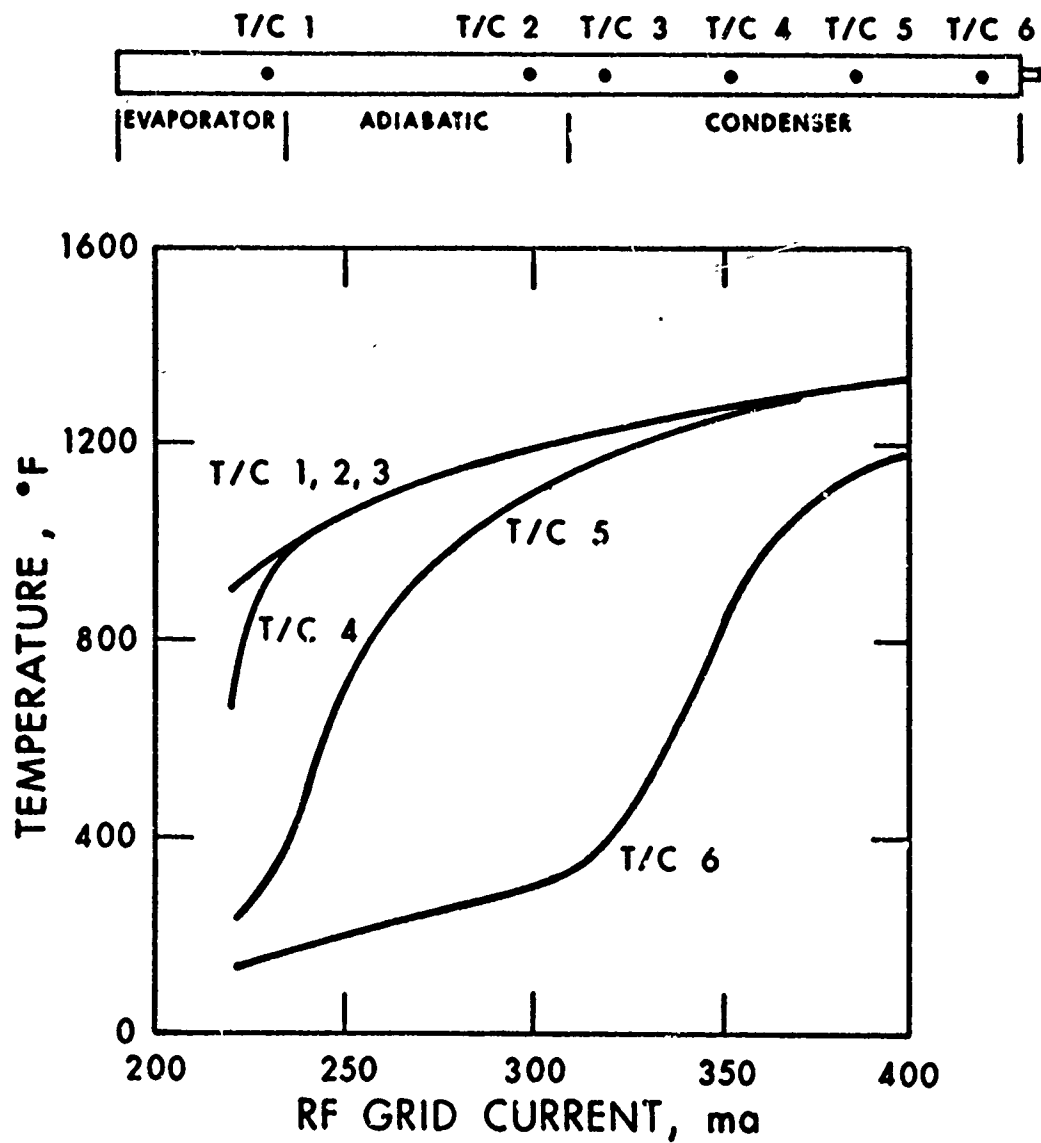


Figure 10. Stainless Steel/Sodium Variable Conductance Heat Pipe Operation

43658a

Extensive work has been performed in this area by TRW Systems and other companies (Reference 3). Of the various materials considered, three materials emerge as likely coating materials:

- Iron Titanate (Fe_2TiO_5)
- Calcium Titanate (CaTiO_3)
- Platinized Aluminum (TRW - 100M)

Pertinent information regarding the properties of these materials is given in Table IV. From the information given, it is obvious that care must be taken as to which material is used since the ability of each material to withstand thermal cycling is highly dependent upon the substrate material. It is obvious that some life testing will be required once the substrate materials are established.

3.6 THERMAL INSULATION

For the TTS to function properly, it is mandatory that the insulation system be highly efficient. Rough calculations indicate that an insulation conductivity goal of at least 0.005 but preferably 0.002 Btu/ft-hr-°F is desirable. This goal allows consideration of only multi-foil systems. In addition, the insulation must exhibit certain other properties:

- a. Low weight
- b. Long duration chemical stability
- c. Ability to withstand vibration and high intensity acoustical environment

In general, there are three basic types of multi-foil systems.

- a. Metal foils separated by non-conductive fibrous separators
- b. Metal foils upon which has been deposited on one surface of each foil tiny refractory oxide particles
- c. Metal foils which have been wrinkled or dimpled in such a manner that adjacent sheets touch each other in isolated areas only

In all cases, the objective is to eliminate conductive heat transfer between adjacent metal foils, leaving radiation the only means of heat transfer (References 4 through 12).

TABLE IV
HIGH TEMPERATURE, HIGH EMITTANCE COATINGS

<u>Coating candidates</u>	<u>Temperature (°F)</u>	<u>Initial emittance in. vac.</u>	<u>Emittance after 20,000 hr</u>	<u>Thermal cycling</u>	<u>Cost</u>
1. Fe ₂ TiO ₅ Iron Titanate	1300	0.90	0.87	Excellent on Columbium Poor on Inconel 718	\$10-15/lb
	1500	0.88	0.84 (10,000 hr)		
	1700	0.85	0.84 (10,000 hr)		
2. CaTiO ₃	1300	0.88	0.86	Good on 310 stainless, Poor on Columbium	\$10-15/lb
	1500	0.85			
	1700	0.83			
3. TRW-100M	1300	0.90	0.87 (Est.)	Excellent on Inconel 817	\$1300/lb
	1500	0.88			
	1700	0.85			

3.6.1 MATERIAL DESCRIPTION

3.6.1.1 Metal Foils

The metal foil may be any one of several: tungsten, tantalum, nickel, molybdenum, stainless steel for high temperatures or copper or aluminum for lower temperatures. The choice of foil is determined by the operating temperature range, required emittance, cost, and weight.

The last two items depend to a large extent upon the foil thickness. All of the foils may be obtained in half-mil thickness if sufficient time is allowed for production. However, the foil width is limited for tantalum, tungsten, and molybdenum to 12 inches. The cost varies widely, running from about \$300/lb for molybdenum and tungsten to about \$20/lb for aluminum.

The important physical properties of these foils are listed in Table V.

It can be seen that molybdenum has the lowest emissivity at 2000°F. However, since it may be obtained only in widths less than 12 inches, nickel is probably a better material for use on the TTS since: (1) its emissivity is fairly low and, (2) insulation edge losses in a nickel system will certainly be less because it comes in wider sheets.

In areas of reduced temperature, copper and aluminum could be used. The most efficient multi-foil insulation system would consist of aluminum foil for the outer (cold) layers, and nickel foil for the inner layers. Due to the high temperatures, most of the layers will have to be nickel since the temperature drops slowly in the high temperature zone of multi-radiation-shield insulation systems.

3.6.1.2 Fibrous Separators

Fibrous separators now available are fibrous zirconia (Zircar by Union Carbide), Refrasil (amorphous silica fiber by E. I. duPont), and glass cloth. All of these materials are available in fabric form weighing about 10 ounces per square yard, and a thickness of about 0.016 inch.

The choice of material is almost totally dependent upon the operating temperature level. Glass cloth may be used up to 1200°F, Refrasil to approximately 1700°F, and Zirconia to temperatures in excess of 2500°F. Failure occurs as the material begins to decompose and causes the emittance of the adjacent metal foil to increase markedly.

All materials are relatively easy to handle. However, Refrasil must be baked out at about 600°F prior to fabrication.

TABLE V

FOIL PROPERTIES

Material	Temp. limit °F (vacuum)	Emittance at temperature (Hemispherical)					
		3000°F	2500°F	2000°F	1500°F	1200°F	800°F
Tungsten (Ref. 13)	> 3000	0.25	0.21	0.17	0.12		
Tantalum (Ref. 13)	> 3000	0.22	0.20	0.17	0.14		
Nickel (Ref. 13)	2100			0.21	0.17	0.15	
Molybdenum (Ref. 13)	> 3000	0.20	0.18	0.14	0.11	0.08	
Stainless Steel (Ref. 14)	2000			0.28	0.25	0.23	0.19
Copper (Ref. 13)	1600					0.24	0.04
Aluminum (Ref. 13)	900						0.06
							0.3
							0.5

3.6.1.3 Foils with Depositions of Refractory Oxide Particles

Several companies, notably Thermo Electron Corporation of Waltham, Massachusetts (References 5, 10, and 12), have worked with multi-foil insulation systems which utilize metal foils upon which has been deposited refractory oxide particles on one surface of each foil. The purpose of the oxide deposition is to prevent heat conduction between adjacent foil layers. ZrO_2 and ThO_2 oxides have been studied extensively as to compatibility with substrate materials, effect of thickness, and long duration thermal stability. In general, this type of insulation appears excellent but rather expensive. The material does not come in rolls, but must be made to fit each particular project.

One point not covered in the literature is the resistance of the material to damage occurring from vibration or relative motion between adjacent foil layers. There might be a tendency in such a situation for the oxide to rub off. Prior to use, this point should be explored, particularly if a high intensity acoustic environment is expected.

3.6.1.4 Dimpled Metal Foil

The literature search did not reveal any systematic study of dimpled or wrinkled foil insulation systems for use at high temperatures. Some results of tests performed on plain foil systems are reported. They indicate either very high conductances or that possibly the tests were performed incorrectly with relatively high gas pressures. For this reason, a pure foil insulation system is not recommended unless additional data becomes available which clarifies the issue.

3.6.2 PERFORMANCE OF INSULATION SYSTEMS

The conductivity of the various insulation systems as determined by test show a wide variation. Reported conductivity values for the same insulation vary by as much as two orders of magnitude. This is probably due to actual variations in the insulation materials as well as the experimental techniques employed. Tremendous variations will result from test to test if the insulation is not uniformly applied. Packing density, wrapping pattern, and general workmanship must all be closely controlled if similar results from successive tests are to be obtained. However, by comparing the reported data it is possible to establish general characteristics and safe conductivity values which may be used for design purposes.

Typical test results for various systems are given in Figures 11 through 13. In all cases, these results are for idealized systems; that is, no edge or joint losses. Figure 14 indicates the general magnitude of edge losses which may be expected.

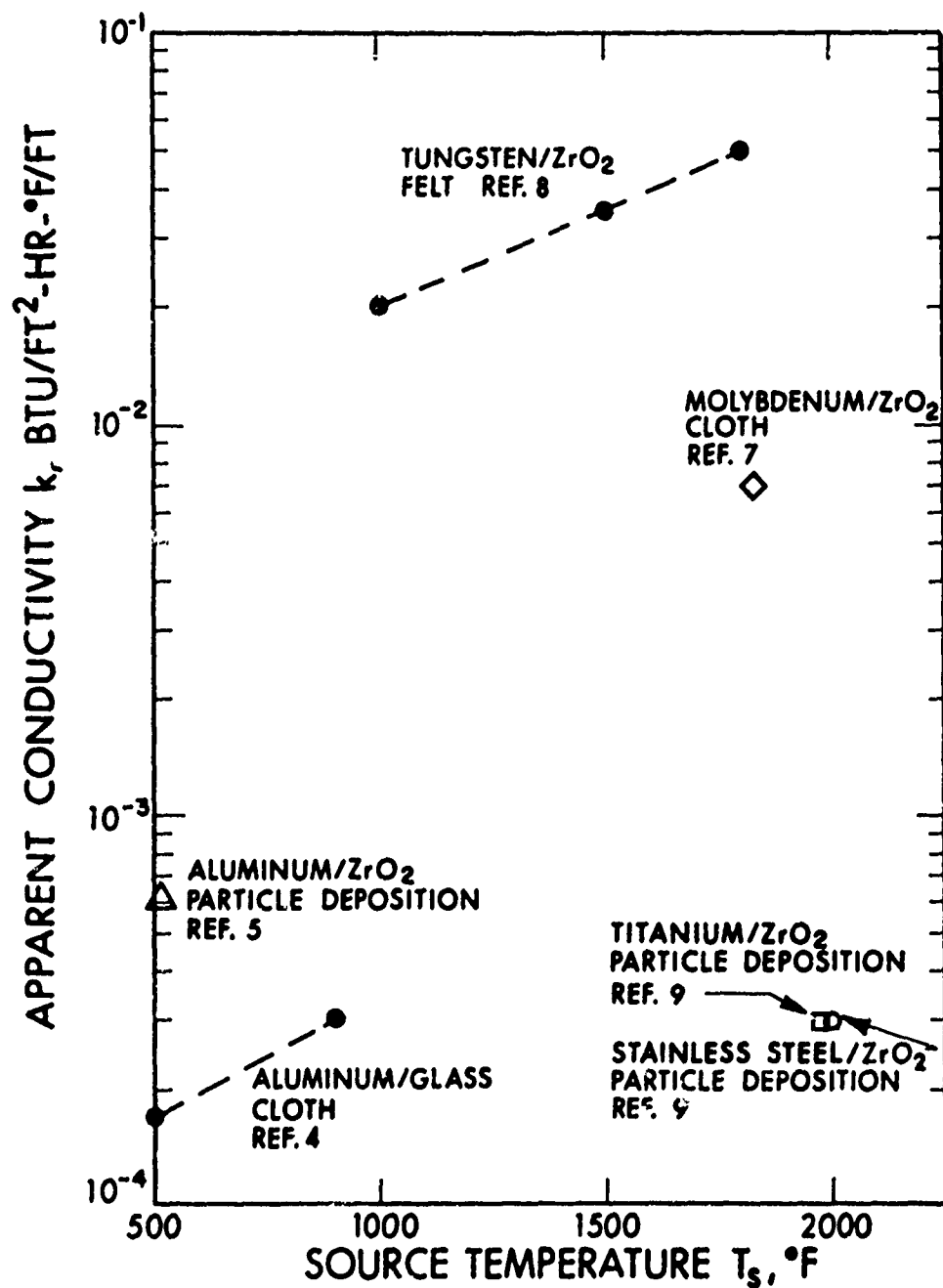


Figure 11. Apparent Conductivity of Idealized Test Samples
(Sink Temperature Approximately 70°F)

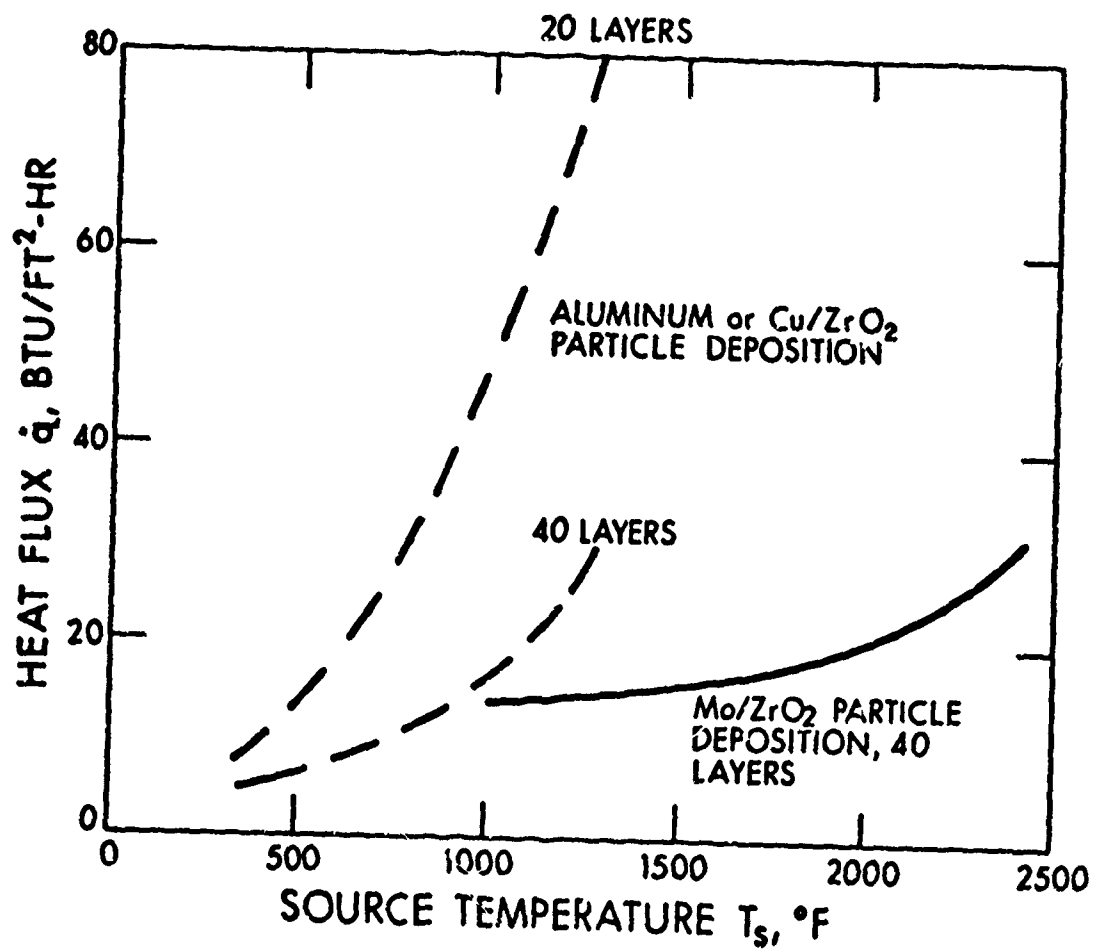


Figure 12. Typical Foil/Oxide Deposition Heat Flux (Sink Temperature Approximately 70°F)

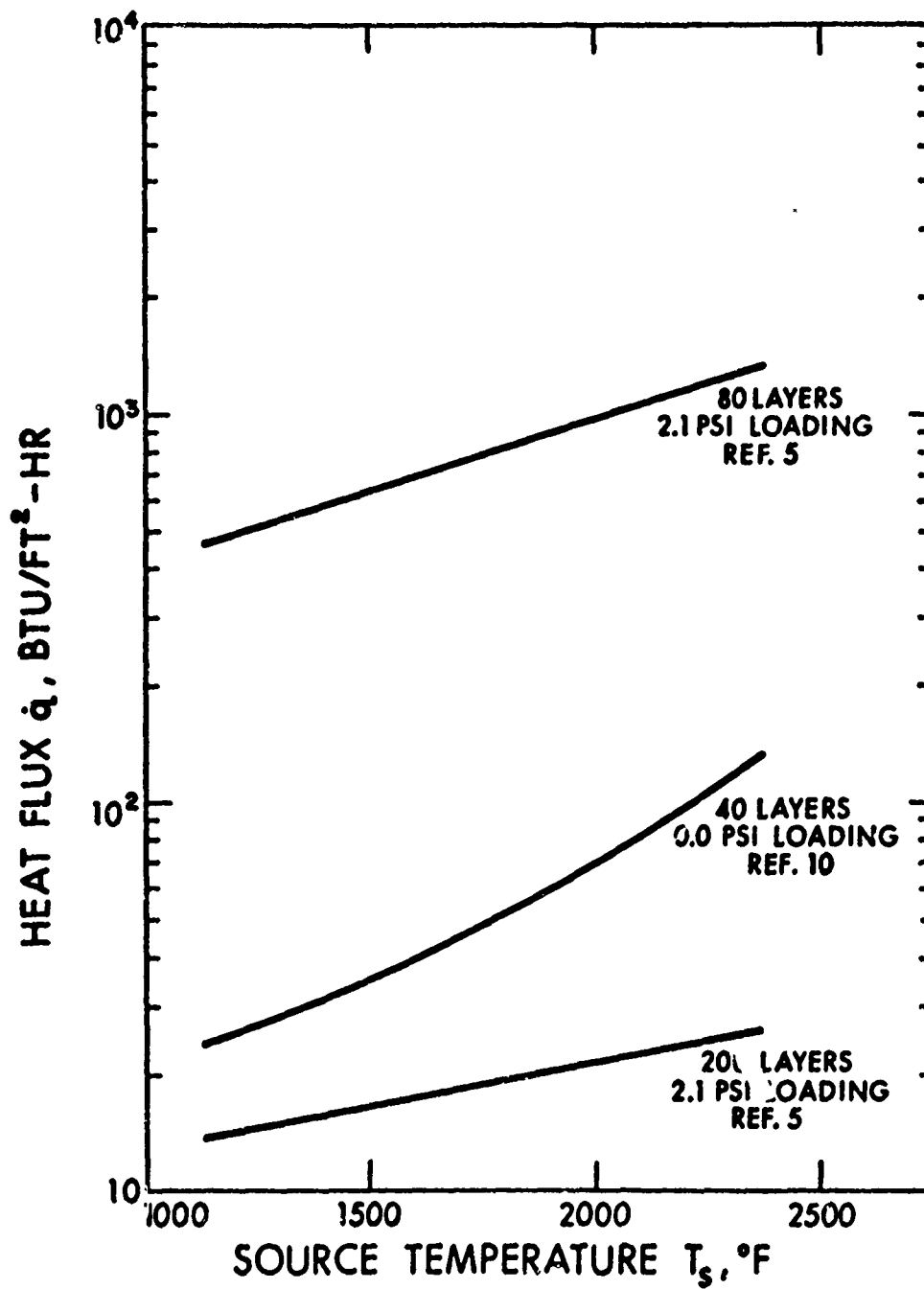


Figure 13. Effect of Compression Loading on Insulation Heat Flux; Tantalum/ThO₂ Particle Deposition (Sink Temperature Approximately 70°F)

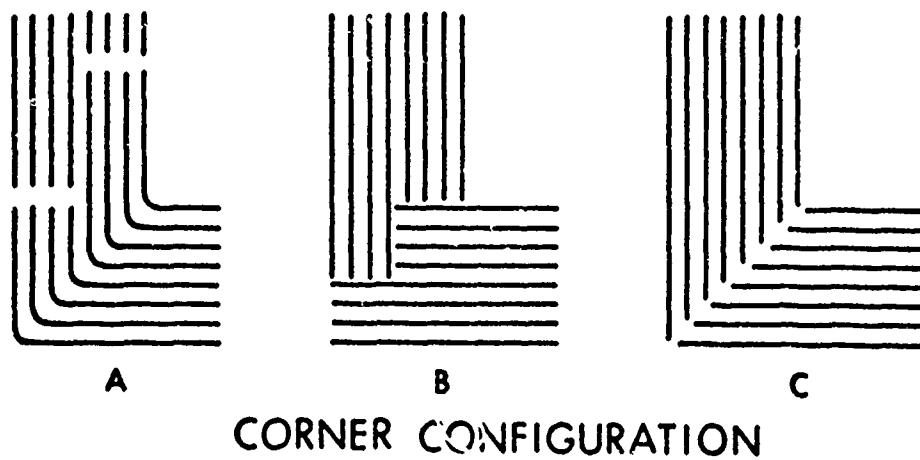
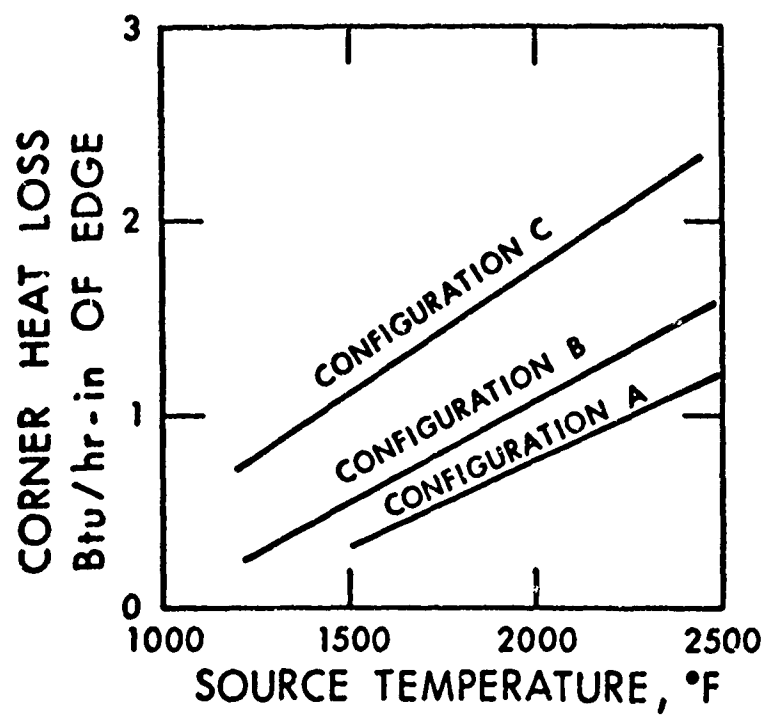


Figure 14. Corner Configuration Performance, Ta/ThO₂ Particle Deposition (Reference 10)

43618

If a realistic insulation system design is considered, it can be shown that much, if not most, of the heat loss can be attributed to edge and/or corner losses. For this reason, it is important to eliminate edges by proper design. Also, Figure 14 shows that corner design is important.

Surveying the available data, including the probable accuracy of the data, and considering edge and corner losses the values listed in Table VI for heat flux and conductivity are recommended for design purposes. Comparing these values with the results given in the graphs (and also the references), it will be seen that these design values allow for about a 100% increase in heat transfer due to insulation discontinuity.

3.7 CONCLUSIONS AND RECOMMENDATIONS

The general conclusions reached from the Thermal Train Subsystem Preliminary Study reported herein are as follows:

- a. The TTS configuration may take several forms. The best configuration can be established only by performing an in-depth systems tradeoff study which considers the mission and design of the vehicle.
- b. The TTS design, to be fully defined, will require full detail of the heat pipes design and operation.
- c. Thermal radiation joints having one or two degrees of freedom can be designed. Their size is primarily determined by the heat transfer rate and allowable temperature drop across the joint.
- d. Insulation materials having the requisite properties to function properly on the TTS are presently available.
- e. High emittance coatings which may be used at elevated temperatures are presently available. However, the choice of the particular material to be used must be guided by the type of substrate material being used.

TABLE VI

RECOMMENDED INSULATION SYSTEM THERMAL DESIGN VALUES

Metal Foil/Refractory System Heat Flux
(For 100°F Cold Side Temperature)

<u>Type</u>	<u>Heat Flux*</u> <u>Btu/ft² - hr</u>	<u>Hot side</u> <u>temperature - (°F)</u>
W-ThO ₂		
20 layers	475 316	1400-1800 1000-1400
40 layers	255 158	1400-1800 1000-1400
Mo-ZrO ₂ or Ni-ThO ₂		
40 layers	63	1000-1800
Cu-ZrO ₂		
20 layers	95 63 32	900-1100 750-900 500-750
40 layers	32	750-1100
Al-ZrO ₂		
40 layers	19	400-750

Metal Foil/Fibrous Separator System Conductivity

<u>Type</u>	<u>Conductivity**</u> <u>(Btu/ft - hr - °F)</u>	<u>Hot side</u> <u>temperature - (°F)</u>
Mo-ZrO ₂	0,077	1800
ZrO ₂ (w/o foil)	0.02	1800
Ni-Refrasil	0.004 0.002	1600 1250
Al-Glass	0.0006 0.0003	900 500

*Assumes no compression of insulation

**One layer of foil/separator is about 0.020 inch thick

SECTION IV
SUBSCALE HEAT PIPE
DESIGN AND MANUFACTURING

4.1 INTRODUCTION

Minimum lifetime design goals for the solar collector thermal power system hardware is 3 years with a desired lifetime of 5 years. This lifetime exceeds any available active lifetime data for liquid metal heat pipes. Furthermore, the diversity of possible failure mechanisms makes extrapolation from or comparison of different sets of conditions highly qualitative.

Specific processes limiting the life of heat pipes are varied. Of particular concern is the dissolution of the wick and wall materials by the sodium working fluid. Such take-up may either involve basic solubility limits between various elements or may involve more complex mechanisms in which contaminants, particularly oxides play an active role. Upon take-up by the working fluid, a cycle may be established whereby material picked up at the condenser region of the pipe is carried through the wick structure to the evaporator. Upon evaporation of the sodium, the transferred material may be left behind. Life limiting aspects associated with these processes include corrosion of the wall, loss of capillary structure, and blockage of the wick structure by deposited material. If this occurs in the evaporator, the result would be equivalent to wick dry-out and in the extreme case could lead to burn-out.

The purity of the sodium and all surfaces are important preconditions for minimizing possible material reactions. Phenomenologically, the higher the temperature to which a given system is subjected, the greater the possibility for mass pick-up. Also, the size of the evaporation and condensation areas are important parameters for the amount of material deposition or dissolution that could take place. For the rate at which deposition at the evaporator occurs, the total power and liquid circulation rate are primary parameters.

It is impractical and often impossible to scale all operating and design features of subscale hardware to full-scale values, but many of the pertinent parameters can be modeled. Multiple subscale units of the same material combinations of interest must be tested simultaneously to establish some statistical sample base. To demonstrate the long-lifetime compatibility of sodium and high nickel-chrome alloys (such as Inconel 600) for the thermal train subsystem, an experimental effort was initiated.

The endurance test was designed to operate with modeled heat transfer conditions representative of ranges required for anticipated flight hardware designs of the future. In all other respects the materials and processes were applied consistent with a 15-foot primary heat pipe described in Section

A design summary between the endurance test units and the 15-foot unit is provided in Table VII. The evaporator flux that was selected for the endurance test design was more representative of the flux to be encountered in the solar collector. The 15-foot heat pipe will have to be operated with a large evaporator area as there are limits to high power and high density heating with electrical heaters.

4.2 HARDWARE DESCRIPTION

Six subscale heat pipes were fabricated and numbered SN 1 through SN 6. All units were identical in design except as noted in the following text. Elements of the six subscale heat pipes are shown in Figures 15 and 16.

The endurance test hardware and set-up are summarized in Figure 17. The heat pipe consists of a 1-inch o.d. Inconel 600 tube and is 12 inches long. The tube contains a double wrap of 60 mesh nickel screen spot welded around the circumference. A diametral wick structure extends along the longitudinal axis which provides for the liquid return from the condenser to the evaporator. The diametral wick was formed from 24 layers of folded screen held between two 0.025-inch Inconel straps by twelve 1/8-inch diameter nickel stakes on 1-inch centers. For SN 2, the diametral wick was fabricated from 40 mesh nickel screen. The remaining four units incorporate 38 mesh Inconel bolting cloth. The nominal diametral wick dimensions are 0.250 inch wide by 0.806 inch high by 11-3/8 inches long.

A 2-inch long by 0.8-inch wide by 0.001-inch thick zirconium foil was placed between the center fold of the evaporator end of each diametral wick. This material was provided as getter of oxygen should any be present. Table VIII provides a complete bill of material for items used in the endurance test hardware.

Following mechanical installation of the diametral wick into the tubes by compressing them out of round, the end caps were welded to the tube structure. The fill tube was placed at the condenser end. The units were helium leak checked to verify seal integrity and die penetrant inspected for weld structural soundness.

Individual close wound Nichrome V Inconel sheathed resistance heaters were vacuum furnace brazed to the evaporator sections at 1850°F using 82 Au - 18 Ni (ASTM B-260-BAU-4). Four Inconel sheathed chromel-alumel thermocouples were attached by resistance spot welded Inconel tabs to

TABLE VII

SOLAR COLLECTOR PRIMARY HEAT PIPE
COMPARISON OF DESIGN PARAMETERS

	<u>Primary</u>	<u>Subscale</u>	<u>Comments</u>
HEAT PIPE			
Tube o.d. (in.)	2.50	2.25	1.0
Wall (in.)	0.0625	0.0625	0.0625
Length (in.)	180	12	12
Evaporator Length (in.)	24	24	1.25
Condenser Length (in.)	37.5	37.5	5.0
WICK			
Diametral Wick			
Width (in.)	1.1	1.1	0.25
Cross Section Area (in. ²)	2.4	2.1	0.21
Mesh (Bolting Cloth)	38	38	38
Circumferential Wick			
Number of layers	2	2	2
Mesh	60	60	60
OPERATING CONDITIONS			
Temperature (°F)	1600	1600	1600
Power Input (watts)	8000	8000	600
Evaporator Heat Input Flux (watts/in. ²)	42	47.2	150**
Condenser Heat Flux (watts/in. ²)	31	22.6	34.6
Axial Mass Transport Flux (lb/hr-in. ²)	6.0	8.0	6.0
INSULATION			
Number of layers	3	3	2*
Heat Loss (watts/ft)	110	100	90

* Includes 0.25 in. air gap.

** A 2.0 in. radius hemispherical evaporator has a 480 watt/in.² peak flux for 6 kW system.

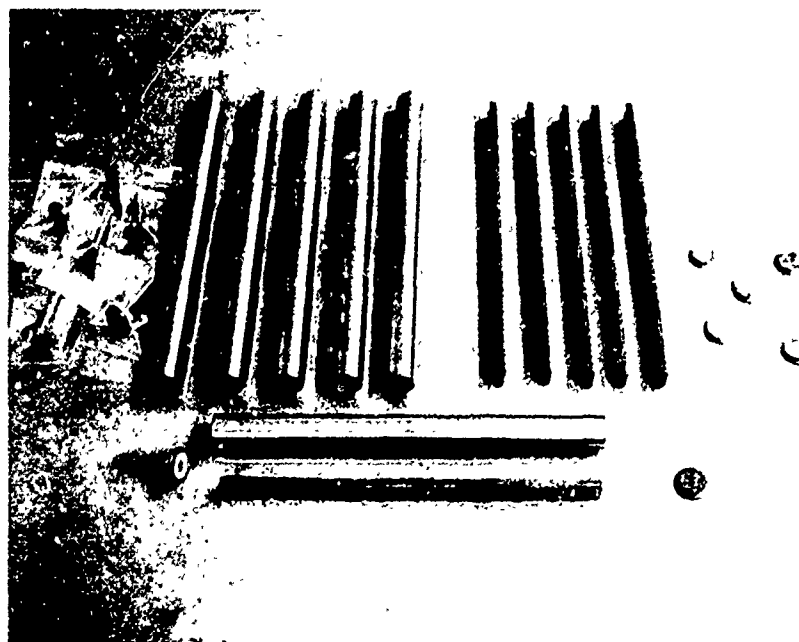


Figure 15. Parts for Six Subscale Heat Pipes



Figure 16. Close-up of Subscale Parts

006566

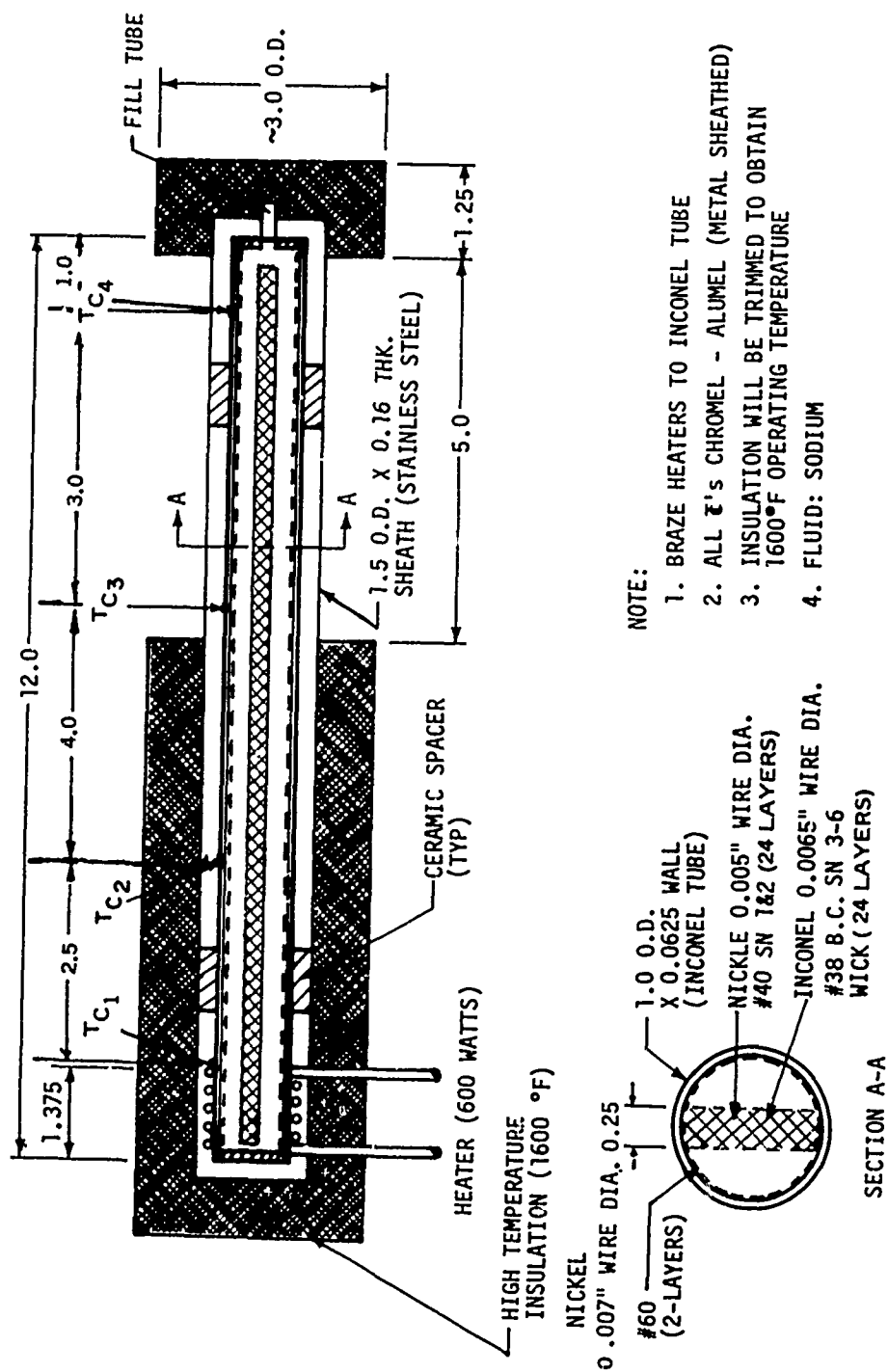


Figure 17. Subscale Heat Pipe Assembly

TABLE VIII
SUBSCALE HEAT PIPE
BILL OF MATERIALS

<u>Item</u>	<u>Size/Type</u>	<u>Material</u>
Diametral Wick (SN 3 thru 6)	38-Mesh Bolting Cloth 0.0065" Dia. Wire	Inconel 600
Diametral Wick (SN 1 and 2)	40-Mesh Screen 0.005" Dia. Wire	Nickel 200
Diametral Retainer	Sheet 0.025" thick	Inconel 600
Diametral Wick Connectors	Rod 0.125" Dia.	Nickel 200
Circumferential Wick	60-Mesh Screen 0.007" Dia. Wire	Nickel 200
Getter	Foil 4" x 0.001" thick	Zirconium
Tube	1.0" o.d. x 0.063" Wall	Inconel 600
End Caps	Sheet 0.125" thick	Inconel 600
Fill Tube	0.250" o.d. x 0.035" Wall	Inconel 600
Heat Pipe - Fluid	Bulk	MSA High Purity Sodium
Braze Material	Foil, Rod	82 Au - 18 Ni
Heater	0.063" o.d. x 63 \pm 3" Nichrome V 1.7 Ω /ft.	Sheathed Inconel 600
Thermocouples	Cr-Al 1063K6E 1063K12E 1063K16E	Sheathed Inconel 600
Air Cap Tube	1.5" o.d. x 0.016" Wall	316 S.S.
Spacers	0.250" Rod	Quartz
Insulation	Sheet x 3/8"	J.M. Flex-Min-K
Power Supply	Variable Transformer	Model 3PN116B

the tube o.d. For SN 1, 3, 4, 5, and 6 the sensing tips were torch brazed with 82 Au - 18 Ni braze to improve thermal contact. The locations of the thermocouples are shown in Figure 17. SN 2, which was the first subscale heat pipe to be placed in endurance test, had only three thermocouples in locations 1, 2 and 4 which were not brazed to the tube. The addition of a fourth thermocouple was contemplated. However, brazing cannot be accomplished on a processed heat pipe.

4.3 PRELIMINARY ENDURANCE TEST EVALUATION AND PROCESSING

Only heat pipes SN 1 and 2 were initially processed to check out the sodium transfer method to be used at a later date for the 15-foot long heat pipe and to establish the self-processing procedure of the heat pipes after charging with the working fluid and prior to closure. It was further felt that before committing all six subscale heat pipes, this design should be experimentally verified.

Subscale units SN 1 and SN 2 were charged with sodium, self-processed while vented to vacuum, and closed. Each unit was then set up for test as illustrated in Figure 17. Upon start-up for life test, it became apparent that in SN 1 a leak to atmospheric pressure had occurred from the time of self-processing to the permanent closure of the fill-tube. SN 2 was placed into life test on 25 July 1972. A series of adjustments to the power was necessary as oxidation of the metals occurred and some aging of the heater took place. Table IX summarizes the modeled subscale design parameters with the nominal values for SN 2.

SN 1 was opened and the sodium removed. The unit was reprocessed with SN 3 through 6.

Operation of SN 2 pointed out two important functional aspects regarding the endurance test hardware. The adequacy of the subscale heater design and its method of attachment appears good. The desirability of improving the method of thermocouple attachment by brazing was pointed out by the difference between temperature readings in the evaporator, adiabatic, and condenser regions. These differences are believed directly related to differences in the individual conduction couplings and radiation environment.

As a consequence, efforts were made to adapt the 82 Au - 18 Ni braze using a torch method in air. It was found that successful brazes could be made by evacuating the unfilled heat pipes to prevent internal oxidation.

TABLE IX
SUBSCALE HEAT PIPE
COMPARISON OF TEST WITH CALCULATED DESIGN PARAMETERS

	<u>Design</u>	<u>SN 2 Test</u>	<u>Comments</u>	
TUBE				
Tube o.d. (in.)	1.0	1.0	Inconel	
Wall (in.)	0.0625	0.0625		
Length (in.)	12.0	12.0		
Evaporator Length (in.)	1.25	1.375		
Condenser Length (in.)	5.0	5.0		
WICK				
Diametral Wick				
Width (in.) (nominal)	0.25	0.25	SN 1&2 (40)/SN 3-6 (38)	
Cross Section Area (in. ²)	0.21	0.21		
Mesh	38	(40)/(38)		
Circumferential Wick				
Number of Layers	2	2		Nickel
Mesh	60	60		
OPERATING CONDITIONS				
Temperature (°F)	1600	1606	(Adiabatic) & attached to wall	
Power Input (watts)	600	~595*	Includes insulation loss*	
Evaporator Heat Input Flux (watts/in. ²)	150	138	Outside Evaporator area	
Condenser Heat Flux (watts/in. ²)	34.6	34.3	Based on outside condenser area	
Axial Mass Transport Flux (lb/hr-in. ²)	6.0	6.0	Based on Power Input	
INSULATION				
Number of Layers	2	2	J-M Flex Min-K (0.375" layers plus 0.25" air gap)	
Heat Loss (watts/ft)	90	90		

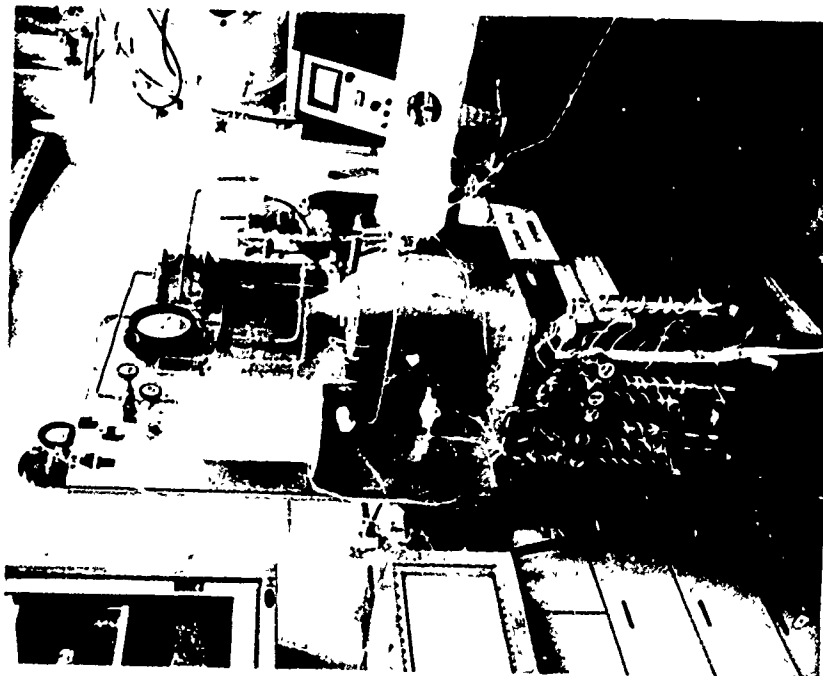
* Accuracy of current measurement is no better than ± 0.1 ampere

In addition to the operational aspects determined by early operation of SN 2, the leakage of air into SN 1 resulted in a procedural modification used during self-processing of the remaining hardware. Whereas originally the valves were removed, self-processing was conducted with the valve in place. This insured both the maintaining of high-purity sodium and also allowed the positive leak-tight closure from the time of cool-down to the time when the fill tube was closed. All other aspects of the method of sodium transfer, self-process, and closure were acceptable.

Processing of the heat pipe hardware started at the raw material level where screen and parts materials were cleaned prior to fabrication. Final cleaning was accomplished using TRW specification PR 2-2J, Level 1. Following welding of the structure, a thermal vacuum step was performed. In this instance, this was accomplished during the heater braze. Following addition of a fill valve, the individual units were connected to a sodium fill system. All connections were helium leak-checked and the pipes, transfer lines, and reservoirs vacuum-baked at $\sim 300^{\circ}\text{F}$. The sodium was transferred at $\sim 300^{\circ}\text{F}$ from a primary source (MSA container) using argon as a drive gas. The sodium was transferred into a secondary glass receiver which was volumetrically graduated. From the secondary reservoir, 35 grams of material was transferred into each of the individual pipes. Figure 18 shows the subscale units attached to the fill system. Weight measurement was taken before and after fill to verify the fill inventory. Figure 19 shows five units following fill prior to self-processing. The transferred sodium is stored under 10 psig argon prior to self-processing.

During self-processing, the heat pipe was connected with its valve to a liquid nitrogen trapped vacuum system and initially evacuated while still cold to remove the argon gas. The unit was then heated to a temperature of 800°F using both an auxiliary heater and the brazed on heater and the valve opened momentarily (vent to vacuum). The unit was then heated to 1600°F to self-process the sodium, allowing any buried noncondensable gases to accumulate in the vapor space. Temperature was lowered to 1400°F for a momentary valve opening (exhausting of sodium vapor to vacuum) to remove any gases which have accumulated. Following cooldown, the unit is permanently closed using an electrode-fusion weld to crimp and weld the fill tube.

After charging and self-processing, the remaining five subscale heat pipes were installed for testing in the same fashion as described for unit SN 2.



595900

Figure 18. Fill System

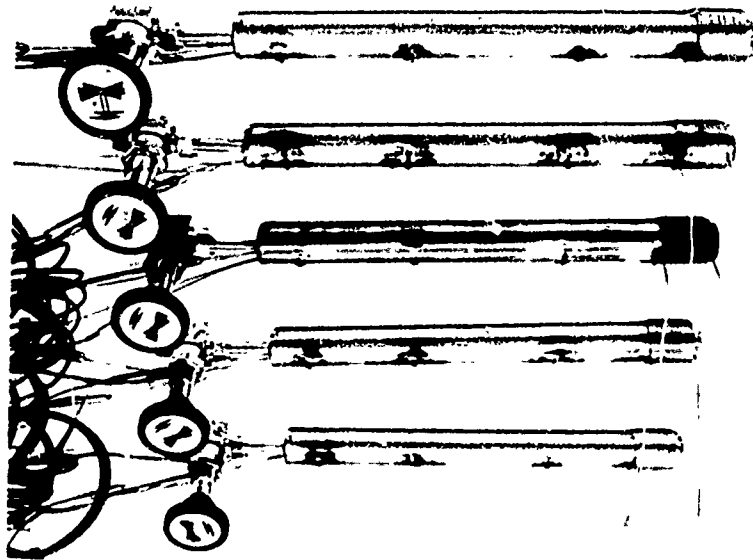


Figure 19. Filled Endurance Test Heat Pipes

4.4 ENDURANCE TESTING

Each subscale heat pipe was independently operated from a variable voltage transformer with an ammeter in series for accurate setting of the heater power. The four thermocouples which were attached to the heat pipe as indicated in Figure 17 allowed monitoring of the temperature of the heat pipe. The endurance test conditions were based upon an operating level of 1600°F at a power input of 600 watts at the evaporator. During the initial start-ups, a power input of considerably less than 600 watts raised the temperature to 1600°F. On an average the operating temperature was achieved with about 450 watt input power. As oxidation of the outer heat pipe surface and the air cap heat rejection tube progressed, the emittance value of the surface increased. The resulting higher heat rejection permitted an upward adjustment of the input powers to 90 and 110 percent of the design power input.

Periodically, temperature readings were taken and power adjustments made. The data for the six units are tabulated in Tables X to XV. Physically the six units were operated in a laboratory fume hood enclosure in which each test unit was supported on fire brick. Natural air convection occurred through the hood exhaust. No continuous temperature recording or automatic power control systems were used.

Table XVI summarizes the endurance test history for the six units.

Following several hundred hours of operation, units 1, 4, and 5 were found with open heaters. An examination of these three units was made to ascertain the nature of test termination. Subsequently, units 3 and 6 terminated after several thousand hours. Only SN 2 remained operational until the end of the endurance test.

Upon termination of units 1, 4, and 5, the following chronology of observations occurred:

- a. For all three units the brazed-on heaters proved open by the resistance test.
- b. Units 1 and 4 were removed from the test setup and the heaters ground off the tubes. Inspection of the heater surface of SN 1 prior to grinding indicated a small region suggestive of sodium leakage.
- c. A single 1-2 mm diameter hole was found in the evaporator region of the heat pipe tube of SN 1.
- d. Similarly, a single pin hole was found in the SN 4 evaporator region when examined under 20X magnification.

TABLE X
HEAT PIPE LIFE TEST

Heat Pipe No.: 1

Heat Pipe Description: Sodium Nickel-Nickel Screen Inconel Tube

Date Time	T. Amb.	T ₁ Chart Reading °F	T ₂ Chart Reading °F	T ₃ Chart Reading °F	T ₄ Chart Reading °F	Volts	Amperes	Notes
								START-UP 10/16/72
10/17/72 11:00	78°F	1605	1560	1552	1552	69	6.4	Raised power reag with bot.
10/17/72 16:00	78°F	1649	1600	1590	1591	71	6.6	
10/18/72 9:00	77°F	1600	1589	1578	1579	71	6.6	Raised power
10/19/72 9:00	76°F					72	6.7	
10/19/72 9:00	76°F	1609	1598	1585	1587	73	6.75	Raised power
						74	6.80	
10/20/72 9:00	77°F	1622	1607	1595	1597	74	6.80	
10/23/72 9:00	78°F	1606	1594	1582	1583	74	6.80	Raised power
10/23/72 9:00						75	6.85	
10/24/72 11:00	78°F	1614	1600	1589	1590	76	6.9	
10/26/72 9:00	80°F	1611	1598	1585	1586	76	6.9	Raised power
10/26/72 9:00						77	6.95	
10/27/72 9:00	78°F	1611	1598	1585	1585	76	6.95	
11/1/72 11:00	78°F	1601	1586	1573	1571	76	6.95	
11/1/72 16:00	78°F					77	7.00	Raised power
11/6/72 16:00	79°F	1592	1577	1564	1561	76	7.05	
11/6/72 17:00						77	7.2	Raised power
11/14/72 10:45	NOTICED - HEATER OPEN CIRCUIT							

TABLE XI
HEAT PIPE LIFE TEST

Heat Pipe No.: 2

Heat Pipe Description: Sodium-Nickel-Nickel Screen Inconel Tube

Date	T. Amb.	T ₁	T ₂	T ₃	T ₄			Notes
Time		Chart Reading °F	Chart Reading °F	Chart Reading °F	Chart Reading °F	Volts	Amperes	
7-25-72 10:30	76°F	76	76	76				Start Power on
13:30	76°F	1610	1605	1566		65	5.9	Decrease power
14:00	76°F	1600	1595	1559		65	5.9	Calibrate clamp on meter
16:25	76°F	1603	1598	1560		65	6.9	
7-26-72 8:30	76°F	1591	1586	1547		65	6.9	
11:10	76°F	1583	1577	1538		65	6.9	
13:00	76°F	1585	1579	1540		65	6.9	Increase power
16:40	76°F	1600	1593	1554		67	7.1	
7/27/72 8:30	76°F	1600	1593	1554		67	7.1	
11:45	76°F	1593	1586	1547		67	7.1	
14:45	76°F	1588	1580	1542		67	7.1	Change potentiometer Galvo batt. weak
7/28/72 8:30	77°F	1600	1592	1549		67	7.1	
13:00	76°F	1596	1589	1549		67	7.1	
16:30	76°F	1602	1595	1555		67	7.1	
7/31/72 8:30	76°F	1585	1576	1537		67	7.1	
13:00	76°F	1586	1577	1536		67	7.1	
17:30	78°F	1590	1583	1540		67	7.1	
8/1/72 8:30	76°F	1582	1575	1535		67	7.1	(449 watts)
11:30	76°F	1608	1599	1558		69	7.3	(503 watts) Raise power
13:00	74°F	1604	1596	1555		69	7.3	
17:15	74°F	1597	1588	1547		69	7.3	

TABLE X1

HEAT PIPE LIFE TEST (Contd)

Heat Pipe No.: 2Heat Pipe Description: Sodium Nickel-Nickel Screen Inconel Tube

Date Time	T. Amb.	T ₁ Chart Reading °F	T ₂ Chart Reading °F	T ₃ Chart Reading °F	T ₄ Chart Reading °F	Volts	Amperes	Notes
8/2/72 8:30	76°F	1592	1583	1543		69	7.3	
8/3/72 10:20	76°F	1596	1587	1547		69	7.3	Raised power
11:40	76°F	1626	1616	1572		71	7.5	
17:15	75°F	1631	1620	1574		72	7.6	
8/4/72 16:50	76°F	1625	1616	1571		72	7.6	
8/7/72 0940	76°F	1568	1559	1518		76	7.0	Raised power
8/8/72 0810	76°F	1640	1629	1580		79	7.3	
8/9/72 1100	76°F	1543	1630	1573		79	7.3	
8/10/72 0815	76°F	1643	1631	1586		79	7.2	
8/11/72 0805	75°F	1639	1626	1581		79	7.2	
8/14/72 0850	76°F	1634	1621	1575		80	7.2	
8/16/72 0900	76°F	1635	1622	1577		80	7.2	
8/16/72 8:45	76°F	1633	1620	1577		82	7.5	Honeywell Digital voltmeter
8/17/72 8:30	76°F	1629	1615	1573		82	7.5	
8/18/72 16:45	76°F	1633	1620	1576		81	7.5	
8/21/72 8:45	76°F	1628	1614	1571		81	7.5	
8/22/72 13:35	76°F	1619	1605	1564		81	7.3	
8/23/72 17:25	76°F	1626	1610	1567		82	7.4	
8/25/72 8:30	75°F	1622	1609	1565		81	7.3	
8/29/72 15:20	76°F	1522	1509	1566		81	7.3	
9/1/72 9:00	75°F	1621	1605	1563		81	7.3	

TABLE XI
HEAT PIPE LIFE TEST (Contd)

Heat Pipe No.: 2

Heat Pipe Description: Sodium Nickel-Nickel Screen Inconel Tube

Date Time	T. Amb.	T ₁ Chart Reading °F	T ₂ Chart Reading °F	T ₃ Chart Reading °F	T ₄ Chart Reading °F	Volts	Amperes	Notes
9/16/72 10:15	74°F	1619	1605	1567		81	7.4	
9/17/72 8:30	75°F	1632	1614	1571		81	7.5	
9/11/72 17:15	75°F	1624	1606	1565		81	7.4	
9/14/72 9:30	74°F	1624	1606	1564		81	7.4	
9/15/72 15:00	74°F	1614	1596	1557		80	7.4	
9/18/72 8:30	74°F	1631	1614	1571		81	7.2	
9/29/72 8:30	75°F	1626	1606	1568		81	7.2	
10/6/72 16:15	76°F	1626	1604	1566		81	7.1	
10/16/72 10:45	75°F	1618	1600	1558		80	7.42	Ammeter in circuit
10/17/72 11:05	78°F	1596	1554		1538 *	78	7.4	Volt drop could be due to line load
10/17/72 16:00	78°F	1623	1602		1563	80	7.55	Raised power
10/18/72 9:00	77°F	1620	1600		1560	80	7.55	
10/19/72 9:00	76°F	1618	1597		1559	80	7.55	Raised power
10/19/72 9:00						82	7.70	
10/20/72 9:00	77°F	1645	1623		1583	83	7.70	
10/23/72 9:00	78°F	1643	1621		1581	83	7.75	Lower power
10/23/72 9:00						82	7.6	
10/24/72 11:00	78°F	1636	1615		1575	83	7.65	
10/26/72 9:00	80°F	1639	1617		1578	83	7.7	Lower power
10/26/72 9:00						82	7.59	
10/27/72 9:00	78°F	1619	1598		1559	81	7.6	

* Change column to compare with others.

TABLE XI

HEAT PIPE LIFE TEST (Contd)

Heat Pipe No.: 2Heat Pipe Description: Sodium Nickel-Nickel Screen Inconel Tube

Date Time	T. Amb.	T ₁ Chart Reading °F	T ₂ Chart Reading °F	T ₃ Chart Reading °F	T ₄ Chart Reading °F	Volts	Amperes	Notes
11/1/72 11:00	78°F	1616	1594		1555	81	7.55	
11/1/72 16:00	78°F							Did not raise power
11/6/72 16:00	79°F	1631	1607		1567	81	7.6	
11/16/72 9:30	79°F	1633	1609		1571	83	7.6	
11/22/72 13:00	75°F	1624	1601		1565	82	7.6	
11/27/72 1300	77°F	1623	1600		1565	83	7.6	
11/28/72 1:45	76°F	1633	1609		1573	84	7.62	
12/1/72 17:00	78°F	1629	1605		1569	83	7.61	
12/8/72 10:00	76°F	1637	1613		1577	83	7.7	
12/19/72 15:00	76°F	1618	1594		1560	82	7.55	
12/19/72 15:30						83	7.61	Raised power
1/8/73 9:00	76°F	1635	1610		1577	83	7.68	
1/15/73 9:00	75°F	1626	1600		1567	84	7.62	
1/23/73 17:00	76°F	1632	1606		1574	85	7.62	
2/6/73 9:00	76°F	1629	1602		1571	83	7.63	
2/12/73 17:00	76°F	1629	1602		1571	82	7.63	
3/2/73 15:00	76°F	1628	1599		1569	80	7.65	
3/15/73 9:00	77°F	1636	1605		1576	83	7.75	
3/28/73 9:00	76°F	1633	1600		1574	83	7.50	
4/6/73 10:00	76°F	1621	1588		1563	83	7.65	Raised power
4/6/73						84	7.75	

TABLE XI

HEAT PIPE LIFE TEST (Contd)

Heat Pipe No.: 2

Heat Pipe Description: Sodium Nickel-Nickel Screen Inconel Tube

[illegible]

TABLE XII
HEAT PIPE LIFE TEST

Heat Pipe No.: 3

Heat Pipe Description: Sodium - Inconel Screen and Tube

Date Time	T. Amb.	T ₁ Chart Reading °F	T ₂ Chart Reading °F	T ₃ Chart Reading °F	T ₄ Chart Reading °F	Volts	Amperes	Notes
								Start-up 16:00 hrs 10/16/72
10/17/72 11:10	78°F	1618	1609	1600	1592	69	6.4	
10/17/72 16:00	78°F	1619	1609	1600	1593	70	6.45	
10/18/72 9:00	77°F	1602	1592	1582	1575	69	6.4	Raised power
10/18/72 9:00						70	6.5	
10/19/72 9:00	76°F	1603	1591	1580	1575	71	6.5	Raised power
10/19/72 9:00						73	6.70	
10/20/72 9:00	77°F	1629	1616	1606	1600	74	6.70	
10/23/72 9:00	78°F	1603	1590	1579	1572	74	6.70	Raised power
10/23/72 9:00						75	6.80	
10/24/72 11:00	78°F	1620	1605	1594	1587	76	6.80	
10/26/72 9:00	80°F	1614	1600	1588	1583	76	6.80	
10/27/72 9:00	78°F	1614	1600	1588	1583	76	6.80	
11/1/72 11:00	78°F	1604	1589	1577	1571	76	6.82	
11/1/72 16:00	78°F					76	6.90	Raised power
11/6/72 1600	79°F	1614	1596	1583	1583	76	6.90	
11/16/72 9:30	79°F	1599	1579	1567	1561	76	6.95	
11/16/72 9:30						77	7.00	Raised power
11/21/72 13:00								Fuse blown
11/22/72 13:00	75°F	1614	1592	1579	1573	78	7.1	
11/22/72 13:00						78	7.15	Raised power
11/27/72 1000	77°F	1617	1595	1581	1576	79	7.15	

TABLE XII
HEAT PIPE LIFE TEST (Contd)

Heat Pipe No.: 3

Heat Pipe Description: Sodium - Inconel Screen and Tube

Date Time	T. Amb.	T ₁ Chart Reading °F	T ₂ Chart Reading °F	T ₃ Chart Reading °F	T ₄ Chart Reading °F	Volts	Amperes	Notes
12/1/72 17:00	78°F	1621	1600	1587	1582	79	7.2	
12/8/72 10:00	76°F	1607	1665	1591	1586	79	7.2	
12/19/72 15:00	76°F	1563	1590	1576	1569	78	7.15	
12/19/72 15:30						79	7.25	Raised power
1/8/73 9:00	76°F	1587	1606	1591	1584	79	7.30	
1/15/73 9:00	75°F	1584	1602	1588	1580	80	7.30	
1/23/73 17:00	76°F	1585	1602	1587	1581	81	7.30	
2/5/73 9:00	76°F	1587	1602	1587	1579	79	7.33	
2/12/73 17:00	76°F	1585	1599	1584	1575	78	7.35	
3/2/73 15:00	76°F	1577	1589	1575	1566	76	7.30	
3/2/73 15:00						77	7.40	Raised power
3/15/73 9:00	77°F	1589	1599	1584	1574	79	7.40	
3/28/73 9:00	76°F	BAD	1596	1581	1568	79	7.4	
3/28/73 9:30						81	7.5	Raised power
4/6/73 1000	76°F	BAD	1605	1590	1576	82	7.4	
4/13/73		HEATER	SHORTED OUT					Power off
4/20/73 9:00	76°F	START-UP	SLOWLY		3 AMP	25 V		Install 10 AMP fuse
9:45					4 AMP	30 V		
10:00		BAD	863	400	452	30	4	Raised power
10:50			1047	1042	992	40	5	Raised power

TABLE XII

Heat Pipe No.: 3

Heat Pipe Description: Sodium - Inconel Screen and Tube

[illegible]

TABLE XIII

HEAT PIPE LIFE TEST

Heat Pipe No.: 4Heat Pipe Description: Sodium Inconel Screen and Tube

Date Time	T. Amb.	T ₁	T ₂	T ₃	T ₄			Notes
		Chart Reading °F	Chart Reading °F	Chart Reading °F	Chart Reading °F	Volts	Amperes	Start-up 10/17/72
10/17/72 11:15	78°F	1605	1590	1561	1569	69	6.35	Raised power
10/17/72 16:00	78°F	1620	1604	1569	1579	71	6.45	
10/18/72 9:00	77°F	1601	1585	1544	1556	70	6.45	Raised power
10/18/72 4:00						71	6.6	
10/19/72 9:00	76°F	1608	1590	1547	1555	73	6.60	Raised power
10/19/72 9:00						74	6.70	
10/20/72 9:00	77°F	1613	1594	1551	1558	74	6.70	Raised power
10/20/72 9:00						75	6.80	
10/23/72 9:00	78°F	1609	1588	1545	1552	76	6.80	Raised power
10/23/72 9:00						76	6.85	
10/24/72 11:00	78°F	1617	1596	1552	1559	77	6.90	
10/26/72 9:00	80°F	1618	1597	1554	1560	78	6.92	Raised power
10/26/72 9:00						79	6.95	
10/27/72 9:00	78°F	1621	1600	1555	1562	78	6.95	
11/1/72 11:00	78°F	1614	1593	1549	1555	78	6.92	
11/1/72 16:00	78°F					79	7.00	
11/6/72 16:00	79°F	1625	1601	1557	1560	79	7.01	
11/16/72 8:30		HEATER	OPEN					

TABLE XIV

HEAT PIPE LIFE TEST

Heat Pipe No.: 5Heat Pipe Description: Sodium - Inconel Screen and Tube

Date Time	T. Amb.	T ₁ Chart Reading °F	T ₂ Chart Reading °F	T ₃ Chart Reading °F	T ₄ Chart Reading °F	Volts	Amperes	Notes Start-un 10/17/72
10/17/72 11:20	78°F	1603	1594	1577	1558	70	6.4	Raised power
10/17/72 16:00	78°F	1608	1599	1582	1585	72	6.45	
10/18/72 9:00	77°F	1590	1582	1564	1567	71	6.4	Raised power
10/18/72 9:00						72	6.6	
10/19/72 9:00	76°F	1605	1596	1578	1581	74	6.6	Raised power
10/19/72 9:00						75	6.7	
10/20/72 9:00	77°F	1619	1608	1569	1592	75	6.7	
10/23/72 9:00	78°F	1594	1583	1566	1567	76	6.75	Raised power
10/23/72 9:00						77	6.80	
10/24/72 11:00	78°F	1607	1596	1578	1579	77	6.85	
10/26/72 9:00	80°F	1600	1588	1571	1572	78	6.85	Raised power
10/26/72 9:00						78	6.90	
10/27/72 9:00	78°F	1608	1596	1579	1579	78	6.90	
11/1/72 11:00	78°F	1596	1585	1569	1569	78	6.95	
11/1/72 16:00	78°F					79	7.00	Raised power
11/6/72 16:00	79°F	1599	1584	1568	1567	79	6.98	
11/6/72 17:00						79	7.01	Raised power
11/16/72 9:30	79°F	1605	1589	1575	1575	79	7.1	
11/16/72 9:30						81	7.15	Raised power
11-21-72 1900		OBSERVED	OFF - HEATER OPEN					

TABLE XV
HEAT PIPE LIFE TEST

Heat Pipe No.: 6

Heat Pipe Description: Sodium - Inconel Screen and Tube

Date Time	T. Amb.	T ₁	T ₂	T ₃	T ₄			Notes Start-up 10/17/72
		Chart Reading °F	Chart Reading °F	Chart Reading °F	Chart Reading °F	Volts	Amperes	
10/17/72 11:25	78°F	1593	1582	1569	1570	66	6.4	Raised power
10/17/72 16:00	78°F	1613	1602	1586	1589	69	6.55	
10/18/72 9:00	77°F	1598	1587	1570	1573	68	6.5	Raised power
10/18/72 9:00						69	6.7	
10/19/72 9:00	76°F	1607	1594	1576	1578	71	6.7	Raised power
10/19/72 9:00						72	6.8	
10/20/72 9:00	77°F	1620	1606	1587	1590	72	6.8	
10/23/72 9:00	78°F	1609	1589	1571	1573	73	6.85	Raised power
10/23/72 9:00						74	6.90	
10/24/72 11:00	78°F	1616	1600	1581	1584	74	6.95	
10/26/72 9:00	80°F	1616	1598	1579	1582	75	7.0	Raised power
10/26/72 9:00						76	7.2	
10/27/72 9:00	78°F	1626	1608	1589	1593	75	7.05	
11/1/72 11:00	78°F	1615	1596	1576	1581	75	7.1	
11/6/72 16:00	79°F	1604	1584	1564	1567	75	7.1	
11/6/72 17:00	79°F					77	7.2	Raised power
11/16/72 9:30	79°F	1640	1616	1596	1600	77	7.4	
11/16/72 9:30						77	7.35	Lower power
11/22/72 13:00	75°F	1617	1595	1574	1578	77	7.4	
11/22/72 13:00						78	7.42	Raised power
11/27/72 1000	77°F	1621	1599	1580	1585	79	7.42	

TABLE XV
HEAT PIPE LIFE TEST (Contd)

Heat Pipe No.: 6

Heat Pipe Description: Sodium - Inconel Screen and Tube

Date	T. Amb.	T ₁	T ₂	T ₃	T ₄	.		Notes
Time		Chart Reading °F	Chart Reading °F	Chart Reading °F	Chart Reading °F	Notes	Amperes	
12/1/72 17:00	78°F	1623	1600	1580	1585	78	7.5	
12/8/72 10:00	76°F	1628	1605	1587	1591	79	7.5	
12/19/72 15:00	76°F	1604	1582	1562	1565	77	7.4	
12/19/72 15:30						78	7.45	Raised power
1/8/73 9:00	76°F	1624	1601	1580	1585	78	7.55	
1/15/73 9:00	75°F	1610	1588	1567	1572	80	7.50	
1/15/73 9:30						81	7.60	Raised power
1/23/73 17:00	76°F	1616	1594	1573	1577	82	7.60	
2/12/73 9:00	76°F	1608	1585	1564	1569	79	7.60	
2/12/73 9:30	76°F					81	7.70	Raised power
2/12/73 17:00	76°F	1616	1594	1572	1577	79	7.72	
3/2/73 15:00	76°F	1613	1591	1570	1575	78	7.75	
3/2/73 15:00						78	7.80	Raised power
3/15/73 9:00	77°F	1626	1604	1582	1588	81	7.80	
3/28/73 9:00	76°F	1620	1599	1576	1583	81	7.8	
4/6/73 10:00	76°F	1613	1591	1569	1575	82	7.75	Raised power
4/6/73 10:00						83	7.82	
4/16/73 8:30	76°F	1628	1607	1585	1591	81	7.8	
4/20/73 10:30	76°F	1722	1691	1666	1673	81	9.1	Cut back
4/20/73 10:45	76°F					73	8.4	
4/20/73 12:00	76°F	1631	1603	1581	1588	74	8.55	Raised power

TABLE XV

HEAT PIPE LIFE TEST (Contd)

Heat Pipe No.: 6

Heat Pipe Description: Sodium - Inconel Screen and Tube

[illegible]

TABLE XVI

SUMMARY OF INTEGRATED TEST TIMES
SUBSCALE ENDURANCE TEST

<u>Unit</u>	<u>Start Test</u>	<u>End Test</u>	<u>Test Time (Days)</u> <u>as of 7-25-73</u>
SN 1	10-17-72	11-14-72	28
SN 2	7-25-72	Continuing	365
SN 3	10-17-72	4-23-73	182
SN 4	10-17-72	11-16-72	30
SN 5	10-17-72	11-21-72	35
SN 6	10-17-72	5- 7-73	202

- e. Both units were opened and the sodium removed to permit metallographic and other characterization of the inner heat pipe surfaces.
- f. Examination of the wick and tube structures showed no indication of general corrosion or mass transport processes anywhere except local spots in the evaporator.
- g. The penetration regions evidenced a highly localized catastrophic process.
- h. SN 5 was subsequently removed from test, deactivated, and the evaporator region examined.

A metallographic examination and microprobe analysis of the evaporator tube wall and penetration regions was performed. The results of this investigation are presented in the next subsection of this report. Details in the results differed only slightly for the three units leading to the conclusion that the process or processes producing wall penetrations were the same in all three heat pipes.

Two possible processes were suggested.

- a. The occurrence of an unidentified high order eutectic at the penetration point where trace amounts of higher vapor pressure elements within the heat pipe would be deposited in the evaporator. This process would lead to a penetration from the inside out due to local melting of the eutectic. Heater failure would be produced as a secondary reaction.
- b. The penetration was triggered by arcing over from the heater and was a result of heater burnout.

Testing of SNs 2, 3 and 6 continued until April 1973 when SN 2 was observed to experience a sudden step increase in power associated with a decrease in resistance. Before current limiting fuses had been added into all circuits, SN 6 similarly experienced a step power increase. This was the first indication that the heaters failed by initially shorting to the heat pipe rather than by immediate open-circuiting. With both SN 3 and 6, sufficient heater resistance (typically 6 ohms) remained to attempt to restart and continue the test by a downward adjustment of the voltage to hold 600 watts and 1600°F. Ten ampere line fuses were added to all three units.

SN 3 was restarted after a 7 day interruption. SN 2 and 6 remained in continuous test. Though SN 3 could successfully be restarted, the heater degraded rapidly. The current limit fuse was found to have blown over the following weekend. Similarly, the heater of SN 6 opened after a short period. After the removal of the heaters and during examination of the external surfaces of the heat pipe evaporator regions, no evidence of localized tube penetration or sodium release could be found.

While circumstantial, the prevention of a sustained gross overheating due to a progressive shorting of the heater could explain why no tube wall failure occurred in units SN 3 and SN 6. In light of these results the possible cause leading to a localized penetration of the heat pipe wall of heat pipes SN 1, 4 and 5 must be assumed to have been heater failures. That the heat pipe wall were penetrated only in the area of these heaters must be considered as further evidence that the heaters were the prime cause of heat pipe failure when it occurred.

4.5 METALLURGICAL INVESTIGATION OF LOCALIZED TUBE WALL PENETRATIONS

The metallurgical investigation of the subscale heat pipe failures was initiated with the analysis of pipe SN 1.

Upon discovery of the failure of the heater, it was removed from the endurance test and the heater removed from the pipe. After removal of the heater the location and extent of the damage to the heat pipe could be recognized.

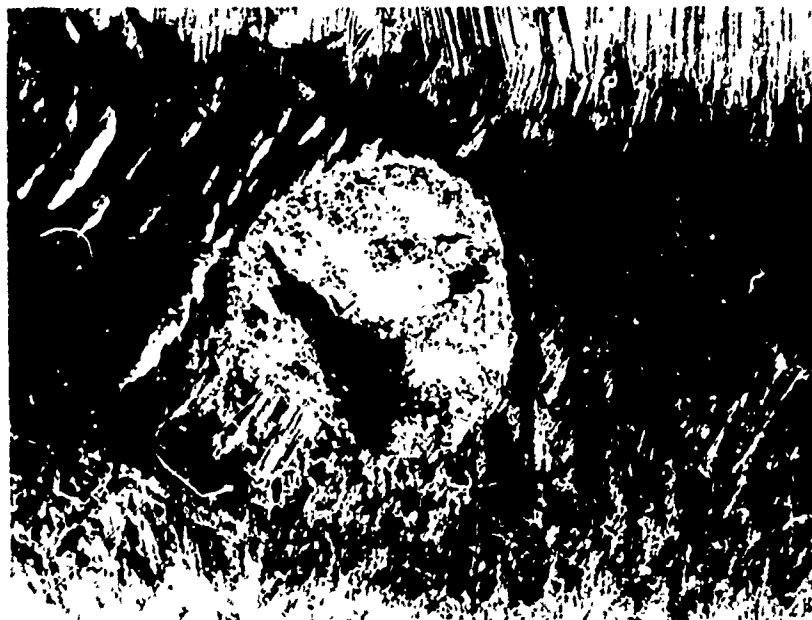
Visibly, only a single small spot located in about the middle of the evaporator region was found. This damage can be seen in Figure 20. The pipe was emptied of its remaining sodium charge and a more detailed failure analysis undertaken.

The sodium was removed by cutting off the condenser end cap in an argon atmosphere and then oxidizing the sodium with alcohol. The pipe was then cleaned with water and the evaporator end cap was removed. Visual examination of the pipe interior showed only a slight build-up of material on the diametral wick adjacent to the indicated wall penetration. The heat pipe was then sectioned along the diametral wick within the evaporator section of the pipe.

Macro examination of the inside of the pipe near the wall penetration showed no material build-up on the internal screens. This region of the pipe can be seen in Figure 21. The screen (wick) was then removed a layer at a time. The photographic record shown in Figures 22 and 23 revealed the damage to the wall and screens.



a) $\sim 2.5X$



006698

b) $\sim 10X$

Figure 20. Location and Extent of Tube Wall Change in Inconel Type SN-1

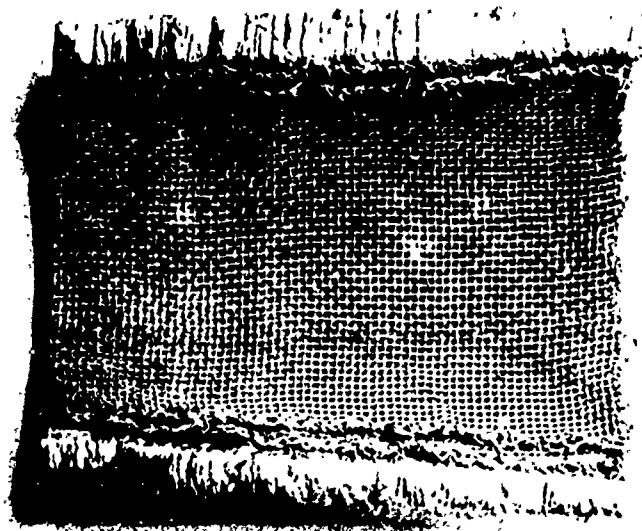
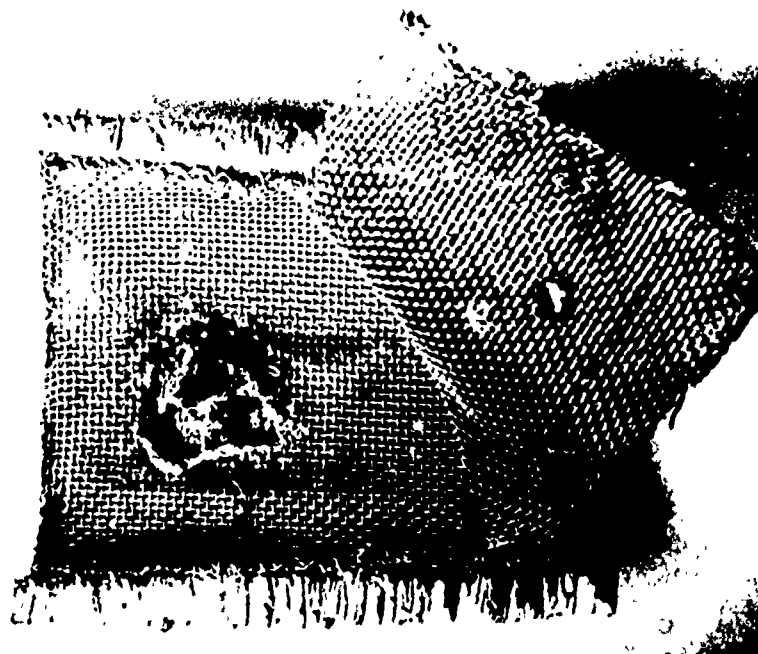
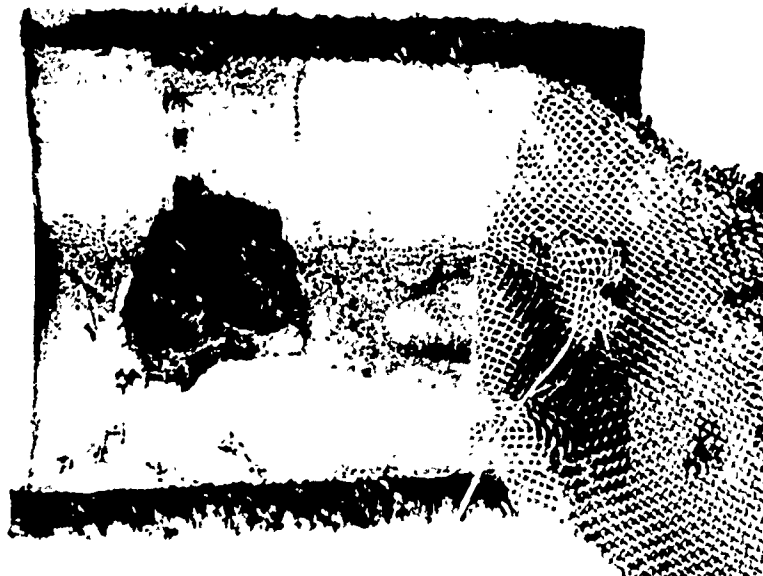


Figure 21. View of Tube I.D. Hole is located under the small white spot ~ in the center of the photograph. ~ 2.5X



006699

Figure 22. Damage Revealed as Inner Screen Was Removed



a) ~ 2X



b) ~ 10X

Figure 23. Wall Damage Seen after Removal of Screen

The section containing the hole was then prepared for microscopic cross section and for microprobe analysis. The balance of the tube was sectioned lengthwise for further examination.

Visually the screens showed no evidence of mass transport or other damage. However, as the screens were removed a second reacted region was found on the tube wall almost 180° from the primary penetration point. A view of this region is shown in Figure 24.

Since the analysis of the wall penetration could be obscured by the effect of a high temperature oxygen-sodium reaction as well as by infiltration of the region by external materials, a section of the reaction region was also prepared for metallographic and microprobe analysis.

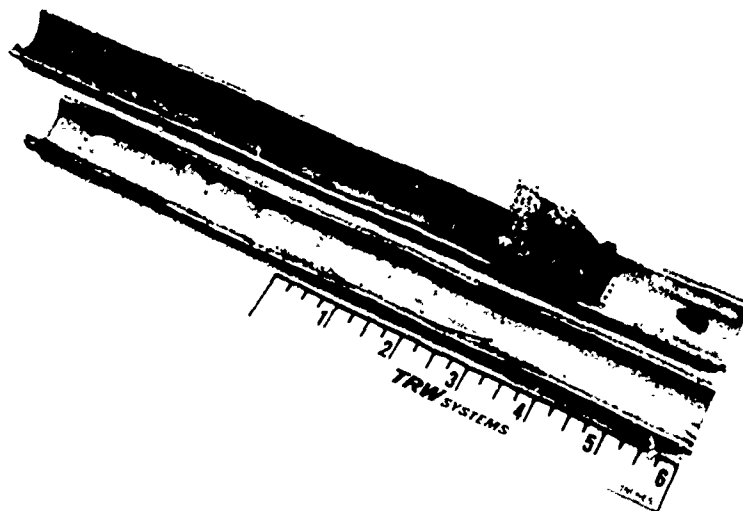
The metallographic examination consisted of standard mounting and polishing a cross section of the failed and reacted regions. The sections were etched with the recommended etchants and the microstructures examined. Figure 25 shows the cross section of the failed region at 50X. Higher magnification views of this region were prepared as part of the microprobe analysis and are shown later in this report. Analysis of this region failed to reveal the cause of the penetration and the porous structure remaining did not lend itself to metallurgical analysis.

The reacted region, which was found approximately 180° away from the penetrated area, is shown in Figure 26. Examination of this region shows a heavy grain boundary precipitate of chromium carbide and some attack on the tube wall. The presence of the carbide is not entirely unexpected because at temperatures between 1000° and 1800°F , chromium carbide precipitates out of solid solution. This precipitation will occur both at the grain boundaries and in the matrix¹. The attack, which is seen, is both transgranular as well as intergranular in nature. A detailed view of the intergranular attack is shown in Figure 27.

Quoting from the Inco Bulletin, "Because of the grain boundary precipitation, the corrosion behavior of alloy 600 is similar to that of other austenetic alloys in that the material can be made susceptible to intergranular attack in some aggressive media (sensitized) by exposure to temperature of 1000°F to 1400°F . At temperature above 1400°F , the predominant carbide is Cr_7C_3 . Below 1400°F , the Cr_{23}C_6 carbide is also present."

Since the pipe was operated above 1400°F , the sensitization of the alloy is not expected. However, it may be a partial explanation of the failure, especially if accompanied by a slight change in chemical composition.

1. Inconel Alloy 600- Huntington Alloy Products Division Bulletin.



006701

Figure 24. Reacted Region Seen on Tube Wall
as Screens Were Removed

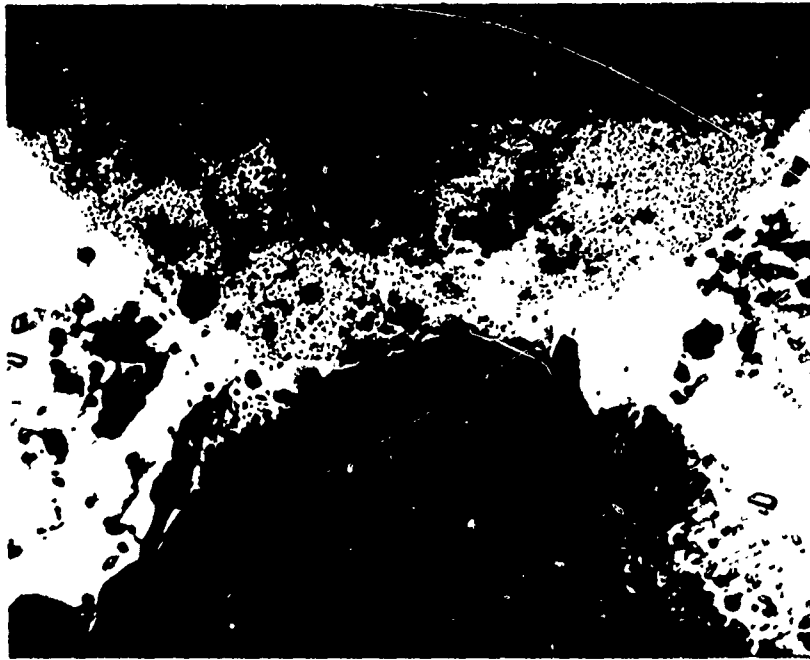


Figure 25. Cross Section of Wall Penetration (50X)



006702

Figure 26. Cross Section of Reacted Zone Found 180° from Wall Penetration (50X)

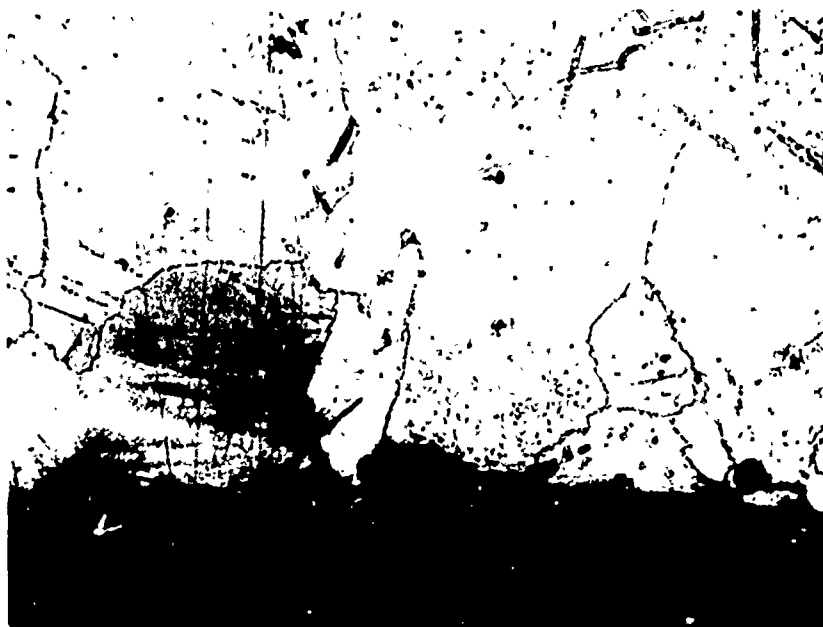


Figure 27. Details of the Corrosion Attack at the Reacted Region.
 (a) shows the transgranular and general corrosion of the surface, and (b) shows the intergranular attack.

The reaction region was further examined using the electron microprobe. In addition to the spectral scans on the failed specimens, a comparative analysis of the area near and at the reaction zone was undertaken to determine if the ratio of major components of Inconel had changed due to the presence of liquid sodium. The locations of the microprobe sites are shown in Figure 28. Table XVII presents the results of these investigations. This data confirms very little difference in the composition of the major constituents between a nonreacted area and the region of failure. Titanium, which forms both a carbide and nitride, had a higher concentration in the non-reacted areas. There appears to be an increase of phosphorus content in the failed area as compared to a nonreacted area. Such variations in chemical composition could lead to conclusion that complex micro-chemical reactions occur in the heat pipes. At a given point on the tube wall, the composition may be changed sufficiently to result in localized melting.



Figure 28. Location of Regions Evaluated by Microprobe Analysis

- 1) In grain boundary in the center of the reacted zone
- 2) Large white inclusion on tube i.d.
- 3), 4) Inside edge of tube
- 5) Grain center near reacted zone
- 6) Unreacted area out of picture

TABLE XVII
RELATIVE X-RAY INTENSITY
(UNCORRECTED)

<u>Location*</u>	<u>Element</u>					
	<u>Ni</u>	<u>Fe</u>	<u>Cr</u>	<u>Cu</u>	<u>P</u>	<u>Ti</u>
1. Grain Boundary	3,918	5,046	164,600	0	64	79
2. Large White Inclusion	2,806	2,876	175,500	0	0	0
3. Inside Edge	114,400	14,600	28,200	1,000	351	56
4. Incide Edge	108,800	18,400	23,900	2,102	321	139
5. Grain Center	106,200	18,000	33,200	150	53	225
6. Unreacted Area	108,200	18,000	33,000	250	28	306
7. Unreacted Inclusion	-	-	-	-	-	75,900

* As shown in Figure 28

The analysis of the other two failed units (SN-4 and 5) was confined to the removal of the sodium and a visual search for the failed area and a possible reaction zone.

In both cases, the locations of the failed regions are at the zero flow point. This is the location where any lower vapor pressure material, if present, would accumulate as the sodium evaporates. In SN 4 as in SN 1, a reaction site was found at approximately 180° away from the primary penetration region. (See Figure 29.) In SN 5 a small penetration of the wall at approximately the same location as was seen in SN 4 was found. However, there was no evidence of a reaction on the opposite side of the pipe. In all of the failed units it was observed that the reaction was in or on the Inconel while the nickel screen showed no involvement in the primary reaction. Thus, any reaction involving the formation of a low melting compound would be a higher order alloy system for which phase diagrams are not available. A complete analysis of this hypothesis is not possible at this time.

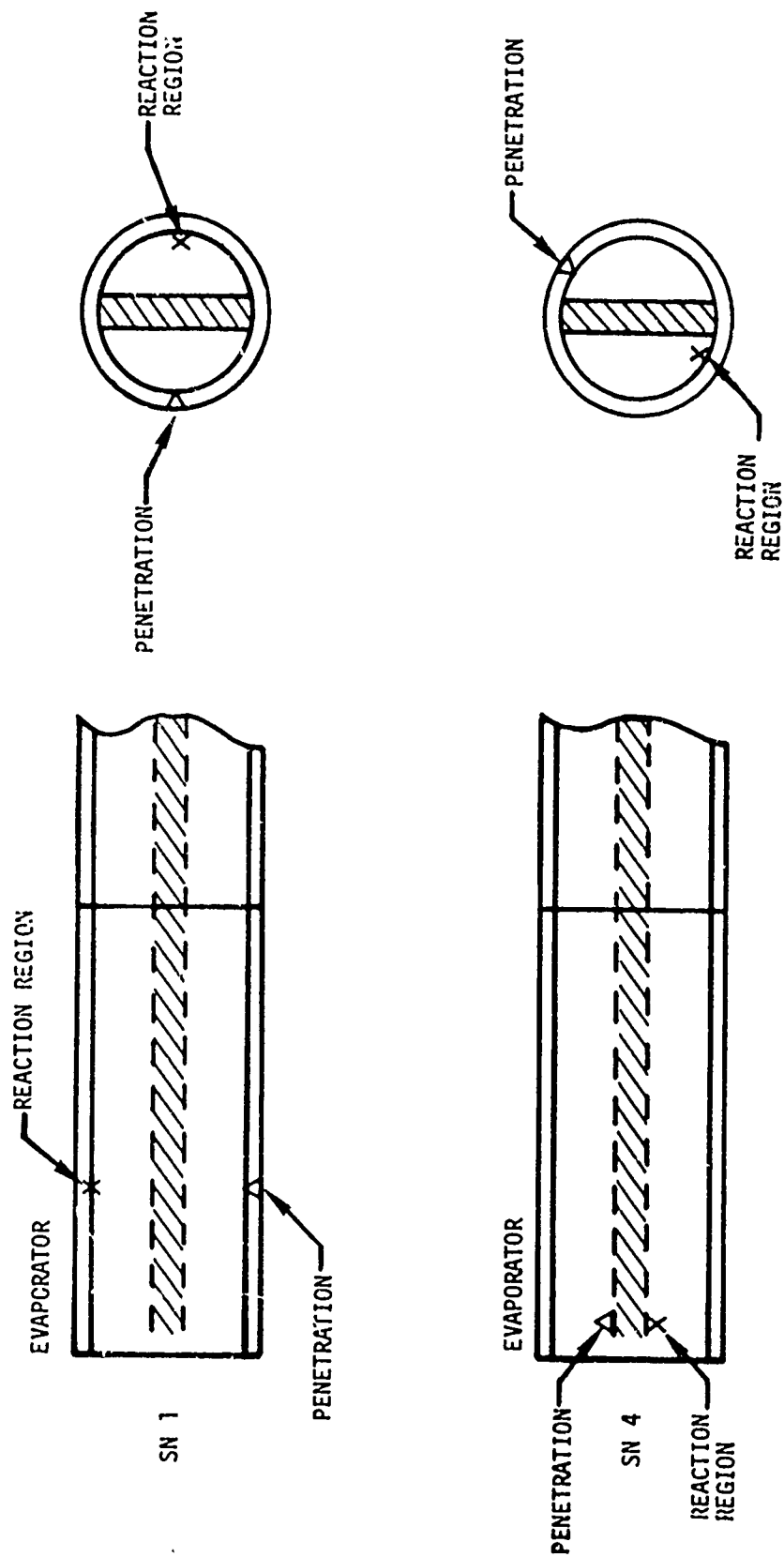


Figure 29. Location of Failures in Subscale Heat Pipes SN 1 and SN 4

In an attempt to gain a fuller understanding of the material and the failure, discussions were held with International Nickel Company (Inco) to determine whether the as-received material was typical and whether wall penetration failures had been experienced in these material combinations.

It was confirmed by the manufacturer that the single unit tubing used for the subscale heat pipes had been in the typical compositional range of alloy Inconel 600.

By examination of the grain structure of the as-received material, it was concluded that the material had been correctly heat treated and was completely normal. The vendor stated that wall failures in alloy 600 with sodium are known. They are usually accompanied with a broad corrosion zone and a large amount of mass transport. In addition, failures in a sodium-Inconel system are usually attributed to a gross amount of impurity in the sodium (normally oxygen). For the failures that lacked indication of mass transport, had a very small corrosion site, and were associated with sodium free from large amounts of impurity, the Inco representative could not provide any answer.

For completeness, a microprobe analysis was also performed on the failed section of the heat pipe resulting in the following data recorded in a microprobe analysis report.

4.6 MICROPROBE ANALYSIS REPORT

4.6.1 BACKGROUND

A metallographically prepared cross section (See Figure 30) showing a failed area in a heat pipe tube wall was submitted for microprobe analysis. The tube is Inconel with a heating element brazed to the outer surface with nickel-gold braze. The inner surface of the tube was in contact with liquid sodium.

4.6.2 ANALYSIS PERFORMED

Spectral scans were run on five locations within the cross sectioned sample and on two particles which were removed from the inner surface near the failed area. Electron beam scanning techniques were used to show two dimensional X-ray images of three different areas within the cross section. In the X-ray images, the brighter the area the higher the concentration of the element being analyzed.

4.6.3 RESULTS OBTAINED

The elements detected in the seven spectral scans are shown in Table XVIII. Figure 31 is a photomicrograph showing location No. 1. Figure 32 is a photomicrograph showing location No. 2. Figure 33 is a photomicrograph showing location No. 3. Figure 34 is a photomicrograph showing locations Nos. 4 and 5. Location No. 6 was a black particle which was removed from

TABLE XVIII

ELEMENTS DETECTED IN SPECTRAL SCANS OF FAILED TUBE

Element	X-Ray Intensity Location						
	1	2	3	4	5	6	7
Cu	T	-	H	H	M	-	-
Ni	H	H	H	H	H	L	H
Fe	H	L	M	H	H	T	T
Mn	T	-	-	T	-	-	T
Cr	H	H*	H	H	H	M	T
Ti	T	-	-	-	-	-	T
K	-	-	-	-	-	H	-
S	-	-	T	-	T	T	T
Au	-	-	T	T	-	-	T
Si	T	-	-	-	-	-	T
P	T	-	T	T	T	-	-
Na	-	-	T	-	H	H	-
Cl	-	-	H	T	H	T	-
Ca	-	-	T	-	T	-	-

*~4 times higher than Ni estimate only

T = trace = less than 1%

L = Low = ~.5 to ~ 3%

M = Medium = ~2 to ~5%

H = High = greater than 5%

the inner surface of the tube (near the failure) before mounting. Location No. 7 was metallic particle removed from the same area as location No. 6. Figures 35 through 39 are X-ray images of the boxed area shown in Figure 32. Figures 40 through 44 are X-ray images of the boxed area shown in Figure 33. Figures 45 through 50 are X-ray images of the boxed area shown in Figure 34. Figure 51 is a photomicrograph of the outer surface of the tube away from the failed area. Figure 52 is a Au Mx X-ray of the boxed area shown in Figure 51. The total thickness of the tube wall is 0.070 inch. The inner surface is irregular and is not therefore good as reference for measuring the original wall thickness. Gold at the outer surface was measured at intervals away from the failed area 0.001", at $500\mu \approx 0.0$, at $1000\mu \approx 0.0$, at $1500\mu \approx 0.003$ ", at $3500\mu \approx 0.010$ ".

No conclusions have been formulated from this analysis as to the cause of failure. More samples were prepared for analysis.

The major points that were brought out by the metallurgical investigation of the heat pipe failures can be summarized as follows:

- a. The failed region and the reacted zone show a large amount of grain boundary chromium carbide.
- b. The Inconel tube at the zero flow point is apparently undergoing both transgranular and intergranular attack.
- c. The micro-chemistry of the tube i.d. is substantially different than the bulk of the parent material.
- d. The failures cannot be related to the diffusion of the gold-nickel braze into the heat pipe.

4.7 CONCLUSIONS

- a. Based upon SN 3, 4, and 6 performance under extended testing at 1600°F , the basic long-term compatibility between sodium and Inconel in heat pipes (experiencing heat fluxes and circulation rates modeled on solar power system requirements) appears good.
- b. Termination of test for SN 3 and SN 6 was simple heater degradation and not related to the heat pipes themselves.
- c. Though the evidence is circumstantial and unconfirmed, the most probable cause of the highly localized tube penetration found in subscale heat pipes SN 1, 4, and 5 is thought to have been induced by run-away shorted heaters.
- d. Extended life testing of high temperature heat pipes in which heaters themselves have a limited life time should provide for:



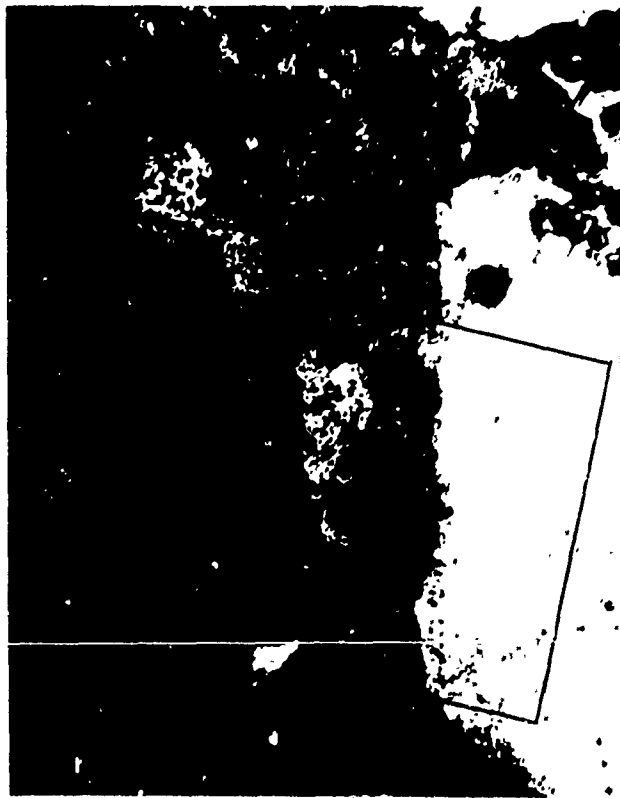
Figure 30. Photomicrograph Showing the Cross Section of a Failed Area of the Inconel Tube (4X)



Figure 31. Photomicrograph Showing Location No. 1 (80X)



Figure 32. Photomicrograph Showing Location No. 2 (80X)



82 Figure 33. Photomicrograph Showing Location No. 3 (80X)



Figure 34. Photomicrograph Showing Location Nos. 4 and 5 (80X)



Figure 35. Ni K α X-Ray Image (~150X)

006706



Figure 36. Fe K α X-Ray Image (~150X)



Figure 37. Cr K α X-Ray Image (~150X)



Figure 38. Cu K α X-Ray Image (~150X)



Figure 39. P K α X-Ray Image (~150X)

006707

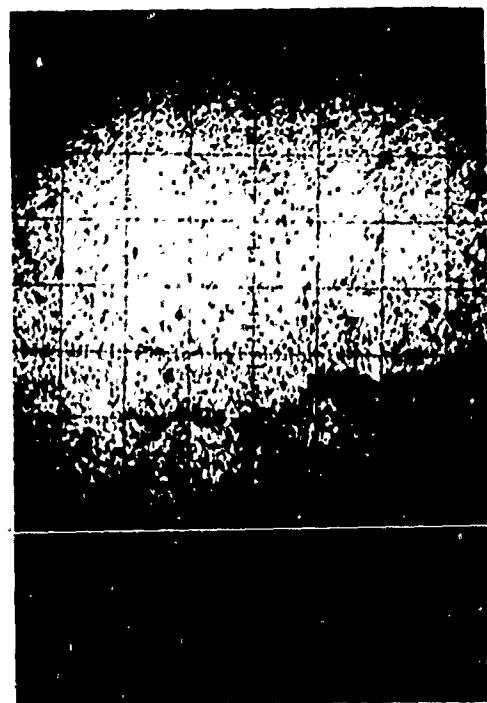


Figure 40. Ni K α X-Ray Image (~ 150X)

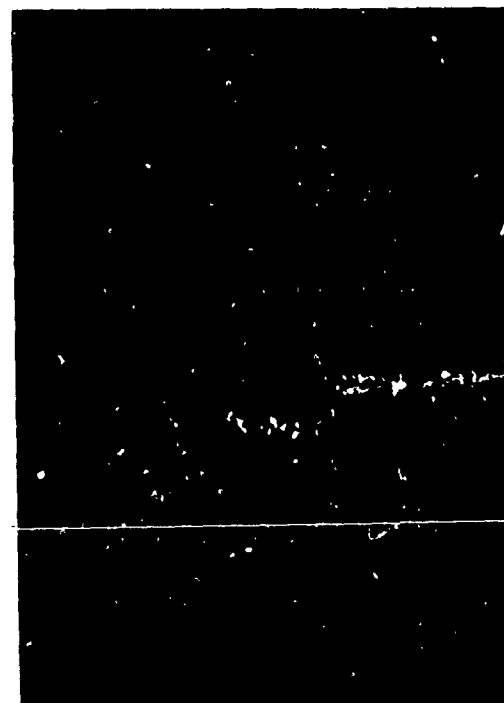


Figure 42. Na K α X-Ray Image (~ 150X)



Figure 41. Cr K α X-Ray Image (~ 150X)



Figure 43. Fe K α X-Ray Image (~ 150X)

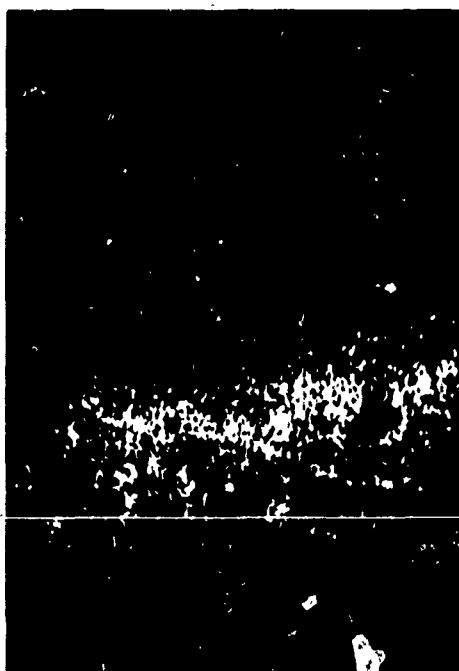


Figure 44. Cu K α X-Ray Image (~150X)



Figure 45. Ni K α X-Ray Image (~150X)

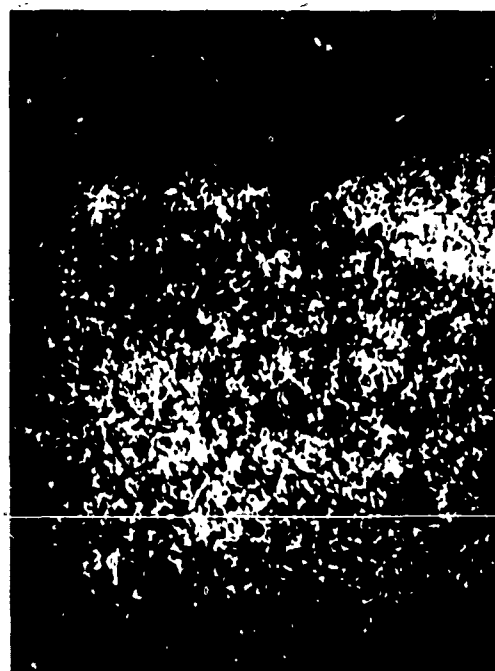


Figure 46. Fe K α X-Ray Image (~150X)

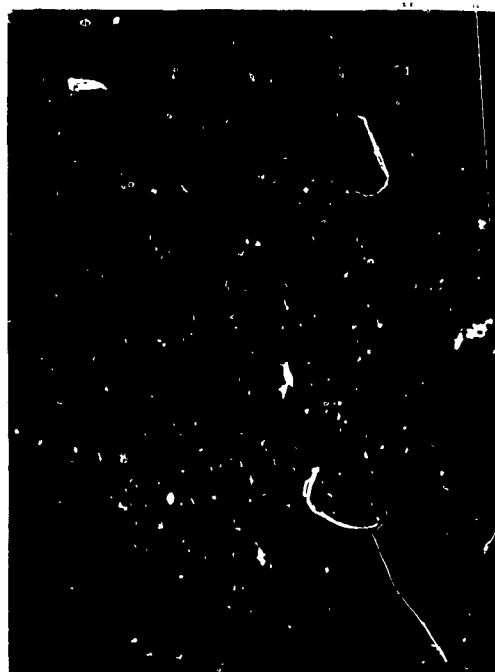


Figure 47. Au M α X-Ray Image (~150X)



Figure 48. Cu K α X-Ray Image (~ 150X)



Figure 49. Cr K α X-Ray Image (~ 150X)

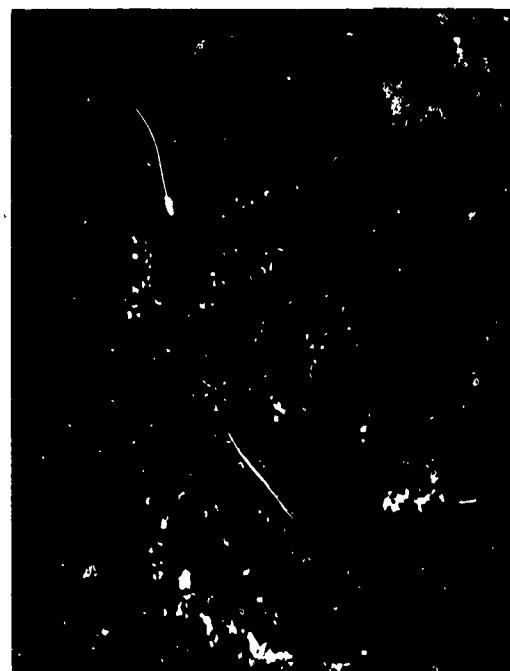


Figure 50. Na K α X-Ray Image (~ 150X)

006710

006711



Figure 51. Photomicrograph Showing the Outer Surface of the Inconel Tube Away from the Failed Area (100X)

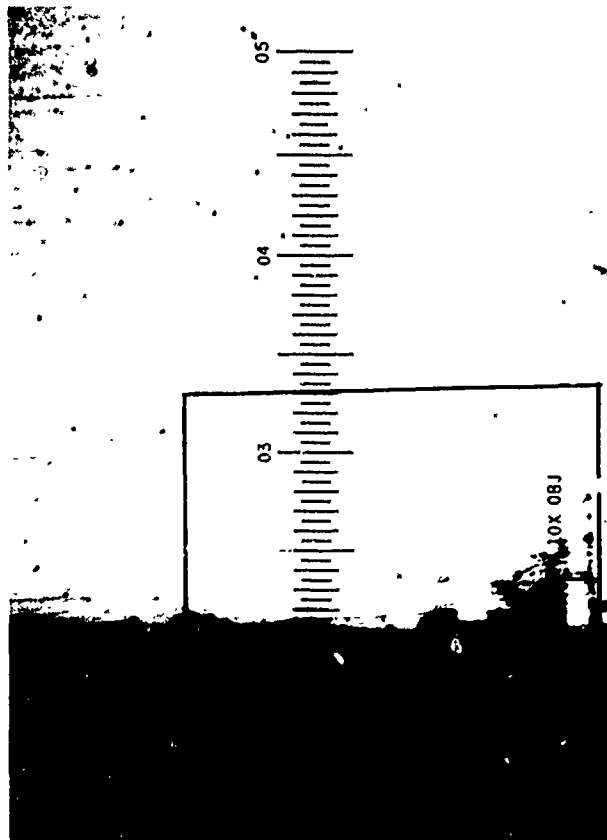


Figure 52. Au $M\alpha$ X-Ray Image of the Outer Surface of the Inconel Tube Away from the Failed Area

- (1) A convenient way of replacing failed heater elements.
- (2) Positive over power/over temperature protection to preclude possible heater induced failures.

In this particular endurance test series, the desired heat fluxes dictated the use of a heater design involving brazing to the evaporator. Replacement at equivalent fluxes after the heat pipe is completed is not practical.

An oversight occurred in not providing some protection against over-power run-aways.

SECTION V

THERMAL ENERGY STORAGE CAPSULE EVALUATION

5.1 INTRODUCTION

For the evaluation of lithium fluoride as thermal energy storage material, a heat pipe-thermal storage unit had been previously constructed and operated in air for 100 simulated cycles of 100 minutes duration, with 65/35 (sun/shade) periods. This test unit consisted of a primary heat pipe coupled to a secondary heat pipe which contained thermal storage material (lithium fluoride) within a cylindrical container (cartridge). Although no absolute calorimetric measurements were made on this unit, temperature variations were observed during simulated orbital operation with thermal storage material contained within a cylindrical cartridge. Posttest radiographic inspection of the cartridge showed no apparent distortion of the cartridge attributable to alternate freezing and thawing of the thermal storage material (lithium fluoride). The cylindrical cartridge geometry for storage salt containment thus showed considerable promise as a simple method of compartmentalizing thermal storage material while permitting ease of fabrication and loading. In addition, thermal behavior of the system can be changed by variation in cartridge diameter, and scaling up to larger storage capacity simply involves increasing the number of cartridges.

Three separate test categories will be reported. The first two categories were conducted under the technical direction of Dr. T. F. Lyon of the General Electric Company while the last category was undertaken by the author of this report. Because different approaches were taken in the testing and evaluation of data, categories two and three are reported separately, though the investigations overlap in many areas. The first is the additional testing of a previously tested heat pipe-thermal storage unit which involved cycling tests with calorimetric measurement of the power output. The second category, denoted Cartridge Geometry Optimization Tests, involved investigation of the cyclic thermal behavior of two heat pipe-thermal storage units with different cartridge diameters. A further goal in the cartridge geometry tests was to explain on a theoretical basis the variation in temperature observed during the heating and cooling portions of the cycle, and to determine the dependence of this variation on both the cartridge diameter and heat flux. The third test category addressed itself to the energy balance in the thermal energy storage system during each cycle. The entire test series was completed with the endurance testing of two subscale thermal energy storage units.

Three heat pipe-thermal storage (HP-TES) units were fabricated and tested. The reported series of tests with the previously tested unit (double heat pipe with single storage cartridge) is denoted test series TTIV (for thermal train #1 tested in vacuum). The cartridge geometry optimization tests and the endurance test involved two test units.

The series of tests involving the single heat pipe with single storage cartridge is denoted test series TT2V, and tests of the single heat pipe with three thermal storage cartridges is TT3V.

5.2 TEST SERIES TTIV

5.2.1 TEST SYSTEM - TEST TTIV

The HP-TES (heat pipe thermal energy storage) unit consists of a primary sodium heat pipe directly coupled to a secondary sodium heat pipe containing a cylindrical cartridge of lithium fluoride. The cartridge is 9.5 inches long, 1.25 inches o.d., with an 0.028-inch wall, and was constructed of Cb-1Zr alloy. The cartridge contained 257 grams of LiF giving a total fusion energy of 2.68×10^5 joules. The nominal power rating was 128 watts determined by the mass of LiF; that is, 128 watts of continuous power was available for 35 minutes from fusion of the salt. Thus

$$\text{Nominal Power Rating} = \frac{m_{\text{LiF}} \Delta H_f}{35 \times 60} = \frac{257 \times 1044}{35 \times 60} = 128 \text{ watts} \quad (1)$$

where

m_{LiF} the mass of LiF

ΔH_f heat of fusion of LiF (1044 joules per gram).

The primary heat pipe was 16 inches long and 0.75 inch in diameter and six inches extended into the secondary heat pipe. The secondary heat pipe was 1.75 inches in diameter and 17.5 inches long. Figure 53 shows the HP-TES unit after fabrication and before insertion of the sodium. The containment material was type 321 stainless steel. Each heat pipe was lined with 5 layers of 100-mesh screen (type 304 stainless steel) for wicking, and the thermal storage cartridge was covered with 3 layers of the same screen.

The HP-TES unit was instrumented with ten thermocouples to measure the temperature at various locations along the heat pipe. A radiant heater, made by winding Pt/Pt + 10% RH wire (0.020-inch-diameter) on a threaded ceramic tube, enclosed an 8-inch length of the primary heat pipe. The HP-TES unit with heater and thermocouples attached is shown in Figure 54.

006408

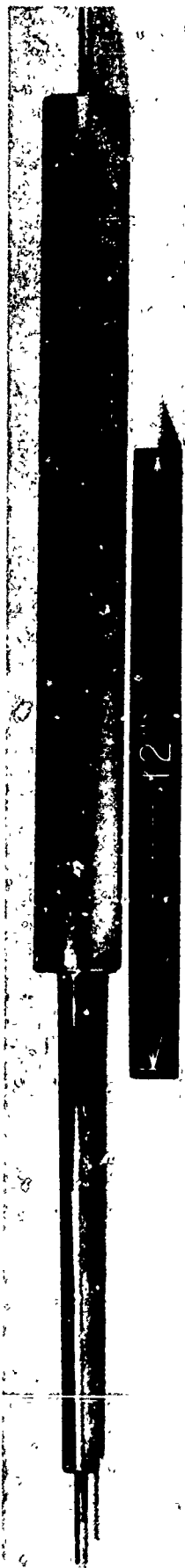


Figure 53. Heat Pipe - Thermal Storage Unit Before Filling and Sealing

006406



Figure 54. Heat Pipe - Thermal Storage Unit with Heater and Thermocouples Attached

The HP-TES unit with heater and thermocouples attached was mounted inside a vacuum enclosure, 9 inches in diameter and 40 inches long. Vacuum pumping was provided by a mechanical pump with molecular sieve trap. Heat rejection from the end of the secondary heat pipe was measured with an air calorimeter surrounding that section. The calorimeter consisted of a 42-inch length of 0.25-inch-diameter stainless steel tubing helically wound on a 2.25-inch diameter. Air flow rate to the calorimeter was measured with a Fischer and Porter Flowmeter (type FP-1/4-25-G-5). A schematic of the test system is shown in Figure 55.

Variable power input was supplied by an autotransformer and power was measured with a wattmeter (Scientific Columbus, Inc., Model 310K605P). Temperature readout was provided by a Bristol Dynamaster multipoint recorder.

5.2.2 TEST CONDITIONS

Thermal cycling of the test system simulated a near-earth orbit (400 nautical miles) of 100-minute period, with 65-minute solar illumination and 35-minute eclipse. For the thermal cycling, an overall thermal balance may be written

$$P_{in} = P_{lost} + P_{TES} + P_{out} \quad (2)$$

where

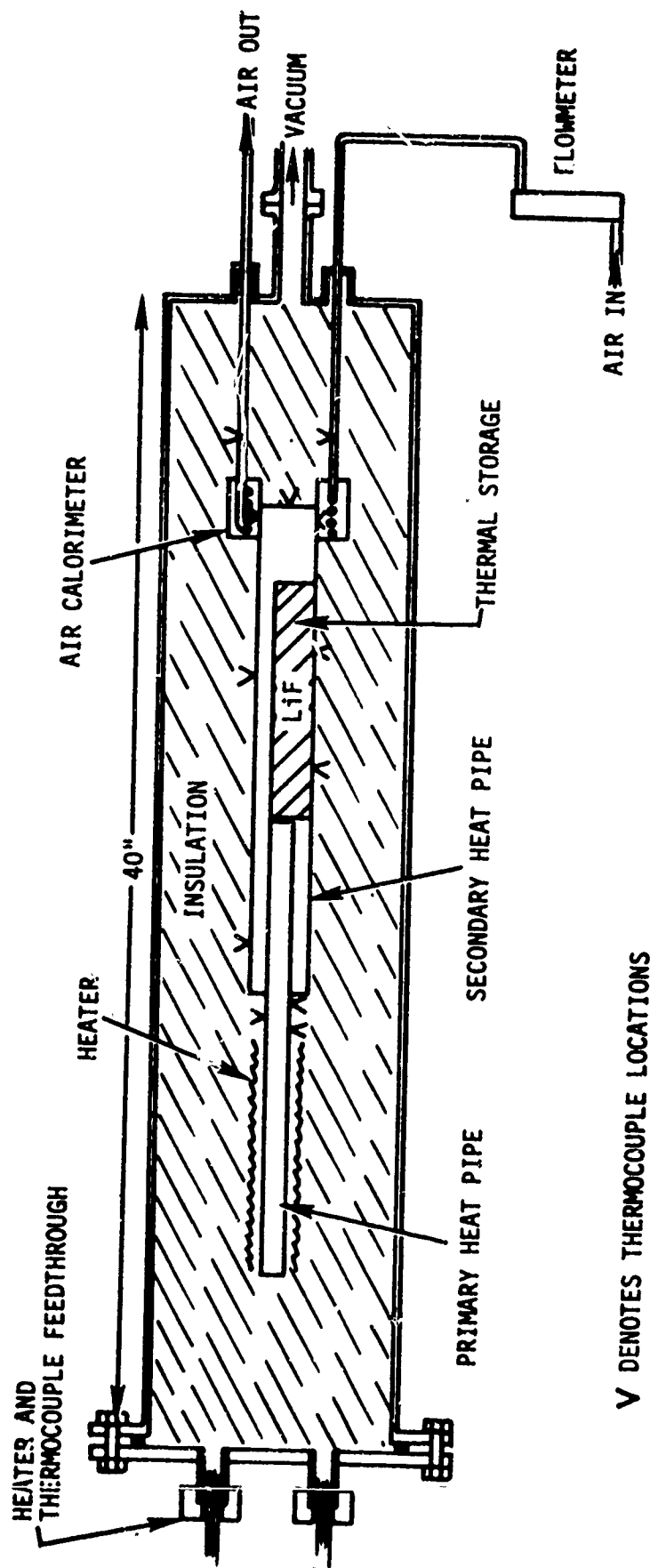
- P_{in} total electrical power to the heater
- P_{lost} thermal power lost through the insulation
- P_{TES} power to or from the thermal energy storage (positive on heating, negative on cooling)
- P_{out} power to the calorimeter

P_{TES} includes the effect of the LiF fusion energy and the effect of the thermal mass (specific heat effect) on the entire system.

P_{lost} was obtained by operating the system at steady state (isothermal) conditions at temperatures near the melting point of LiF. Since P_{TES} is zero under these conditions,

$$P_{lost} = P_{in} - P_{out} \quad (3)$$

TEST SETUP FOR HEAT PIPE/THERMAL STORAGE CALORIMETRIC TESTS NOMINAL STORAGE RATING - 128 WATTS FOR 35 MIN.



V DENOTES THERMOCOUPLE LOCATIONS

Figure 55. Test System for Heat Pipe - Thermal Storage Unit Calorimetric Tests

During these measurements, P_{out} was adjusted to be the nominal power rating of the unit. For the present case, the nominal power rating was 128 watts (35-minute cooling period). The power to the LiF during the heating (simulated sun) portion was the power required to melt the LiF in 65 minutes, that is, 69 watts. During the heating portion the power balance is:

$$P_{in} = P_{lost} + P_{TES} + P_{out} = P_{lost} + 69 + 128 \quad (4)$$

During the cooling (simulated shade) cycles, the heater supplied only the power lost so that $P_{in} = P_{lost}$ and $P_{TES} = P_{out} = 128$ watts. The nominal cyclic power conditions were thus determined.

Figure 56 shows the steady state heat loss plotted against temperature at various temperatures near the LiF melting point (1558°F). From this plot, a power loss of 150 watts at the melting point was obtained. The approximate heater power settings were thus determined (from Eq. 10):

$$\text{Heating Portion (65 min)} \quad P_{in} = 150 + 69 + 128 = 347 \text{ watts;}$$

$$\text{Cooling Portion (35 min)} \quad P_{in} = 150 \text{ watts.}$$

The desired output to the calorimeter, 128 watts, was obtained by adjustment of the air flow.

Variations in the thermal balance obtained in this matter were due to two effects. The first caused heat loss to be greater during heating and lower during cooling than during steady state, because the heater was at a higher temperature during heating and at a lower temperature during cooling than during steady state operation. The second effect, neglected in the thermal balance (Eq. 2), is the power required to change the temperature of the entire system due to the specific heat of each of the components. Although the effective "thermal mass" of the HP-TES unit can be readily calculated, the corresponding value for other components (heater, insulation, etc.) was difficult to evaluate.* As with the LiF fusion energy, the energy required to change the system temperature must be supplied during the heating portion but is regained during the cooling portion of the cycle. Thus, it is not energy lost from the system.

5.2.3 TEST SYSTEM CYCLIC OPERATION

Figure 57 shows the location and identification of the thermocouples attached to the HP-TES unit. All thermocouples were of the wall-junction type, each thermocouple wire being spot welded directly to the wall. Thermocouples 1 and 2 are attached to the primary heat pipe, near the point where it joins the secondary heat pipe. Thermocouples 11 and 3

*See approach taken in Subsection 5.4.1 by author of this report.

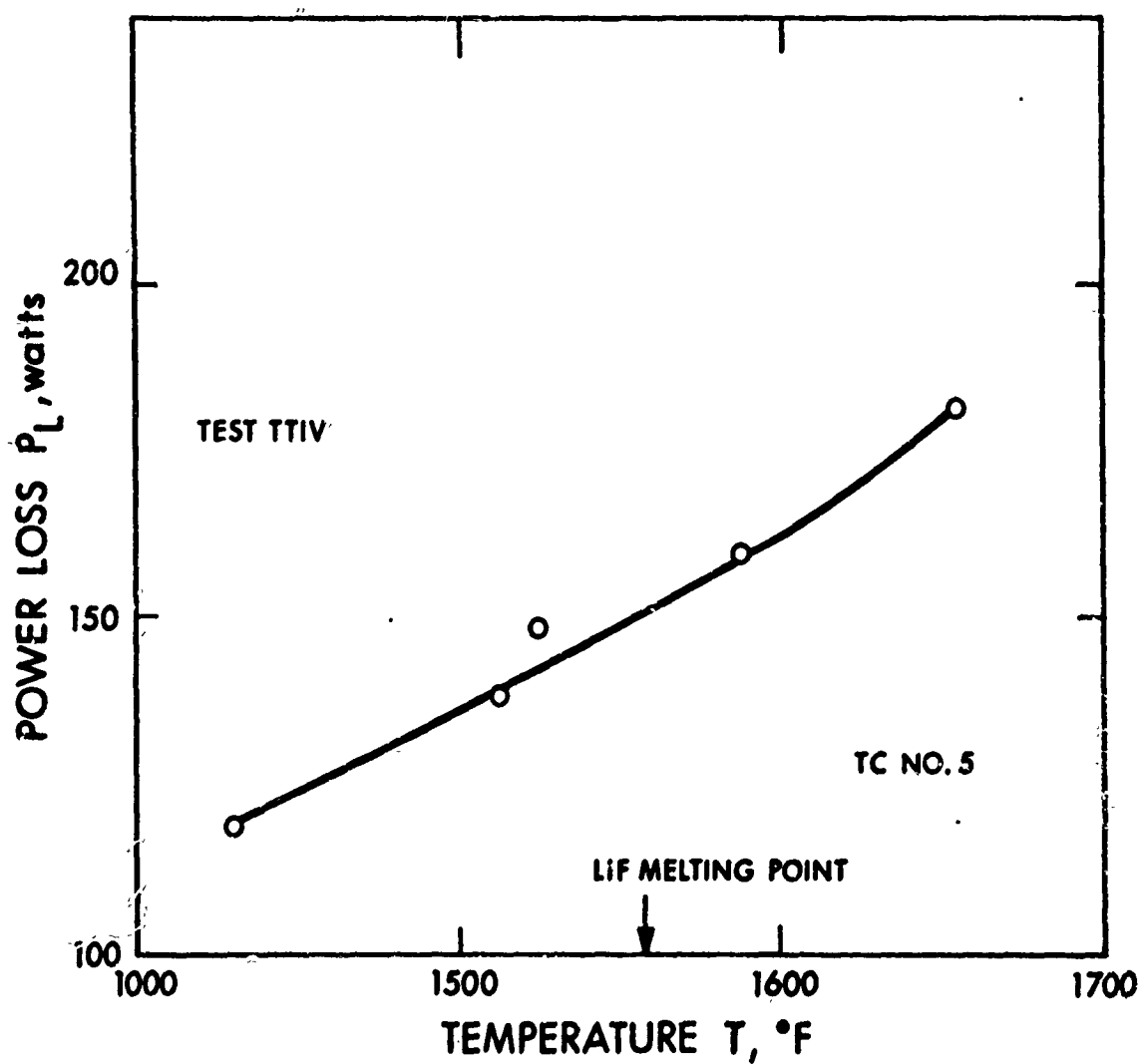


Figure 56. Steady-State (Isothermal) Heat Loss of HP-TES Unit TTI for Temperatures Near the LiF Melting Point

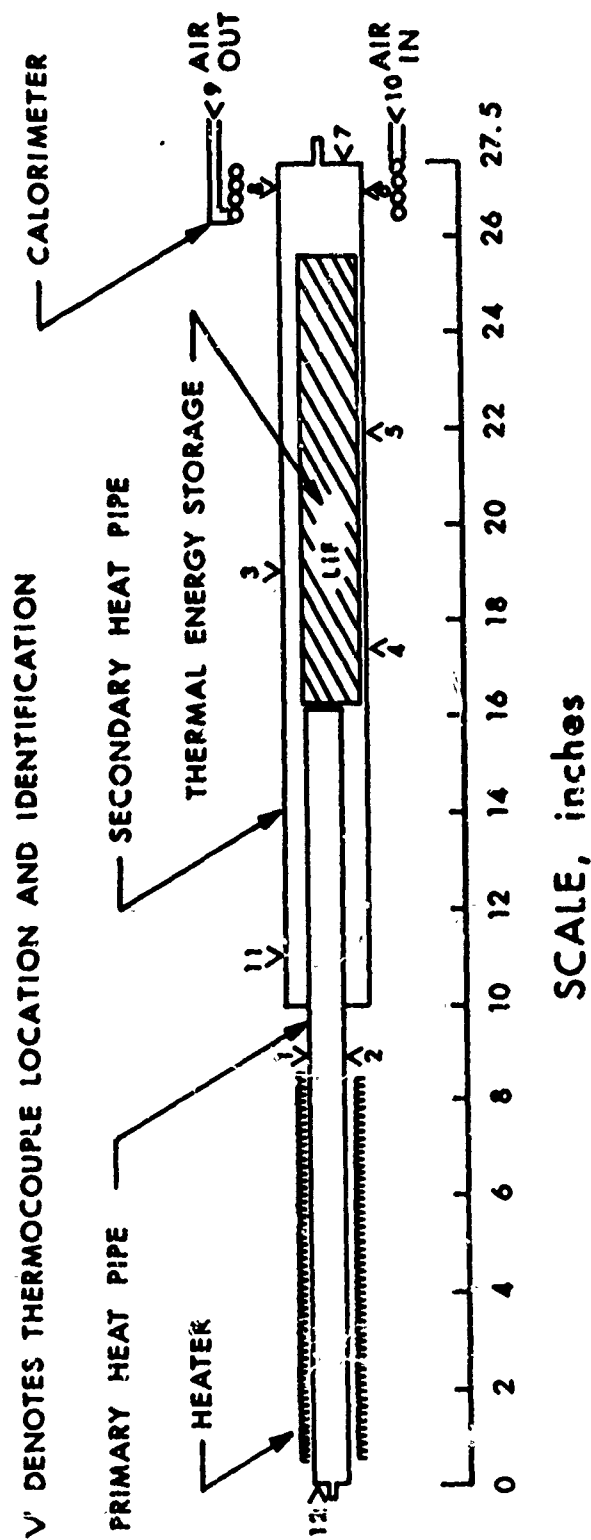


Figure 57. Heat Pipe - Thermal Energy Storage Unit Showing Thermocouple Locations

measured the secondary heat pipe temperatures. Being well insulated from heat losses, these thermocouples should have given the sodium vapor temperature in the secondary heat pipe. Thermocouples 4 and 5 were attached to the secondary heat pipe wall adjacent to the LiF cartridge and should have thus read approximately the cartridge wall temperature. Thermocouples 6, 7, and 8 were located at the heat rejection end of the secondary heat pipe facing the calorimeter. Unfortunately, thermocouples 6 and 8 were lost early in the tests and no readings of these thermocouples are available.

Figure 58 shows the temperature variation of the HP-TES unit measured during the first thermal cycle. Plotted in this curve are temperatures indicated by thermocouple 1, located on the primary heat pipe near the heater No. 5 located under the LiF cartridge, and No. 7 located near the output end of the secondary heat pipe. The extremes of T5 during the 100-minute period of cycle No. 1 were 1528° and 1560°F; the extremes of T7 are 1518° and 1560°F; the extremes of T1 were 1550° and 1590°F. All temperatures along the HP-TES unit may be arranged in 3 groups, with temperatures in each group being roughly equal. The highest temperatures occurred in the primary heat pipe (TC Nos. 1, 2, 11, and 12). TC No. 11, although located on the secondary heat pipe, indicated a temperature close to that of the primary heat pipe due to the very effective thermal conductance of the secondary heat pipe in the radial direction. Thermocouples 3, 4, and 5 reflected the temperature of the secondary heat pipe and LiF cartridge. TC No. 7 measured the output temperature.

The most notable feature of the temperature variation shown in Figure 58 was that during the heating portion of the cycle, T5 was very nearly equal to the LiF melting point (except for the period required to heat up to that value). However, during the cooling portion of the cycle, the temperature at station 5 slowly decreased, reaching a value about 16°F below the LiF melting point (1558°F). This behavior had been noted on previous operation of this unit and was attributed to a ΔT within the LiF. During the heating portion the ΔT was small since the heat flux to the cartridge was lower than on the cooling portion and the heat was conducted through a liquid film which was a higher thermal conductivity than the solid. Perhaps the most important factor, however, was that when a liquid layer formed near the wall during the heating portion, the remaining solid LiF sink in the gravity field (since the solid was denser than the liquid) and maintained good contact with the lower cartridge wall throughout the heating portion. These factors affecting the ΔT within the LiF are discussed in more detail in subsection 5.3.4 of this report.

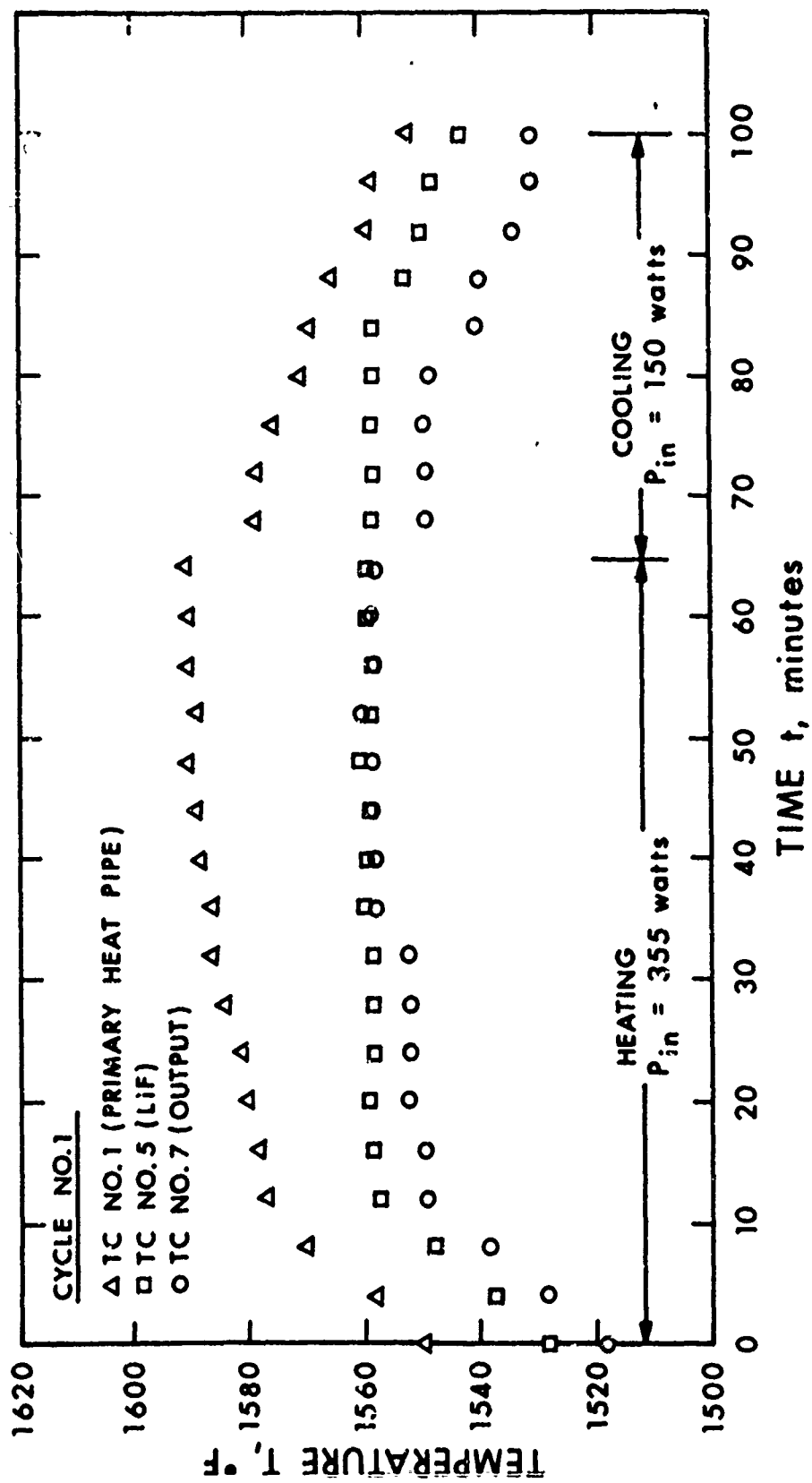


Figure 58. Temperature Variations of HP-TES Unit During Thermal Cycle #1

During cycle No. 1, the air flow through the calorimeter was maintained at a constant value. Due to variation in temperature of the heat pipe, P_{out} varied slightly over the cycle, with a maximum of 126 watts, a minimum of 121 watts, and an average of 125 watts.

Examination of the data of cycle No. 1 raised the question of whether or not the LiF was completely melted at the end of the heating portion of the cycle. It appeared that the only reliable method of determining the state of the LiF was to observe the rapid increase in temperatures which occurs after complete melting. Figure 59 shows the variation of the LiF temperature over three cycles obtained in the "excess power" condition. The rapid increase in T5 was apparent at the end of the heating portion of cycle No. 6 and cycle No. 7. It should be noted that the average power input over the three cycles was 287 watts compared to 283 watts average in cycle No. 1 (Figure 58). The fact that this small change in average power (4 watts) resulted in obvious complete melting of the LiF indicated that the LiF was very nearly completely melted during cycle No. 1. The thermal behavior of the unit was thus very sensitive to the power input when nearly 100 percent of the LiF was melted. This can be better understood if one examines the integrated power over the complete cycle, that is, the total energy input during the cycle. A change of 1.3 percent (4 watts) in average power input over the 100-minute cycle is a change of 2.4×10^4 joules over the cycle which is 9 percent of the fusion energy of the LiF in the cartridge.

The above considerations illustrate the very delicate thermal balance that was necessary to run consecutive thermal cycles on this system with nearly 100 percent melting of the LiF. The correct power input is critical because any deviation from the balanced power condition is cumulative over the total cycling time and not simply for one period. After several attempts, three consecutive thermal cycles were successfully completed with balanced power conditions and nearly 100 percent melting of the LiF. The variation in temperature of the LiF (TC No. 5) is shown in Figure 51 for the three cycles. The balanced power condition was determined from the fact that the same temperature was attained at the end of each cycle. Nearly 100 percent melting of the LiF was inferred from the fact that P_{in} during the heating portion was only 10 watts less than that used for the "excess power" condition (see Figure 50).

Complete data for cycle No. 18 (plotted in Figure 60) given in Table XIX. Thermocouple locations are shown in Figure 57. From these data one can determine the total swing (maximum to minimum) of the temperatures and power output attained during one cycle under nominal conditions. These values are:

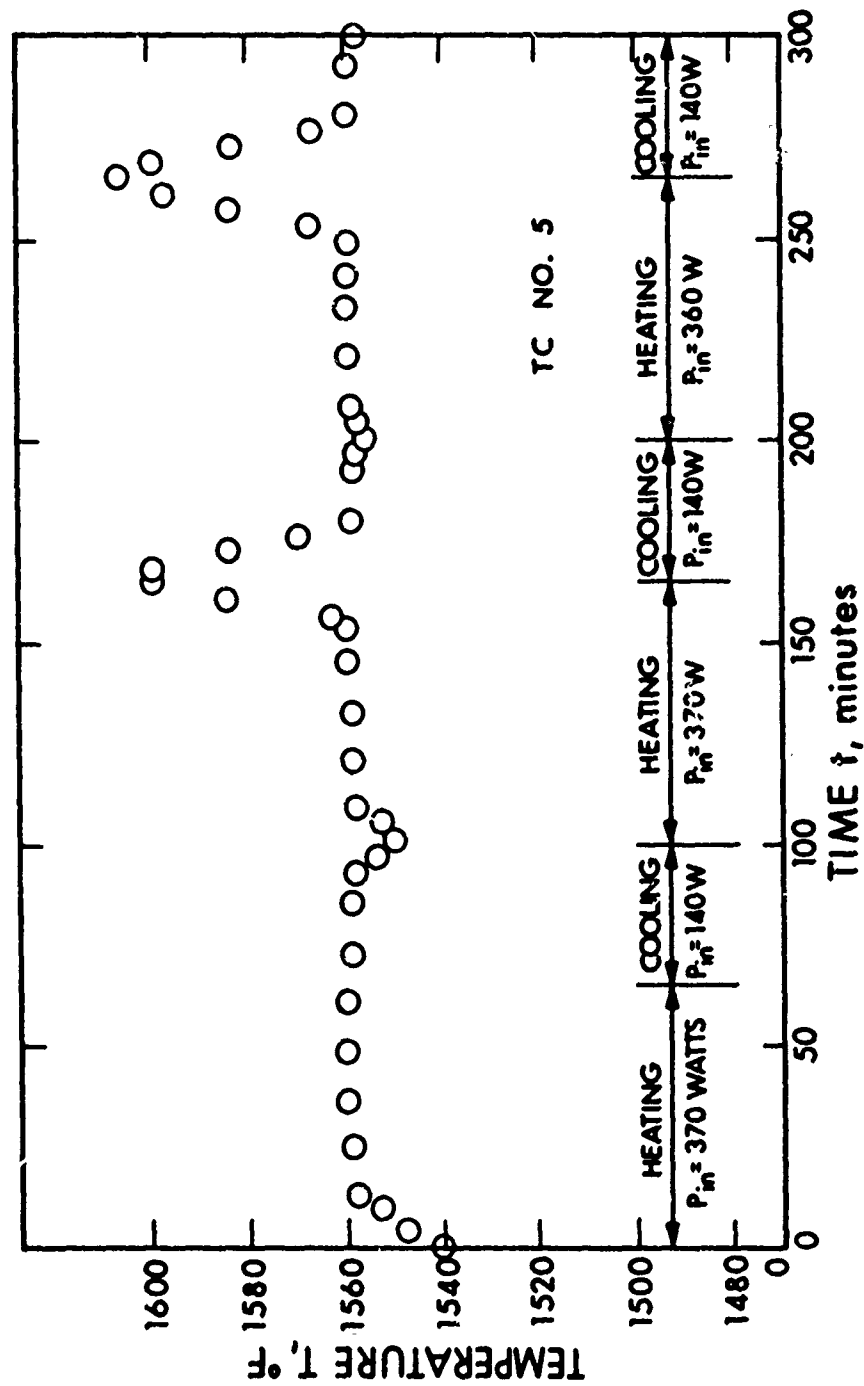


Figure 59. Variation in Temperature (TC #5) During Three Cycles Under Excess Power Conditions for Test Unit TTI

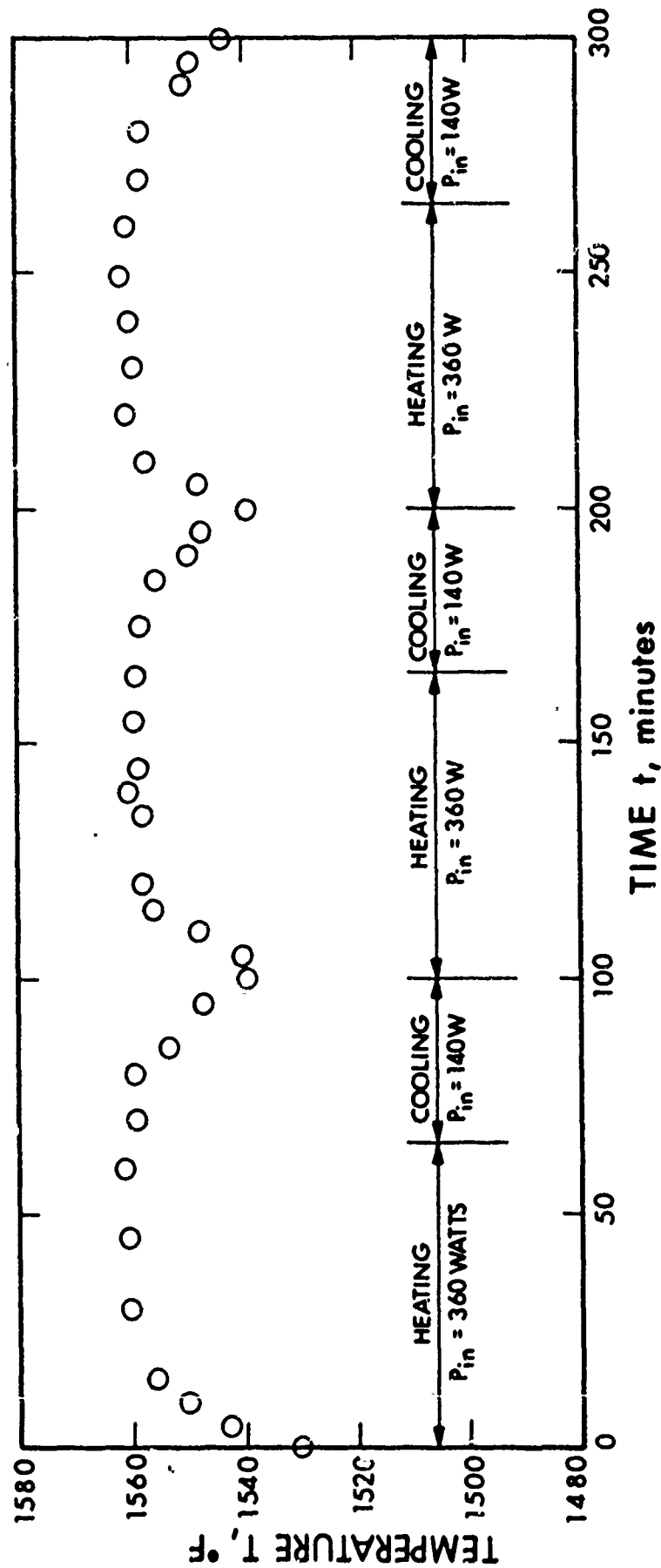


Figure 60. Temperature Variation (TC #5) of HP-TES Unit TTI During Three Cycles Under Nominal Power Input Conditions

TABLE XIX

COMPLETE TEST DATA FOR CYCLE NO. 18 (TEST TTIV) UNDER NOMINAL POWER CONDITIONS

Time (min)	P _{in} (watts)	P _{out} (watts)	Temperature, T, °F									
			1	2	3	4	5	7	9	10	11	12
200	360	120	1551	1558	1538	1538	1539	1513	991	110	1545	1545
205		121	1563	1565	1548	1545	1548	1526	995	110	1556	1556
210		122	1579	1585	1560	1552	1557	1538	1006	110	1567	1570
215		125	1582	1588	1561	1560	1559	1545	1020	110	1571	1576
220		125	1582	1592	1562	1560	1560	1548	1022	111	1577	1578
225		125	1588	1598	1568	1560	1560	1550	1022	110	1577	1578
230		125	1590	1598	1569	1560	1559	1549	1023	110	1577	1578
235		125	1593	1598	1569	1560	1559	1550	1027	111	1577	1582
240		126	1598	1599	1568	1561	1560	1550	1030	111	1578	1582
245		126	1598	1600	1570	1562	1561	1551	1031	111	1581	1588
250		126	1598	1602	1572	1562	1561	1552	1033	111	1582	1588
255		126	1598	1602	1573	1563	1560	1552	1033	111	1582	1588
260		127	1598	1603	1574	1563	1560	1552	1035	111	1582	1588
265		127	1599	1605	1577	1562	1560	1552	1038	111	1588	1591
270		126	1577	1580	1558	1558	1558	1540	1030	111	1570	1570
275		125	1578	1580	1558	1558	1558	1539	1020	111	1567	1568
280		124	1573	1578	1558	1558	1558	1538	1018	110	1567	1567
285		124	1569	1572	1553	1553	1554	1532	1013	110	1560	1560
290		123	1562	1569	1550	1550	1550	1529	1010	110	1558	1559
295		122	1558	1562	1544	1547	1549	1523	1002	110	1551	1551
300		121	1551	1556	1540	1540	1543	1519	998	110	1548	1548

Note: Thermocouple locations are shown in Figure 57.

Primary Heat Pipe (TC No. 1): $T_{\max} - T_{\min} = 47^{\circ}\text{F}$
 LiF (TC No. 5): $T_{\max} - T_{\min} = 22^{\circ}\text{F}$
 Output Temperature (TC No. 7): $T_{\max} - T_{\min} = 39^{\circ}\text{F}$
 P_{out} : $P_{\max} - P_{\min} = 7 \text{ watts (6 percent)}$

After completion of the cyclic operation of the HP-TES unit, radiographs were taken to determine if stresses induced by alternate freezing and thawing of the LiF had caused distortion of the cartridge. No distortion of the cartridge was noted in careful examination of the radiographs. A total of about 120 thermal cycles had been made with this unit. The radiographs revealed rather extensive cracking of the LiF, as had been noted in other radiographs of the solid salt at room temperature. This cracking is believed to be due to the rather large contraction of the LiF from the melting point to room temperature. Though the cracks have no consequences structurally, they inhibit heat transfer within the material and cause temperature gradients.

5.2.4 START-UP TESTS

A total of five start-up tests were performed with the HP-TES unit with various values of power input to a maximum of 360 watts. The power was applied continuously at a fixed value until the unit reached nearly isothermal conditions. In each start-up test, normal heat pipe start-up behavior was noted; that is, the evaporation section increased in temperature rapidly until appreciable vaporization of sodium began (800 to 900°F). Thereafter, adjacent sections were heated successively until the entire unit reached nearly isothermal conditions. Figure 61 shows the temperature variation during start-up with $P_{\text{in}} = 360$ watts. Air flow to the calorimeter was off during this period so that $P_{\text{out}} = 0$. Thermocouple locations are shown in Figure 57. Approximately 80 minutes were required for the unit to reach nearly isothermal conditions with this power input.

5.3. CARTRIDGE GEOMETRY OPTIMIZATION TESTS

Cyclic operation of test unit TT1, described above, demonstrated that the temperature remained quite constant during the melting (energy storage) portion of the cycle but decreases markedly over the solidifying (energy extraction) portion, even though the LiF existed as two phases. Analysis of this effect showed that as heat was extracted from the cartridge, a solid LiF layer formed adjacent to the cartridge wall and increased in thickness as progressively more LiF solidified. The increase in thickness resulted in an increase in the ΔT . Qualitatively then, the ΔT observed

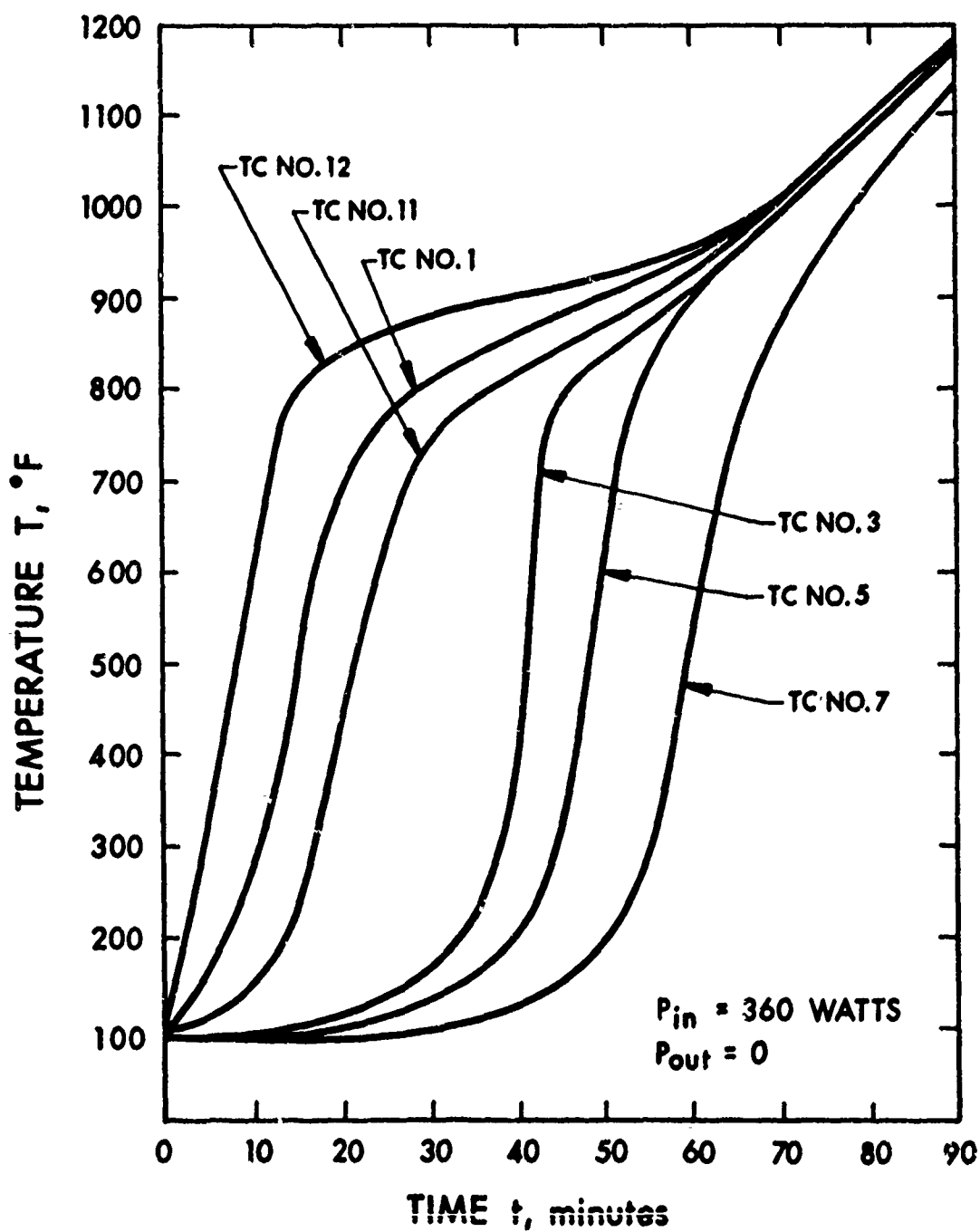


Figure 61. Temperature Variation of Heat Pipe-Thermal Storage Unit During Startup with Power Input of 360 watts and No Power Output

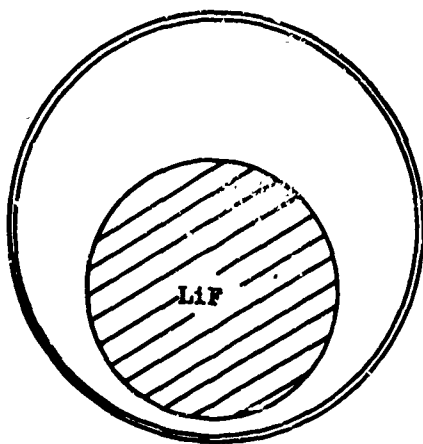
should have been only a function of the cartridge diameter. The ΔT would also have been a function of the heat flux from the cartridge but this too was fixed by the cartridge diameter, since the cartridge volume determined the mass of LiF contained within, which in turn determined the nominal thermal power rating (see Eq. 7). Optimization of cartridge geometry thus involves basically an investigation of the effect of differences in cartridge diameter on the thermal behavior during temperature cycling. For the experimental verification of the effect of the cartridge two HP-TES units were constructed and tested. The units were identical except for the diameter of the LiF cartridges.

5.3.1 TEST SYSTEM - TESTS TT2V and TT3V

The heat pipes which had an outside diameter of 2.25 inches and were 20 inches long, were constructed of type 321 stainless steel. Heat pipe TT2 contained a single Cb-1Zr cartridge, 1.40 inches i.d. and 10 inches long, enclosing 402 grams of LiF for a total fusion energy of 4.20×10^5 joules and a nominal power rating of 200 watts (calculated from Eq. 7). Heat pipe TT3 contained three LiF cartridges, 0.81 inch i.d. and 10 inches long. Each cartridge contained 134 grams of LiF so that the total quantity in the three cartridges was the same as that in TT2 (402 grams). Thus the essential difference between the two units was the cartridge surface areas, i.e., TT3 unit had a surface area 1.73 times that of TT2. Figure 62 shows the two HP-TES configurations.

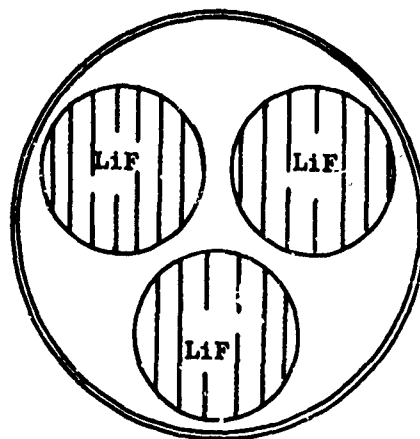
The wicking used in both units was similar to that employed in TT1. Five layers of 100-mesh type 304 stainless steel screen formed the main reflux wick which lined the interior wall of the heat pipe, while each cartridge was wrapped with three layers of 100-mesh screen. Figure 63 shows the interior of the TT3 test unit. Several layers of wick material were forced between the cartridges at their contact points pressing the cartridges against the outer wick. Short pieces of wick material were then spot welded to the ends of the cartridges and to the wall wick to hold the cartridges in position.

The test setup and test conditions for operation of both test units was similar to that employed in testing TT1V. The same vacuum system, power controls, and instrumentation were utilized. Figure 64 shows the test setup and thermocouple location for test TT2V. The semi-cylindrical wire-wound heaters (Lindberg Type 3708-SP) provided radiant heat input to an 8-inch length of the heat pipe. Thermocouples 1 and 2 indicated the temperatures near the heat input surface. Thermocouples 3 and 4 should have indicated the approximate sodium vapor temperature. Thermocouples 5 and 6 were attached to the heat pipe wall, adjacent to the thermal storage cartridge, and thermocouples 7, 8, and 9 indicated the temperatures at the heat rejection end of the heat pipe. Thermocouples 10 and 11 gave the air inlet and outlet temperatures to the calorimeter. The test setup for Test TT3V (with three thermal storage cartridges) was essentially identical.



TT2

One 1.40-inch i.d. Cartridge
in 2.25-inch o.d. Heat Pipe



TT3

Three 0.81-inch i.d. Cartridges
in 2.25-inch o.d. Heat Pipe

Cartridge Length	- 10 inches
Heat Pipe Length	- 20 inches
Weight of Thermal Energy Storage Material (LiF)	- 402 grams
Nominal Power Rating	- 200 watts (35 min)

Figure 62. Heat Pipe/Thermal Energy Storage Configurations
Investigated in Cartridge Geometry Optimization Tests

006407

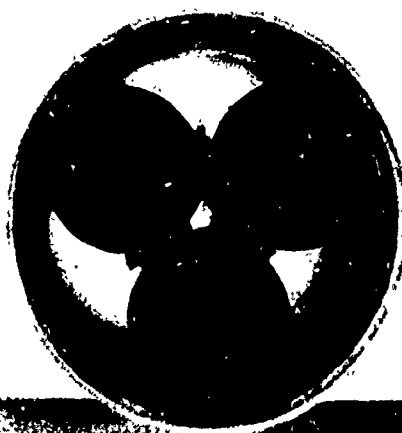


Figure 63. Interior of TT3 Test Unit Showing Three LiF Thermal Storage Cartridges

V DENOTES THERMOCOUPLE LOCATION AND IDENTIFICATION

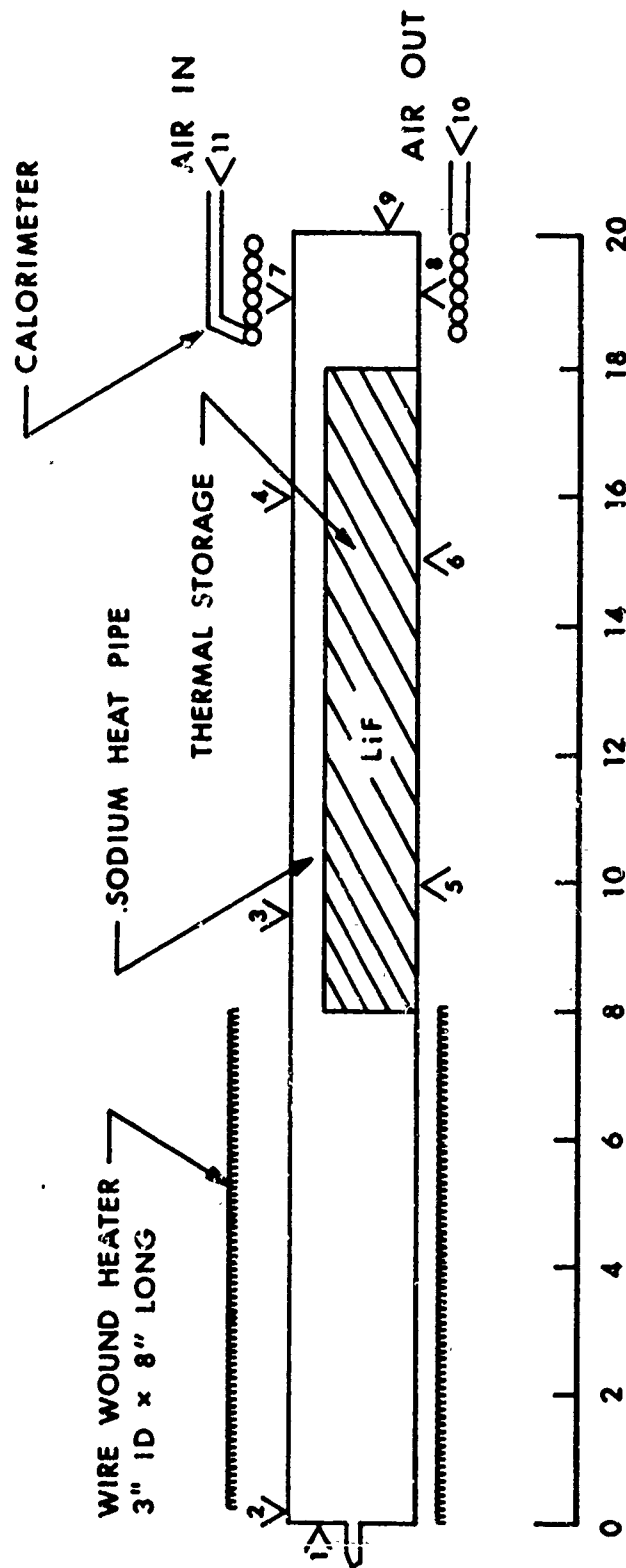


Figure 64. Heat Pipe/Thermal Energy Storage Test Setup for Test TT2V
Showing Thermocouple Locations. Setup for Test TT3V is Similar.

5.3.2 THERMAL CYCLE TESTS

Single Cartridge Unit (Test TT2V)

As in previous tests, the power lost from the system was determined from steady state (isothermal) operation of the unit at temperatures near the LiF melting point. Under these conditions, the heat loss was simply the difference between the power input and power output as described previously (see Eq. 9). A plot of the heat loss values so obtained is shown in Figure 65. From this plot the power lost at 1558°F was 175 watts. Subsequent measurements, however, showed that the power lost was higher during heating and less during cooling than this value. This indicated that considerable heat is lost directly from the heater. This was not surprising since the heater had a large external area (99 square inches) and operated at a higher temperature. To account for this effect, the heat loss was estimated to be 190 watts on heating and 150 watts on cooling. These estimates were substantiated by the observed duration of the thermal arrest on heating and cooling which was in good agreement with the value calculated from the heat of fusion of LiF (1044 joules per gram).

The nominal power conditions for this test unit were determined as follows:

$$\text{Charging: } P_{in} = P_{lost} + P_{TES} + P_{out} = 190 + 107 + 200 = 497 \text{ watts}$$

$$\text{Discharging: } P_{in} = P_{lost} = 150 \text{ watts}$$

$$- P_{TES} = P_{out} = 200 \text{ watts}$$

Temperature variations over two cycles under nominal power conditions are shown in Figure 66 where temperatures for TC No. 5 (located adjacent to the cartridge) and TC No. 7 (located under the calorimeter) are plotted. The maximum swing in TC No. 5 was noted during cycle No. 3 and was 45°F. The slight increase in T5 near the end of the heating portion of each cycle indicated nearly complete melting of the LiF. The temperature indicated by TC No. 7 was typically 2 to 8°F lower than that indicated by TC No. 5. This magnitude of temperature difference was typical of both the TT2 and TT3 test series and was attributed to conduction ΔT through the wick and wall in the heat output region of the heat pipe. This will be discussed in a later section of this report.

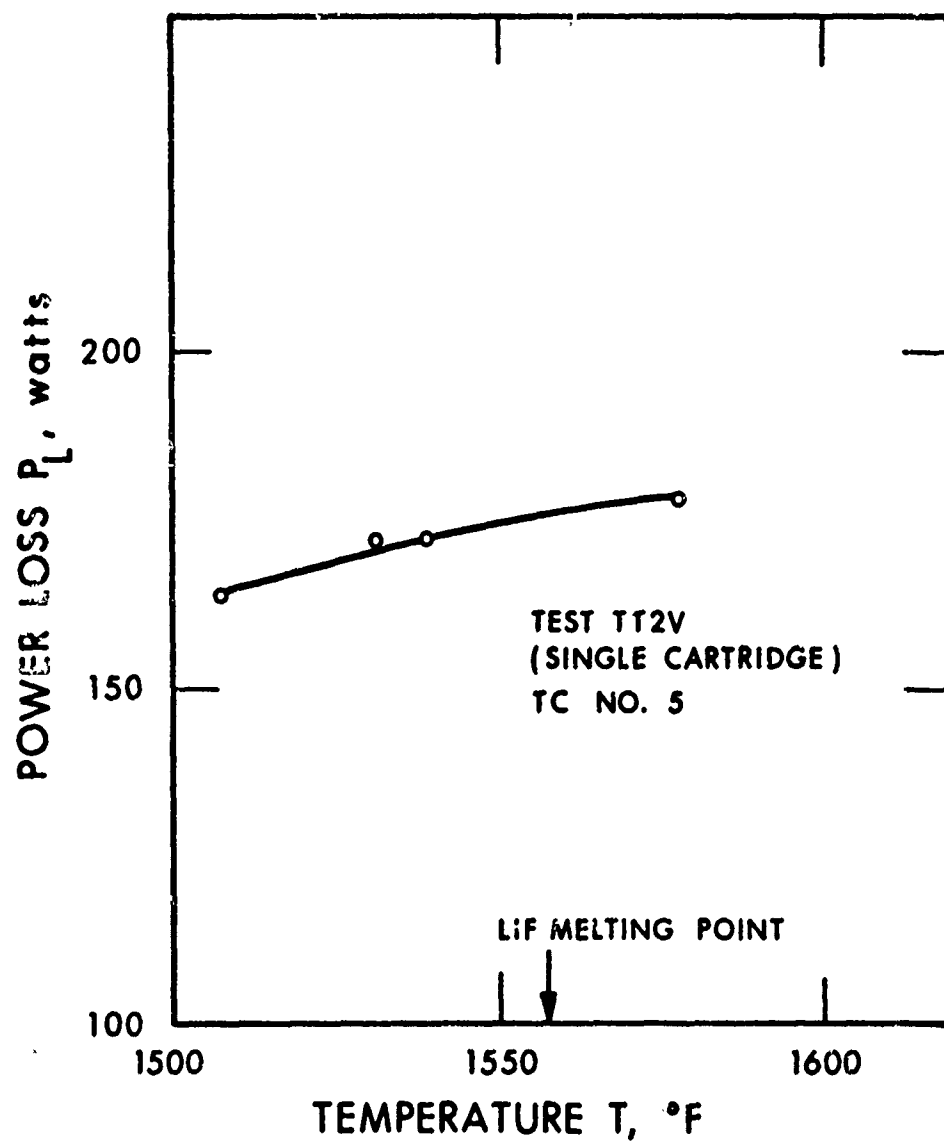


Figure 65. Steady-State (Isothermal) Heat Loss for HP-TES Test TT2V for Temperatures Near the LiF Melting Point.

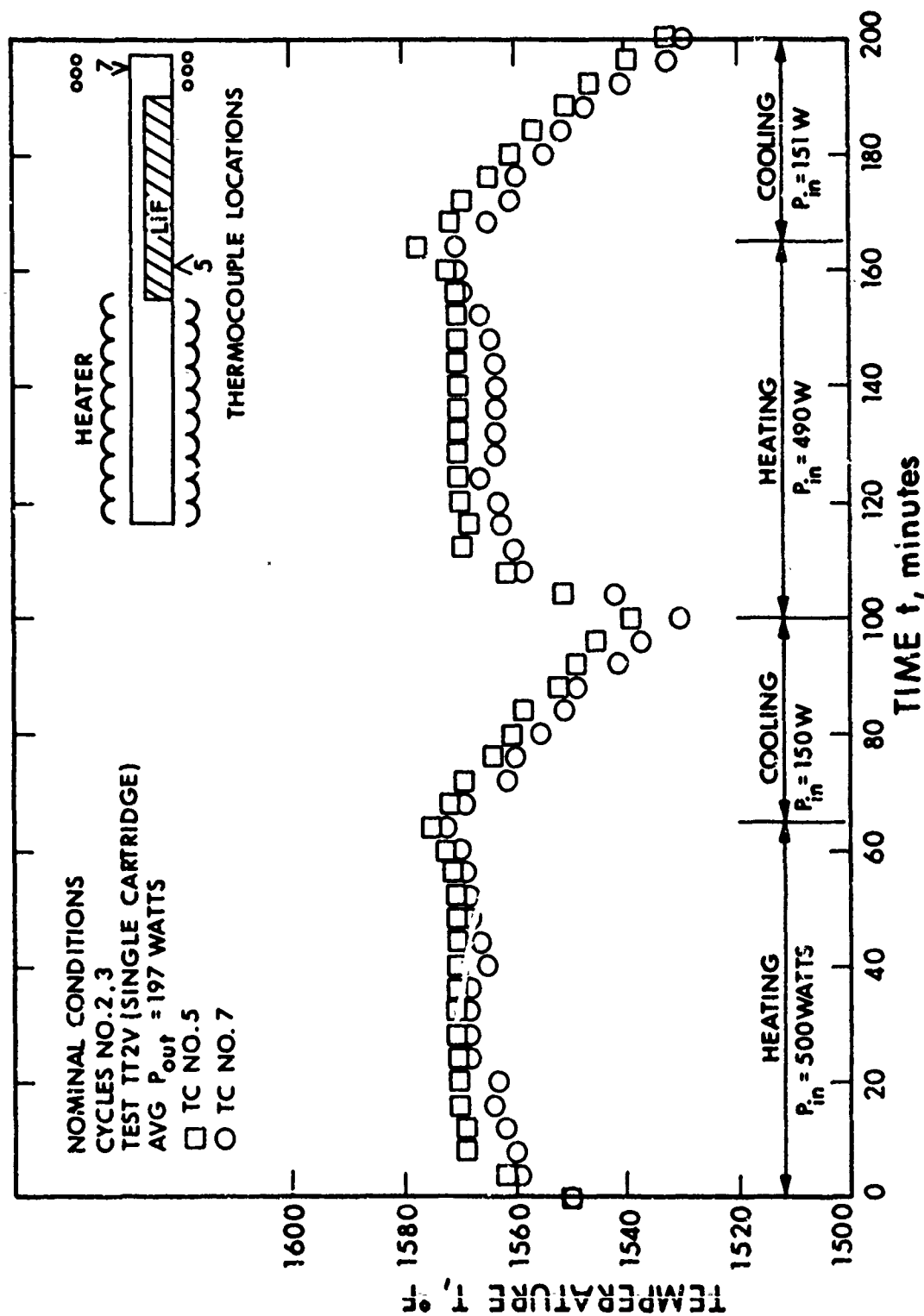


Figure 66. Temperature Variation During Two Cycles Under Nominal Power Conditions for Test TT2V (Single LiF Cartridge)

The constant temperature at thermal arrest during the heating portion of both cycles was about 10°F higher than the melting point of LiF (1558°F). This discrepancy was attributed to thermocouple error. The temperature differences should be reliable in spite of this small error in absolute value.

In addition to measurements made under nominal power conditions, several cycles were run on the TT2 unit under "excess salt" conditions. These tests simulated conditions under which the total energy stored in the LiF during energy storage and the energy extracted during energy release is less than the energy that can be stored in fusion energy in the LiF. Where tests both liquid and solid phases were present during all phases of each cycle. Under these conditions rapid temperature changes will not occur. An additional benefit was that since all heat fluxes were less than under nominal power conditions, the temperature differences were correspondingly reduced.

In order to simulate the 10 percent "excess salt" condition, P_{TES} and P_{out} were reduced by 10 percent. The resulting conditions for the 10 percent excess salt cycles were thus:

$$\text{Charging: } P_{in} = P_{lost} + P_{TES} + P_{out} = 190 + 96 + 180 = 466 \text{ watts}$$

$$\text{Discharging: } P_{in} = P_{lost} = 150 \text{ watts}$$

$$- P_{TES} = P_{out} = 180 \text{ watts}$$

Temperature variations of TC No. 5 over two cycles under 10 percent excess salt conditions are shown in Figure 67. The maximum variation in TC No. 5 was 40°F

Two cycles were also run under 20 percent excess salt conditions. Calculated power values for this condition were:

$$\text{Heating: } P_{in} = P_{lost} + P_{TES} + P_{out} = 190 + 86 + 160 = 436 \text{ watts}$$

$$\text{Cooling: } P_{in} = P_{lost} = 150 \text{ watts}$$

$$- P_{TES} = P_{out} = 160 \text{ watts}$$

Temperature variations of TC No. 5 over two cycles under 20 percent excess salt conditions are shown in Figure 68. The maximum variation in TC No. 5 was 28°F.

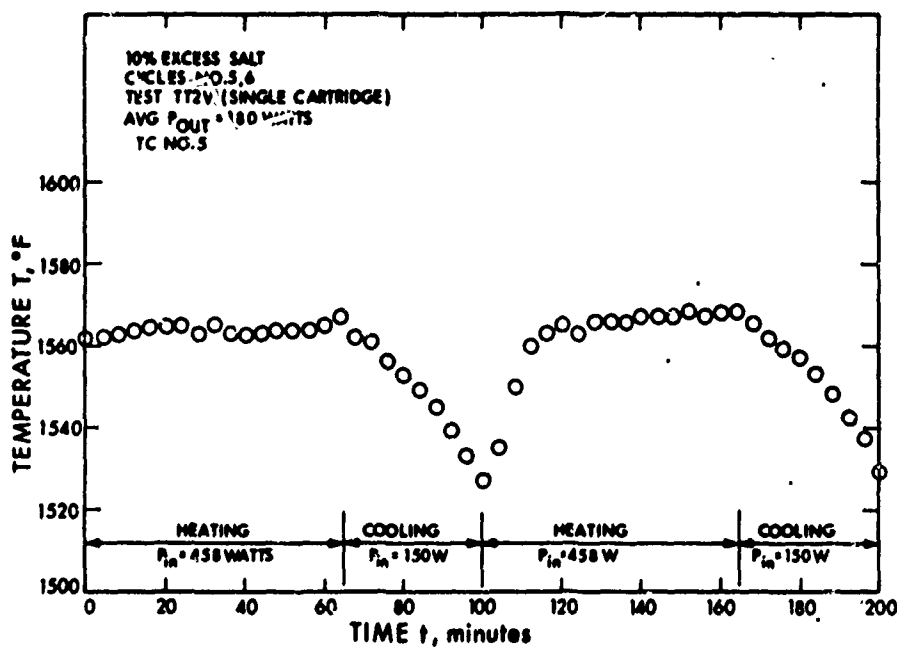


Figure 67. Temperature Variation of TC #5 During Two Cycles Under 10% Excess Salt Conditions for Test TT2V (Single Cartridge)

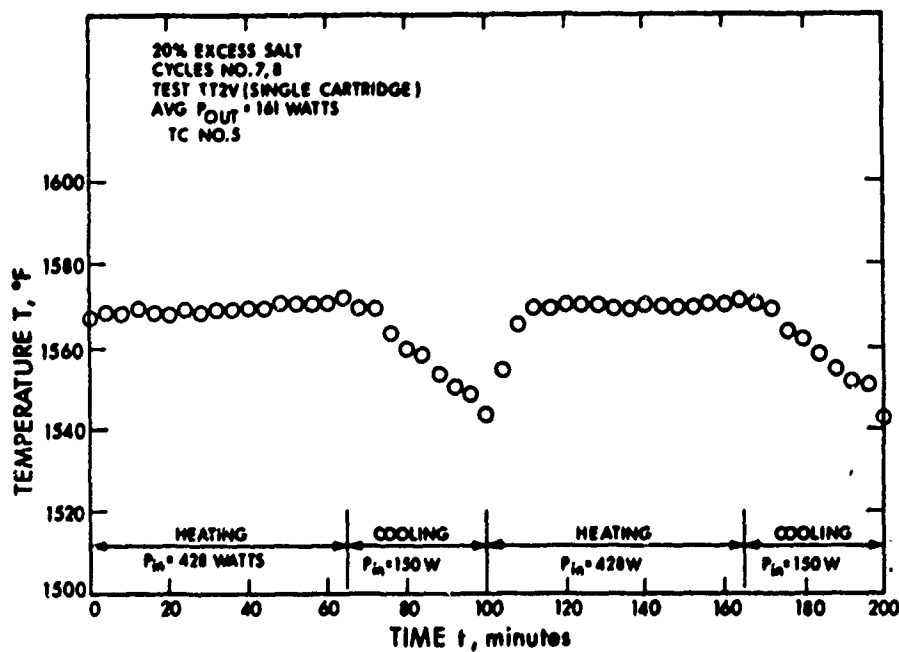


Figure 68. Temperature Variation of TC #5 During Two Cycles Under 20% Excess Salt Conditions for Test TT2V (Single Cartridge)

Triple Cartridge Unit (Test TT3V)

A plot of the heat loss measurements obtained under steady state (isothermal) conditions with 200 watts output for the triple cartridge unit (TT3) is shown in Figure 69. From this plot, the power lost at 1558°F was 165 watts. This was about 10 watts less than for TT2V (see Figure 65). This difference could be attributed to the lower pressure in the vacuum system maintained during the TT3 tests. Higher pressures in the TT2 test were caused by a small leakage in the calorimeter coil which was located and repaired following the TT2 test.

Power loss estimated for the TT3 test were made on the same basis as the previous test; that is, 15 watts greater on heating and 25 watts less on cooling than that measured during steady state conditions. The resulting estimates of power loss were 180 watts on heating and 140 watts on cooling.

The nominal power conditions for the TT3 test unit were thus:

$$\text{Heating: } P_{in} = P_{lost} + P_{TES} + P_{out} = 180 + 107 + 200 = 487 \text{ watts}$$

$$\text{Cooling: } P_{in} = P_{lost} = 140 \text{ watts}$$

$$- P_{TES} = P_{out} = 200 \text{ watts}$$

Temperature variations over two cycles under nominal power conditions are shown in Figure 70. Temperatures indicated by TC No. 5 (located adjacent to the lower cartridge) and for TC No. 7 (located under the calorimeter) are plotted. The effects of cartridge diameter was apparent in this plot. The total swing in TC No. 5 was only 20°F compared to 45°F observed on the single cartridge unit under similar heat flux conditions. The difference between TC No. 5 and TC No. 7 varied from 4 to 9°F over the two cycles. This difference was essentially the same as that observed in tests of the TT2 unit, as would be expected, since the heat fluxes were the same.

Power conditions for the 10 percent excess salt cycles were determined, as with the TT2V tests, by reducing the power output and stored power by 10 percent. Thus, the power conditions for the 10 percent salt cycles for TT3V were:

$$\text{Heating: } P_{in} = P_{lost} + P_{TES} + P_{out} = 180 + 96 + 180 = 456 \text{ watts}$$

$$\text{Cooling: } P_{in} = P_{lost} = 140 \text{ watts}$$

$$- P_{TES} = P_{out} = 180 \text{ watts}$$

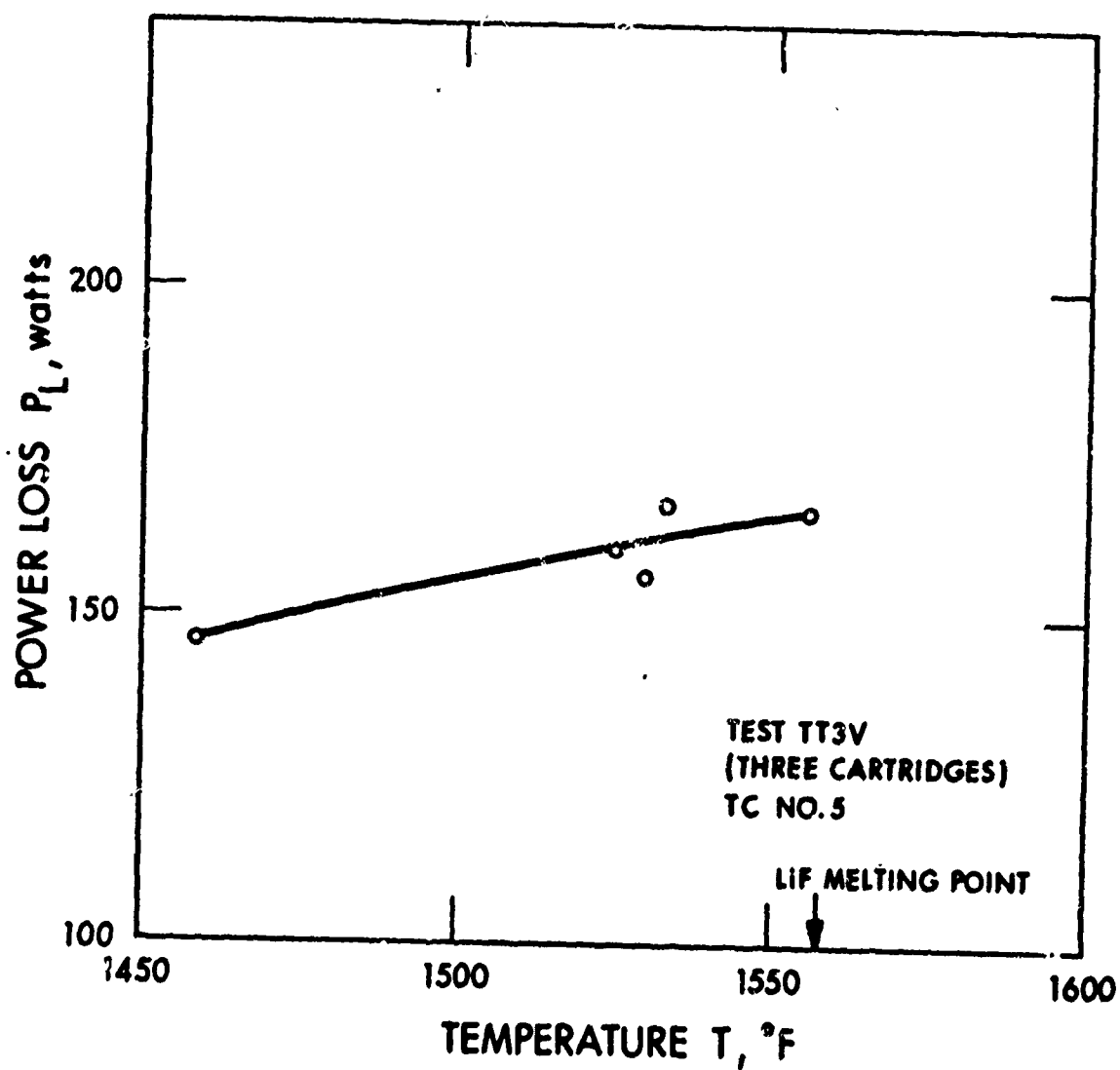


Figure 69. Steady-State (Isothermal) Heat Loss for HP-TES Test TT3V (Three Cartridges) for Temperatures Near the LiF Melting Point.

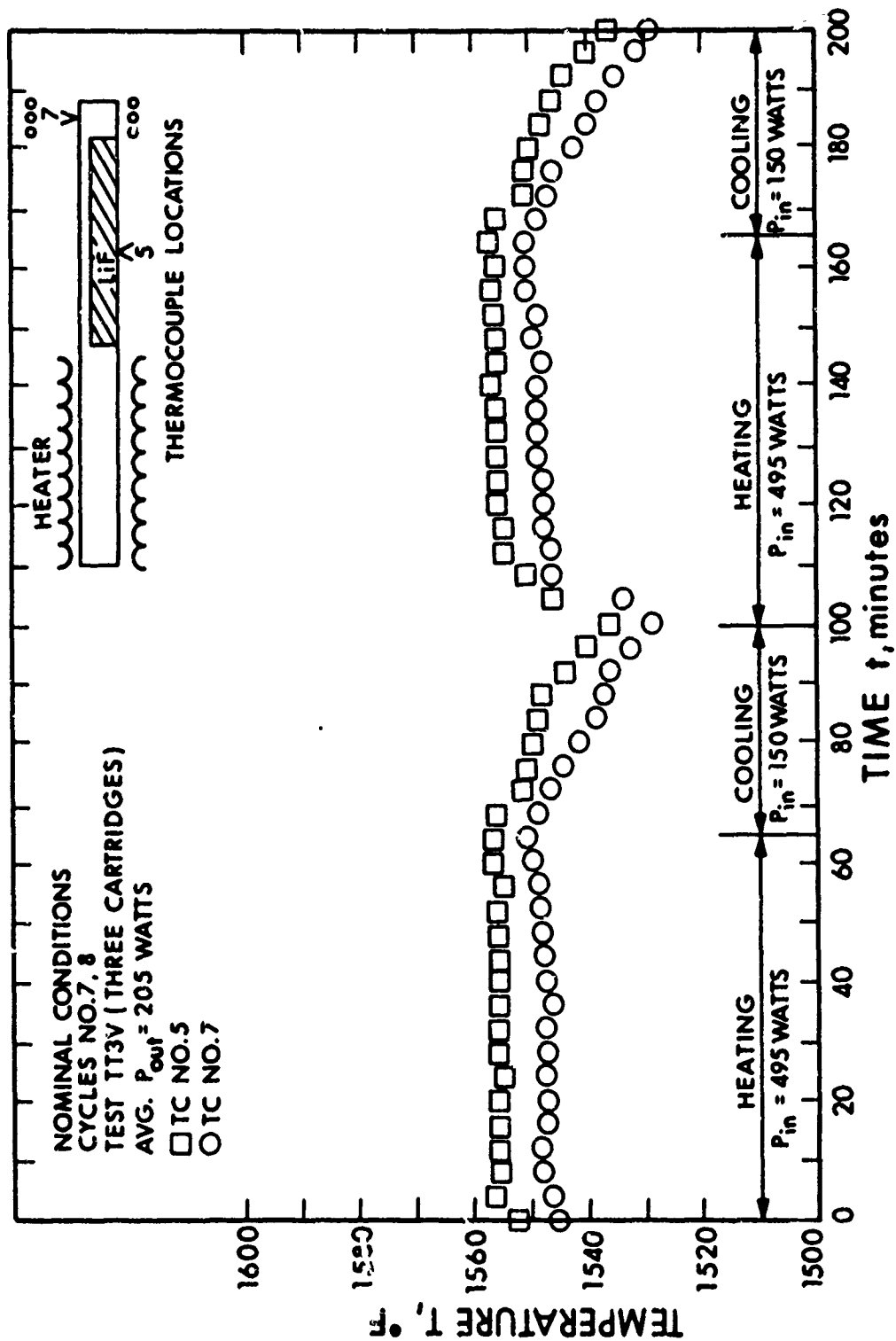


Figure 70. Temperature Variation During Two Cycles Under Nominal Power Conditions for Test TT3V (Three LiF Cartridges)

Temperature variations of TC No. 5 during two cycles under these power conditions are shown in Figure 71. The maximum variation in TC No. 5 was 16°F.

Power conditions for the 20 percent excess salt cycles for test TT3V were:

$$\text{Charging: } P_{in} = P_{lost} + P_{TES} + P_{out} = 180 + 86 + 160 = 426 \text{ watts}$$

$$\text{Discharging: } P_{in} = P_{lost} = 140 \text{ watts}$$

$$- P_{TES} = P_{out} = 160 \text{ watts}$$

Temperature variations of TC No. 5 during two cycles under 20 percent excess salt conditions are shown in Figure 72. The maximum variation in TC No. 5 was 12°F.

Table XX presents the maximum temperature variations of TC No. 5 during operation of test units TT2 and TT3. It is apparent that for a given quantity of thermal energy storage material, the smaller cartridge diameter significantly reduces the temperature variation. The temperature variation for the three-cartridge geometry (0.81-inch i.d. cartridges) was only 42 percent of the variation for the single cartridge configuration under all power conditions. The presence of excess thermal energy storage material also had significant effect in reducing the cyclic temperature variation for both cartridge diameters.

43440

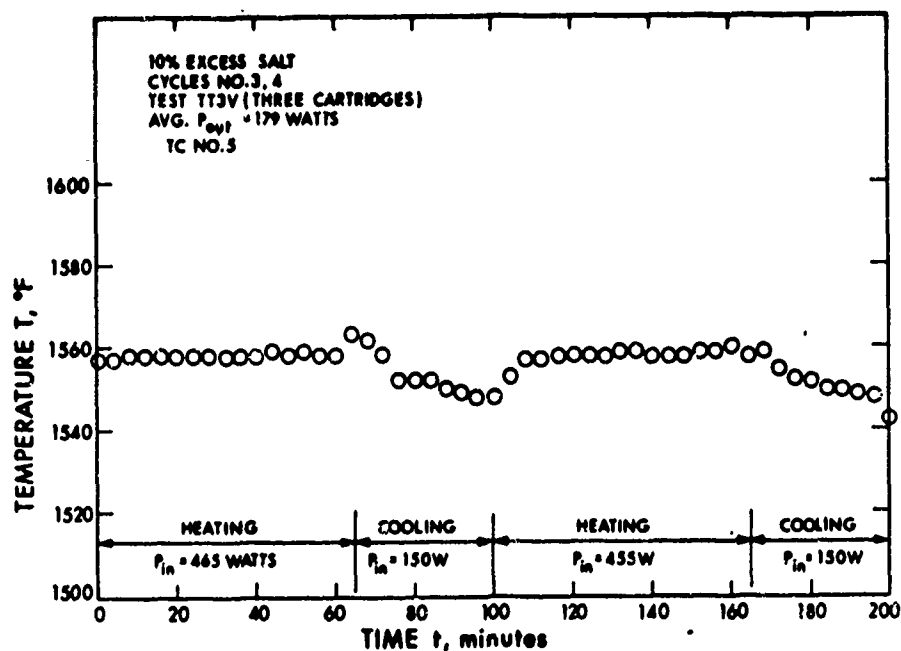


Figure 71. Temperature Variation During Two Cycles Under 10% Excess Salt Conditions for Test TT3V (Three LiF Cartridges)

43459

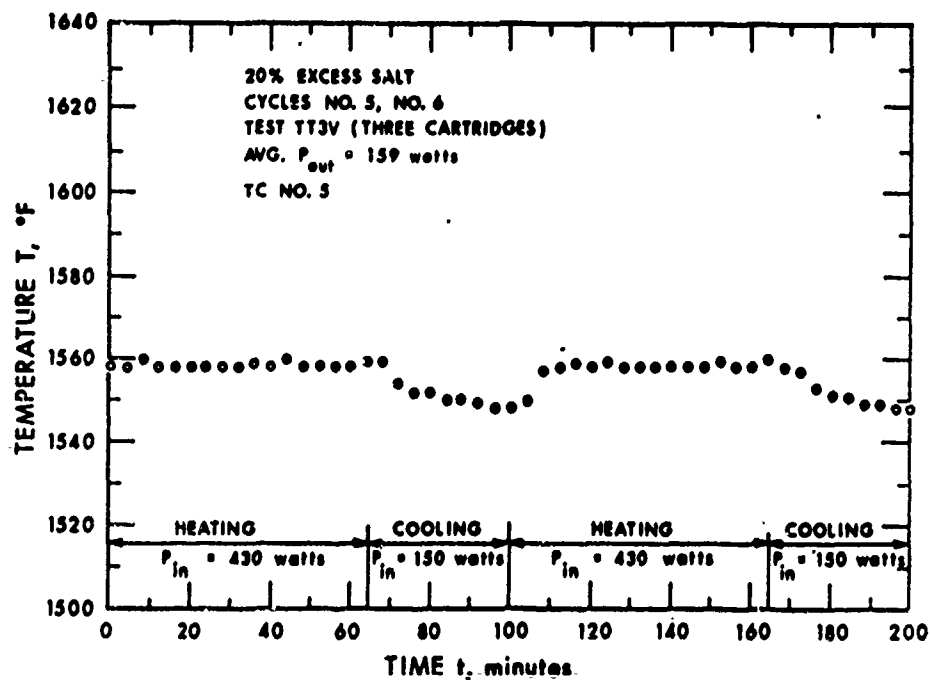


Figure 72. Temperature Variation During Two Cycles Under 20% Excess Salt Conditions for Test TT3V (Three LiF Cartridges)

TABLE XX

COMPARISON OF MAXIMUM TEMPERATURE VARIATION OF T5
DURING CYCLIC OPERATION FOR TEST SERIES TT2V and TT3V

<u>Condition</u>	<u>Power Output (W)</u>	<u>Maximum Variation in T5, °F</u>	
		<u>One Cartridge (TT2V)</u>	<u>Three Cartridges (TT3V)</u>
Nominal	200	45	20
10% excess salt	180	40	16
20% excess salt	160	28	12

5.3.3 FIRST ENDURANCE TEST

Test System

The experimental setup for automatically cycling TT2V and TT3V for 1000 hours is shown in Figures 73 and 74. The thermocouple locations are indicated along with the necessary heater circuitry to ensure complete melting of the LiF during the heating portion of the cycle and complete freezing of the LiF during the remaining portion of the cycle.

Test Results

The endurance testing of the two HP-TES units was completed without interruption except for a blown fuse in the control circuit for TT2 at the end of 344 cycles. This caused a lag of 32 cycles for TT2 which extended the test for this unit two days.

The test setup was monitored at least once a day and a chart recording was made for all thermocouples for the duration of the test. Data for the two HP-TES units during six complete cycles at various stages of the test are shown in Table XXI. These data are representative of the performance of the test units during the 1000 cycles.

5.3.4 ANALYSIS OF THERMAL BEHAVIOR DURING LiF FREEZING

The principal reason for the temperature variation during cyclic operation of the HP-TES units in 1-g has been shown, at least qualitatively, to be the temperature difference which occurs across the solid LiF on freezing. In order to quantitatively evaluate this temperature difference, it was first necessary to calculate the freezing pattern, which is

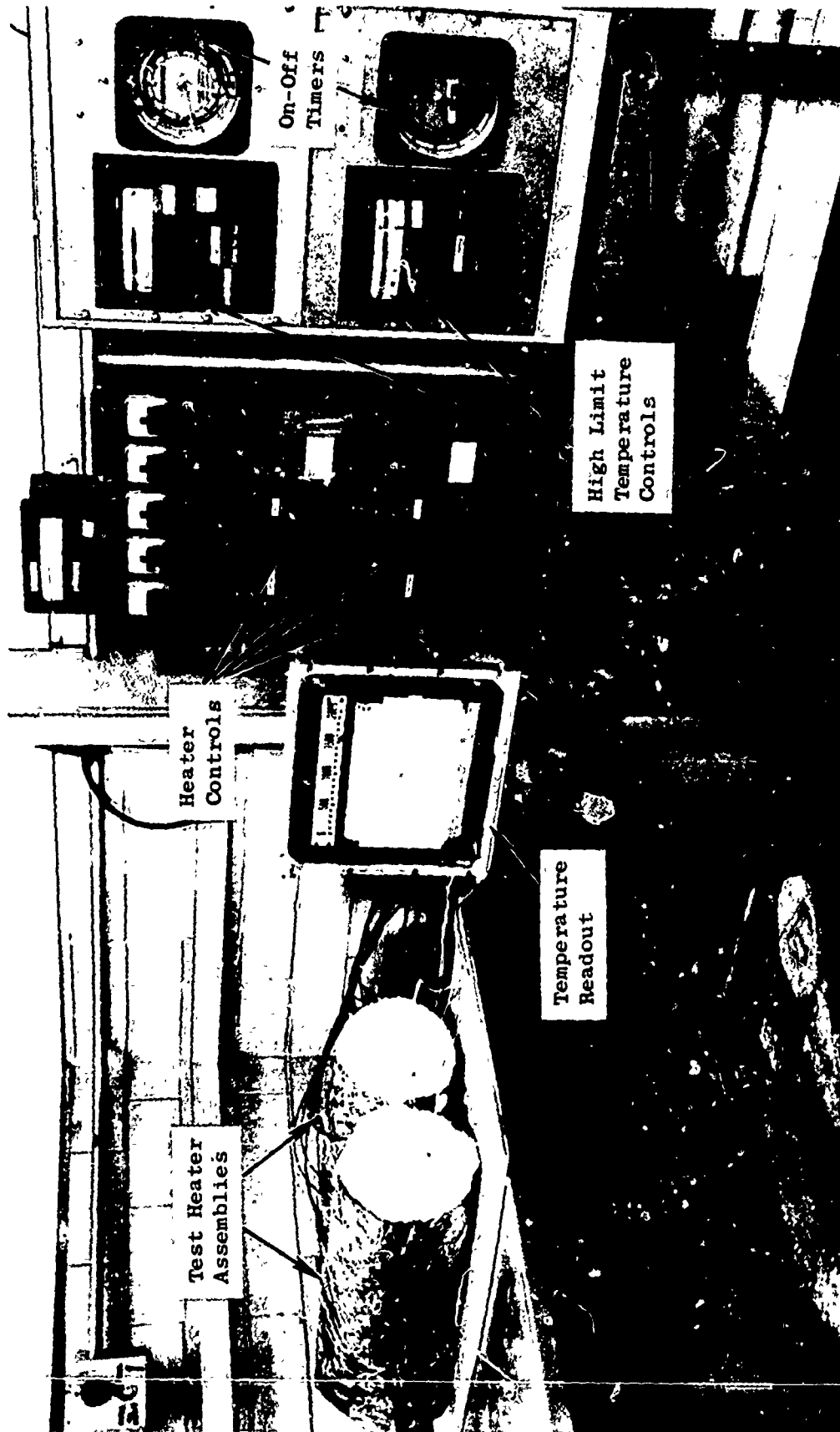
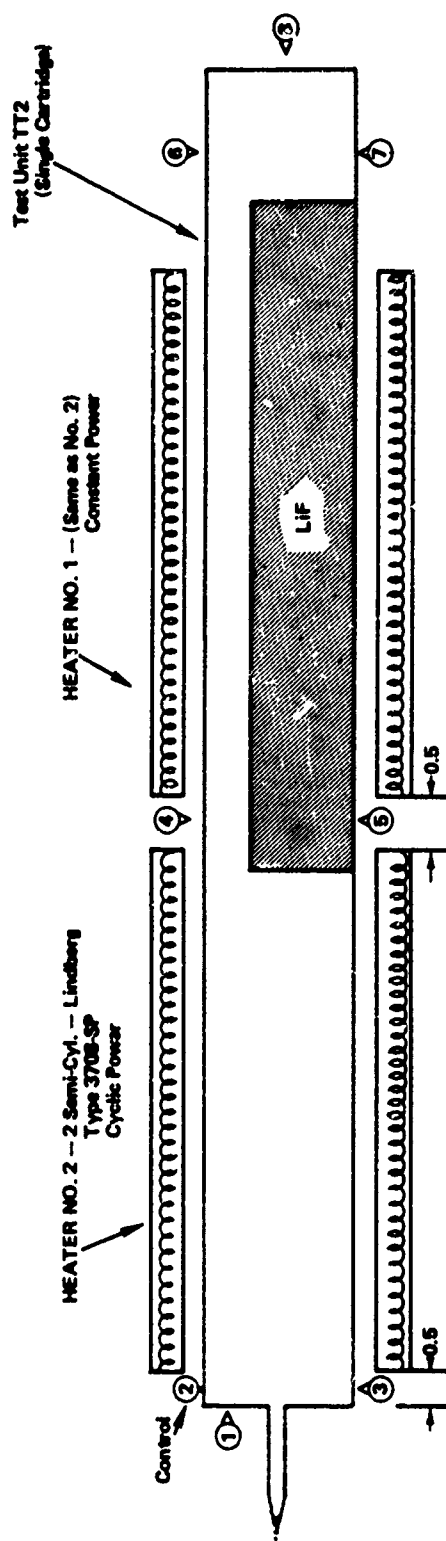


Figure 73. Endurance Test Setup

695900



NOTES:

1. Mark and locate TC's as indicated (CA Type K 20 GA.) Connect to Multipoint Recorder (Bristol Model 84A)
2. Insulate with 3 in. (Min) Fiberfrax Entire Unit.
3. Heater Resistance $\sim 10 \Omega$. Do not exceed 7.5 Amp (~ 580 watts) on each Heater.
4. Set-up for TT3 Test Unit is identical.
5. Timer-Eagle Signal Corp. Type H698A6.
6. Control-Honeywell "Pyr-O-Vane" Model: ID524-PSC

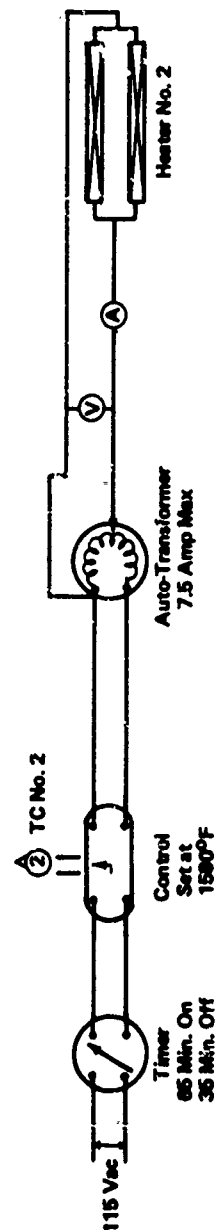
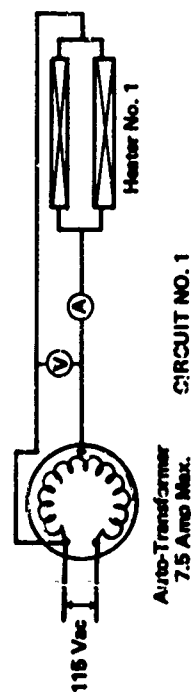


Figure 74. Schematic of Endurance Test Setup

TABLE XXI

TEST DATA FROM 1000-HOUR CYCLING TEST

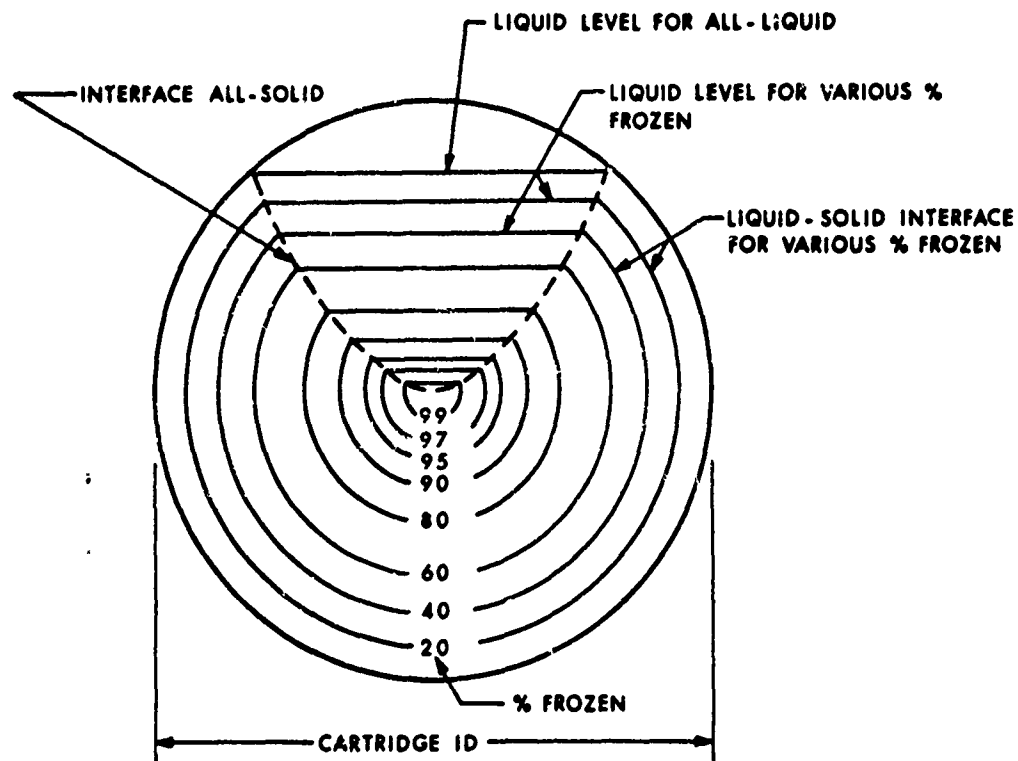
Cycle Number	HP/TES TT2										HP/TES TT3															
	Control					T/C °F					Control					T/C °F										
	Heater #1 amps	Heater #1 volts	Heater #2 amps	Heater #2 volts	Setting P	1	2	3	4	5	6	7	8	Heater #3 amps	Heater #3 volts	Heater #4 amps	Heater #4 volts	Setting P	11	12	13	14	15	16	17	18
100.00	3.3	35.9	Off	Off	1600	1520	1518	1522	1523	1523	1512	1512	1512	3.3	35.8	Off	Off	1560	1542	1542	1542	1542	1542	1533	1542	1542
100.65	3.3	35.8	6.4	64.8	1600	1572	1576	1581	1578	1573	1572	1572	1576	3.3	35.9	6.4	66.5	1560	1583	1587	1586	1586	1582	1585	1582	1582
214.00	3.3	36.0	Off	Off	1600	1522	1523	1525	1532	1523	1523	1523	1529	3.3	35.3	Off	Off	1560	1542	1543	1538	1538	1532	1535	1535	1535
214.65	3.3	35.7	6.3	64.2	1600	1579	1581	1582	1583	1578	1578	1578	1578	3.3	35.2	6.2	65.3	1560	1572	1576	1572	1572	1562	1572	1572	1572
315.00	3.3	36.1	Off	Off	1600	1510	1512	1511	1517	1510	1510	1511	1511	3.4	36.1	Off	Off	1560	1543	1541	1540	1540	1525	1538	1540	1540
315.65	3.3	35.9	6.3	64.5	1600	1572	1578	1578	1572	1573	1572	1572	1575	3.4	36.2	6.3	66.0	1560	1578	1580	1580	1578	1561	1571	1577	1577
503.00	3.4	36.3	Off	Off	1600	1519	1520	1525	1532	1525	1526	1529	1529	3.3	35.8	Off	Off	1560	1532	1531	1531	1530	1522	1522	1530	1530
503.65	3.4	36.3	6.4	64.5	1600	1581	1585	1581	1579	1579	1579	1579	1579	3.3	34.8	6.3	65.8	1560	1568	1571	1570	1570	1553	1554	1565	1565
633.00														3.4	35.2	Off	Off	1560	1540	1540	1540	1540	1530	1530	1533	1533
633.65														3.4	35.2	6.4	66.6	1560	1574	1576	1570	1570	1560	1556	1565	1565
833.00	3.4	36.1	Off	Off	1600	1523	1523	1524	1528	1524	1525	1525	1525													
833.65	3.4	36.1	6.5	64.2	1600	1574	1575	1575	1574	1574	1574	1574	1575													
975.00														3.4	36.8	Off	Off	1600	1528	1530	1531	1535	1532	1530	1531	1531
975.65														3.4	36.8	6.6	65.7	1600	1582	1578	1580	1580	1580	1580	1579	1579
993.00	3.5	36.0	Off	Off	1600	1550	1547	1547	1547	1536	1537	1542	1542													
994.00	3.5	36.0	6.4	66.4	1600	1579	1582	1582	1582	1573	1573	1580	1580													

the distribution of solid and liquid within the cartridge for various fractions of salt frozen. For the analysis, an all-liquid condition of the thermal energy storage material was assumed with 6.5 percent void volume in the cartridge. The void volume was based on the mass of LiF in the cartridge prepared for the cartridge geometry optimization tests and on the cartridge dimensions with the LiF density taken as 1.735 g/cc for the liquid at the melting point. This value was based on the liquid density measurements reported in the Reactor Handbook (Ref. 12). This more recent value was used here rather than the more widely quoted value of 1.799 g/cc from the International Critical Tables (Ref. 14). From this void volume, the position of the interface for the all-liquid condition was calculated.

Assuming only radial heat flux to the cartridge wall, an annular layer of solid LiF forms adjacent to the wall with a concurrent decrease in volume, since the solid is denser than the liquid. The ratio of the solid-to-liquid density at the melting point is 1.297 calculated from data of Ref. 15. The liquid level thus falls to a new position, based on the fraction of salt frozen. The calculation is repeated stepwise. With each successive increment of salt frozen against the outer surface, the liquid level decreases. The liquid interface is determined by the diameter of the solid-liquid interface and by the angle, θ , which is the angle subtended at the cartridge center by the chord representing the liquid-void interface.

The results of these calculations are summarized in Figure 75 where the interface is drawn for various values of percent LiF frozen. Also tabulated in dimensionless form are liquid volume, solid volume, void volume, and angle θ for the various values of percent LiF frozen. Since these values are dimensionless, they apply to any cartridge diameter for which the initial liquid volume is 93.5 percent at the melting point. Note that the all-solid interface appears to be parabolic, although this cannot be verified since an analytical solution was not obtained. The minimum in the all-solid interface must occur at the cartridge center since the rings, representing successive increments of LiF frozen, are concentric. The basic assumptions underlying the calculation of the freezing pattern are: (1) heat transfer occurs only by radial conductive heat flux to the cartridge wall and no energy is radiated from the flat liquid surface, (2) The wetting effect is negligible so that there is no curvature of the liquid surface at the solid interface, and (3) heat transfer at the flat ends of the cartridge are negligible

Radiographs of test unit TT2 are shown in Figure 76. The freezing pattern of the solidified LiF appears to be in agreement with that calculated and shown in Figure 75. However, some "webbing" is apparent, that is, the solid internal surface is quite irregular. This would result from heat flux from the surface by some mechanism other than radial conduction



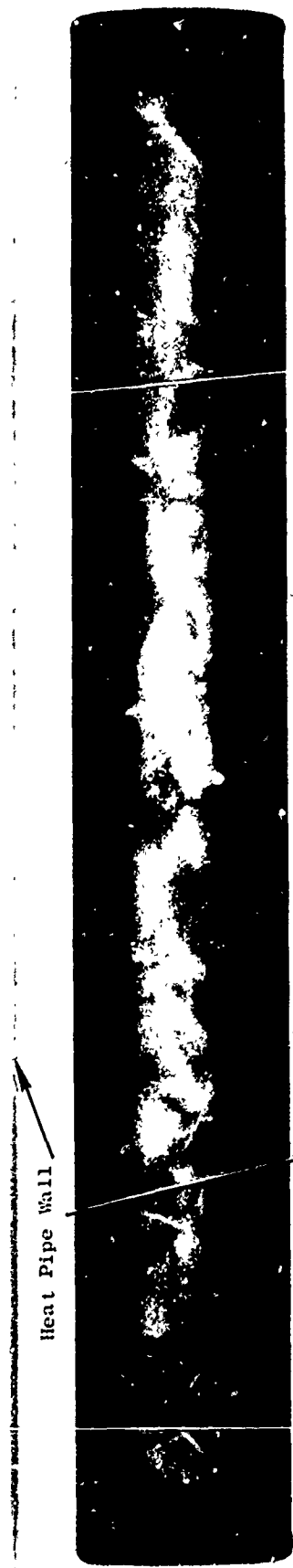
	ALL LIQUID	20	40	60	% FROZEN					ALL SOLID
					80	90	95	97	99	
LIQUID VOL.										
CARTRIDGE VOL.	.935	.748	.561	.374	.187	.094	.0467	.0280	.0094	0
SOLID VOL.										
CARTRIDGE VOL.	0	.144	.288	.432	.576	.649	.6848	.6992	.7136	.720
VOID VOL.										
CARTRIDGE VOL.	.065	.108	.151	.194	.237	.258	.2685	.2728	.2770	.280
INTERFACE DIA.										
CARTRIDGE ID	1.00	.900	.785	.646	.465	.338	.243	.191	.115	0
θ (DEGREES)	80	84	89	96.5	106	114	124	129.5	141	180

θ = ANGLE SUBTENDED BY LIQUID LEVEL.

Figure 75. Calculated Freezing Pattern for Cylindrical Thermal Storage Cartridge Containing Lithium Fluoride (Parameters Determined by Interface Position Are Tabulated)

43668

006405



Top View

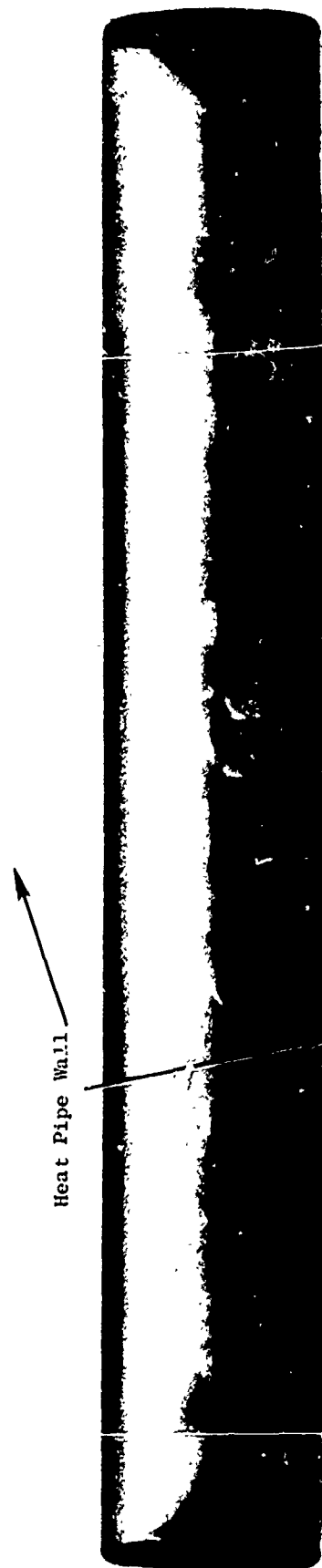


Figure 76. Radiographs of LiF Cartridge Inside Test Unit TT2 Following Testing. Cartridge is 10 inches long. Note cracks in solidified LiF.

through the solid. In addition, rather extensive cracking occurs throughout the solid LiF, but this is believed to occur when cooling to room temperature and does not exist near the LiF melting point.

The LiF freezing pattern calculated and shown in Figure 75 provides the basis for a transient thermal analysis of the HP-TES thermal behavior on cooling, since it shows the relationship between the geometrical parameter (the liquid-solid interface diameter) and the total energy released on freezing, which is related simply to the fraction of LiF frozen. This preliminary thermal analysis is presented here in order to provide a comparison with the actual HP-TES observed cooling curves. A more detailed analysis would include several other variables for which simplifying assumptions have been made for these calculations.

With the assumption of only radial, conductive heat transfer through the solid LiF, and neglecting any evaporative ΔT in the sodium at the cartridge surface, the relation between the thermal power derived from the freezing LiF and the temperature difference is

$$P_F = \frac{(T_m - T_v) \times \phi}{\frac{\ln(D_2/D_1)}{K_s} + \frac{\ln(D_3/D_2)}{K_c}} \quad (5)$$

where

P_F = thermal power from LiF freezing

T_m = LiF melting point

T_v = vapor temperature of sodium (assumed equal to cartridge surface temperature)

D_2 = cartridge i.d.

D_1 = diameter of LiF liquid-solid interface

D_3 = diameter at cartridge surface (diameter of cartridge outer wick)

ϕ = angle (in radians) over which heat flux occurs
($360 - \theta/360$) 2π (where θ is given in Figure 75)

K_s = solid LiF thermal conductivity

K_c = cartridge wall thermal conductivity (including wicks)

x = length of cartridge

If all thermal power were derived from freezing of the LiF, this equation could be directly applied to calculate the sodium vapor temperature during freezing. This, however, is not the case and, except at the time when LiF begins to freeze, a significant fraction of the power is derived from the thermal energy which is stored as sensible heat in the entire system. When the LiF is entirely frozen, all power is derived from the sensible heat of the system. If P_{mc} is the thermal power derived from the sensible heat of the system, then the total power, P_{TES} , is:

$$P_{TES} = P_{mc} + P_F \quad (6)$$

where

P_{TES} = total power

P_{mc} = power derived from sensible heat of system

P_F = fusion power

Now we define a parameter, Σmc , such that

$$\frac{dT_v}{dt} = \frac{-P_{mc}}{\Sigma mc} = \frac{P_F - P_{TES}}{\Sigma mc} \quad (7)$$

This parameter, Σmc , involves a summation of the mass time specific heat of each component in the system, including the LiF, cartridge, wick, sodium, heat pipe wall, insulation, heater, etc.

Two additional relationships may be written. The power from LiF freezing is related to the quantity frozen by

$$P_F = \frac{dW_F}{dt} \Delta H_f \quad (8)$$

where

W_F = weight of solid

ΔH_f = heat of fusion of LiF

The weight of LiF frozen is related to the diameter of the liquid-solid interface by

$$D_1 = D_2 \sqrt{1 - \frac{W_F}{W_T}} \quad (9)$$

where

W_T = total weight of LiF in the cartridge

Equation 3 is a very close fit of the values calculated and given in Figure 75.

Equations 5, 7, 8, and 9 can be combined to give two time-dependent differential equations in terms of the unknowns T_v and W_F . These equations are

$$\frac{dW_F}{dt} = \frac{\frac{\phi K_s}{\Delta H_f} (T_m - T_v)}{-\ln \sqrt{1 - \frac{W_F}{W_T}} + \frac{K_s}{K_c} \ln \frac{D_3}{D_2}} \quad (10)$$

$$\frac{dT_v}{dt} = \frac{1}{\Sigma mc} \left[\frac{\frac{\phi K_s}{\Delta H_f} (T_m - T_v)}{-\ln \sqrt{1 - \frac{W_F}{W_T}} + \frac{K_s}{K_c} \ln \frac{D_3}{D_2}} - P_{TES} \right] \quad (11)$$

These equations are first-order ordinary differential equations which were solved by a computer program (GE identification AMPBXS) which utilizes the fourth-order Adams-Moulton method.

In solving these equations for comparison with the experimentally observed cooling curves ϕ was considered constant. A more accurate comparison would be obtained by using the variation of ϕ with W_F as determined from the freezing pattern. Similarly, P_{TES} was taken as constant at the average experimental value, even though some variation in P_{TES} was observed during the tests.

To evaluate Σmc , measurements were made of the linear change in temperature with time of the HP-TES unit with the LiF in the all-liquid condition. A value of 1870 joule/ $^{\circ}\text{F}$ was obtained under these conditions. Of this value, 1130 joule/ $^{\circ}\text{F}$ can be accounted for by the specific heat of the heat pipe structural material, LiF, and sodium. The remainder is presumably due to the insulation, heater, and other components. In order to account for the variation in Σmc with quantity of LiF frozen, Σmc was taken to be a linear function of W_F . Thus

$$\Sigma mc = 1.32 W_F + 1339 \quad (12)$$

This assumes that the solid LiF is at the sodium vapor temperature and the liquid LiF is, of course, at the melting point. The thermal conductivity, K_c , was estimated to be 9.4 watt/ft- $^{\circ}\text{F}$ (32 Btu/hr-ft- $^{\circ}\text{F}$). The value assumed for K_c has little effect on the calculated T_v . The solid LiF thermal conductivity was taken as 1.49 watt/ft $^{\circ}\text{F}$ (5.1 Btu/hr-ft - $^{\circ}\text{F}$). This value was reported (Reference 16) for solid LiF at temperatures near the melting point and is in good agreement with data obtained (Reference 17) on single-crystal LiF, which is extrapolated to the melting point from 930 $^{\circ}\text{F}$.

5.3.5 COMPARISON OF CALCULATED AND MEASURED COOLING CURVES

For comparing the measured and calculated temperatures during LiF freezing, several cooling curves were run on TT2 and TT3. These runs were accomplished by first stabilizing the temperature at a value well above the LiF melting point. The power input was then reduced to some lower value and the variation in temperature was measured as the test unit cooled through the two-phase LiF region. For these measurements (and for the heating curves to be discussed later), the outputs of thermocouples No. 3 and 5 were displayed on a two-pen strip chart recorder for a continuous record of the temperatures. The cooling curves were obtained for each of the test units with P_{TES} equal to approximately the nominal value (200 watts), 1.3 times the nominal value, and 1.8 times the nominal value. Comparison of calculated and measured values was thus obtained for two different cartridge diameters and three different power levels.

Cooling curves for test unit TT2 are shown in Figures 77, 78 and 79 for thermal storage power conditions, P_{TES} , of 200, 270, and 370 watts. The measured values are compared with the curve calculated as described in the previous section, with LiF thermal conductivity, K_s , of 5.1 Btu/hr-ft- $^{\circ}\text{F}$, as reported in Reference four. The calculated curve is considerably above the measured value over the entire two-phase region. A much closer fit of the data is obtained by assuming an effective thermal conductivity for LiF of 3.1 Btu/hr-ft- $^{\circ}\text{F}$. The curves calculated using this value for K_s are also shown in Figures 77, 78, and 79.

Cooling curves for test unit TT3 (three cartridges are shown in Figures 80, 81, and 82 for P_{TES} values of 190, 264, and 356 watts,

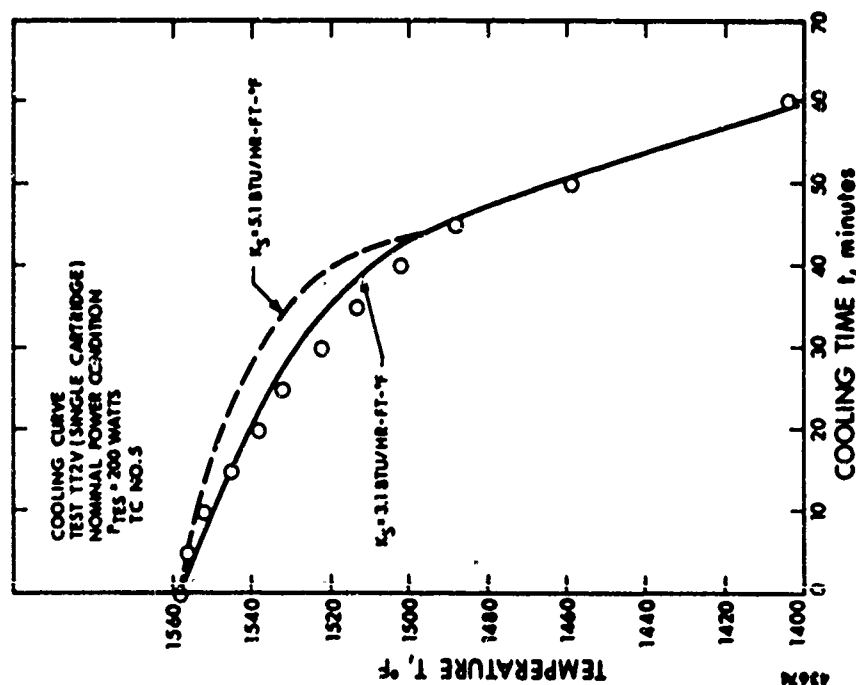


Figure 77. Cooling Curve for Test Unit TT2 (Single Cartridge) Nominal Power ($-P_{TES} = 200$ watts)

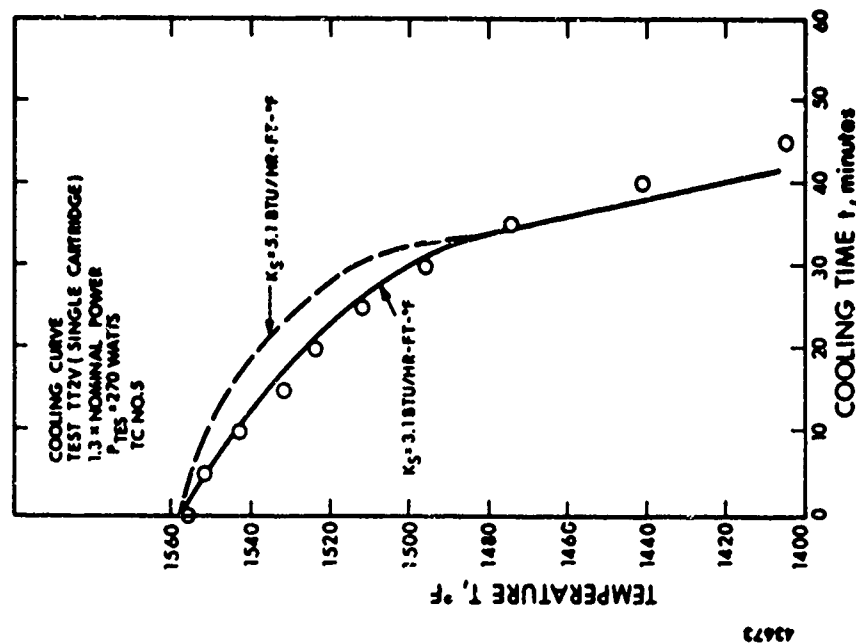


Figure 78. Cooling Curve for Test Unit TT2 (Single Cartridge) with 1.3 Times Nominal Power ($-P_{TES} = 270$ watts)

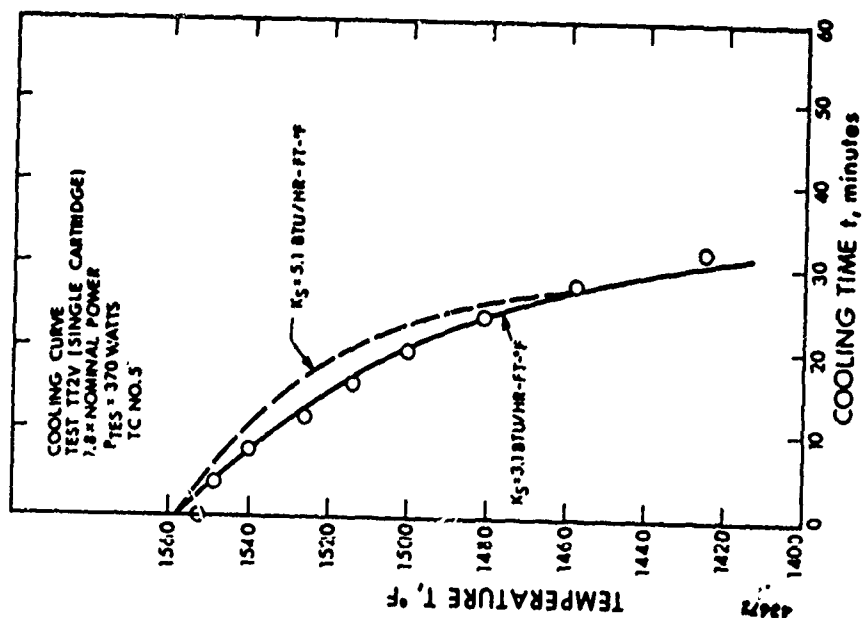


Figure 79. Cooling Curve for Test Unit TT2 (Single Cartridge) with 1.8 Times Nominal Power (-PTES = 370 watts)

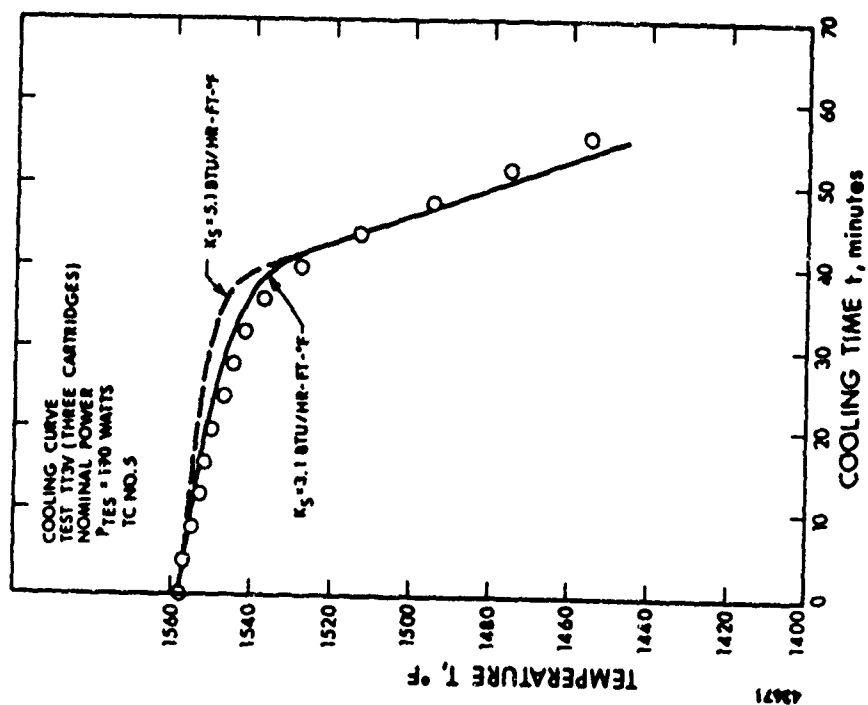


Figure 80. Cooling Curve for Test Unit TT3 (Three Cartridges) for Nominal Power Conditions (-PTES = 190 watts)

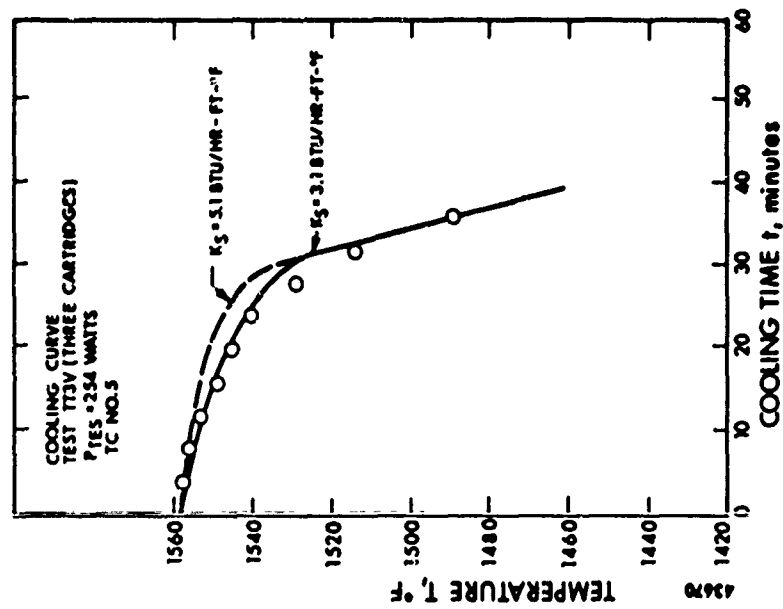


Figure 81. Cooling Curve for Test Unit TT3
(Three Cartridges)
($-P_{TES} = 254$ watts)

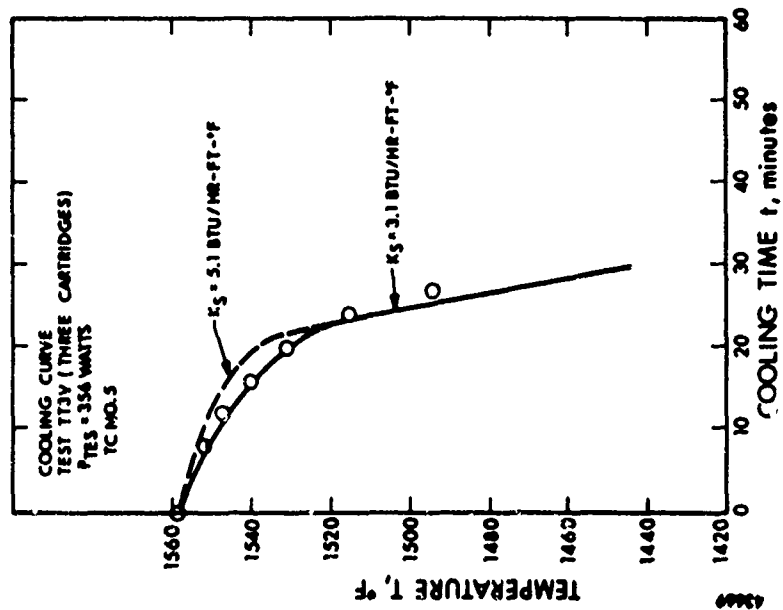


Figure 82. Cooling Curve for Test Unit TT3
(Three Cartridges)
($-P_{TES} = 356$ watts)

respectively. The observed temperatures are again compared with values calculated using the two thermal conductivities 5.1 and 3.1 Btu/hr-ft-°F. Good agreement between the measured and calculated values is again obtained by using $K_s = 3.1$ Btu/hr-ft-°F, while the calculated curve using the value of 5.1 lie appreciably above the measured values.

5.3.6 THERMAL BEHAVIOR DURING LiF MELTING

During HP-TES unit cyclic operation, very small temperature increases during the charging portion of the cycle were observed. In order to investigate this effect, heating curves were run on the TT2 and TT3 test units. These curves were analogous to the cooling curves previously described. The temperature of the HP-TES unit was first stabilized at temperatures below the melting point of LiF. The power input was then increased to some constant value and the temperature observed during melting of LiF. The output of thermocouples 3 and 5 were displayed on the two-pen strip chart recorder. Heating curves were obtained on each of the test units with P_{TES} equal to the nominal value (107 watts), 1.4 and 1.8 times the nominal value.

Heating curves for the TT2 test unit (single cartridge, 1.40-inch i.d.) are shown in Figures 83, 84, and 85 for P_{TES} of 97, 150, and 200 watts, respectively. Also shown on these plots are the ideal heating curves; that is, the curve that would be obtained with a heating rate so low that the entire system remains isothermal throughout the transient condition. The initial and final upward slopes are obtained from the sensible heat term Σmc . Thus $P_{TES}/\Sigma mc$ gives the slope in °F/second. The duration of the thermal arrest at the melting point is related to the total stored fusion energy of the LiF. Thus, W_{LiF}/P_{TES} is the duration of the thermal arrest in seconds.

In Figures 83, 84, and 85 it may be seen that the measured temperatures are in good agreement with the ideal curve over most of the two-phase period for the TT2 test unit. Temperature differences are typically 2° to 4°F in the early portion and increase to 6° to 8°F near the all-liquid condition. Also, only minor differences are noted with increasing P_{TES} . The good agreement between the calculated and measured duration of the thermal arrest shows that the overall thermal balance is consistent with the heat of fusion of LiF.

Figures 86, 87, and 88 show the heating curves obtained on the TT3 test unit (three cartridges, 0.81-inch i.d.). The thermal behavior noted on this unit is quite similar to that observed on the TT2 unit. The general conclusion from these heating curves is that the temperature difference between 75 and the LiF melting point increases slightly during the LiF melting and reached 6° to 8°F just before the all liquid condition. The observed temperature difference does not vary significantly either with cartridge diameter or with heat flux to the cartridge.

43460

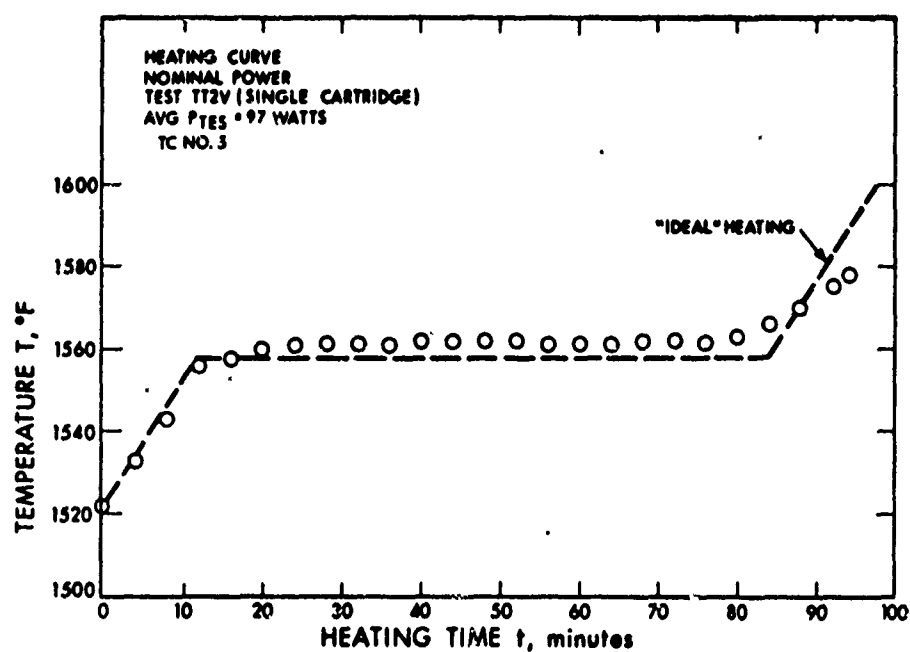


Figure 83. Temperature Variation of Test Unit TT2
During Energy Storage (Single Cartridge)

43479

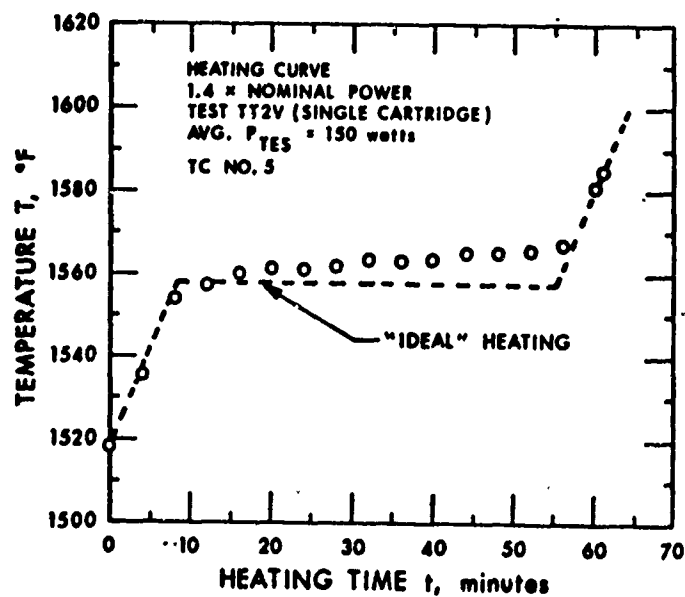


Figure 84. Temperature Variation of Test Unit TT2
During Energy Storage (Single Cartridge)

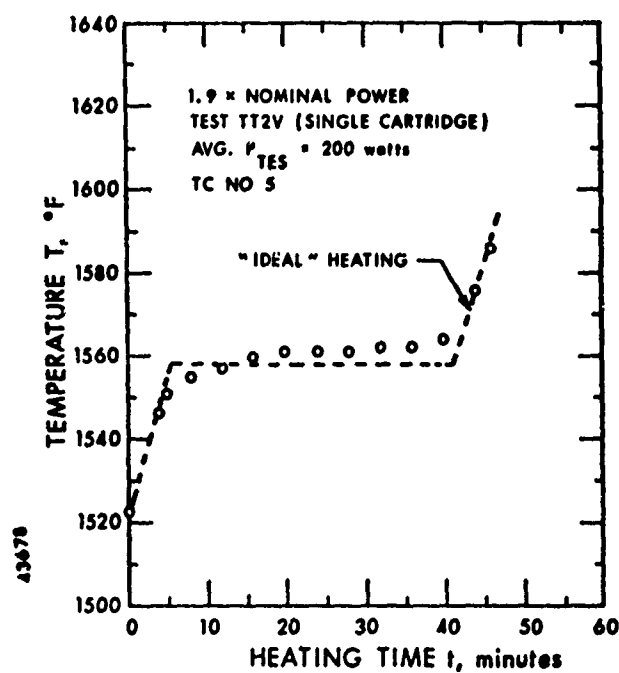


Figure 85. Temperature Variation of Test Unit TT2 During Energy Storage (Single Cartridge)

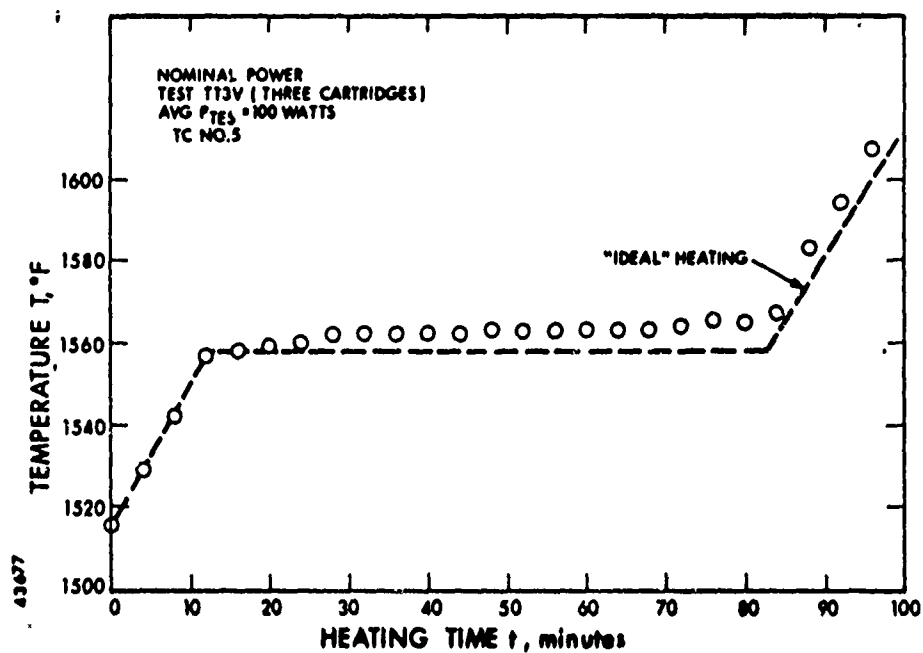


Figure 86. Temperature Variation of Test Unit TT3 During Energy Storage (Three Cartridges)

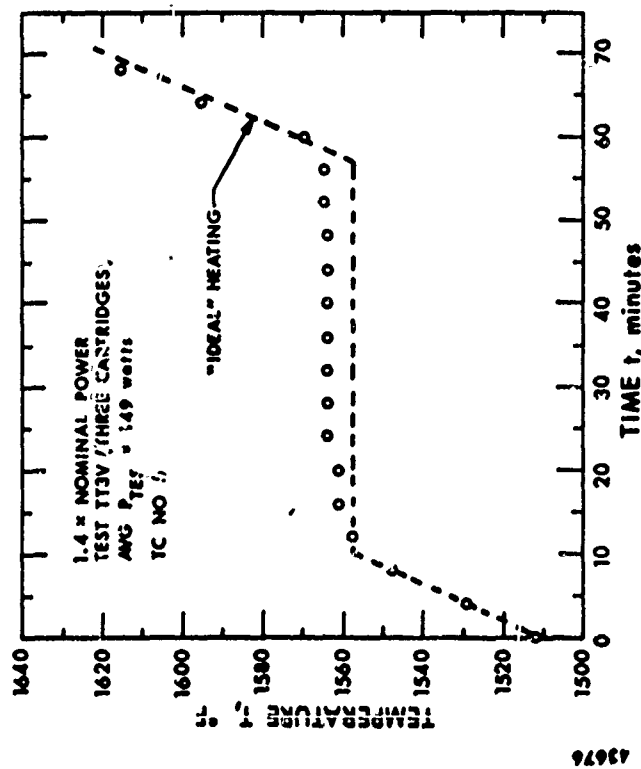


Figure 87. Temperature Variation of Test Unit TT3 During Energy Storage (Three Cartridges)

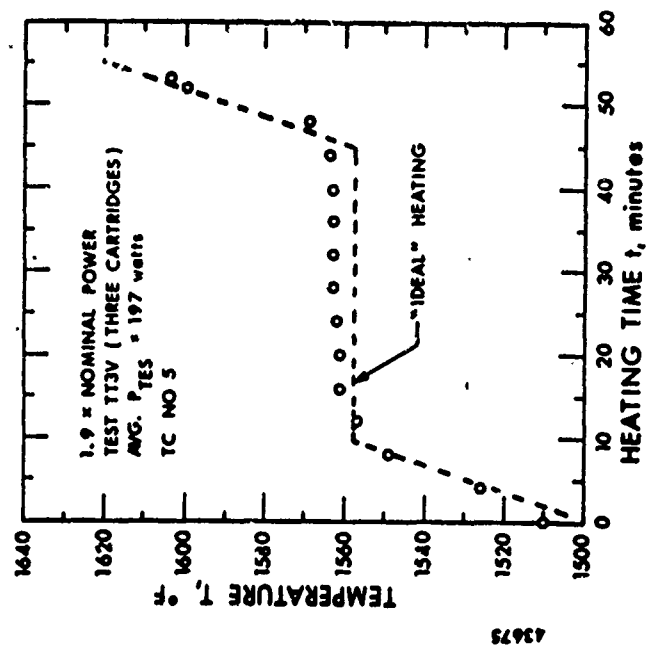


Figure 88. Temperature Variation of Test Unit TT3 During Energy Storage (Three Cartridges)

The relatively constant temperature noted on heating, as compared to the rather rapid decrease in temperature on cooling, is believed to be due to three factors. The first of these is that the solid sinks to the bottom of the cartridge on heating, since the solid is more dense than the liquid, and thus maintains good contact with the cartridge wall during heating. The second factor is that the thermal conductivity of the liquid is about twice that of the solid (11.3 versus 5.1 Btu/hr ft²°F, Reference 16). Since the heat is conducted through the liquid on heating and through the solid on cooling, the temperature drop through the solid is correspondingly less on heating, for equivalent heat fluxes. The third factor is that the nominal thermal power to the LiF is less during energy storage than during energy extraction due to the relative sun/shade periods. The third factor does not appear to contribute greatly to the observed temperature difference.

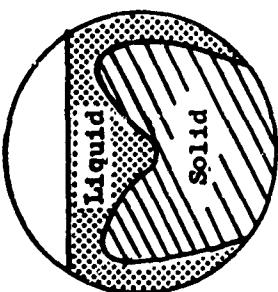
From the melting behavior of LiF, one can conceptually construct the LiF melting pattern. This melting pattern is shown in Figure 89. The first melting occurs adjacent to the cartridge wall. The LiF expands on melting with some liquid possibly spilling into the cavity. Melting of additional LiF occurs primarily at the bottom of the solid slug which is in contact with the lower cartridge wall. This process continues until only liquid remains.

5.4 EXTENDED THERMAL COOLING OF SUBSCALE THERMAL STORAGE UNITS

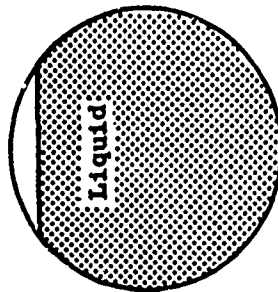
After the completion of the 1000-hour test reported in Subsection 5.3.3 of this report, the two subscale thermal energy storage units TT2 and TT3 were transferred from General Electric Company to Xerox/EOS for an additional long duration test. Several changes in the test setup appeared to be desirable. It was felt that the insulation could be considerably improved, thereby decreasing the losses and lowering the power requirement.

Calculations indicated that flexible Min-K Johns-Manville would be the most practical insulation material for the subscale thermal energy storage units. To keep the energy loss from the subscale thermal energy storage units at approximately 300 watts at the melting temperature of LiF (1558°F), an insulation thickness of 4-inches was required. (See Figure 90).

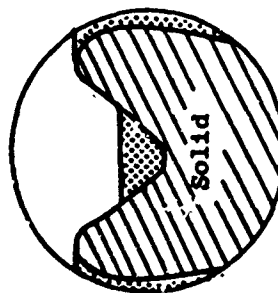
The test set up used at EOS is shown in Figure 91. Each unit was controlled from its own control panel. Each control panel contained one 1-percent accurate current meter and voltmeter for each of the two sets of heaters installed around each unit. In addition, the control incorporated a timer which permitted the power to be turned on and off for the desired cycle. In addition, temperature controllers controlled the



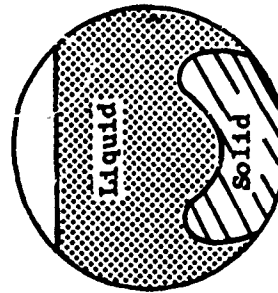
40% Melted



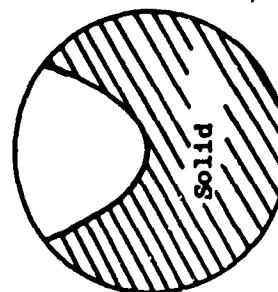
All Liquid



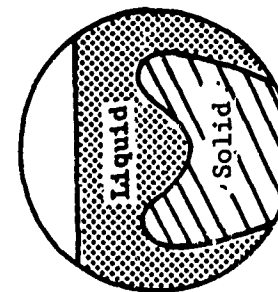
20% Melted



80% Melted



All Solid



60% Melted

Figure 89. Conceptual LiF Melting Pattern in Cylindrical Cartridge

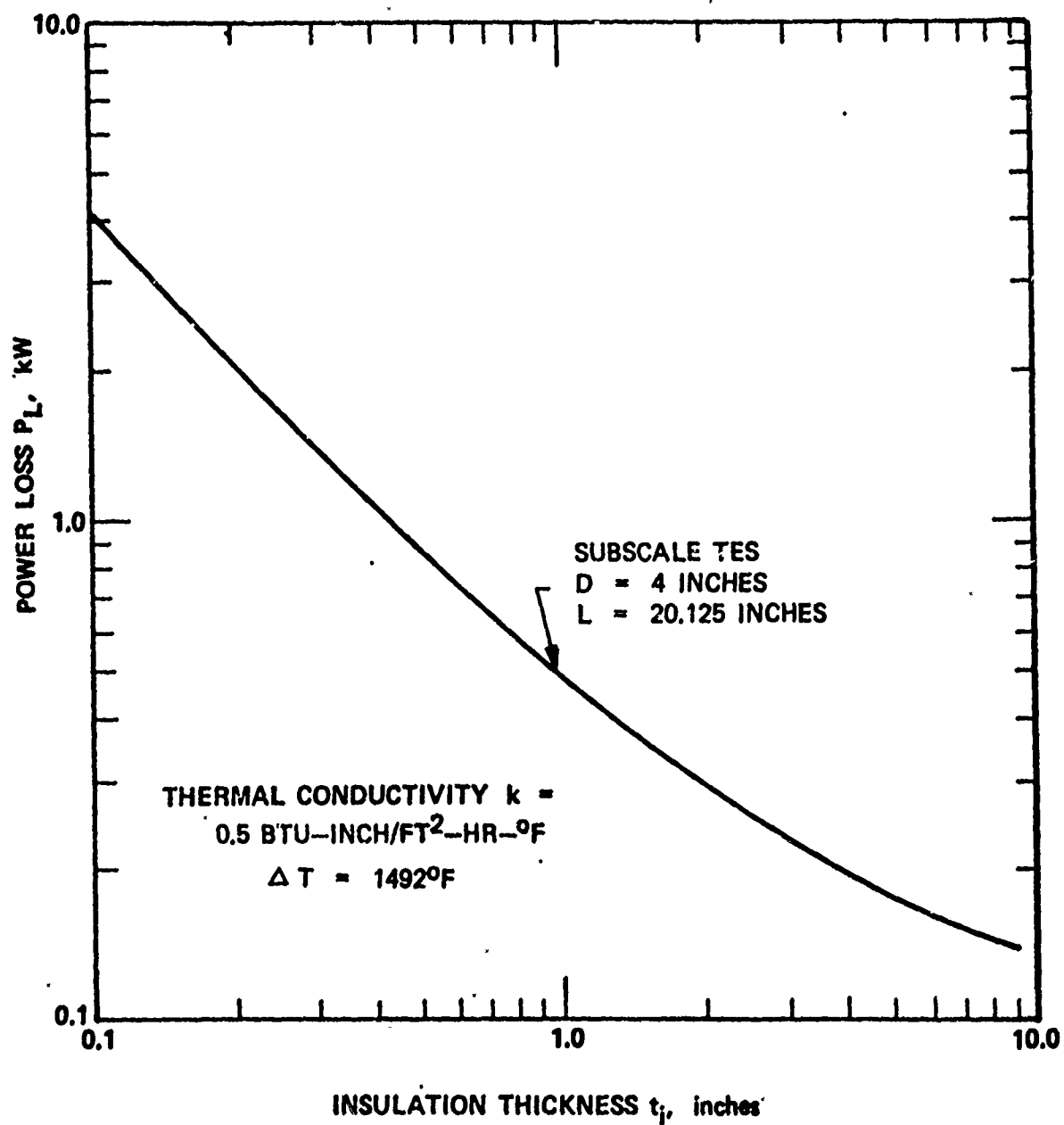


Figure 90. Insulation Requirement for Subscale Thermal Energy Storage System

50784 B



Figure 91. Subscale Thermal Energy Storage Units TT2 and TT3 with Controls



Figure 92. Temperature Measuring Equipment for Subscale Thermal Energy Storage Unit Tests

power to the heaters turning off the power whenever the operating temperature exceeded a preset temperature and turning the power on when the temperature dropped below a lower preset temperature. Switches in the control panel permitted many control combinations, including or excluding the timer or the temperature controller or any of their combinations.

In Figure 92, the temperature measuring instrumentation is shown. All temperatures, except the temperatures measured by thermocouples #2 (see Figure 74) which were used by the temperature controller were recorded on a multipoint 24-channel Weston chart recorder with a scale from 1000 to 1600°F. The strip chart recorder had a cold junction compensator built into the instrument. Accurate temperature measurements were taken with a digital voltmeter which indicated the thermocouple output within 1 microvolt. The thermocouples were compensated against a room temperature cold junction or against an electronic, 32°F, cold junction. With the room temperature known, adequate adjustment to the readings could always be made when the temperature readings were taken against the room temperature cold junction.

5.4.1 THERMAL BEHAVIOR OF THERMAL ENERGY STORAGE MATERIAL

Initially, for the determination of the power losses as a function of the operating temperature of each unit, only heaters #2 (Figure 74) were energized. The power losses, which are equal to the power input, are plotted in Figures 93 and 94 as a function of the operating temperature. The losses could well be correlated to the temperature difference between the operating temperature and the room temperature by the following relation

$$P_{\text{loss}} = C \times (T_o - T_{\text{room}})^n$$

where

P_{loss} = power loss from the unit, watt

C = constant

T_o = operating temperature, °R

T_{room} = laboratory temperature, °R

For the two units, the following values for the constant C and the exponential n were found:

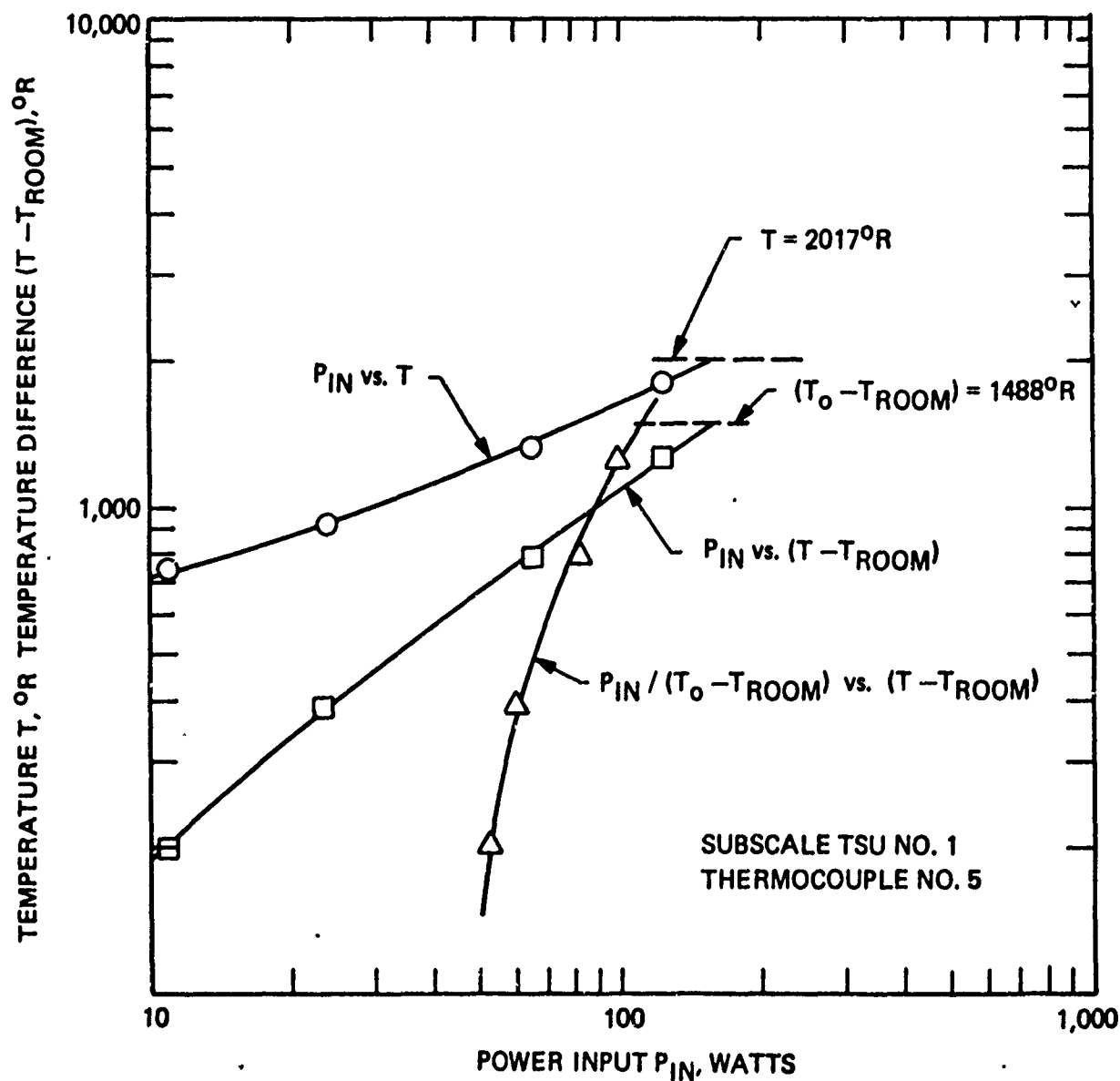


Figure 93. Power Losses as Function of Operating Temperature of Subscale Thermal Energy Storage Unit TT2

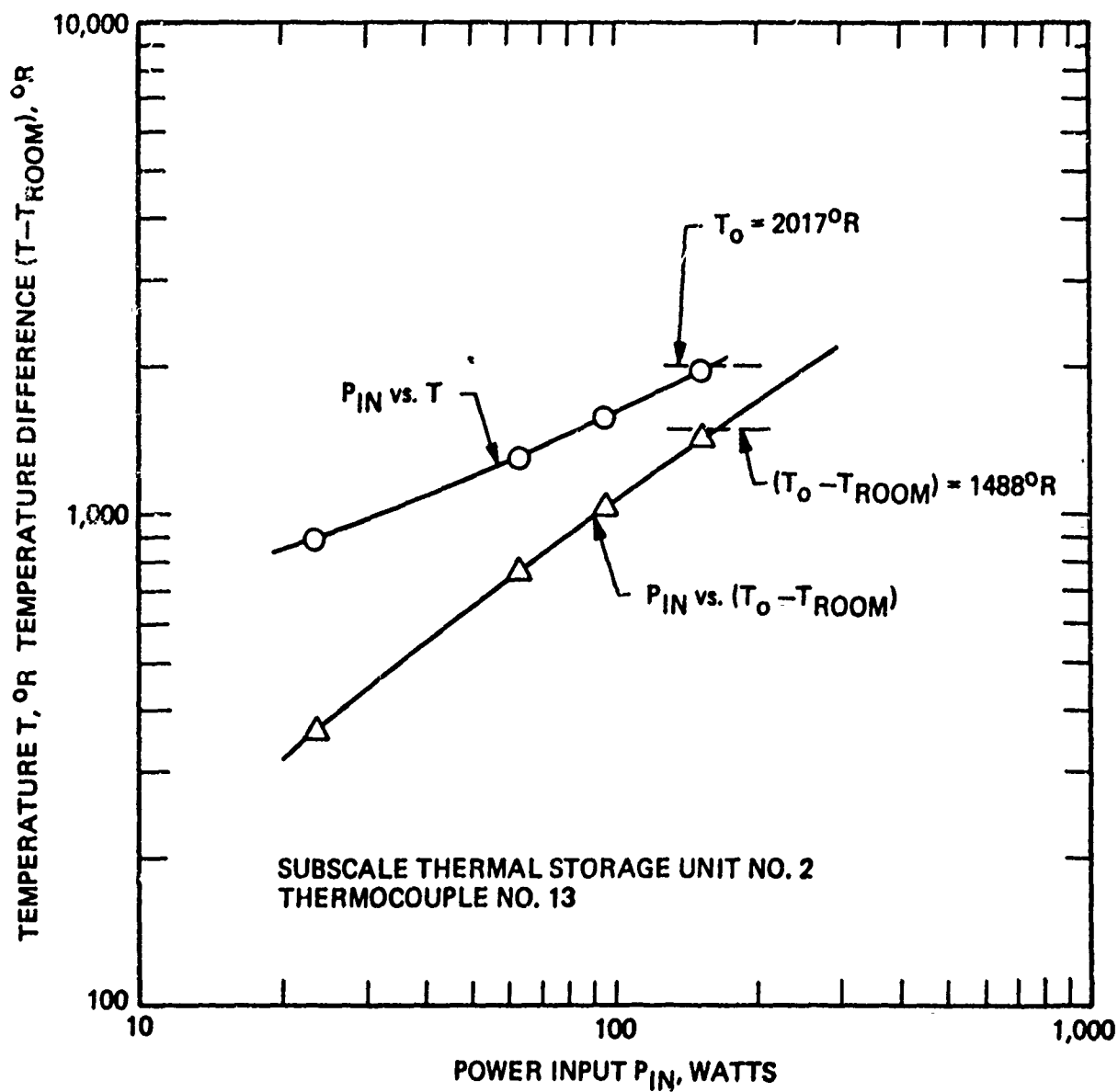


Figure 94. Power Losses as Function of Operating Temperature of Subscale Thermal Energy Storage Unit TT3

	<u>TT2</u>	<u>TT3</u>
C	5.25×10^{-3}	5.00×10^{-3}
n	1.408	1.422

From the losses at the reported melting temperature of the thermal energy storage salt (LiF, 1558°F) were found for unit TT2 and TT3 to be 157 and 162 watt, respectively. Since the losses were lower than the losses needed during the cooling cycle, heaters #1 did not have to be energized.

For the thermal energy storage material LiF, to melt in 65 minutes, the input power had to be raised above the steady-state power requirement according to the amount of salt and the heat of fusion of the salt. Each unit contained nominally 402 g of salt which has a fusion energy of 1044 joules/gram. The total fusion energy was therefore 4.197×10^{-5} joules. The required power for melting the salt in 65 minutes had therefore to be 107.6 watt.

In Figures 95 and 96, one full cycle for each one of the two subscale thermal energy storage units are presented. The cycles were run under temperature control. The upper operating limit of the temperature at which the heater would be turned off was set close to 1600°F to insure that a heating trend could be established well outside the melting temperature of the thermal energy storage salt. The lower temperature at which the heater would be turned on again was set well below the temperature at which it could be expected that the entire thermal energy storage material had solidified.

Contrary to the test results obtained at General Electric Company, all measured temperatures were within one degree of each other. Thus, effectively each unit was at a uniform temperature all the time. This result proved the need for sufficient insulation to obtain valid test data.

Several pertinent values were calculated from the transient temperatures and the constant temperatures during melting of the thermal energy storage material. For unit TT2, the melting of the salt started at an operating temperature of 1557°F and dropped during the melting phase to 1556°F. The melting stopped very distinctly after 64 minutes. The solidification and thus the extraction phase of the cycle appeared to start at an operating temperature of 1549°F and was only completed after the operating temperature had dropped to 1502°F.

For the determination of the final temperature of the extraction cycle, the following calculations had to be made. First, the thermal capacity of the system had to be established. At any point during the heating

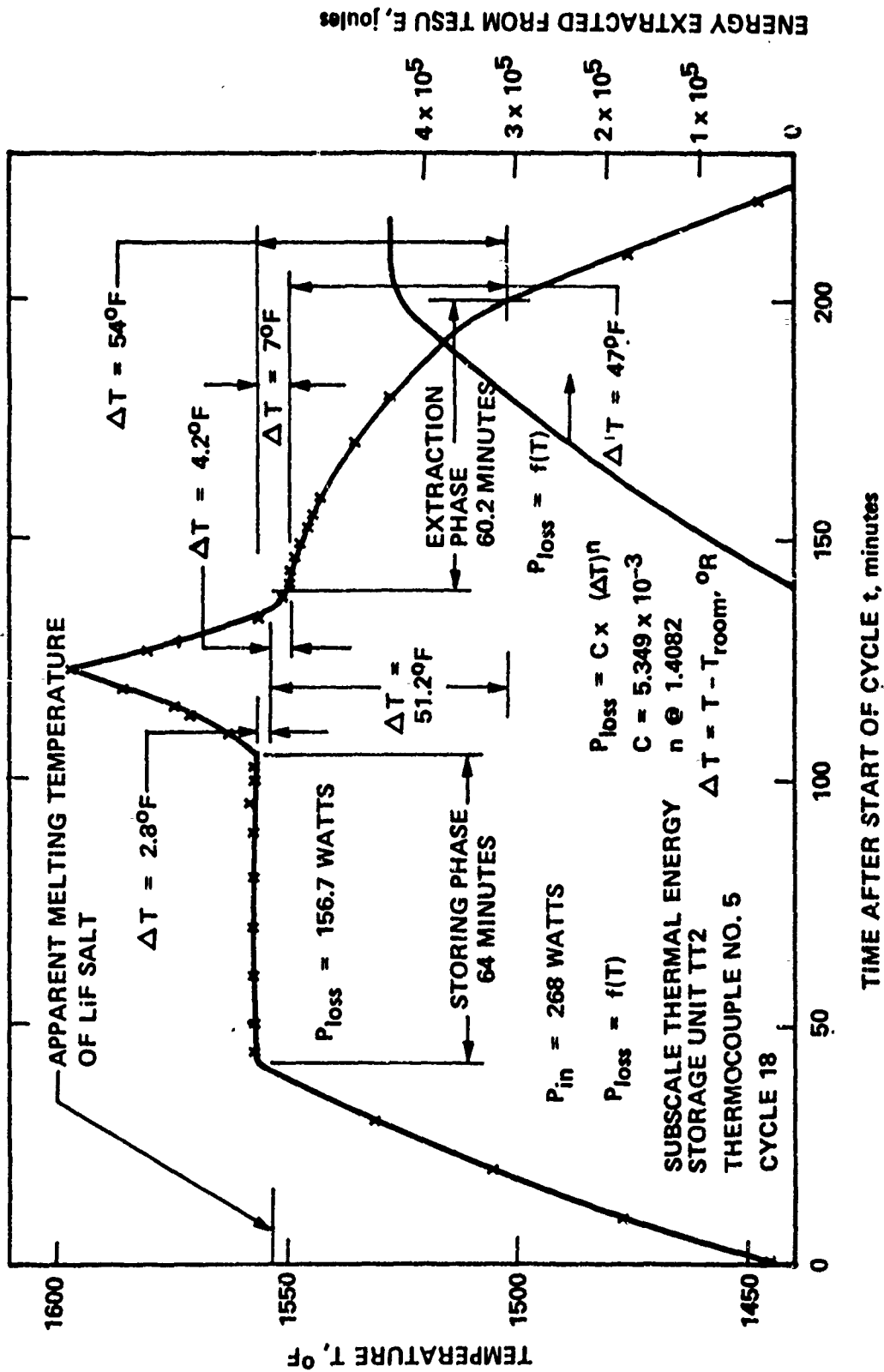


Figure 95. Presentation of Heating and Cooling Cycle of Subscale Thermal Energy Storage Unit TT2

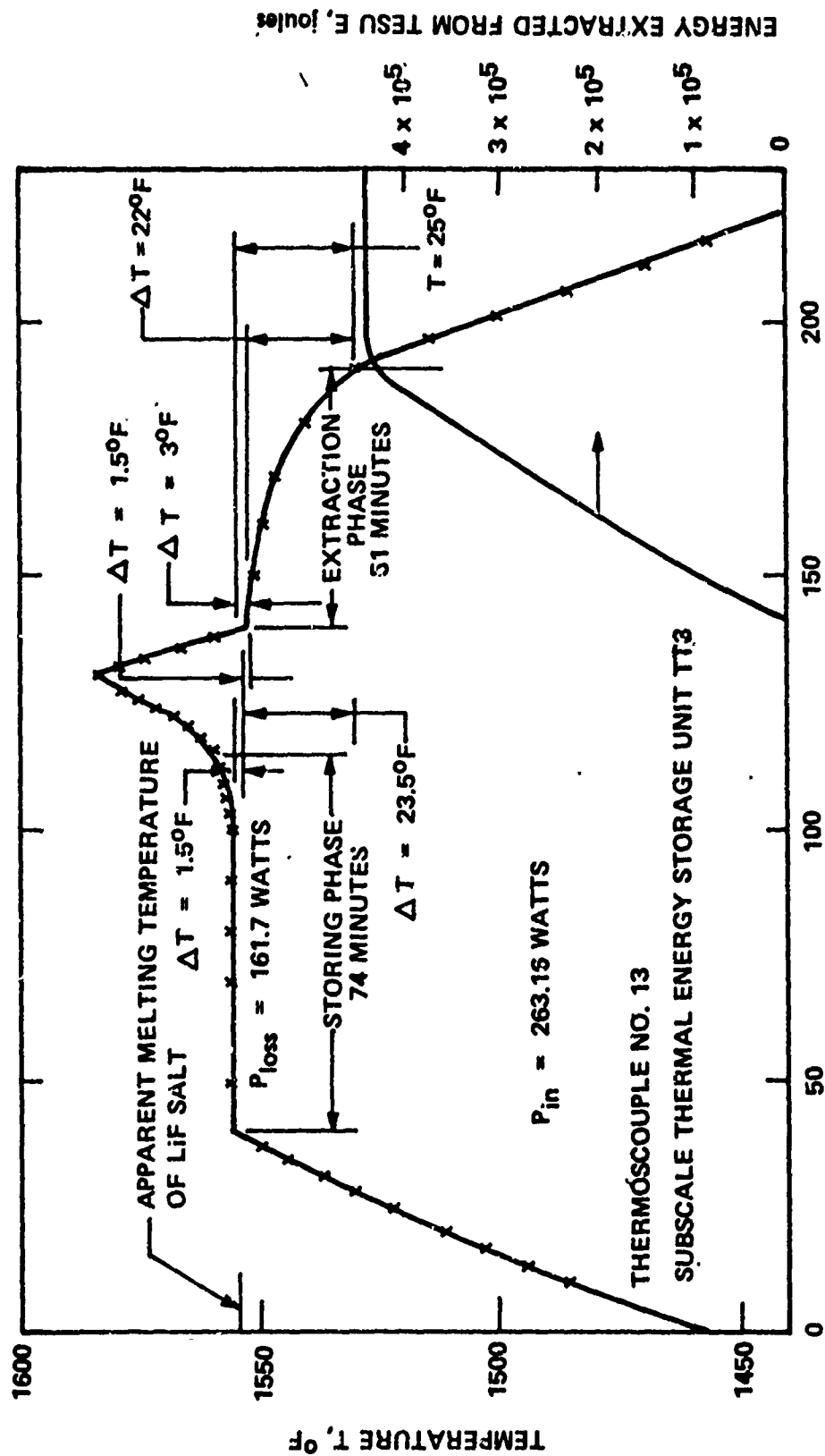


Figure 96. Presentation of Heating and Cooling Cycle of Subscale Thermal Energy Storage Unit TT3

process and before melting of the thermal energy storage material starts, an energy balance can be taken between the power input, the power absorbed by the unit and the losses are shown in the following equation:

$$P_{in} - P_{loss} = (c_p W) dT/dt$$

Selecting any point on the heating curve and using the known power input and the known power loss as a function of the operating temperature, the thermal capacity of the system, $c_p W$, could be calculated. For unit TT2, the thermal capacity was found to be 2.84×10^3 joules/ $^{\circ}R$.

With the thermal capacity of the system established and the power losses known as a function of the operating temperature, the energy release rate from the thermal energy storage unit during the energy release phase of the cycle could be calculated by the relation:

$$dE/dt = P_{loss} - (c_p W) x dT_o$$

where

E = energy released from the thermal storage material, joules

P_{loss} = power loss from the unit as function of operating temperature, watt

$c_p W$ = Thermal capacity of unit, joules/ $^{\circ}R$

T_o = operating temperature, $^{\circ}R$

The results of the calculations are shown in Figure 97. The completion of the energy extraction cycle was not very distinct. Such behavior had been predicted in the analysis presented in Subsection 2.1.4.5 of Volume I. For all practical purposes, the extraction phase apparently required 60.2 minutes. During this phase 4.43×10^5 joules were extracted from the thermal energy storage material. This compared with an energy input of 4.27×10^5 joules. This energy input into the storage material in the form of fusion energy can be calculated from the relation:

$$(P_{in} - P_{loss})_{con} \times t = E_{st}$$

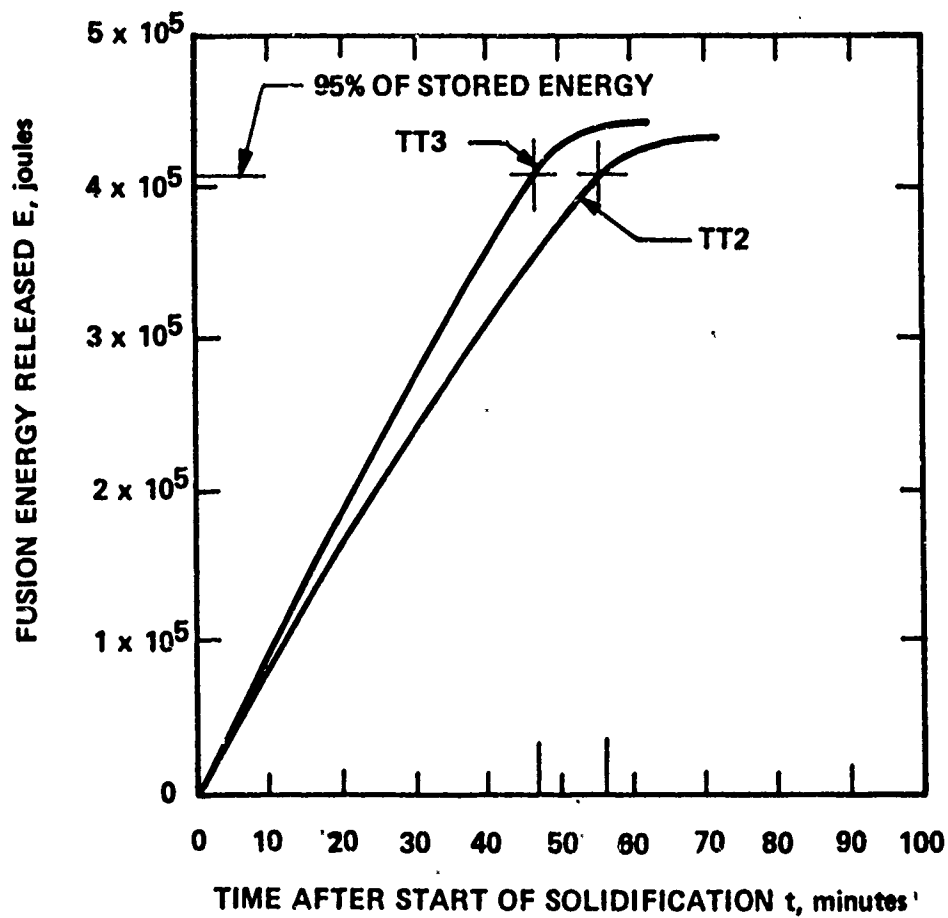


Figure 97. Comparison of Fusion Energy Release Rates for the Two Subscale Thermal Energy Storage Units TT2 and TT3

where

P_{in} = input power, watt

P_{loss} = power loss as a function of operating temperature during the storing phase, watt

t = time duration of storing phase, sec

E_{st} = energy stored, joules

The difference between the calculated stored energy and the extracted energy was only 1.3 percent.

An attempt was made to determine the effective melting and freezing temperature of the storage salt by using the measured temperatures and the measured and calculated powers. During the storage phase, the actual input power into the storage salt was the difference between the power input and the power loss. The actual power input was 268 watt and the power loss at 1556°F was 156.7 watt. Thus, the power transfer into the storage material was 111.3 watt. During the start of the extraction cycle, the power given off by the thermal energy storage material was equal to the total power loss from the unit minus the power given up by the unit itself.

$$P_{TEout} = P_{loss} - (c W)_p \times dT/dt$$

where

P_{TEout} = power given up by the thermal energy storage unit, watt

The following two equations should furnish a good estimate of the effective melting and freezing temperature of the LiF storage thermal energy storage material.

$$\text{Storing phase: } P_{TEin} = kx(T_o - T_F)$$

$$\text{Extraction phase: } P_{TEout} = kx(T_F - T_o)$$

From these two relations, the effective fusion temperature was found to be 1554°F.

Similar calculations were made using the results shown in Figure 96 for the subscale thermal energy storage unit TT3. All indications were that unit TT3 contained slightly more thermal energy storage material than unit TT2. The most pertinent data for both subscale thermal energy storage units are compiled in Table XXII. The differences between the two units were very distinct, as predicted. Unit TT3 utilizing three capsules produced the expected advantages over the single capsule unit TT2. The difference in operating temperature during melting and the onset of solidification of the thermal energy storage material is only 3°F for unit TT3, versus 7°F for unit TT2. The operating temperature of unit TT2 drops almost twice as much as that of unit TT3 during the extracting phase.

TABLE XXII

PERTINENT DATA FOR THERMAL ENERGY
STORAGE UNITS TT2 and TT3

	<u>TT2</u>	<u>TT3</u>
Operating temperature at melting, °F	1556	1556
Operating temperature at onset of freezing, °F	1549	1553
Temperature difference between operating temperature at melting and onset of freezing, °F	7	3
Operating temperature drop from onset of freezing to completion, °F	47	22
Operating temperature difference between melting and completion of freezing, °F	54	25

The differences in the length of time of the storing phase and the extraction phase was solely a function of the power input which is effected by the power setting for the heater and the power losses which are determined by the insulation of the units. The insulation of unit TT2 appeared to be slightly more effective than for unit TT3. During the storing phase, unit TT2 lost only 156.7 watt while unit TT3 lost 161.7 watt. This compared with the expected power loss of 200 watt. Because of the low power losses, the units did not require the operation of heaters #1. This proved to be of great advantage. During the energy extraction cycle, no interference from the second heater occurred. This removed uncertainties from all temperature and power measurements.

5.4.2 LONG DURATION TESTING

With the retesting of the two subscale thermal energy storage units completed, an unattended long duration test of both units was initiated on 23 January 1973. The cycling of the units was controlled by the temperature controller which was adjusted to turn the power to the units off at approximately 20°F above the melting temperature of LiF (1558°F) and restart the power input at approximately 20°F below the melting point. Timed cycling would have required a very fine control on the power input and special provisions for adjusting the power losses during the energy extraction cycle. A special effort for stimulating the exact power cycle of a still undefined satellite orbit did not seem justified for this materials test. Due to the changes in the power input which were caused by variations in the laboratory voltage and changes in the power losses over the length of the test duration, the cycle varied between 94 minutes and 194 minutes.

On 30 October 1973, the unit which contained a single thermal energy storage capsule TT2 failed. Failure was indicated by the apparent opening of the heater. Inspection disclosed a substantial hole in the outer heat pipe wall with the hot sodium having been exposed to the air apparently for a considerable length of time (see Figure 98). The unit had operated with some short interruptions for 2059 cycles over 5415 hours. Since the outer shell of the heat pipe was made of stainless steel, the failure of the heat pipe was not a valid indication of the heat pipe performance. Because of the exposure of the internal part of the heat pipe to the moist air at the elevated temperature, the thermal energy storage capsule was destroyed. The capsule material was completely oxidized. This failure invalidated the test for which it had been operated, i.e., the endurance of the thermal energy storage capsule.

The failure of the first subscale thermal energy storage unit suggested the interruption of the testing of the second subscale thermal energy storage unit, TT3. It was feared that if thermal energy storage unit TT3

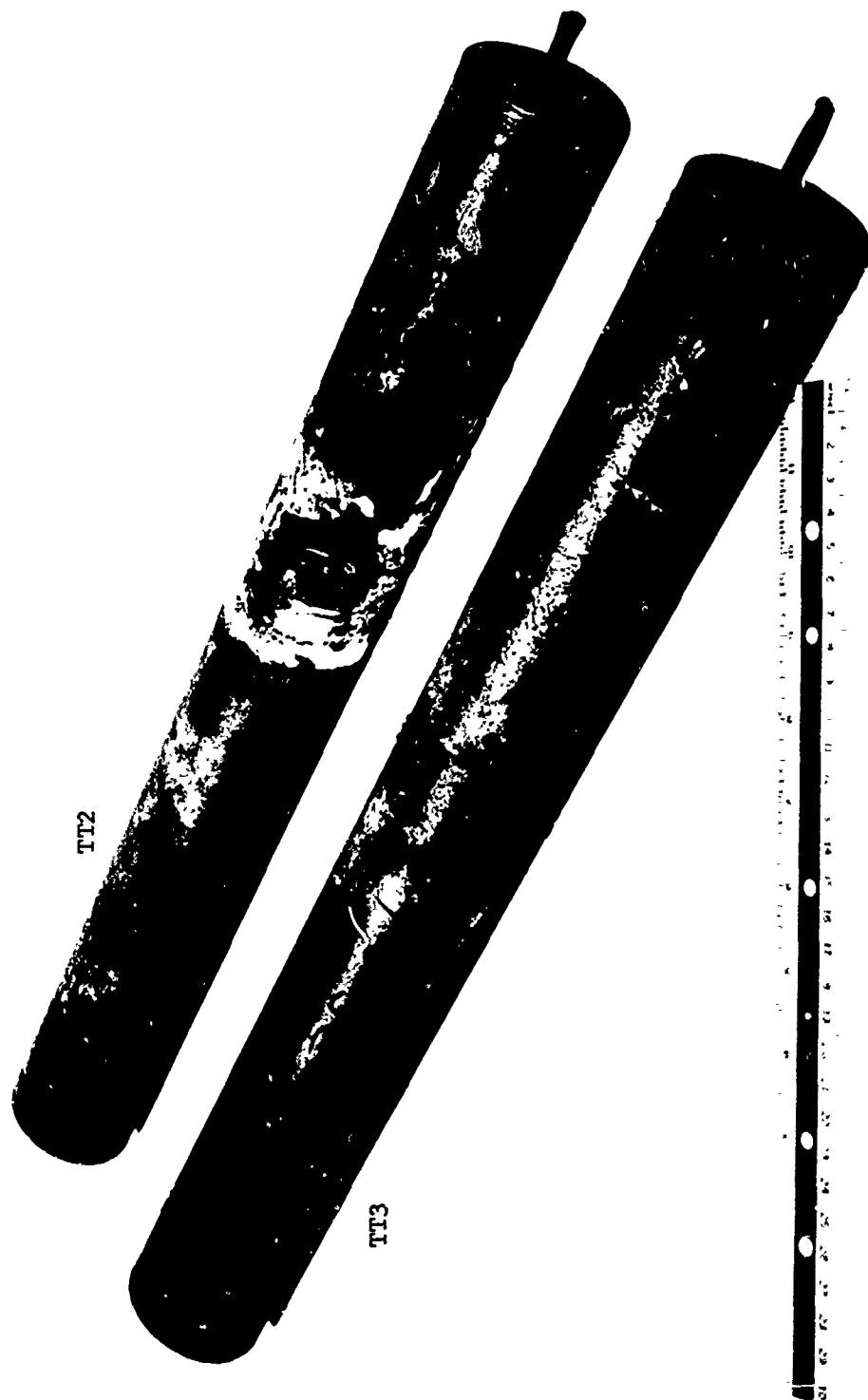


Figure 98. Thermal Energy Storage Capsules TT2 and TT3 after Long Duration Endurance Testing

would fail in the same mode as unit TT2, the three thermal energy storage capsules would also be exposed to the destructive environment making it impossible to inspect the capsules for distortions due to repeated cycling which had been the planned purpose of the cycling tests.

On 23 January 1974, subscale thermal energy storage unit TT3 was shut down. The unit had operated without interruption from 14 February 1973 to 23 January 1974. At the time of shut down, the unit had gone through 3150 cycles of charging and discharging of the thermal energy storage material. The initial cycles had lasted 206 minutes while at the end of the test the cycle time had stabilized at 70 minutes. During the long duration test, the cycle time fluctuated between these two extremes. At the time of the shut down, all temperatures appeared to be consistent with the initially measured temperatures.

The heat pipe did not show any damage or impending failure despite the rather severe cycling it had undergone for almost an entire year of operation. Furthermore, the heat pipe was not made of the most desirable material but was constructed of stainless steel.

Radiographic pictures were taken of the thermal energy storage capsules. These are shown in Figures 99 through 103. No distortion of any of the three capsules could be observed, nor was there any indication that any one of the capsules had sprung a leak.

5.5 SUMMARY AND CONCLUSION

Three heat pipe thermal energy storage units were constructed and tested for evaluating the use of a phase changing material as thermal energy storage material in a solar collector thermal power system. The effort, as reported in this section of the final report of the Solar Collector Thermal Power System Experimental Evaluation Program, has conclusively shown that LiF salt contained in a Columbia -1% Zirconium capsule can fulfill the requirements for storing thermal energy at a temperature of 1558°F and release the energy at that temperature with some minor temperature drop across the solidifying material. After almost a full year of operation, simulating the power budget of a satellite in an orbit which requires thermal energy storage, the thermal energy storage capsules maintained their integrity in construction and configuration.

The effect of configuration on the temperature history during discharge of the thermal energy storage material was investigated by testing the same amount of thermal energy storage material in two capsule configurations. In one configuration, the entire thermal energy storage material, LiF, was contained in a single capsule while in the other configuration, the same amount of LiF salt was contained in three separate capsules.



Figure 99. Radiograph of Thermal Energy Storage Unit TT3 after
11 Months Cycling

007195



Figure 100. Radiograph of Thermal Energy Storage Unit TT3 after 11 Months Cycling

961200



Figure 101. Radiograph of Thermal Energy Storage Unit TT3 after
11 Months Cycling

007197

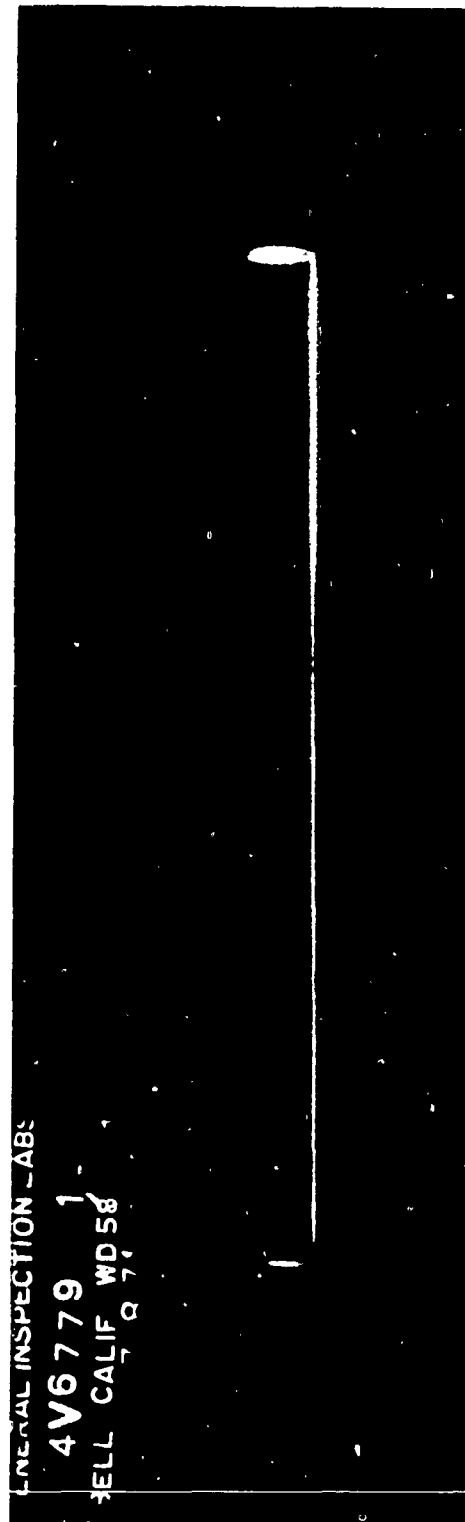


Figure 102. Radiograph of Thermal Energy Storage Unit TT3 after 11 Months Cycling

007199



Figure 103. Radiograph of Thermal Energy Storage Unit TT3 after
11 Months Cycling

All capsules had the same length but the three capsules had an accordingly smaller diameter. The multiple capsule configuration proved definitely to have a great advantage over the single capsule configuration. As predicted analytically, the three capsule configuration maintained the heat pipe temperature closer to the melting temperature during discharge of the stored thermal energy.

SECTION VI

FULL SCALE ROTARY HEAT TRANSFER JOINT

6.1 INTRODUCTION

The basic requirement for the radiation heat transfer joint was the transfer of power over a wide range from the secondary heat at the design operating temperature of the condenser. For the experimental investigation of the radiation heat transfer joint for the secondary heat pipe, it was desirable to vary the power to fulfill these requirements, the radiation heat transfer joint had effectively to present a variable thermal resistance.

6.2 DESIGN

The design of the full scale rotary heat transfer joint considered the use of a variable temperature heat shield which was imbedded in the insulation of the rotary heat transfer joint as shown in Figure 104. The maximum power to be transferred across the rotary radiation joint was to be 2.7 kW. The lowest temperature to which the imbedded heat shield could be cooled was 300°K. In Figure 105, the total heat transfer and the cooling surface diameter is correlated with the cooling surface temperature for the expected thermal conductivity of the heat shield material of 1.5×10^{-3} watt/cm-°K and for an assumed emissivity of $\epsilon = 0.8$ for the two surfaces forming the radiation joint.

The imbedded heat shield was to be cooled by cooling water, air, or steam flowing through four parallel passes. For the highest cooling i.e., when the heat shield temperature had to be near 300°K, cooling water could flow through all cooling coils, while the lowest desired heat transfer coolant could flow only through one of the parallel cooling coils. This design was effectively a variable thermal resistance design in which the resistance could be varied simply by valving the coolant flow. This can be seen from the electrical analogy shown in Figure 106. The final design of the rotary radiation heat transfer joint is shown in Figure 107.

6.3 FABRICATION

In Figure 108, the inner part of the rotary radiation heat transfer joint is shown with the cooling coils and the one layer of glass tape which is holding the cooling coils in place prior to the placement of the inner insulation sleeve as shown in Figure 109. Four layers of 3/8-inch thick Flex Min-K insulation was placed over the inner insulation sleeve as shown in Figure 110. Additional layers of 1/2-inch thick Cera-Felt (Figure 111) completed the entire insulation prior to the placing of the outer insulation sleeve over the joint.

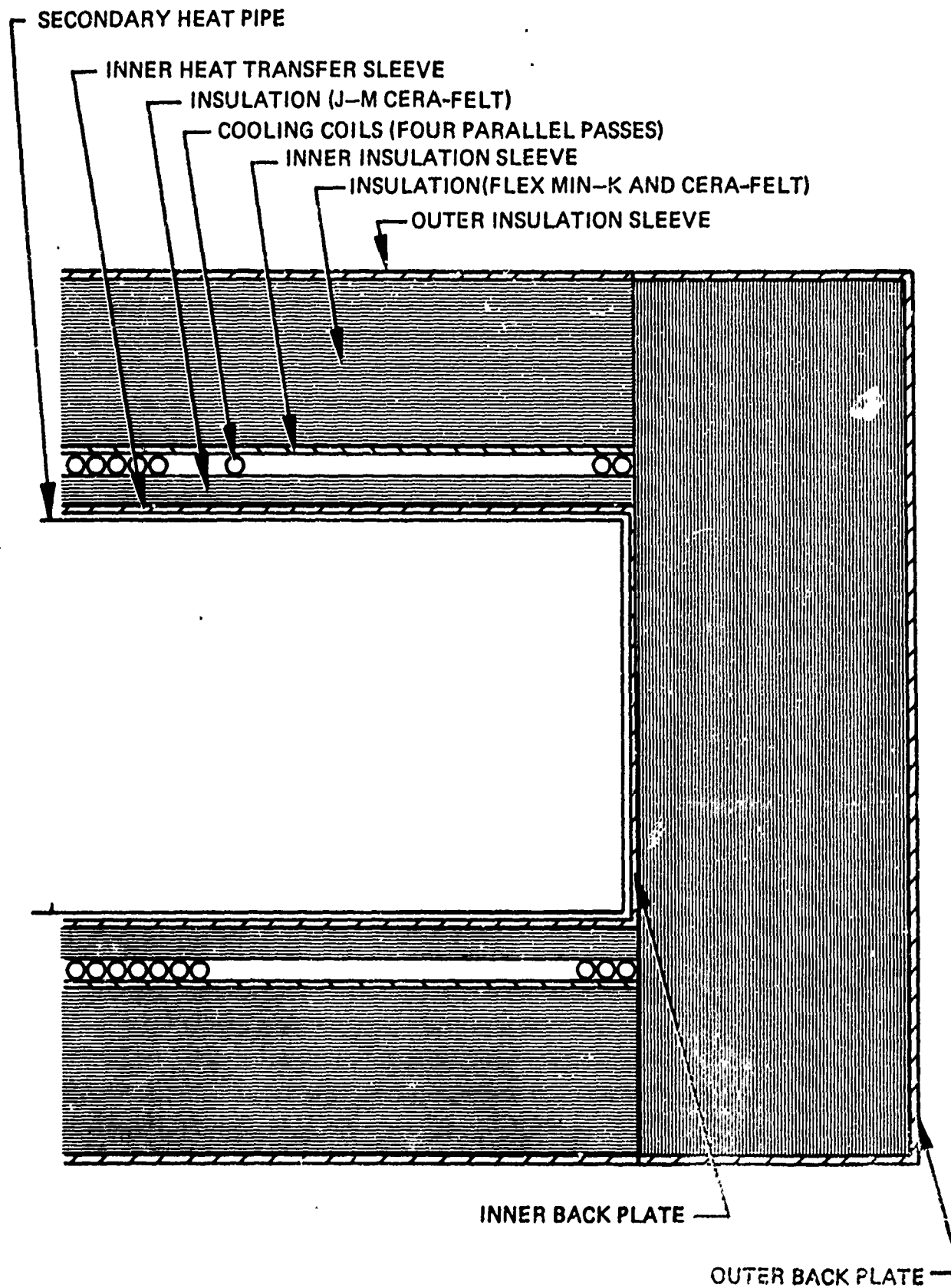


Figure 104. Full Scale Rotary Heat Transfer Joint

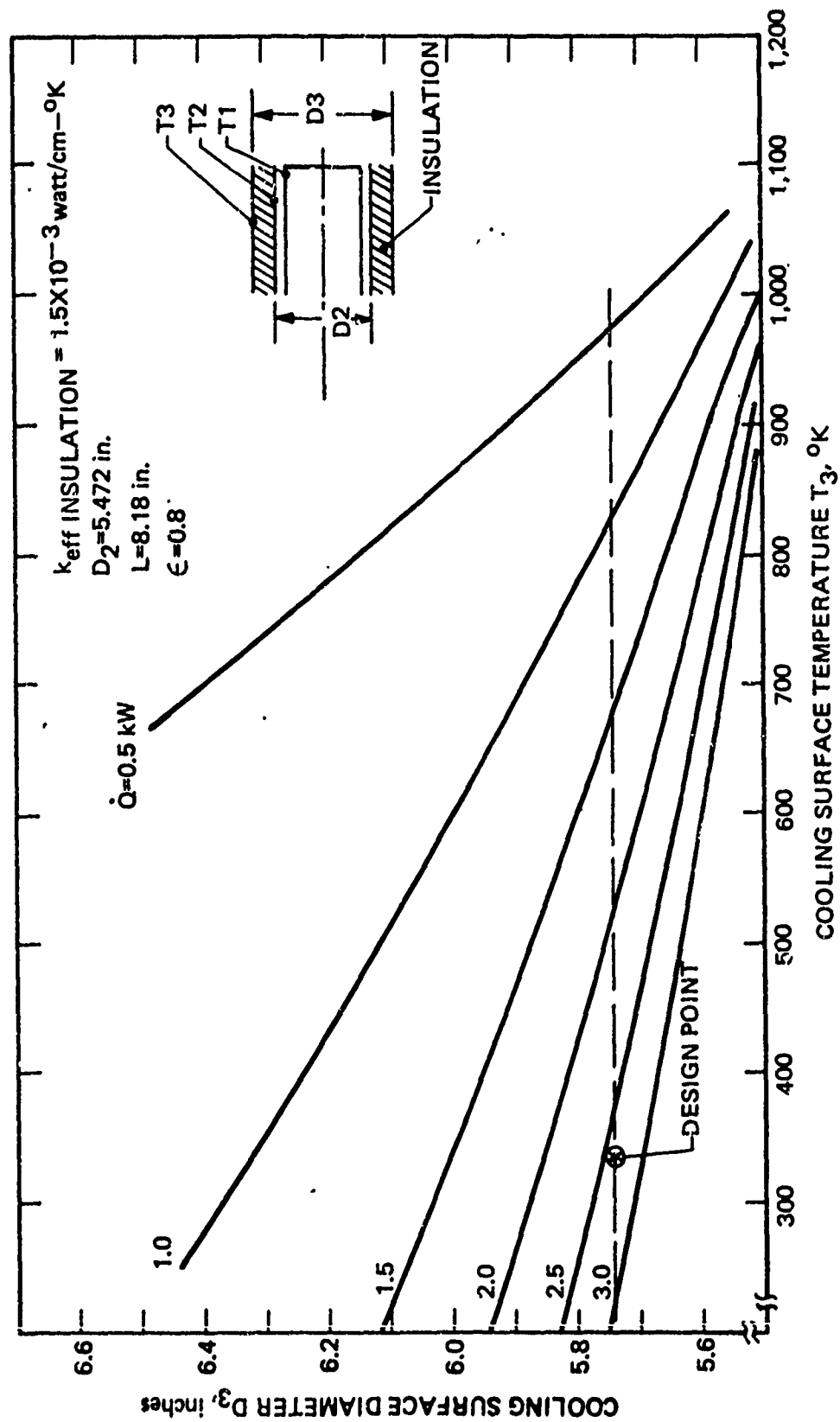
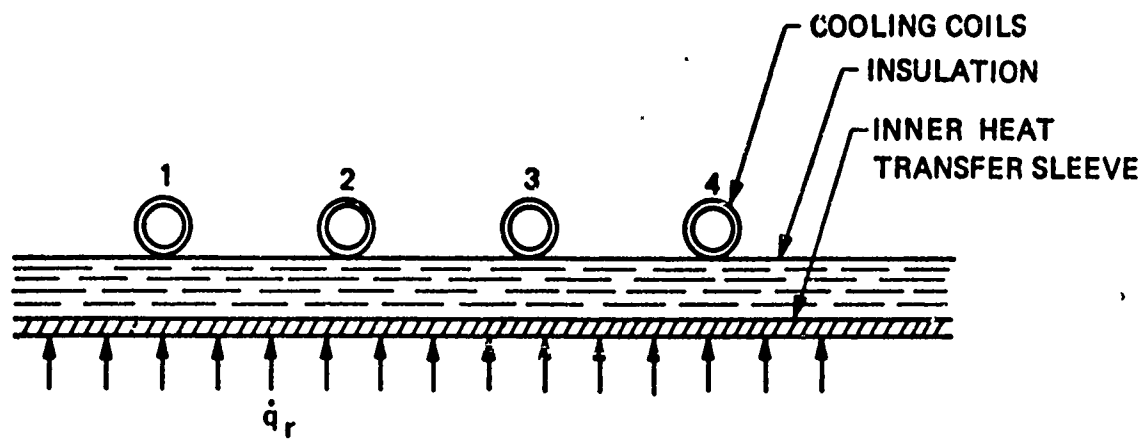
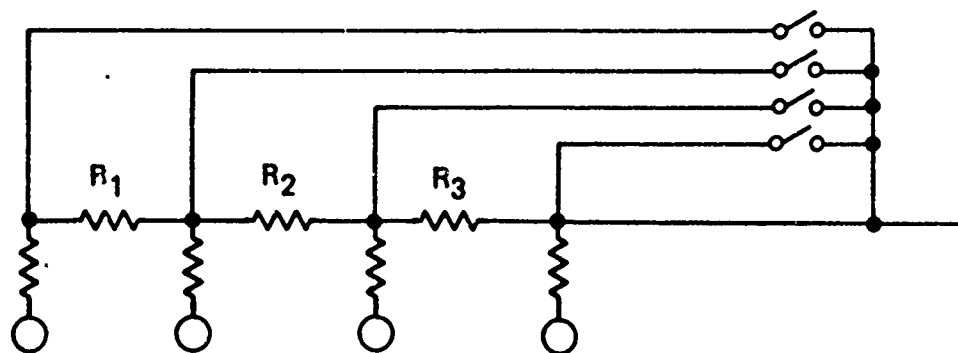


Figure 105. Design Correlation for Rotary Radiation Heat Transfer Joint

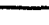


POWER REMOVAL SCHEME WITH FOUR PARALLEL CIRCUITS



ELECTRICAL ANALOG OF PARALLEL COOLING CIRCUIT ARRANGEMENT

Figure 106. Design Concept of Full Scale Rotary Radiation Heat Transfer Joint



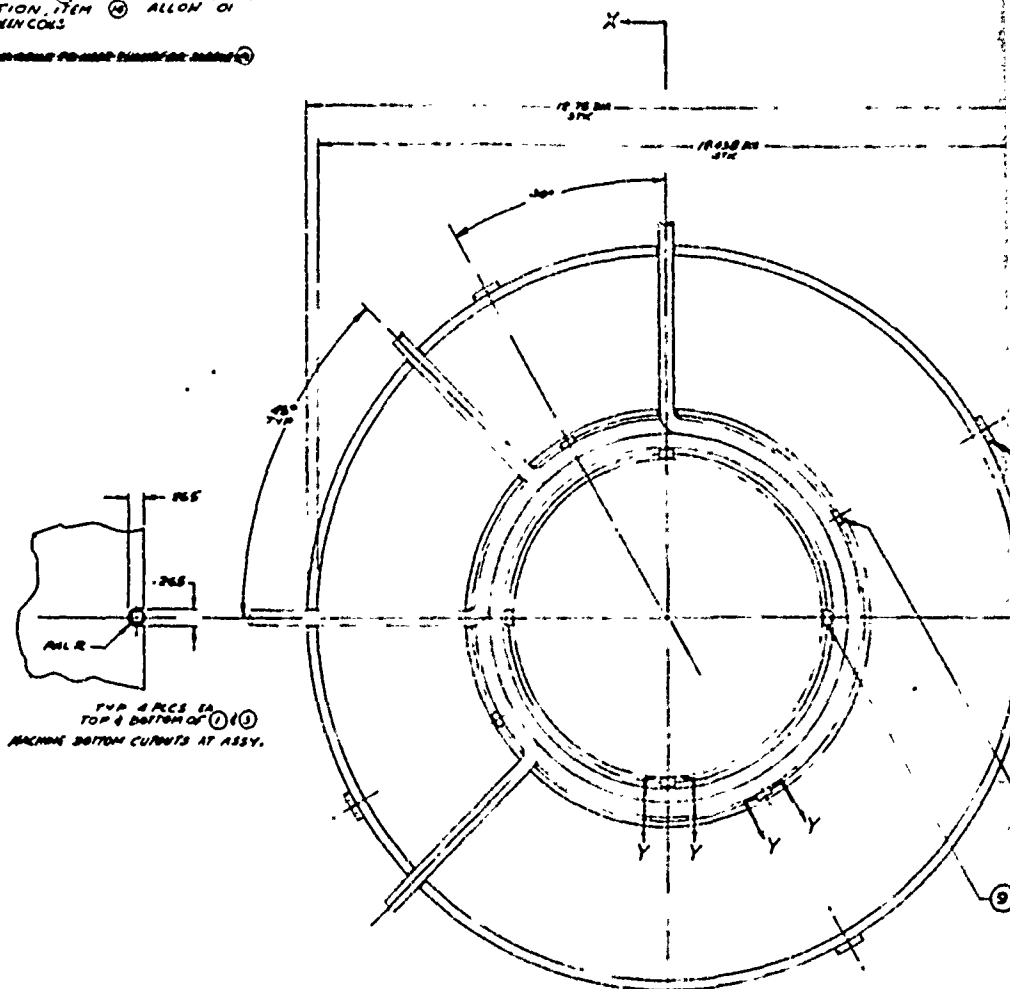
1 REMOVE ALL BURRS & SHARP EDGES

△ FIG WELD PER MH-N-8611

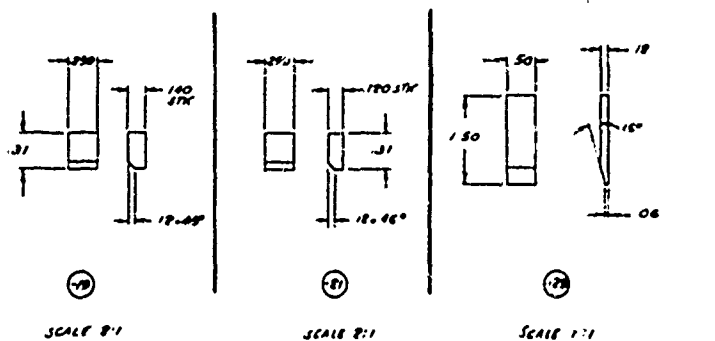
⚠ PLACE LOCATORS (B) APPROX 90° APART

④ LEAD FOUR (4) PARALLEL TRACKS OF COOLING COIL ⑬ AROUND J-MCGRAFELT INSULATION. ITEM ⑭ ALLOW ON GAP BETWEEN COILS

⚠️ WARNING: AUTOMATIC FIREARM FINGER-PROOF SAFETY ⚠️



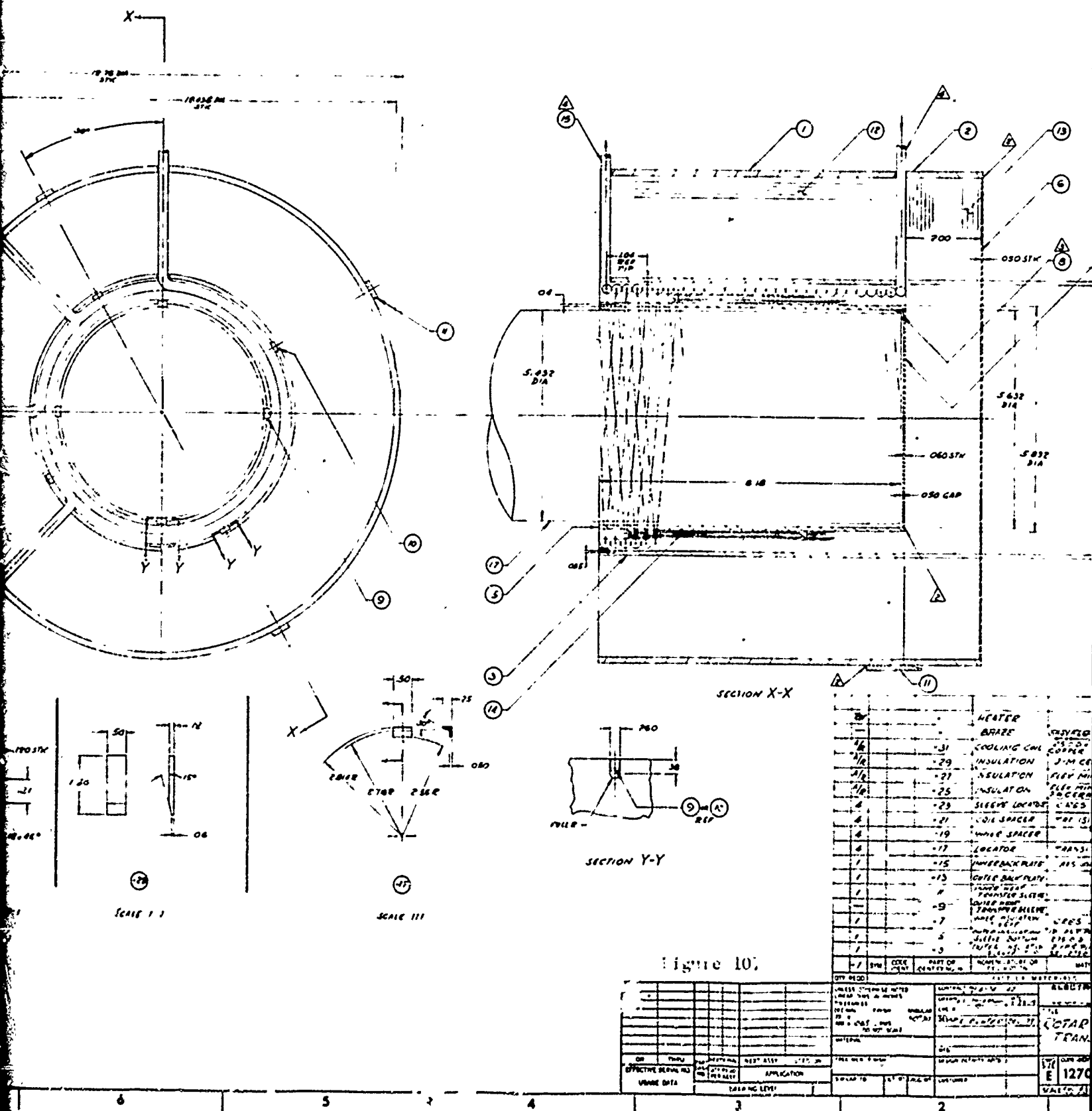
TOP 4 PCS EA
TOP 4 BOTTOM OF ① & ③
MEASURE BOTTOM CURVATURE AT ASSY.



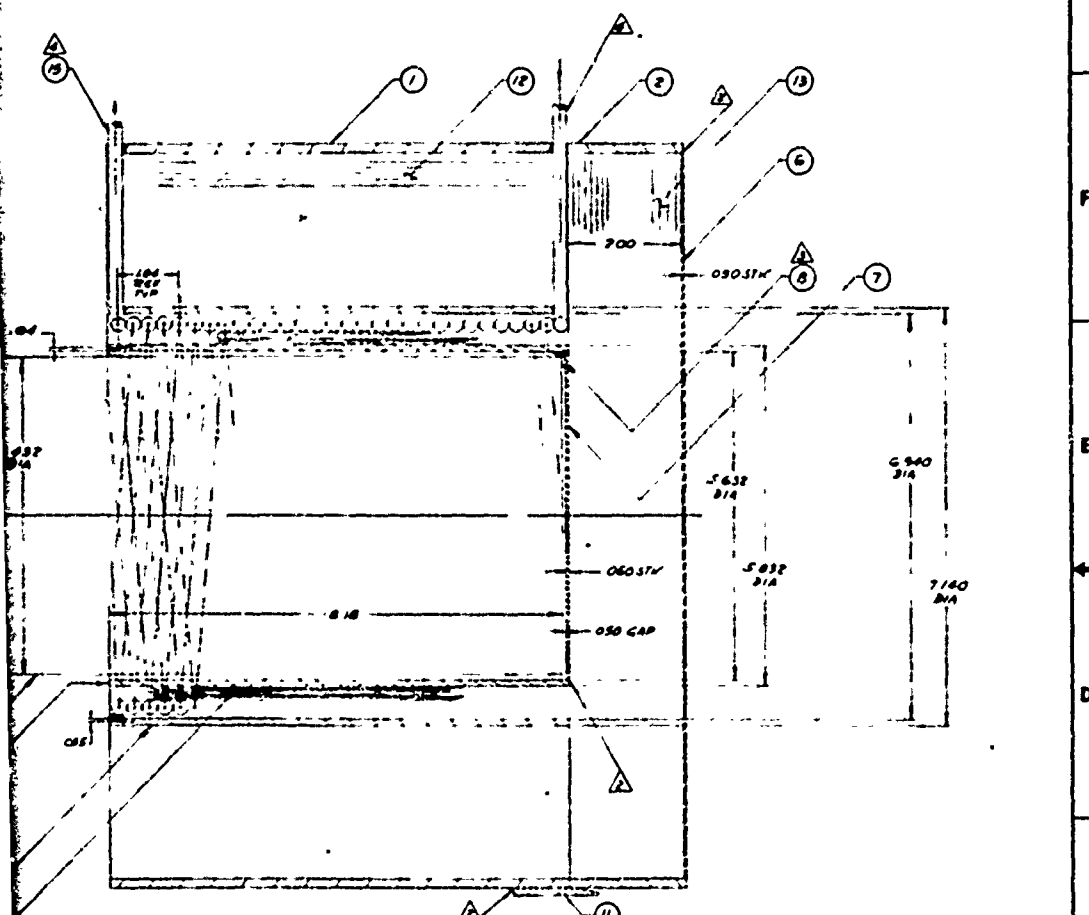
SCALE 8.1

SCALE 2:1

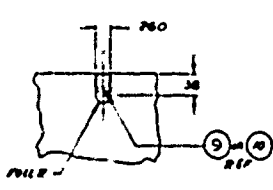
SCALE 1-5



4	3	2	1
REVISIONS			
NO.	DESCRIPTION	DATE	APPROVED
1	REVISED PER 10-10-65		
2	REVISED PER 10-10-65		
3	REVISED PER 10-10-65		



SECTION X-X



SECTION Y-Y

QTY	DESCRIPTION	UNIT	QTY
1	HEATER		16
1	BRACE		17
1	COOLING COIL		18
1	INSULATION		19
1	INSULATION		20
1	INSULATION		21
1	INSULATION		22
1	INSULATION		23
1	INSULATION		24
1	INSULATION		25
1	INSULATION		26
1	INSULATION		27
1	INSULATION		28
1	INSULATION		29
1	INSULATION		30
1	INSULATION		31
1	INSULATION		32
1	INSULATION		33
1	INSULATION		34
1	INSULATION		35
1	INSULATION		36
1	INSULATION		37
1	INSULATION		38
1	INSULATION		39
1	INSULATION		40
1	INSULATION		41
1	INSULATION		42
1	INSULATION		43
1	INSULATION		44
1	INSULATION		45
1	INSULATION		46
1	INSULATION		47
1	INSULATION		48
1	INSULATION		49
1	INSULATION		50
1	INSULATION		51
1	INSULATION		52
1	INSULATION		53
1	INSULATION		54
1	INSULATION		55
1	INSULATION		56
1	INSULATION		57
1	INSULATION		58
1	INSULATION		59
1	INSULATION		60
1	INSULATION		61
1	INSULATION		62
1	INSULATION		63
1	INSULATION		64
1	INSULATION		65
1	INSULATION		66
1	INSULATION		67
1	INSULATION		68
1	INSULATION		69
1	INSULATION		70
1	INSULATION		71
1	INSULATION		72
1	INSULATION		73
1	INSULATION		74
1	INSULATION		75
1	INSULATION		76
1	INSULATION		77
1	INSULATION		78
1	INSULATION		79
1	INSULATION		80
1	INSULATION		81
1	INSULATION		82
1	INSULATION		83
1	INSULATION		84
1	INSULATION		85
1	INSULATION		86
1	INSULATION		87
1	INSULATION		88
1	INSULATION		89
1	INSULATION		90
1	INSULATION		91
1	INSULATION		92
1	INSULATION		93
1	INSULATION		94
1	INSULATION		95
1	INSULATION		96
1	INSULATION		97
1	INSULATION		98
1	INSULATION		99
1	INSULATION		100

Figure 107

QTY	DESCRIPTION	UNIT	QTY
1	HEATER		16
1	BRACE		17
1	COOLING COIL		18
1	INSULATION		19
1	INSULATION		20
1	INSULATION		21
1	INSULATION		22
1	INSULATION		23
1	INSULATION		24
1	INSULATION		25
1	INSULATION		26
1	INSULATION		27
1	INSULATION		28
1	INSULATION		29
1	INSULATION		30
1	INSULATION		31
1	INSULATION		32
1	INSULATION		33
1	INSULATION		34
1	INSULATION		35
1	INSULATION		36
1	INSULATION		37
1	INSULATION		38
1	INSULATION		39
1	INSULATION		40
1	INSULATION		41
1	INSULATION		42
1	INSULATION		43
1	INSULATION		44
1	INSULATION		45
1	INSULATION		46
1	INSULATION		47
1	INSULATION		48
1	INSULATION		49
1	INSULATION		50
1	INSULATION		51
1	INSULATION		52
1	INSULATION		53
1	INSULATION		54
1	INSULATION		55
1	INSULATION		56
1	INSULATION		57
1	INSULATION		58
1	INSULATION		59
1	INSULATION		60
1	INSULATION		61
1	INSULATION		62
1	INSULATION		63
1	INSULATION		64
1	INSULATION		65
1	INSULATION		66
1	INSULATION		67
1	INSULATION		68
1	INSULATION		69
1	INSULATION		70
1	INSULATION		71
1	INSULATION		72
1	INSULATION		73
1	INSULATION		74
1	INSULATION		75
1	INSULATION		76
1	INSULATION		77
1	INSULATION		78
1	INSULATION		79
1	INSULATION		80
1	INSULATION		81
1	INSULATION		82
1	INSULATION		83
1	INSULATION		84
1	INSULATION		85
1	INSULATION		86
1	INSULATION		87
1	INSULATION		88
1	INSULATION		89
1	INSULATION		90
1	INSULATION		91
1	INSULATION		92
1	INSULATION		93
1	INSULATION		94
1	INSULATION		95
1	INSULATION		96
1	INSULATION		97
1	INSULATION		98
1	INSULATION		99
1	INSULATION		100

Reproduced from best available copy.

006717



Figure 108. Rotary Radiation Heat Transfer Joint with Cooling Coils under Glass Tape



Figure 109. Rotary Radiation Heat Transfer Joint with Inner Insulation Sleeve over Cooling Coils

006713



Figure 110. Rotary Radiation Heat Transfer Joint with Four Layers 3/8-inch Thick Flex Min-K Insulation over Inner Insulation Sleeve



Figure 111. Rotary Radiation Heat Transfer Joint with Final Layers of 1/2-inch Thick Cera-Felt Insulation

In Figures 112 and 113, the completed radiation heat transfer joint is shown with the end cap. The fully assembled radiation heat transfer joint is presented in Figure 114. Figure 115 shows the rotating radiation heat transfer joint installed over the condenser section of the secondary heat pipe with the coolant hook-up completed, while in Figure 116, the rotating radiation heat transfer joint is shown with the instrumentation for measuring the coolant flow through the cooling coils.

With the rotating radiation heat transfer joint installed on the secondary heat pipe, the steady state tests for the secondary heat pipe were repeated in Section VIII. The heat losses did not appreciably increase with the rotating radiation heat transfer joint. At the operating temperature of 1558°F, the losses were 780 watts compared to 705.5 watts without the joint.

The testing of the radiation heat transfer joint is reported together with the testing of the secondary heat pipe (Section 7.5 of this volume) and the thermal train (Section IV of Volume II).

6.4 OPERATION

The more appropriate way of cooling proved to be the use of water at very low flow rates. The injected water was permitted to evaporate in the cooling tubes and to exhaust as steam at the temperature of the cooling tubes. This scheme had several advantages. For the determination of the cooling rate only two values had to be measured, the water flow rate and the cooling coil temperature at the exits. The temperature had to be measured only within $\pm 10^\circ\text{F}$ to obtain an accuracy of better than 0.5 percent. This is indicated by the data plotted in Figure 117. At a coil temperature of 800°F the enthalpy increase of the water is 3241 joules/g, while 810°F the enthalpy increase is 3252 joules/g. Thus, with a variation of 10°F the enthalpy of the water increases only by 0.33 percent. The water flow rate was measured with a calibrated sharp orifice. The calibration of the nominal 0.010-inch orifice is shown in Figure 118.

The pressure differential across the orifice was measured either with a differential mercury manometer or with two 1/4 percent pressure gages depending on the flow rate. The tests conducted with this test setup and the data are presented in the section on the secondary heat pipe. As a typical sample, a manometer pressure differential of 21 inches of mercury was measured across the orifice. This corresponded to a pressure differential of 10.31 psi. From the calibration of the orifice the water flow rate was $\dot{W}_w = 0.48$ grams/sec. The temperature of the cooling coil at the exit was measured to be $T = 763^\circ\text{F}$. From Figure 117 the enthalpy increase of the water was found to be $\Delta H = 3200$ joules/g. Thus, the power extracted by the water was 1536 watts. This agreed quite closely with the power extraction calculated from the cooling

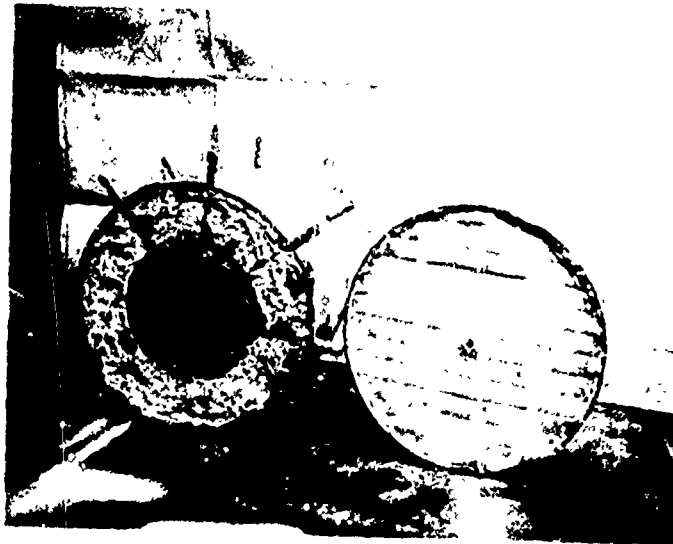


Figure 112. Rotary Radiation Heat Transfer Joint with Insulation Shown

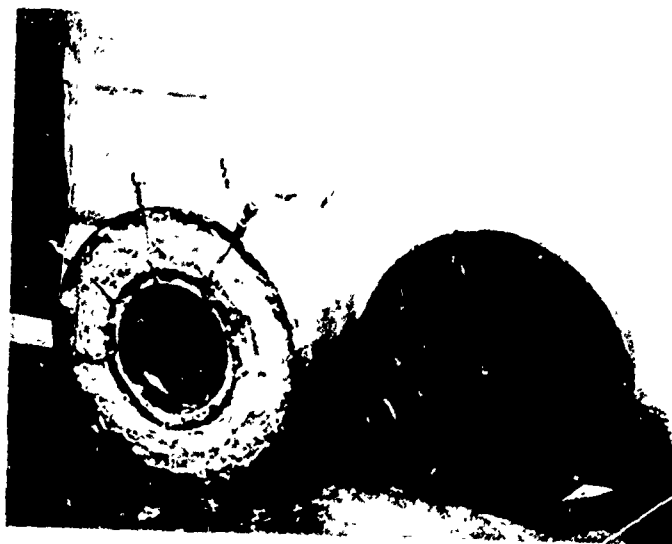


Figure 113. Rotary Radiation Joint (cylindrical section and end section)

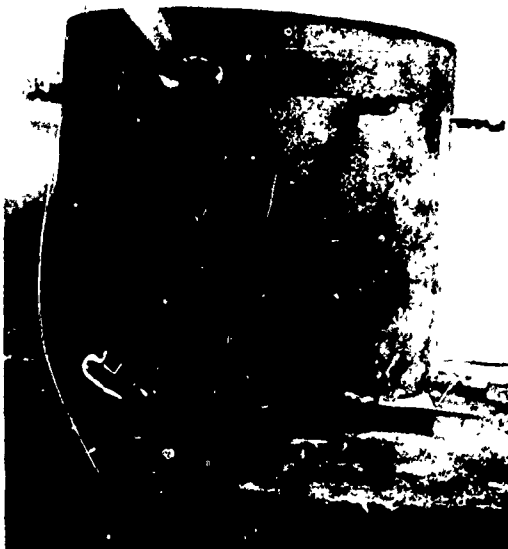


Figure 114. Rotary Radiation Heat Transfer
Joint Fully Assembled

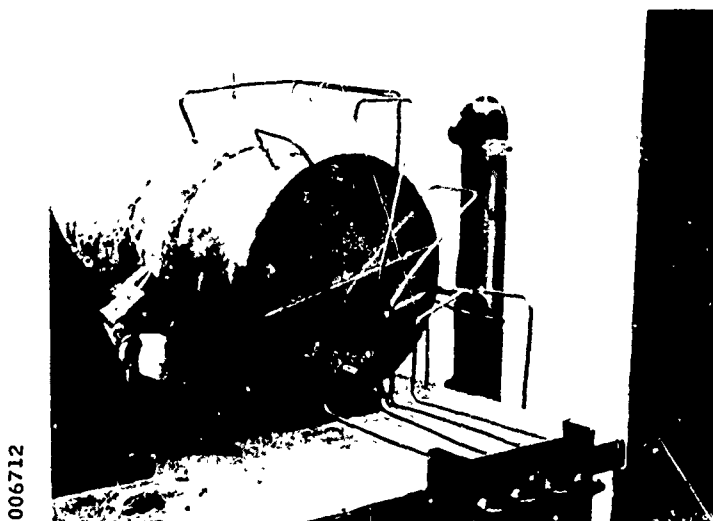


Figure 115. Rotary Radiation Heat Transfer
Joint Installed

006720

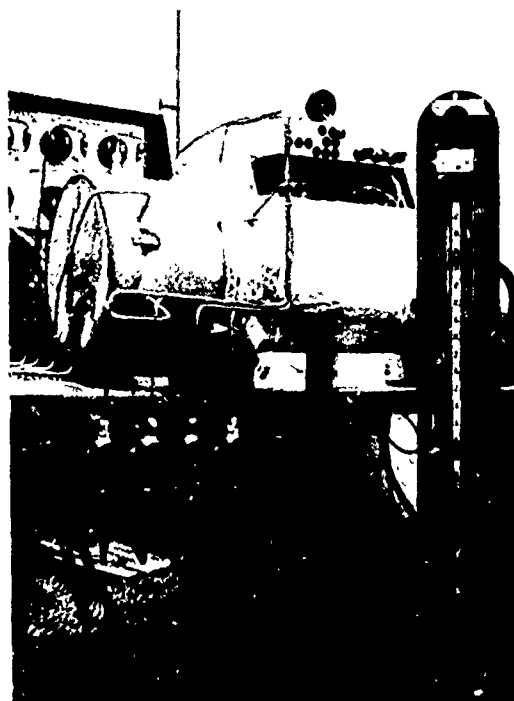


Figure 116. Test Setup of Rotary Radiation
Heat Transfer Joint

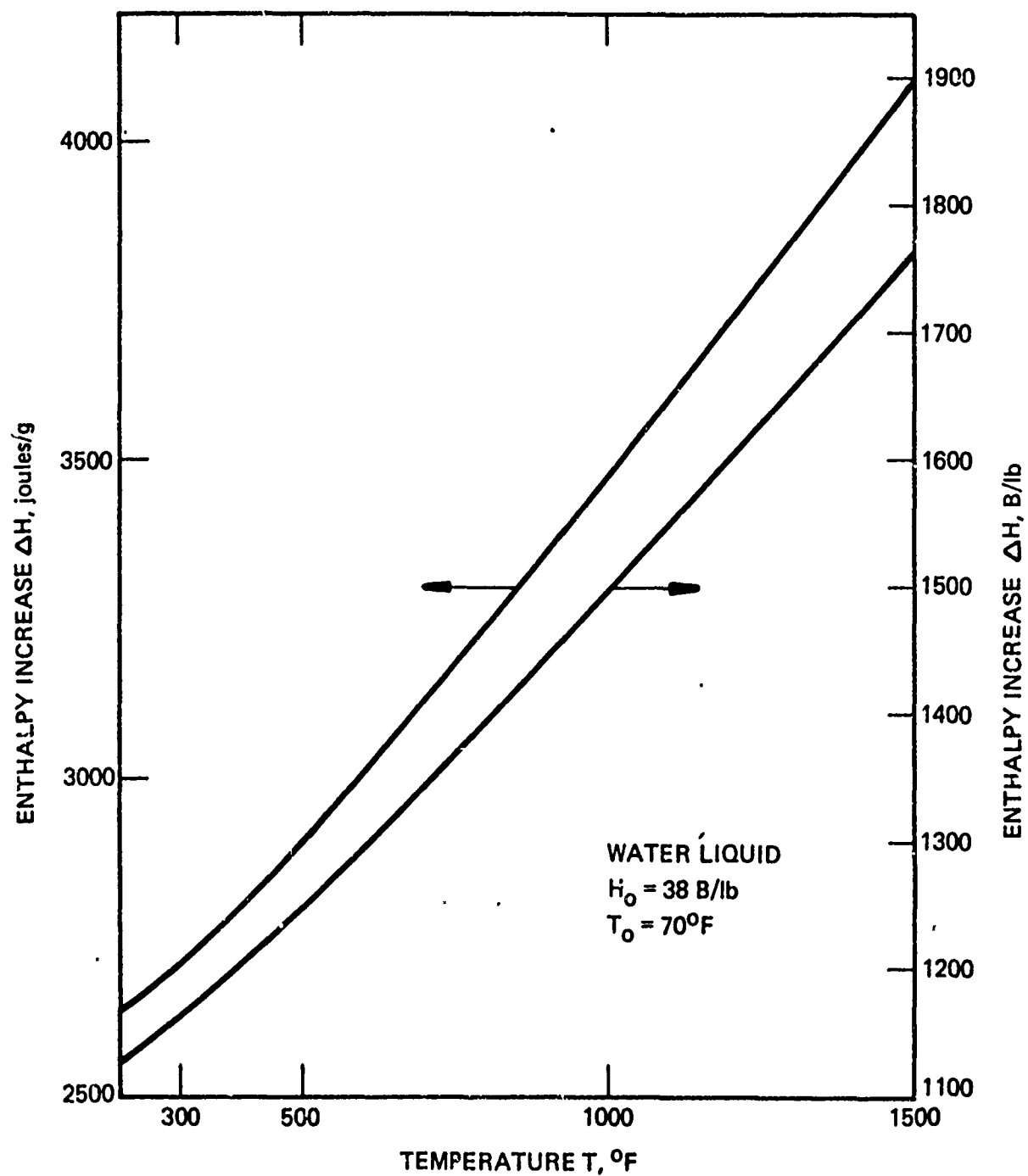


Figure 117. Enthalpy Increase of Water Due to Evaporation and Superheating

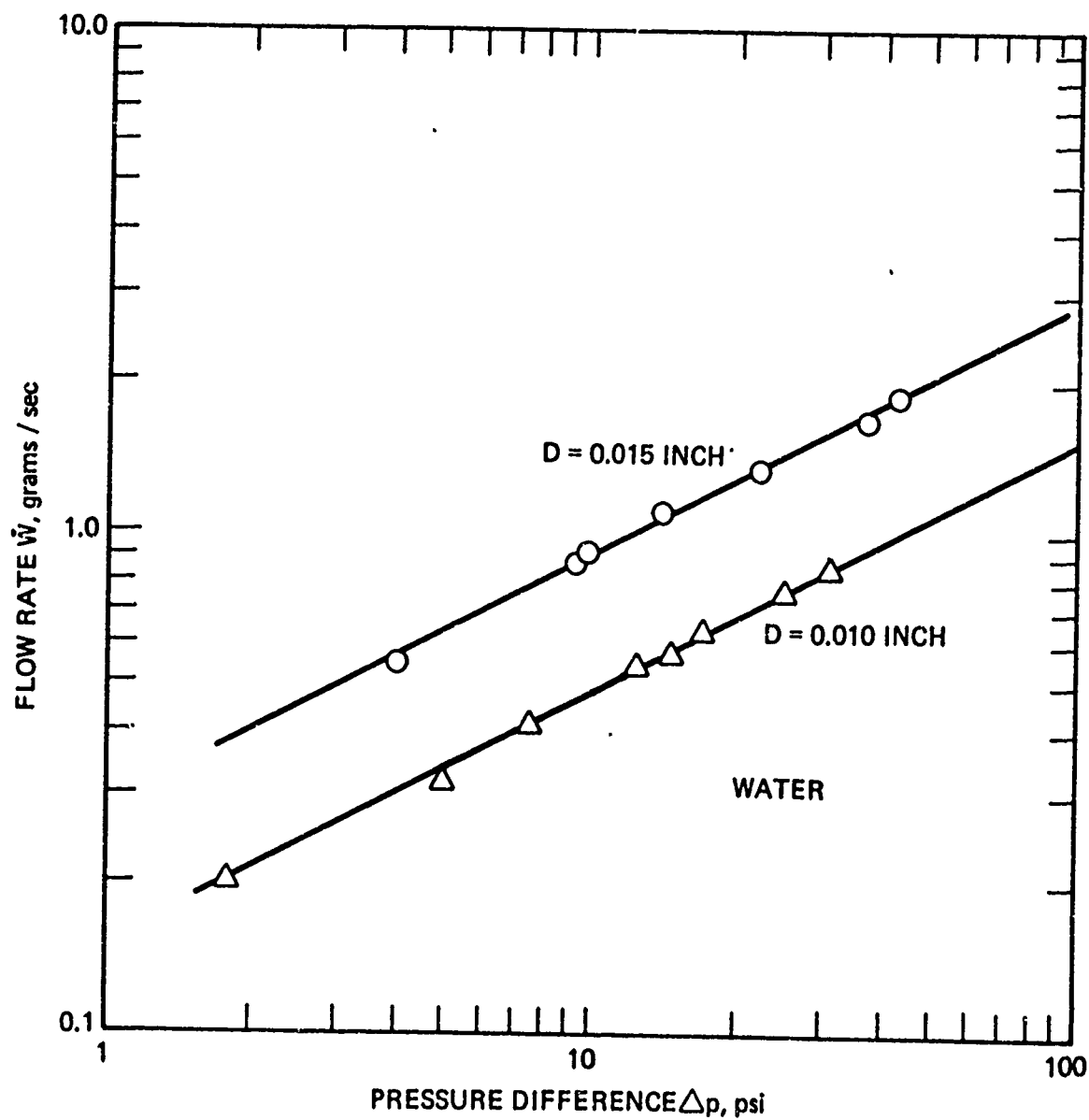


Figure 118. Flow Calibration for Two Orifices (Water)

rate of the heat pipe after freezing of 1500 watts.

6.5 CONCLUSION

The rotary radiation heat transfer joint seemed to perform according to design. The rate of heat transfer appeared to be fully adjustable continuously by solely varying the water flow rate through the cooling coils. The test results, as they are reported under the sections dealing with the testing of the secondary heat pipe with full scale thermal energy storage unit and the testing of the integrated thermal train, proved the capability of the rotary heat transfer joint to transfer the desired amount of thermal power across a joint while maintaining the temperature of the condenser section at the operating temperature of the heat pipe.

SECTION VII

FULL SCALE SECONDARY HEAT PIPE WITH THERMAL ENERGY STORAGE UNIT

7.1 INTRODUCTION

A full scale secondary heat pipe with a full scale thermal energy storage unit was designed and fabricated which can provide three kilowatts of thermal power continuously in a simulated low-earth orbit of 65-minute solar illumination and 35-minute eclipse time. The system was designed to permit its integration with the primary heat pipe described in Section of Volume II of this report.

The completed secondary heat pipe with the thermal energy storage system is shown in Figure 119. Its design is based on the analytical evaluation of the heat pipe study presented in Section III and the experimental results presented in Section VI of this Volume.

7.2 SECONDARY HEAT PIPE AND THERMAL ENERGY STORAGE DESIGN

Figure 120 shows the assembly drawing of the secondary heat pipe with the 3-kW thermal energy storage system.

In Table XXIII all pertinent properties of the materials used in design are tabulated with references to their origin.

The required thermal energy storage capacity for delivering 3 kW for 35 minutes is 6.3×10^6 joules. Allowing 10 percent excess storage salt, the required quantity of lithium fluoride is 6638g (14.63 lb). The LiF is in 27 separate cartridges containing 245.8g each.

The internal cartridge volume was dimensioned to allow a 10 percent void volume when the LiF is in the liquid state at the melting point. The total required volume was thus 256.8 cu. in. or 9.5 cu. in. for each cartridge. The cartridge dimensions were selected for placing the cartridges into the available annular space of the secondary heat pipe while maintaining their diameter between 1.0 and 1.25 inches. The test results reported in Section VI showed reasonably low cyclic temperature variation with cartridge diameters in this range.

The wicking was made of 70 mesh Inconel 600 wire cloth with 0.0065-inch diameter wire. Four layers (0.050-inch thick) were placed over the inner tube and cartridges and eight layers (0.10-inch thick) on the inside diameter of the outer tube. This wicking arrangement is similar to that given in the analytical design study presented in Section III. The maximum suction pressure that can be developed by the wick is calculated to be 2.4×10^4 dyne/cm². This is more than twice the suction required

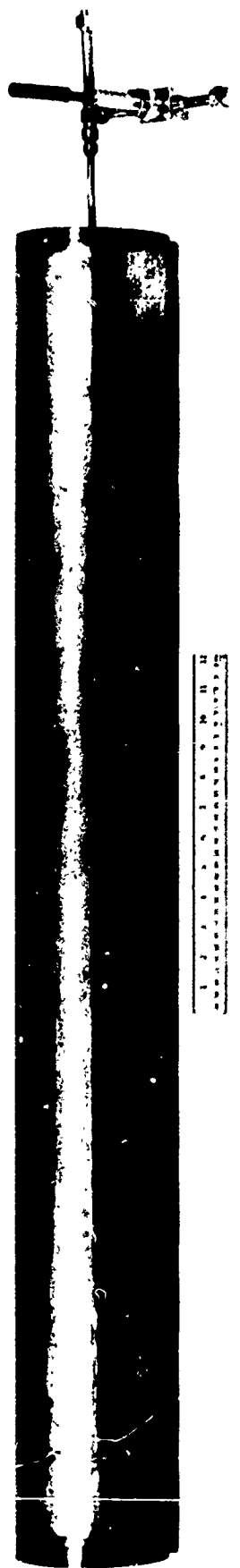
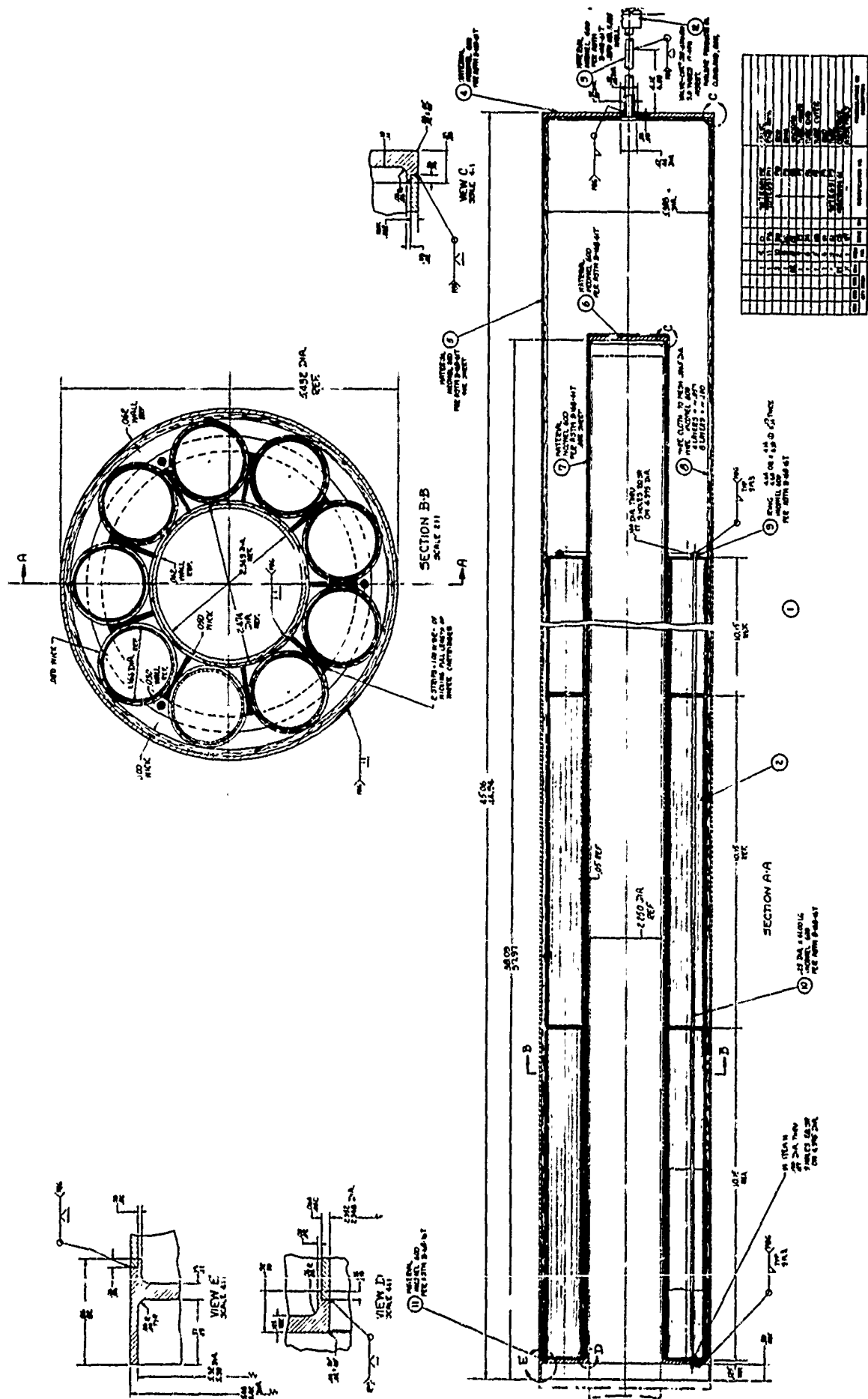


Figure 119. Completed Assembly Filled with Sodium and Sealed

006572



1. HEAT PIPE
2. HEAT PIPE
3. HEAT PIPE
4. HEAT PIPE
5. HEAT PIPE
6. HEAT PIPE
7. HEAT PIPE
8. HEAT PIPE
9. HEAT PIPE
10. HEAT PIPE
11. HEAT PIPE
12. HEAT PIPE
13. HEAT PIPE
14. HEAT PIPE
15. HEAT PIPE
16. HEAT PIPE
17. HEAT PIPE
18. HEAT PIPE
19. HEAT PIPE
20. HEAT PIPE
21. HEAT PIPE
22. HEAT PIPE
23. HEAT PIPE
24. HEAT PIPE
25. HEAT PIPE
26. HEAT PIPE
27. HEAT PIPE
28. HEAT PIPE
29. HEAT PIPE
30. HEAT PIPE
31. HEAT PIPE
32. HEAT PIPE
33. HEAT PIPE
34. HEAT PIPE
35. HEAT PIPE
36. HEAT PIPE
37. HEAT PIPE
38. HEAT PIPE
39. HEAT PIPE
40. HEAT PIPE
41. HEAT PIPE
42. HEAT PIPE
43. HEAT PIPE
44. HEAT PIPE
45. HEAT PIPE
46. HEAT PIPE
47. HEAT PIPE
48. HEAT PIPE
49. HEAT PIPE
50. HEAT PIPE
51. HEAT PIPE
52. HEAT PIPE
53. HEAT PIPE
54. HEAT PIPE
55. HEAT PIPE
56. HEAT PIPE
57. HEAT PIPE
58. HEAT PIPE
59. HEAT PIPE
60. HEAT PIPE
61. HEAT PIPE
62. HEAT PIPE
63. HEAT PIPE
64. HEAT PIPE
65. HEAT PIPE
66. HEAT PIPE
67. HEAT PIPE
68. HEAT PIPE
69. HEAT PIPE
70. HEAT PIPE
71. HEAT PIPE
72. HEAT PIPE
73. HEAT PIPE
74. HEAT PIPE
75. HEAT PIPE
76. HEAT PIPE
77. HEAT PIPE
78. HEAT PIPE
79. HEAT PIPE
80. HEAT PIPE
81. HEAT PIPE
82. HEAT PIPE
83. HEAT PIPE
84. HEAT PIPE
85. HEAT PIPE
86. HEAT PIPE
87. HEAT PIPE
88. HEAT PIPE
89. HEAT PIPE
90. HEAT PIPE
91. HEAT PIPE
92. HEAT PIPE
93. HEAT PIPE
94. HEAT PIPE
95. HEAT PIPE
96. HEAT PIPE
97. HEAT PIPE
98. HEAT PIPE
99. HEAT PIPE
100. HEAT PIPE

Figure 120. Secondary Heat Pipe With 3 kW Thermal Energy Storage Systems

for overcoming the maximum gravity head resulting from the diameter of the secondary heat pipe. Because of the large flow area, the pressure drop associated with the flow of the working fluid through the wick is quite small compared to the suction pressure required to overcome the gravitational effect.

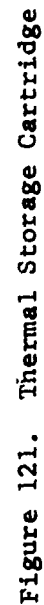
TABLE XXIII
MATERIALS, THERMOPHYSICAL PROPERTIES
FOR 3 kW HP/TES DESIGN

<u>Material</u>	<u>Property</u>	<u>Value</u>	<u>Reference</u>
LiF	Heat of Fusion	1044 j/gm	26
LiF	Liquid Density (1558°F)	1.735 gm/cc	21
Sodium	Heat of Vaporization (1558°F)	1680 BTU/lb	27
Sodium	Vapor Density (1558°F)	0.0120 lb/ft ³	27
Sodium	Liquid Density (1558°F)	0.746 gm/cc	28
Sodium	Liquid Density (600°F)	0.876 gm/cc	28
Sodium	Surface Tension (1558°F)	117 dyne/cm	29
Sodium	Liquid Viscosity (1558°F)	0.38 lb/ft-hr	27
Inconel 600	Density (70°F)	0.3-4 lb/in ³	30
Wicking	Weight Per Area	0.227 lb/ft ²	31

7.3 FABRICATION

7.3.1 CARTRIDGE FABRICATION

The thermal storage cartridges were similar to those previously fabricated and tested in the subscale tests reported in Section VI. The cartridge drawing is shown in Figure 121. A cartridge was fabricated by rolling a Cb-1Zr sheet to the proper diameter, and then welding the seam with the automatic GTA welding equipment of General Electric Company in Evandale, Ohio. (Figure 122). Seamless tubing would have been preferable for the cartridge wall, but procurement of this special size tube was not felt necessary. The tube (P3, Figure 121) was then welded to the end cap (P4). All GTA welding on Cb-1Zr was performed in a vacuum tank under high-purity helium. The partially completed cartridge was annealed and leak checked.



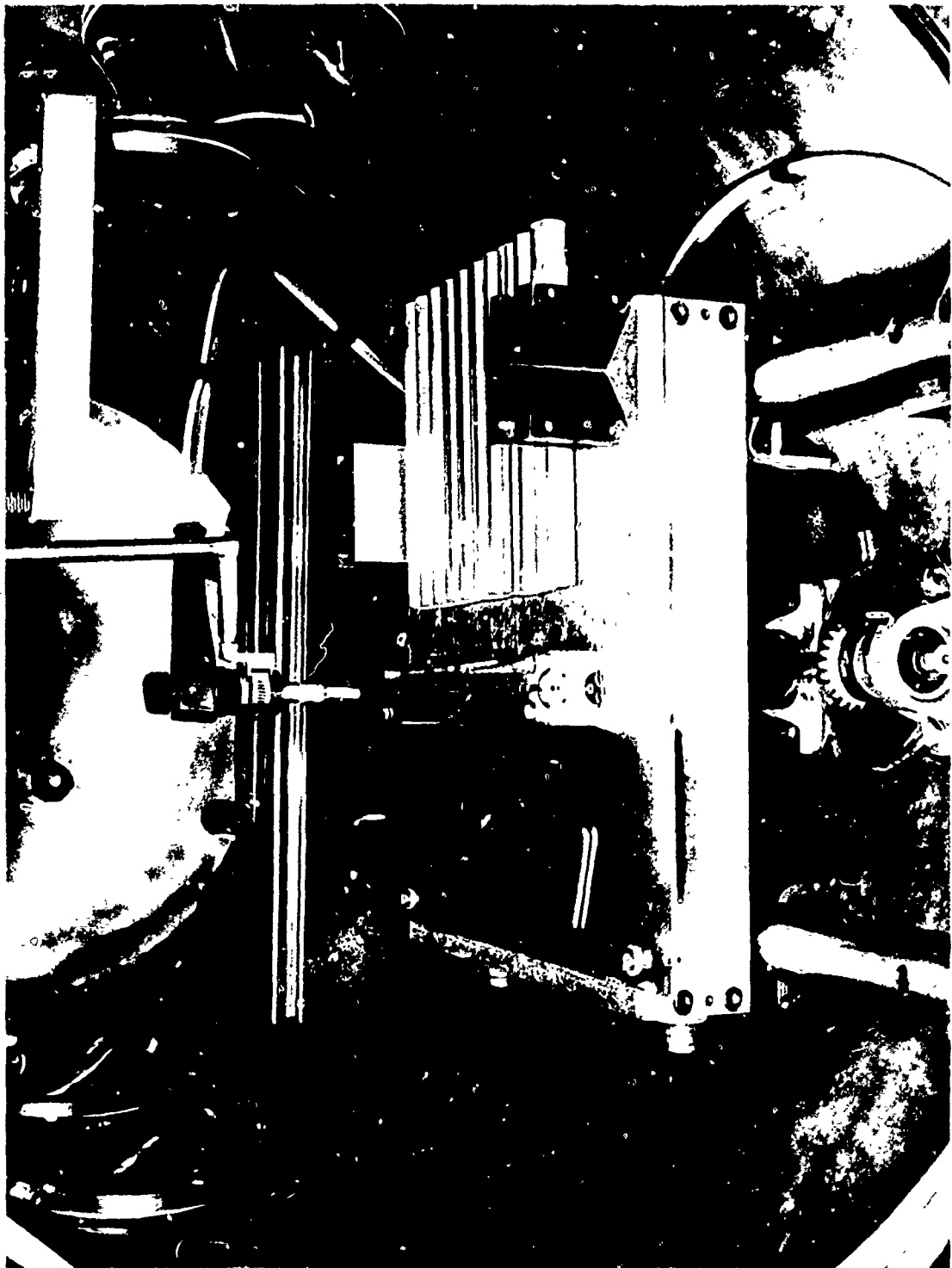


Figure 122. Automatic Welding of Cartridge Tubes

895900

The lithium fluoride of vacuum UV quality and 99.9 percent purity was procured in random cuttings. Since LiF is hygroscopic, it remained in inert gas or in vacuum. The proper quantity of LiF was heated, melted and cast into a cylindrical slug in a heated, tapered graphite mold. Melting and casting was done under vacuum. A pulley arrangement permitted raising the mold furnace slowly after melting of the LiF so that the material will freeze from the bottom up, this preventing "piping" in the casting.

The LiF slugs were then placed into the cartridge tubes and the remaining end cap (P2) was welded on. Finally, the vent hole in P2 was sealed by electron beam welding under high vacuum. The completed cartridge is shown in Figure 123. The weight of each of the 27 cartridges is tabulated in Table XXIV.

7.3.2 FINAL ASSEMBLY OF THE SECONDARY HEAT PIPE

The inner tube (P7 on Figure 120) was rolled of 0.065 inch thick Inconel 600 sheet. The main seal was welded by the automatic GTA process. The machined end parts (P6 and P11) were welded to P7. The inner tube sub-assembly (Figure 124) was leak checked in preparation for the final assembly.

All wicking was applied to the interior parts. It was carefully observed that it was in contact in the appropriate places, so that a continuous liquid flow path would exist from the condensing surface to the evaporating surface. For this reason, the assembly was built up from the inner surface (P7 on Figure 120), and all wicking was spot welded at the contact points. First, four layers of wicking were applied to the inner tube. Three layers of wicking were wound over each of the 27 cartridges. The last layer of wicking on each cartridge was spot welded first to the outer layer of wicking on the inner tube prior to placing the cartridges in position, and wrapping the outer cartridge wick layer around the cartridge and spot welding it in place.

After all cartridges were in position, the gaps between the cartridges were checked. With all dimensions correct, the circumferential gap between cartridges was 0.048 inch, which was maintained with small pads of wicking material placed between the cartridges as required. Axial movement of the cartridges was prevented by the rod and ring arrangement (P9 and P10) as shown in Figure 120. The thermal energy storage units located on the inner tube are shown in Figures 125 and 126.

After positioning of the cartridges, the outer wick layers were spot welded to the cartridge wicks. As successive outer wick layers were applied, the diameter and concentricity was checked to assure proper positioning of the outer tube (P5). Three outer wick layers were built up until the diameter was such that firm contact with the outer shell occurred. The outer shell was then positioned and clamped in place. The final seam welds and welds of P5 to P11 and P5 to P4 were made.

006570

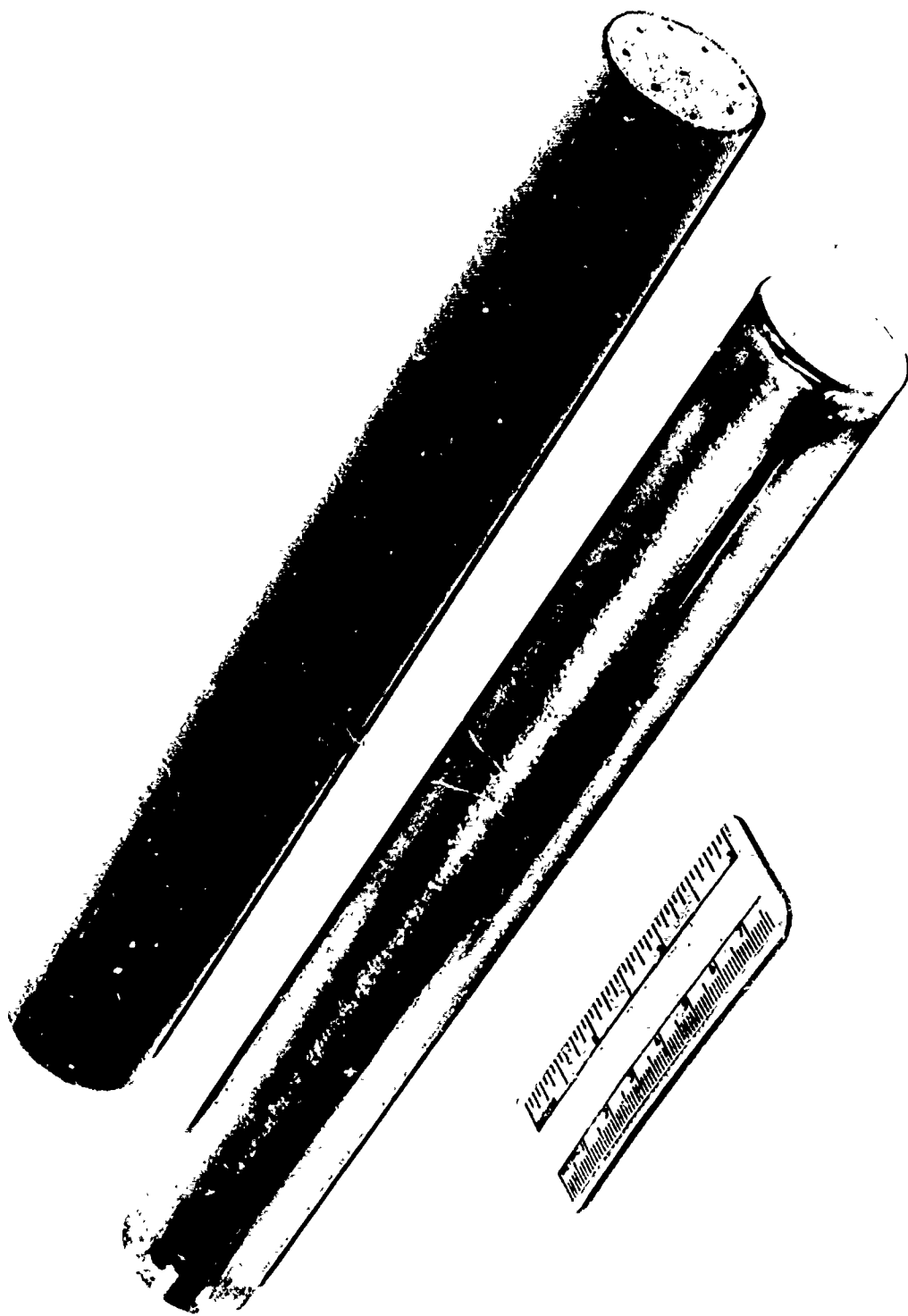


Figure 123. LiF Filled Cartridges before and after Wick Application

TABLE XXIV

CARTRIDGE WEIGHTS

<u>Cartridge No.</u>	<u>Tare</u>	<u>Lif grams</u>	<u>(No Top Cap) Unwelded, gross grams</u>	<u>Final Cartridge Weight grams</u>
1	190.8	245.8	436.6	454.0
2	186.8	246.0	432.8	450.2
3	183.9	246.0	429.9	447.1
4	188.7	245.7	434.4	452.0
5	185.0	246.0	431.0	448.8
6	186.4	245.7	432.1	449.6
7	186.3	245.9	432.7	450.1
8	184.9	245.8	430.7	448.2
9	186.6	245.9	432.5	450.0
10	192.0	245.8	437.8	455.3
11	188.7	246.0	434.7	452.3
12	190.1	246.1	436.2	453.7
13	191.2	246.0	437.2	454.7
14	183.2	245.7	428.9	446.0
15	186.7	245.8	432.5	450.0
16	190.9	245.7	436.8	454.2
17	188.5	245.9	434.4	451.9
18	187.7	245.9	433.6	451.1
19	188.1	245.8	433.9	451.3
20	180.7	245.8	426.5	443.9
21	183.8	246.0	429.8	447.2
22	188.3	245.9	434.2	451.6
23	184.6	246.1	430.7	448.5
24	191.2	245.9	437.1	454.7
25	188.4	245.8	434.2	451.8
26	190.0	245.9	435.9	453.5
27	187.3	245.9	433.2	450.6

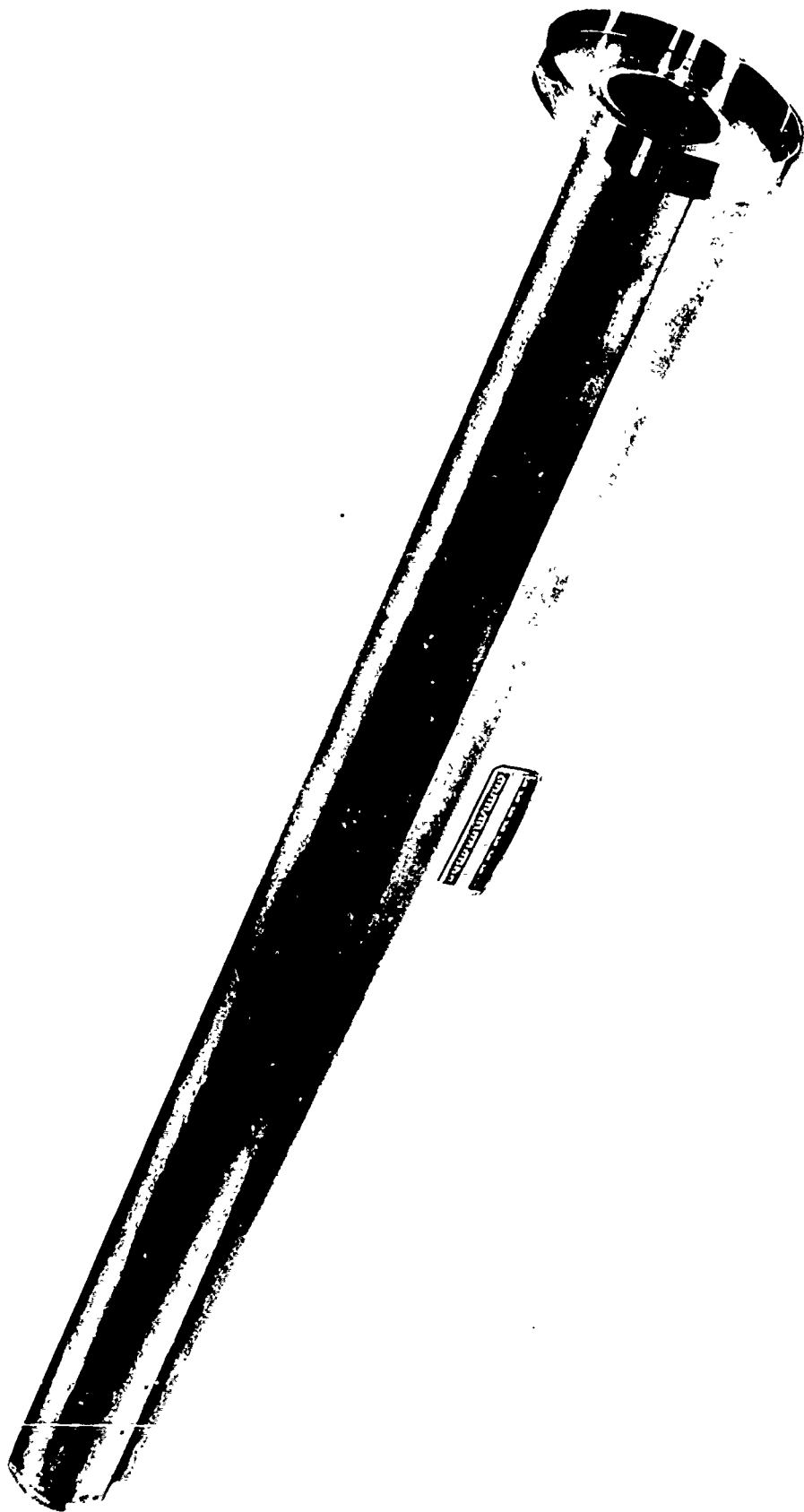


Figure 124. Inner Tube Assembly after Welding (no wicking)

006573

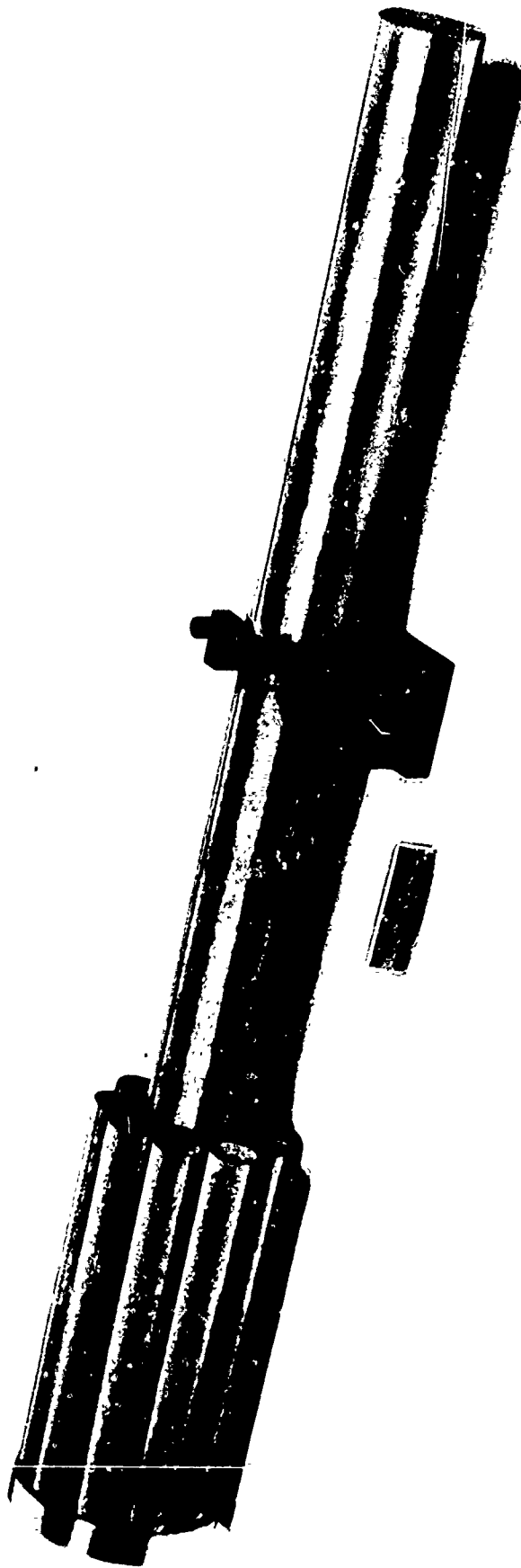


Figure 125. Inner Tube Assembly with One Cluster of Cartridges Attached

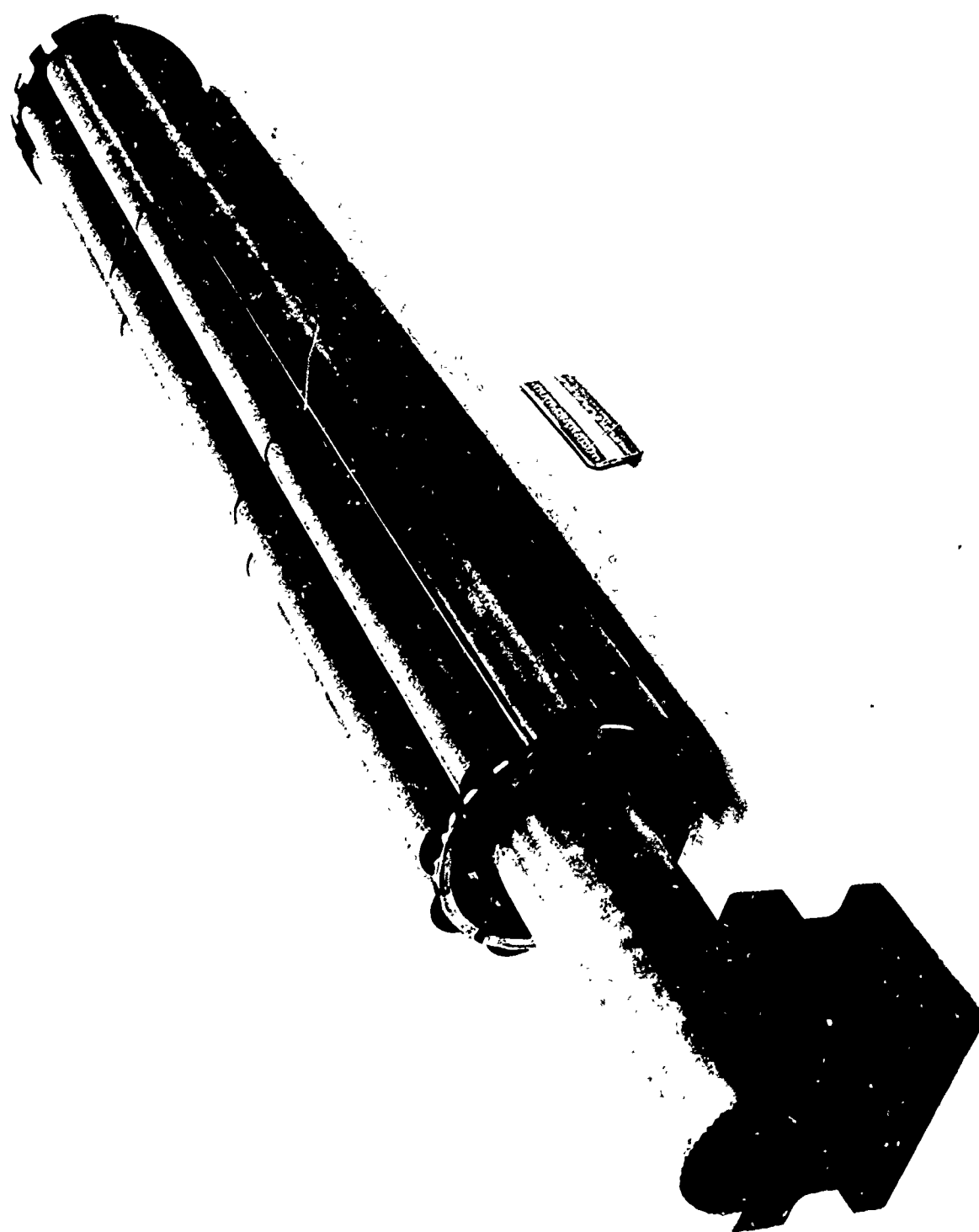


Figure 126. Completed Inner Tube Assembly. All cartridges attached.

006571

7.3.3 TOTAL SYSTEM WEIGHT

The weight of the Secondary Heat Pipe with the Thermal Energy Storage and the weight of each of the components are shown in Table XXV. In calculating the volume of the wicking and the weight of sodium, it was assumed that the screen would be packed as shown in the design drawing (Figure 120); that is, that four layers will have a thickness of 0.050 inch. The calculated void volume fraction in the wick is then 0.58. The required quantity of sodium was calculated for full saturation of the entire wick structure at 600°F, which would result in an excess of 17 percent at the operating temperature (1558°F).

TABLE XXV

THERMAL ENERGY STORAGE SYSTEM WEIGHT

<u>Material</u>	<u>Drawing</u>	<u>Item #</u>	<u>Density, lb/in³</u>	<u>Weight lb</u>
Inconel 600 Shell	707E691	3,4,5,6,7,9,10,11	0.304	22.84
Inconel 600 Wick	707E691	8	0.304	18.23
Cb-1Zr Cartridges	128C8094	2,3,4	0.303	10.80
Lithium Fluoride	128C8094	5	-	14.63
Sodium	-	-	0.0317 (600°F)	<u>2.67</u>
			Total Weight	69.17

7.4 TEST SETUP

After completion of the fabrication of the secondary heat pipe with the thermal energy storage unit by the General Electric Company, the unit was transferred for testing to Xerox/Electro-Optical Systems, Pasadena, California.

For the testing of the secondary heat pipe, a heater was required which could deliver approximately 8 kW of power to the inside of the secondary heat pipe at a heat pipe operating temperature of 1600°F. The design for such a heater envisioned the use of a 2-inch outside diameter Mullite cylinder with an inside diameter of 1-3/4 inch. A Nichrome V heater ribbon, 0.093 inch wide by 0.005 inch thick with a resistance of 1.3 ohms per foot, was to be closely wound over the ceramic cylinder. The heater was to consist of six heater elements, each operating with a maximum voltage of 220 volts and a current of 5.9 amps. This appeared to be a very conservative design for the heater allowing a uniform heat transfer to the secondary heat pipe.

The fabrication of the six heater elements was performed by a heater manufacturer. One of the elements is shown in Figure 127.

During the initial testing of the secondary heat pipe, repeated failure of the heater was experienced. Apparently, not only was the heater wire much too thin for the intended application and power density, but the manufacturing was faulty. After two complete heater failures, no further attempt was made to improve on the heater. A standard heater consisting of four elements (Lindberg 78 KS) was acquired which, however, had only half the desired power density. Each element was half circular, 18 inches long and had a maximum power output of 700 watts. The maximum operating temperature of the heater was 2200°F. The only disadvantage of this heater was its low power density which could not simulate the expected power input from the primary heat pipe. This however, was not important for the intended tests.

For limiting the thermal losses from the adiabatic section of the secondary heat pipe, an insulation thickness of 3 inches was calculated as shown in Figure 128. This insulation was to limit the losses to less than 10 percent of the power transfer capacity of the thermal train of which the secondary heat pipe was to be a component. For measuring the temperature of the secondary heat pipe, seven thermocouples were installed along the heat pipe and in the well which is provided for the condenser section of the primary heat pipe. Six thermocouples had been installed in the rotary heat transfer joint which was to be used for varying the thermal energy extraction rate. The test setup for the testing of the secondary heat pipe is shown in Figure 129.

Figure 130 shows the secondary heat pipe with the main insulation and the heaters installed in the location into which, at a later date, the primary heat pipe would be inserted. Figure 131 shows the two control stands for the secondary heat pipe test. The top panel of the left stand incorporated the temperature controls and measurement instrumentation. On the right side is the temperature controller which was connected to thermocouple #6 in the heat pipe near the heaters. The controller could operate either in an automatic or in a manual reset mode depending on the setting of the switch on the second panel. Left of the controller was the thermocouple selector switch with the thermocouple inputs. The second panel of the stand contained the controls for the heaters. The switching arrangement permitted each heater to be operated either time controlled or continuously. The right stand contained the meters for the four heater circuits and the control for the large Variac autotransformer. A counter and an elapsed timer was included.

7.5 TESTING

7.5.1 STEADY STATE POWER LOSSES

Testing of the secondary heat pipe was initiated with the experimental determination of the heat losses from the insulated heat pipe. For these

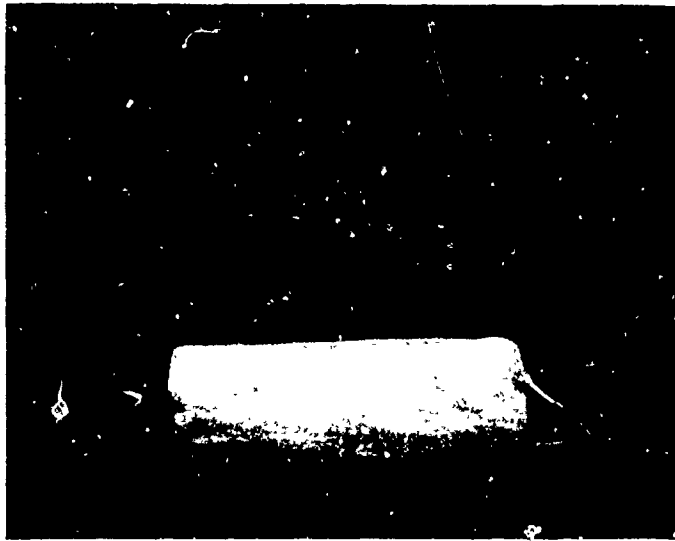


Figure 127. Secondary Heat Pipe Heater

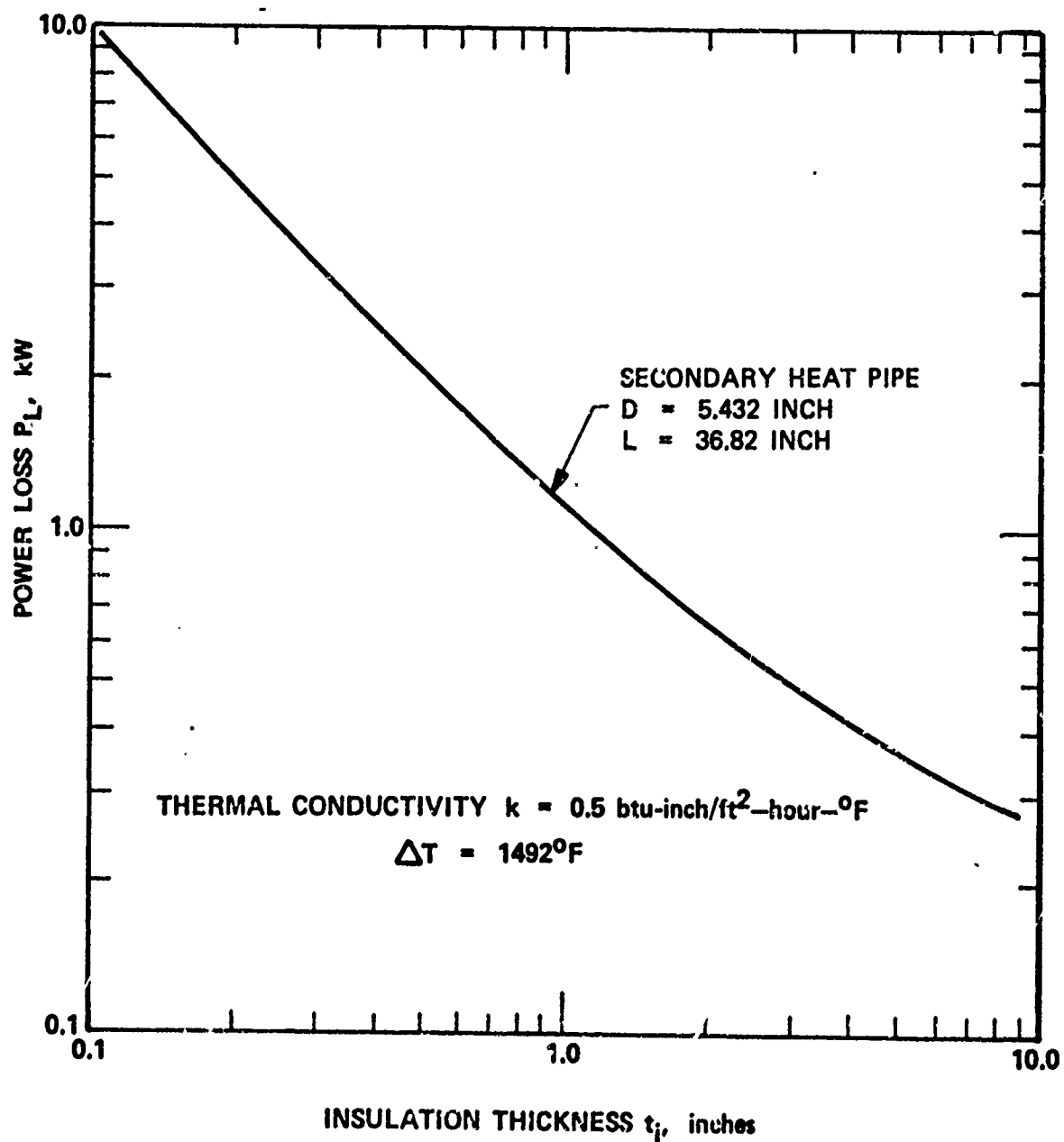


Figure 128. Insulation Requirement for Full Scale Secondary Heat Pipe with Thermal Energy Storage System

50784A

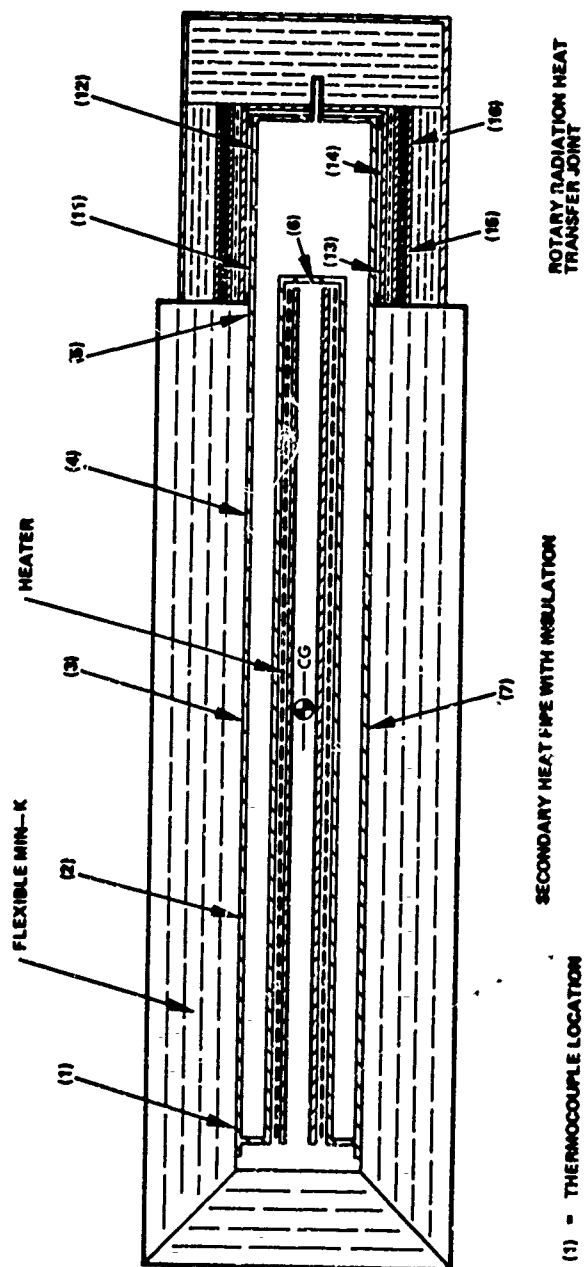


Figure 129. Setup for Testing of Secondary Heat Pipe with Rotary Radiation Heat Transfer Joint

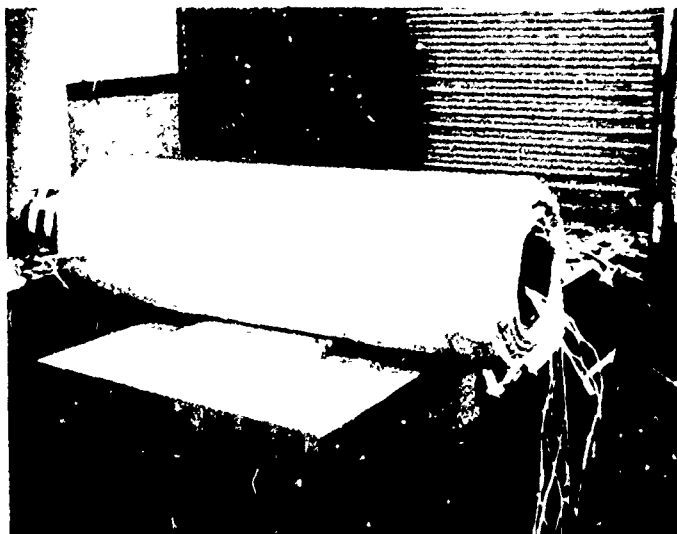


Figure 130. Secondary Heat Pipe with Insulation, Thermocouples, and Heaters Installed



Figure 131. Control Stands for Secondary Heat Pipe Test

initial tests the condenser section of the heat pipe was insulated with one layer of 3/8-inch Flex Min-K insulation and six layers of 1/2-inch Cera-Felt insulation.

The total heat losses from the secondary heat pipe, as a function of the operating temperature, are shown in Figure 132. As shown in Figure 128, the heat losses over the 36.82 inch long adiabatic section had been calculated to be 505 watts at the operating temperature of 1558°F with an insulation thickness of 3 inch Flex Min-K insulation. Because the entire length of the heat pipe was 45 inches, the heat losses were higher for this setup in which the condenser section was also insulated with the less effective Cera-Felt insulation. This insulation was to be removed after the initial testing and to be replaced by the rotary radiation heat transfer joint.

To obtain an individual steady state test point for determining the heat losses as a function of operating temperature, each power setting had to remain constant for at least 2 days. Only after this time, the operating temperature stabilized at a temperature at which the losses were equal to the power input.

The thermal losses as function of the operating temperature from the secondary heat pipe when operating with the rotary radiation heat transfer joint were also determined as shown in Figure 132. They were only slightly higher than for the fully insulated secondary heat pipe. The minimum release rate that could be investigated with the rotary radiation heat transfer joint in place was therefore 780 watts. This was about three times lower than for which the thermal energy storage unit was designed. The rotary radiation heat transfer joint therefore permitted the testing over a very wide range of energy release rates.

7.5.2 TRANSIENT OPERATION

After the correlation between the operating temperature and the power losses had been established, transient tests were conducted to determine the heat capacity of the secondary heat pipe with the thermal energy storage material. One full heating and cooling cycle is shown in Figure 133.

The calculations for the evaluation of the test were similar to those performed for evaluating the tests results obtained with the two subscale thermal energy storage units. (Section V.)

The power losses from the heat pipe could be expressed as a function of the operating temperature, i.e., the temperature measured by thermocouple #7, by the relation

$$P_L = C \times (\Delta T)^n$$

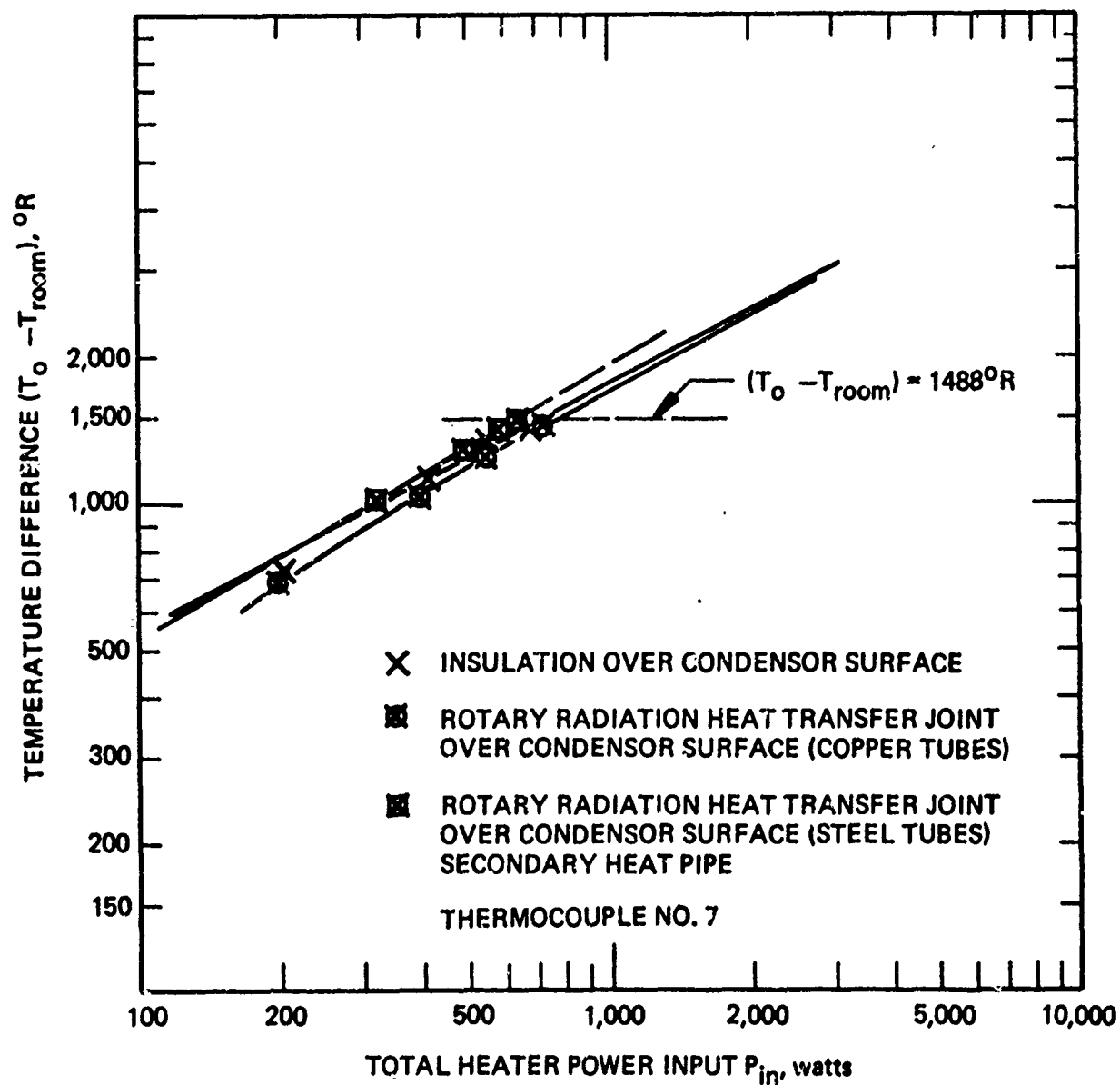


Figure 132. Energy Losses from Fully Insulated Secondary Heat Pipe with Rotary Radiation Heat Transfer Joint

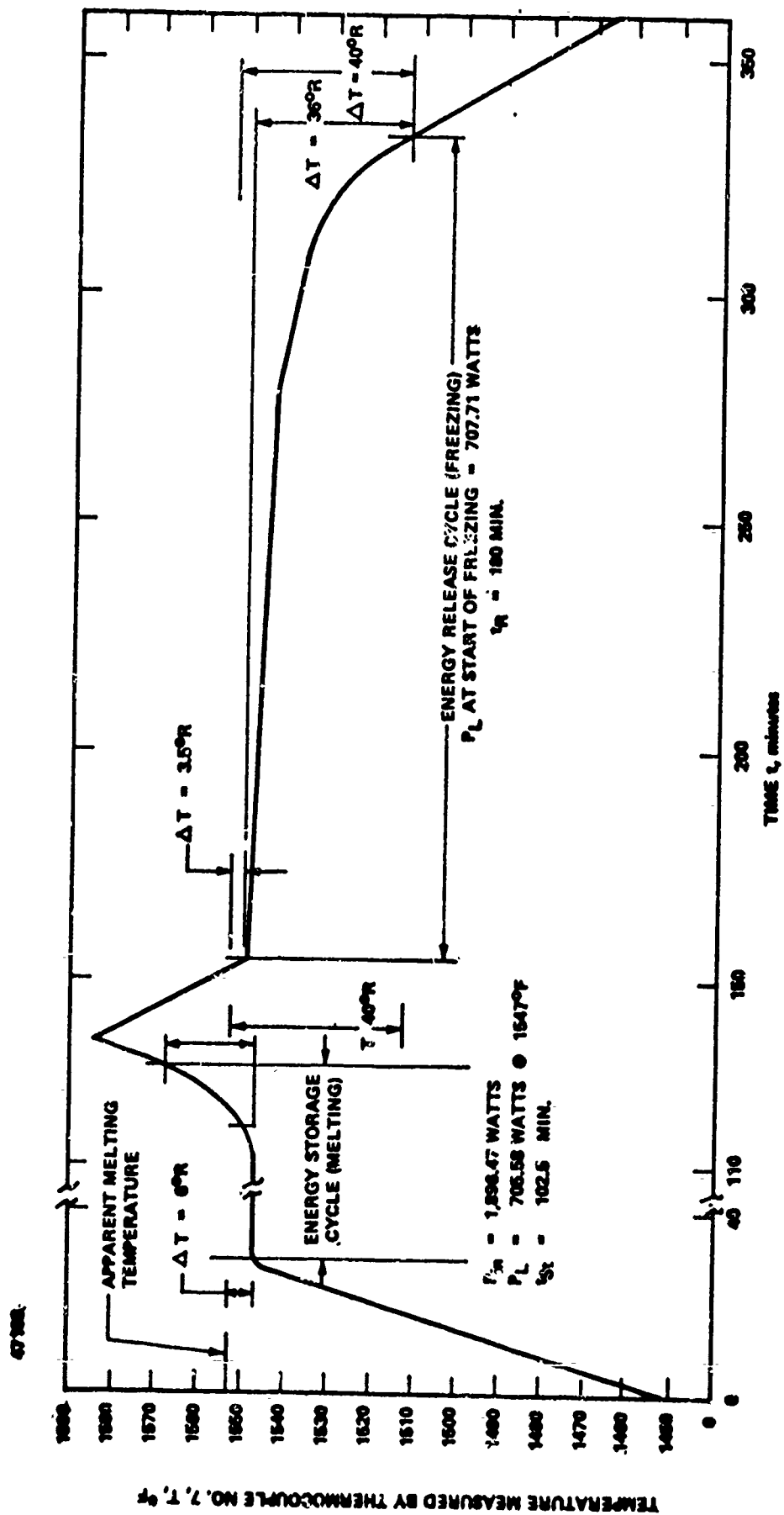


Figure 133. Temperature History of Secondary Heat Pipe and Thermal Energy Storage Unit During One Heating and Cooling Cycle

where

P_L = power loss, watt

C = constant, 2.69×10^{-4}

n = constant, 2.026

ΔT = temperature differential ($T_{\#7} - T_{rooms}$), $^{\circ}R$

During the heating cycle and the energy storage cycle, the input power supplied by the heater was

$P_{in} = 1,897$ watt

The energy absorbed by the secondary heat pipe and the solid thermal energy storage material was

$$\Delta E = (c_p W) \times \Delta T \quad (13)$$

where

ΔE = energy, joules

c_p = effective heat capacity, joules/g- $^{\circ}F$

W = effective weight, gram

ΔT = temperature rise, $^{\circ}R$

The absorbed energy had to be equal to the difference in power input and power loss

$$\Delta E = (P_{in} - P_L) \times \Delta T \quad (14)$$

Equating relations 13 and 14 the effective heat capacity for the secondary heat pipe was found to be

$$c_p \times W = 2.10 \times 10^4 \text{ joules}/^{\circ}R$$

A similar calculation was made taking a condition during the cooling cycle at which the power input was zero but the losses were known as a function of temperature. With this set of data the heat capacity was found to be

$$c_p \times W = 2.12 \times 10^4 \text{ joules}/^{\circ}F$$

The average of the two heat capacity values gave a heat capacity for the secondary heat pipe of

$$(c_p \times W)_{av} = 2.11 \times 10^4 \text{ joules/}^\circ\text{R}$$

This value was used for all the following calculations.

The amount of energy stored in the thermal energy storage material was calculated by integrating the power balance over the entire energy storage cycle, i.e., from the time the power input became greater than to the time it became again equal to the power losses and the power absorbed in the material as sensible heat. Thus, the thermal energy stored in the thermal energy storage material was

$$E_s = \int_{t_1}^{t_2} (P_{in} - C (\Delta T)^n) dt - \int_{T_1}^{T_2} (c_p W) dT$$

where

E_s = energy stored by thermal energy storage material, joules

P_{in} = power input, watt

C = loss constant, 2.68823×10^{-4}

ΔT = temperature difference $T_o - T_{room}$, $^\circ\text{R}$

T_o = operating temperature (T.C. #7), $^\circ\text{F}$

n = exponent, 2.025906

$c_p W$ = effective thermal capacity of secondary heat pipe with thermal energy storage material, joules/ $^\circ\text{R}$ (2.1099×10^4)

T = temperature, $^\circ\text{R}$

t = time, sec

The accumulated stored energy is shown in Figure 134. The calculation determined a total thermal energy storage of

$$E_s = 6.899 \times 10^6 \text{ joules}$$

Similarly, the released energy from the thermal energy storage material was calculated during the thermal energy release cycle which is also shown in Figure 134. The total thermal energy released was calculated to be

$$E_R = 6.812 \times 10^6 \text{ joules}$$

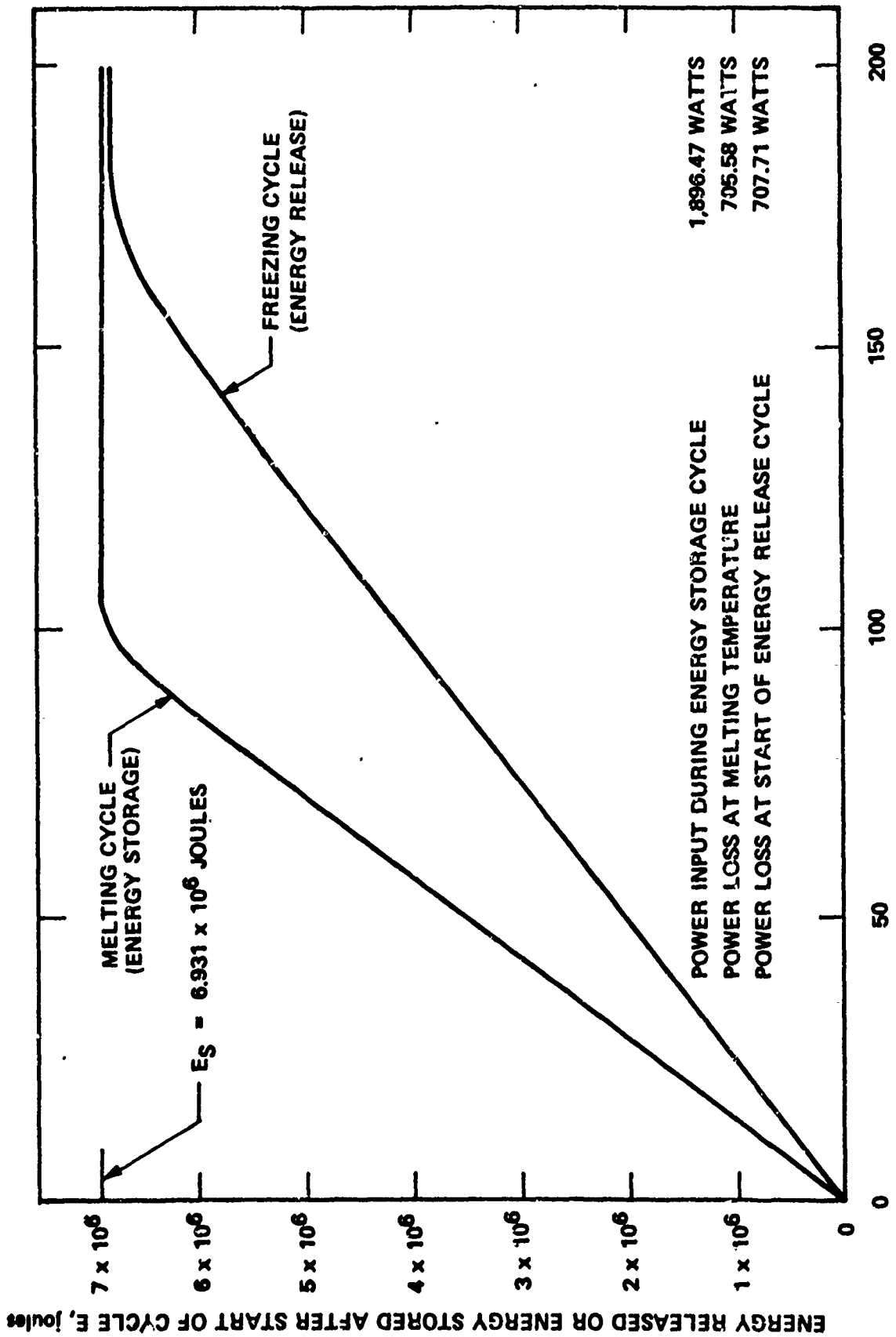


Figure 134. Energy Storing and Energy Release History of Thermal Energy Storage Unit and Secondary Heat Pipe

The average thermal energy storage capacity was thus $E = 6.8555 \times 10^6$ joules. Based on the total amount of thermal energy storage material consisting of 6638.8 grams lithium fluoride which has a latent heat of fusion of 1044 joules/g, the thermal energy storage capacity should have been

$$E = 6638.8 \times 1044 = 6.931 \times 10^6 \text{ joules}$$

The average measured thermal energy storage capacity is thus about 1.1 percent below the thermal energy storage capacity calculated from the weight of the thermal storage capacity material and the accepted value for the heat of fusion of LiF.

The thermal energy storage cycle lasted 102.5 minutes. This time was determined by the power input of 1896.5 watts and the losses of 705.6 watts. The rate of thermal energy storage was thus 1190.9 watts. The thermal energy was stored for about 80 minutes at a constant temperature. The thermal energy storage cycle was completed only after the temperature had increased by about 20 degrees above the temperature which had remained constant for the initial 80 minutes. This temperature increase was very much a function of the rate of thermal energy storage and increased with increasing rate.

During the thermal energy release, the operating temperature decreased by 36°R . The thermal energy storage release cycle lasted for 180 minutes with a release rate of about 705 watts during the initial tests. This rate was determined by the losses through the insulation and was thus not adjustable. The characteristics of the secondary heat pipe with the thermal energy storage unit was thus fully determined.

The effect of the release rate on the temperature difference was investigated with the rotary heat transfer joint which permitted the adjustment of the release rate.

In Figure 135, the result of the test at which energy was extracted at an initial rate of 1.79 kW is presented. The rate is indicated in Figure 136. The freezing cycle lasted 79 minutes while the operating temperature decreased from 1558°F to 1515°F . This indicates a temperature drop of 43°R for a rate of 1.79 kW. When the extraction rate was only 707 watts the temperature drop amounted to only 36°F . The thermal energy released by the thermal energy storage material was calculated by the relation

$$E_r = \int_{t_1}^{t_2} (P_c + C (\Delta T)^n) dt + \int_{T_1}^{T_2} (c_p W) dT$$

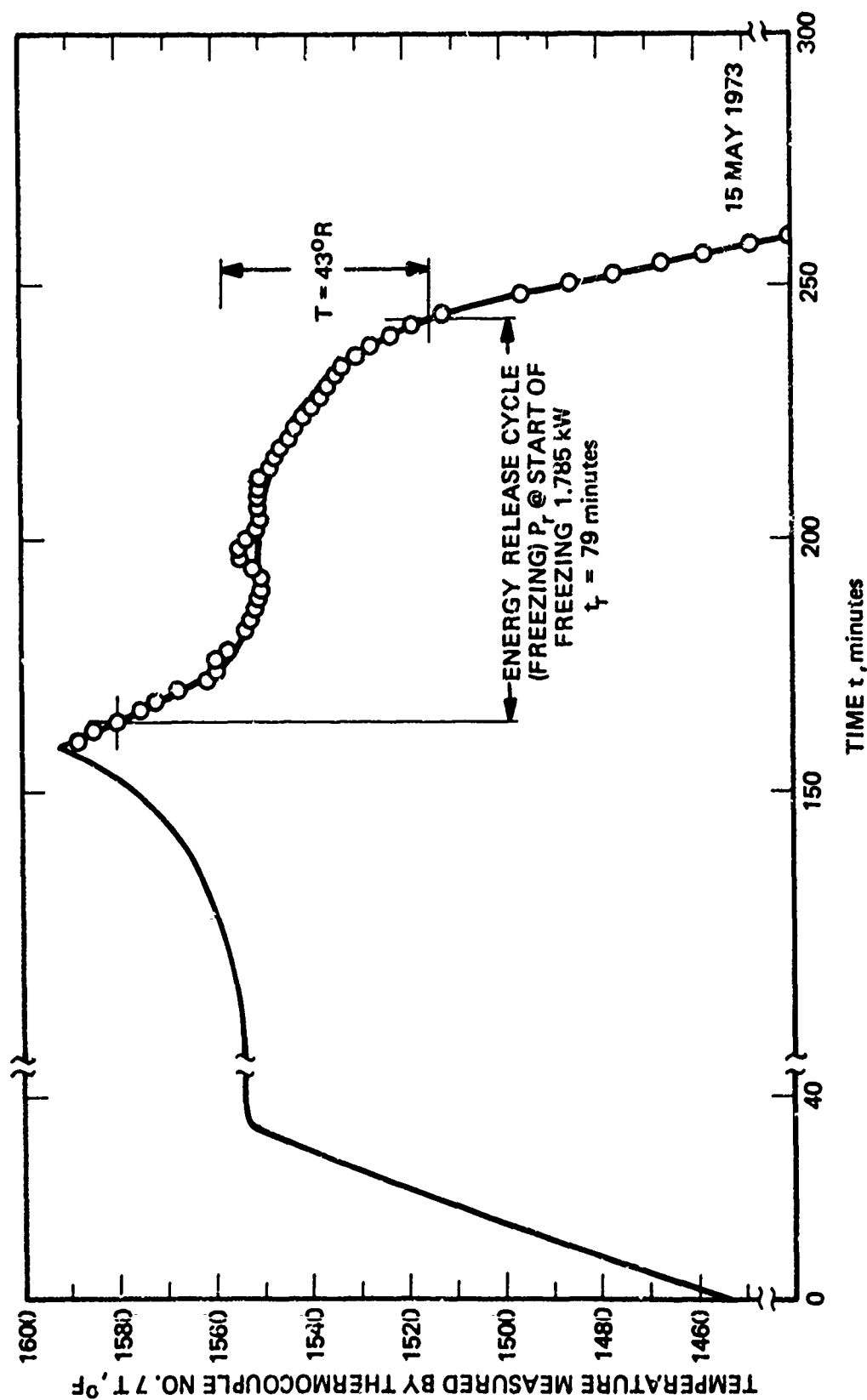


Figure 135. Temperature History of Secondary Heat Pipe and Thermal Energy Storage Unit During One Heating and Cooling Cycle

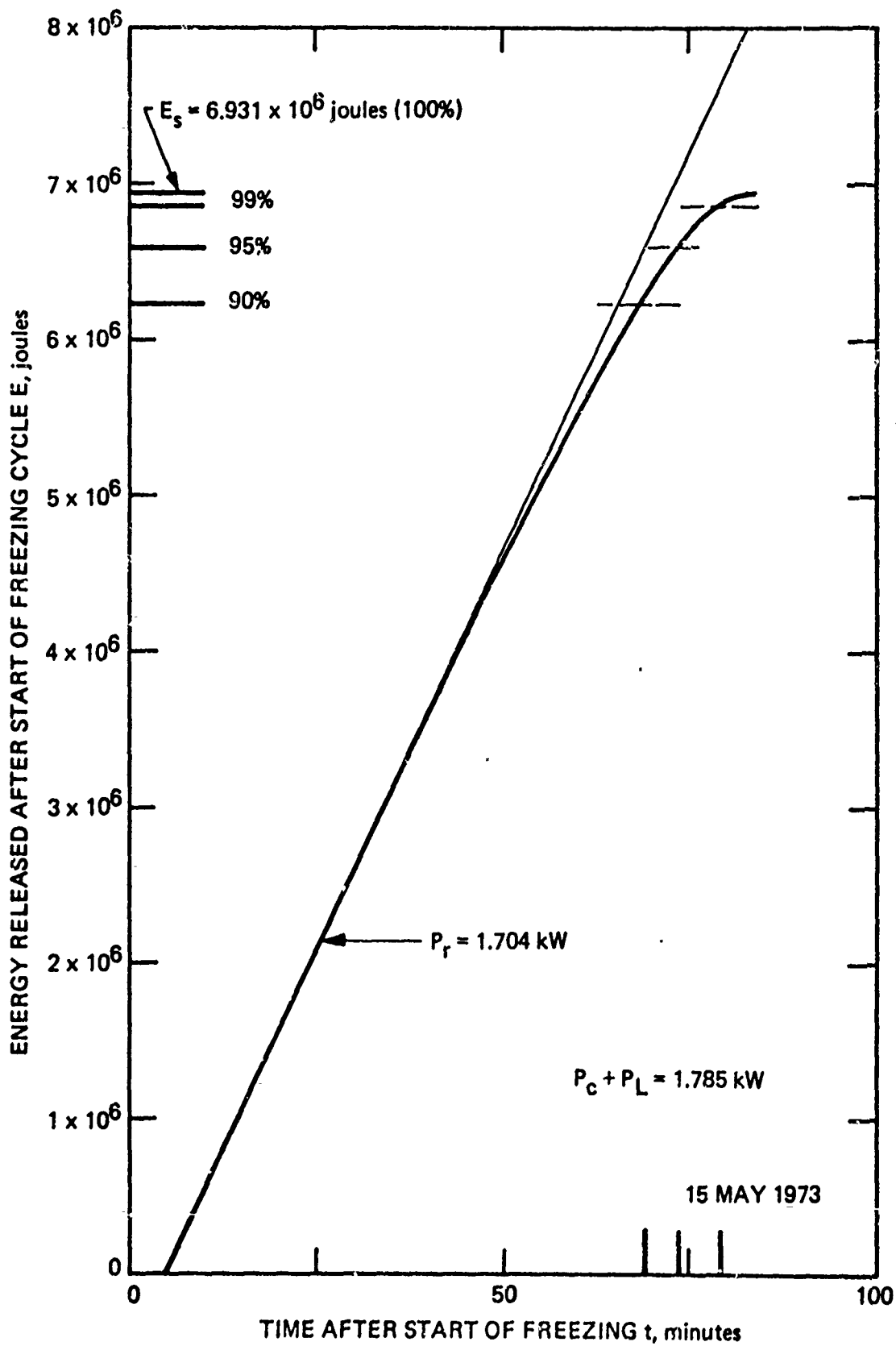


Figure 136. Thermal Energy Release History of Thermal Energy Storage Unit and Secondary Heat Pipe 203

where

- E_r = energy released by thermal energy storage material, joules
 P_c = power extracted by the rotary radiation heat transfer joint, watt
 C = loss constant, 2.688×10^{-4}
 ΔT = temperature difference $T_o - T_{room}$, $^{\circ}R$
 T_o = operating temperature (T.C. #7), $^{\circ}F$
 n = exponent, 2.026
 $c_p W$ = effective thermal capacity of secondary heat pipe with thermal energy storage material, joules/ $^{\circ}R$ (2.1099×10^4)
 T = temperature, $^{\circ}R$
 t = time, sec

A full set of tests was conducted to establish the operation of the thermal energy storage unit as a function of the thermal energy extraction rate. The results of the tests are presented in Figures 137 through 142. In Figures 143 through 148, the temperatures of the secondary heat pipe during the thermal energy extraction cycle are shown. It can be seen that the temperature history does not indicate the amount of energy that has been released up to a given time and temperature, or when the extraction of the stored thermal energy has been completed. The points on the curves indicating the amount of thermal energy extracted were found by integration of the energy extraction, as indicated by the mathematical relation above. The calculated thermal energy extraction history for each test is shown in Figures 143 through 148. For each test and calculation, the total extracted energy agrees amazingly close with the previously calculated thermal energy storage capacity. Because the 100 percent extraction point is very difficult to pinpoint, as it is approached asymptotically, the 90 percent, 95 percent, and 99 percent total thermal energy extraction points have been indicated in all figures.

In Figure 149, the temperature drop at the time of 90, 95, and 99 percent stored energy extraction and are plotted as a function of rate. The results confirm well the calculations that indicated that with increasing extraction rate the final temperature drop of the thermal energy storage unit increases. At an extraction rate of 3 kW, for which the full scale thermal energy storage unit was designed, the temperature will have dropped by about $45^{\circ}R$ when 95 percent of the stored thermal energy has been extracted. This compares with $40^{\circ}R$ anticipated and indicated in Figure 56, Volume I of this report.

The measured and calculated results of the tests are tabulated in Table XXVI. The three powers shown in Table XXVI need explanation. The power transfer is the power carried away by the injected coolant water

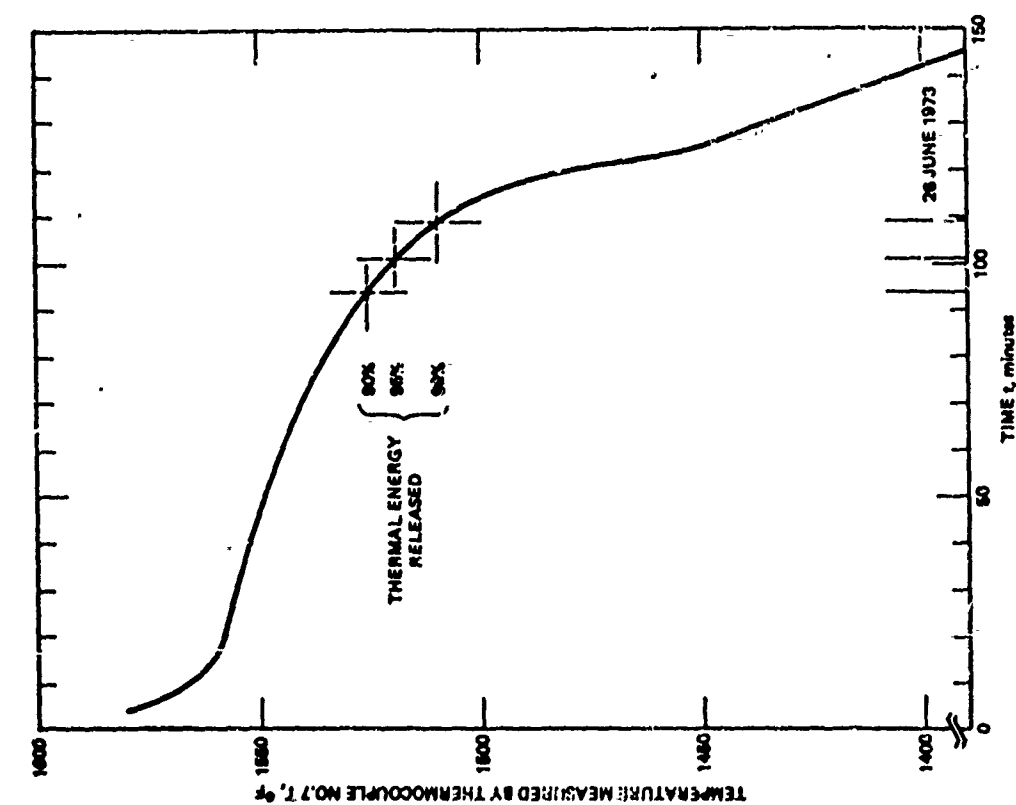


Figure 137. Temperature History of Secondary Heat Pipe and Thermal Energy Storage Unit During Energy Release (1.3 kW)

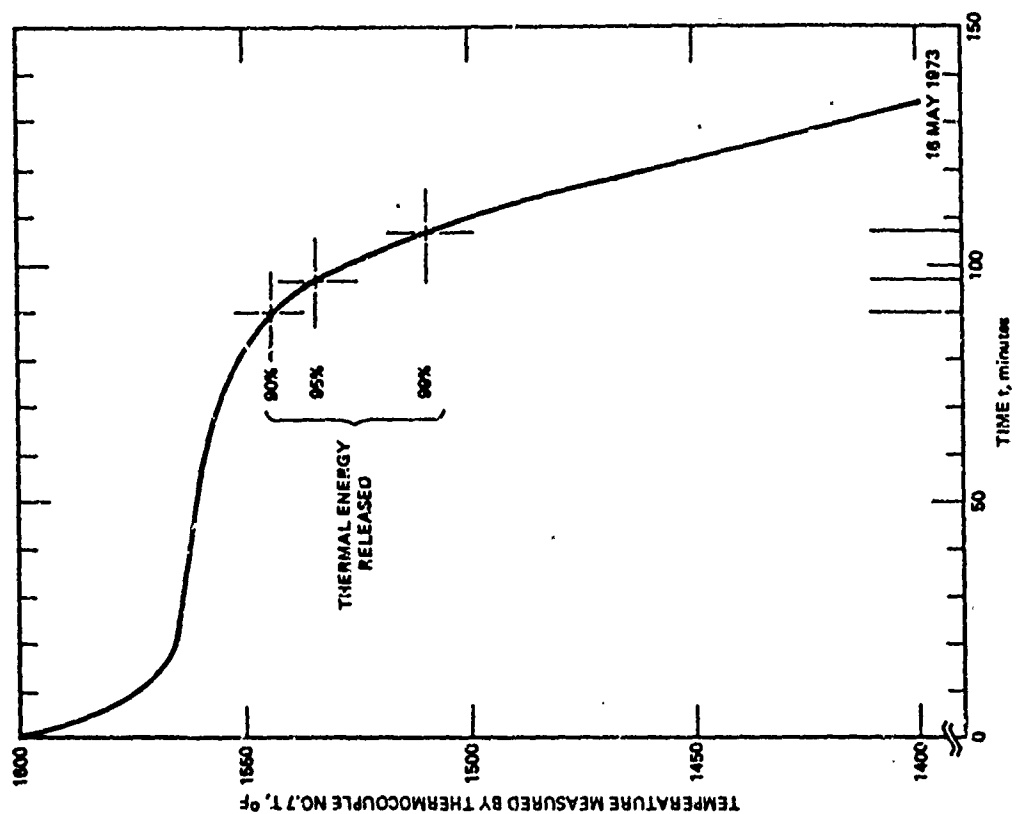
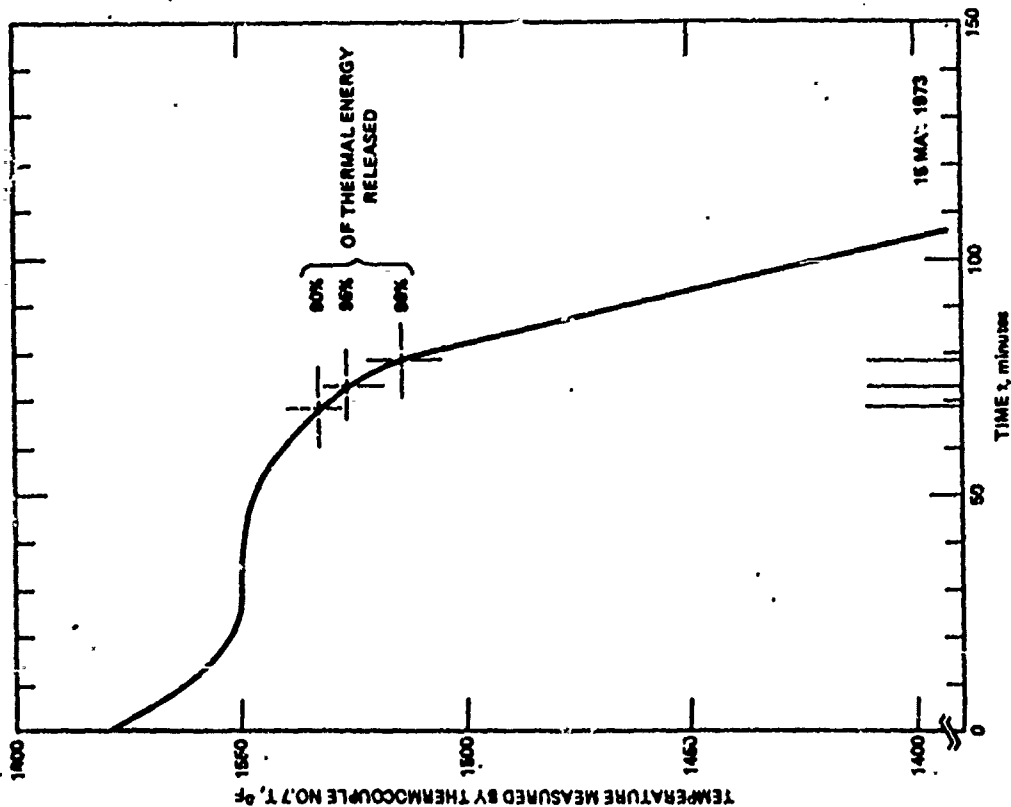


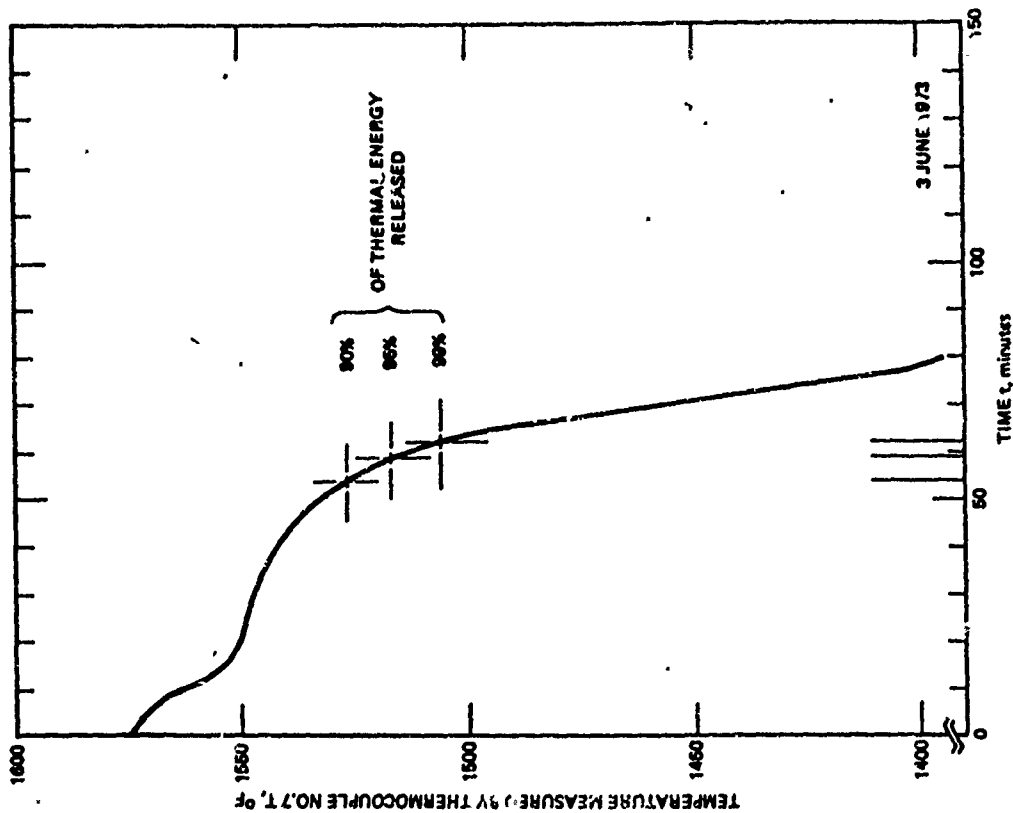
Figure 138. Temperature History of Secondary Heat Pipe and Thermal Energy Storage Unit During Energy Release (1.40 kW)

50928 A



50928

Figure 139. Temperature History of Secondary Heat Pipe and Thermal Energy Storage Unit During Energy Release (1.785 kW)



50927

Figure 140. Temperature History of Secondary Heat Pipe and Thermal Energy Storage Unit During Energy Release (2.25 kW)

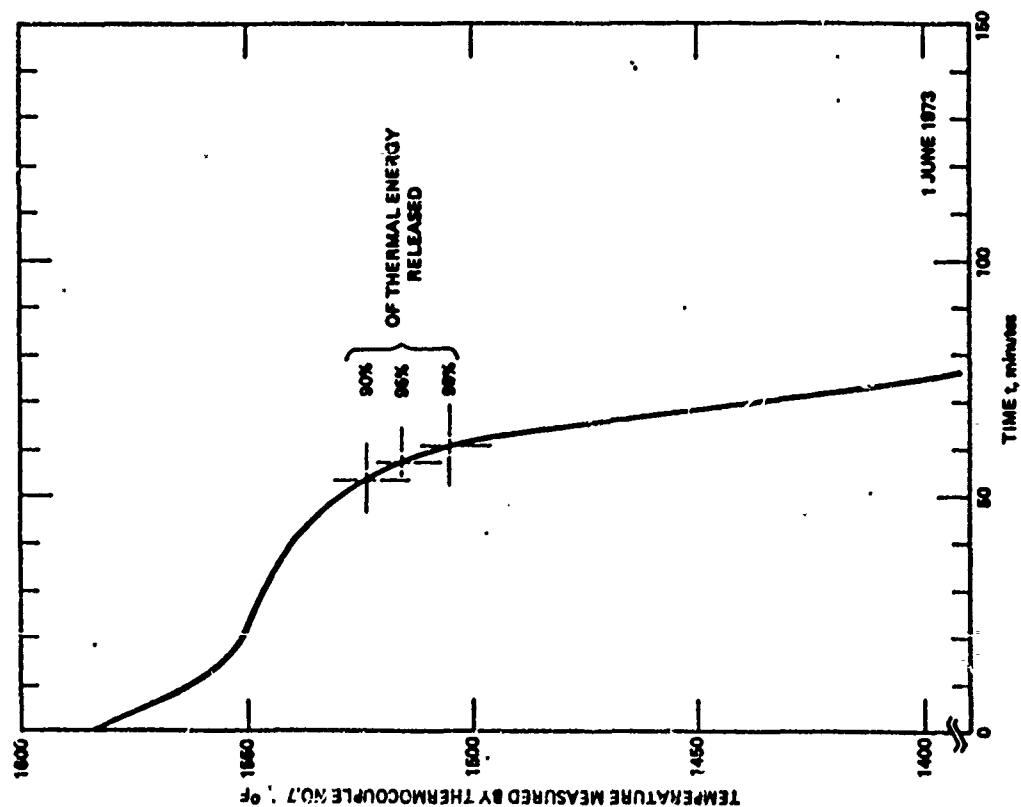


Figure 141. Temperature History of Secondary Heat Pipe and Thermal Energy Storage Unit During Energy Release (2.38 kW)

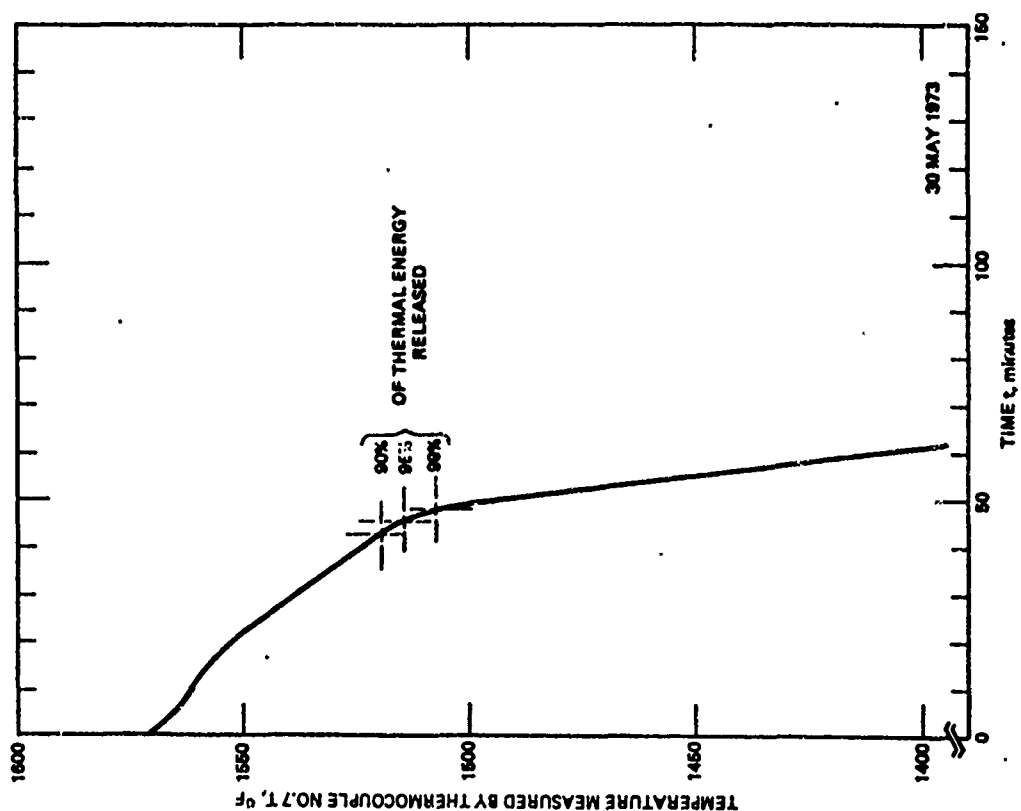


Figure 142. Temperature History of Secondary Heat Pipe and Thermal Energy Storage Unit During Energy Release (2.89 kW)

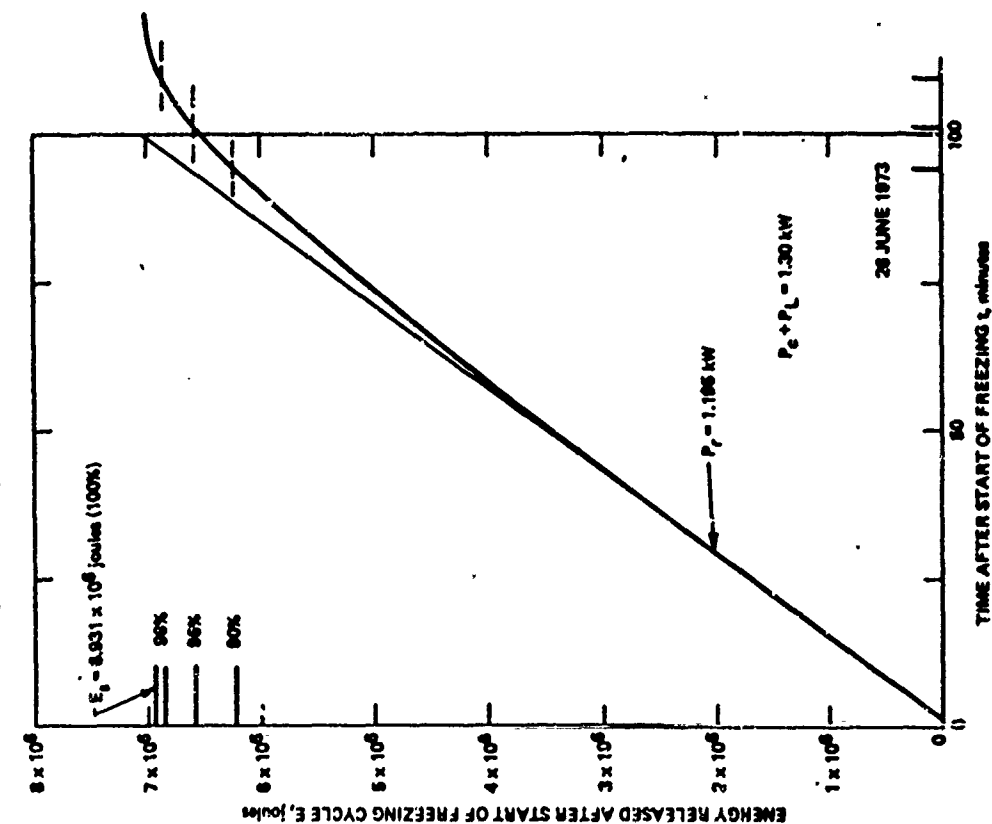


Figure 143. Thermal Energy Release History of Thermal Energy Storage Unit and Secondary Heat Pipe (1.30 kW)

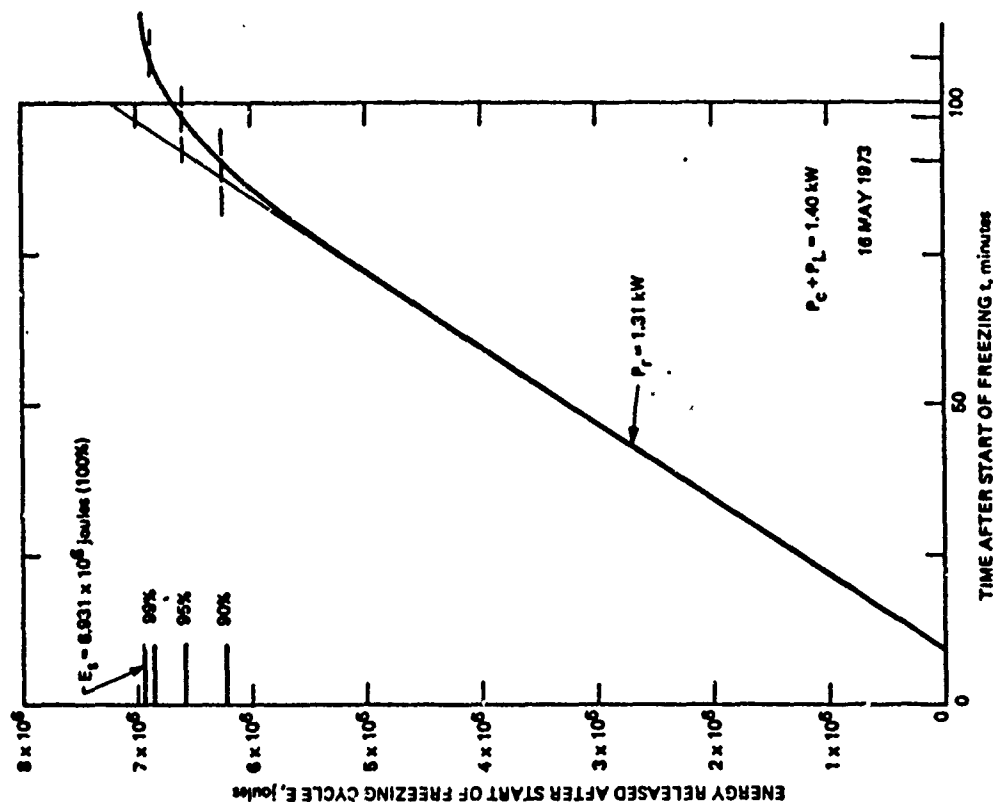


Figure 144. Thermal Energy Release History of Thermal Energy Storage Unit and Secondary Heat Pipe (1.40 kW)

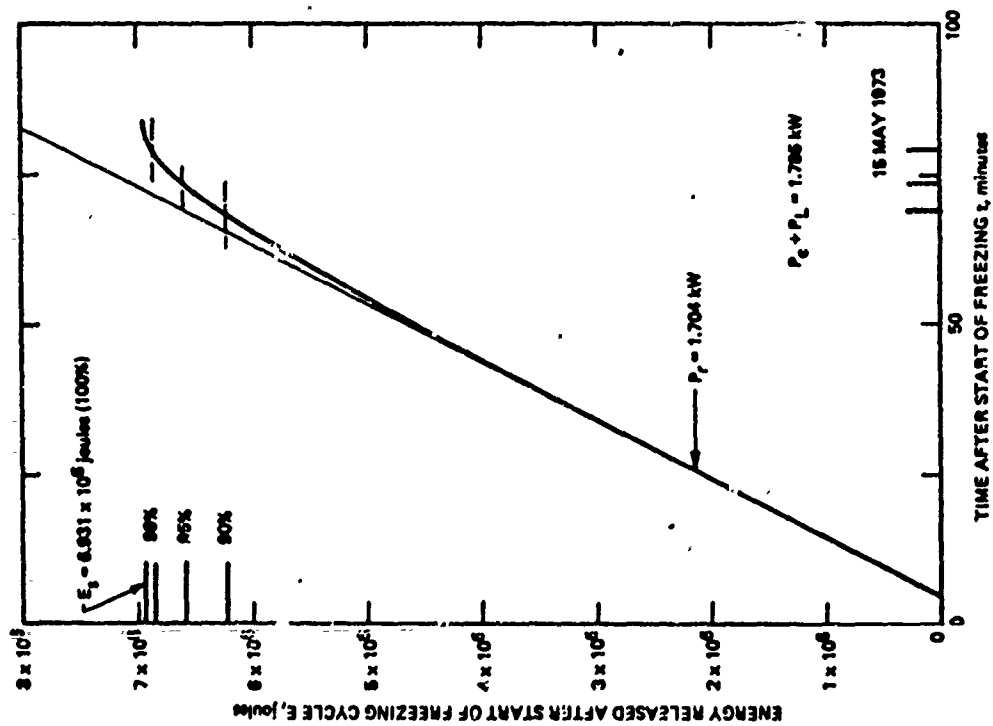


Figure 145. Thermal Energy Release History of Thermal Energy Storage Unit and Secondary Heat Pipe (1.785 kW)

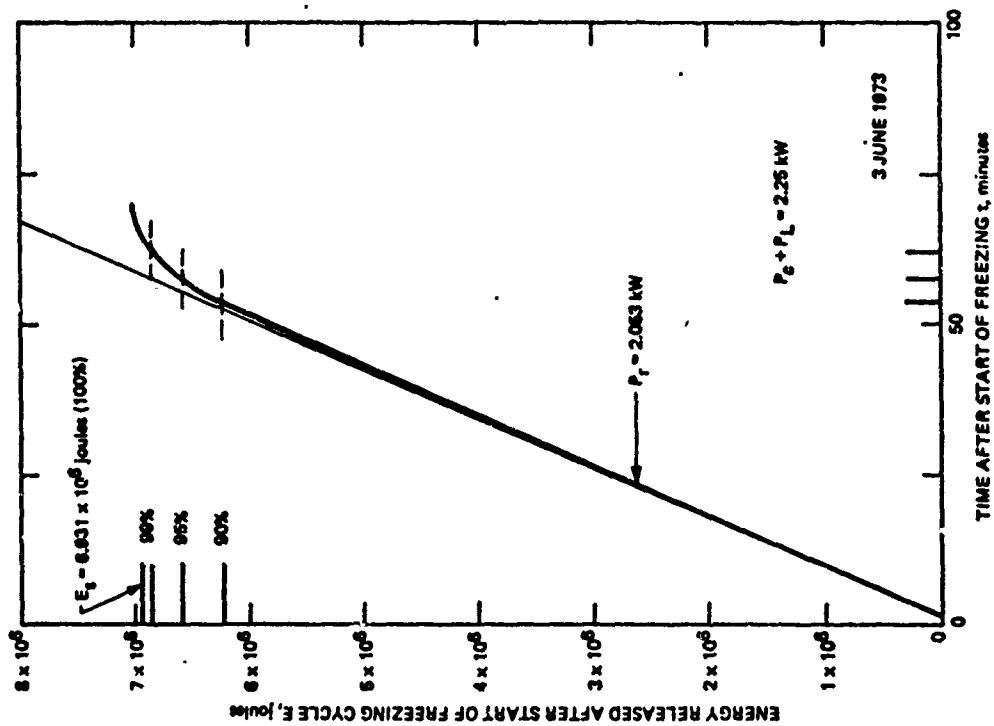


Figure 146. Thermal Energy Release History of Thermal Energy Storage Unit and Secondary Heat Pipe (2.25 kW)

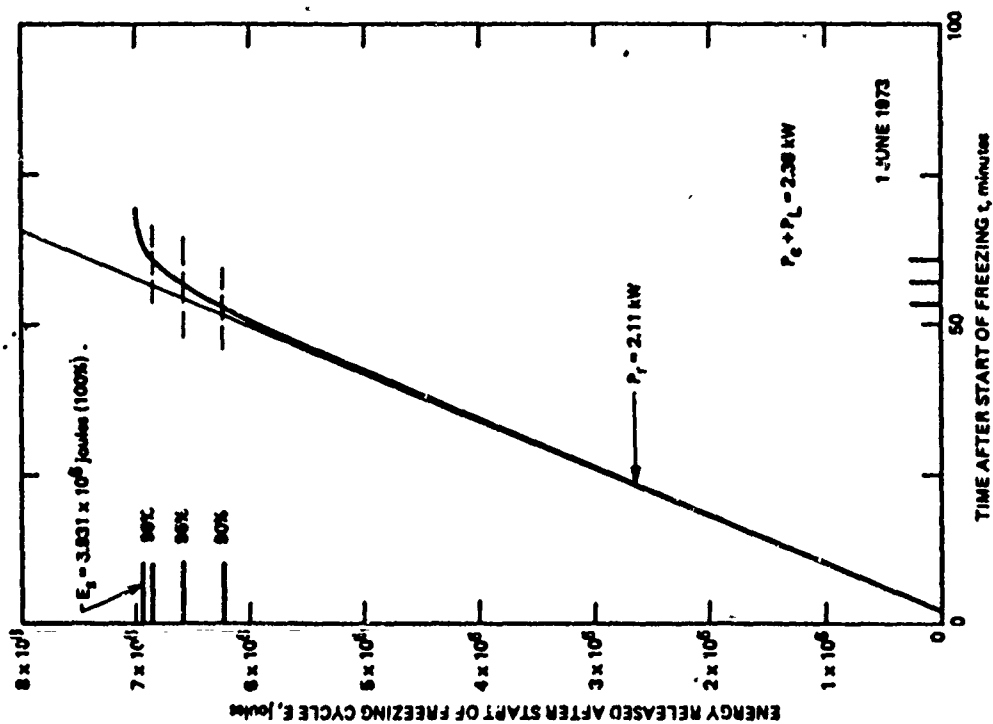


Figure 147. Thermal Energy Release History of Thermal Energy Storage Unit and Secondary Heat Pipe (2.38 kW)

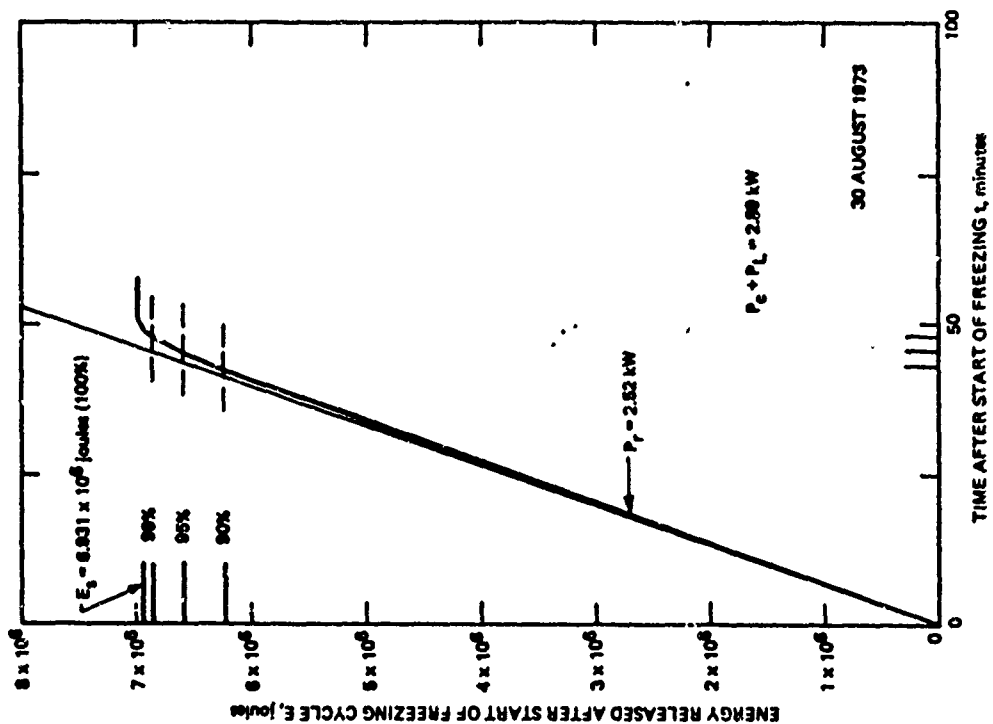


Figure 148. Thermal Energy Release History of Thermal Energy Storage Unit and Secondary Heat Pipe (2.89 kW)

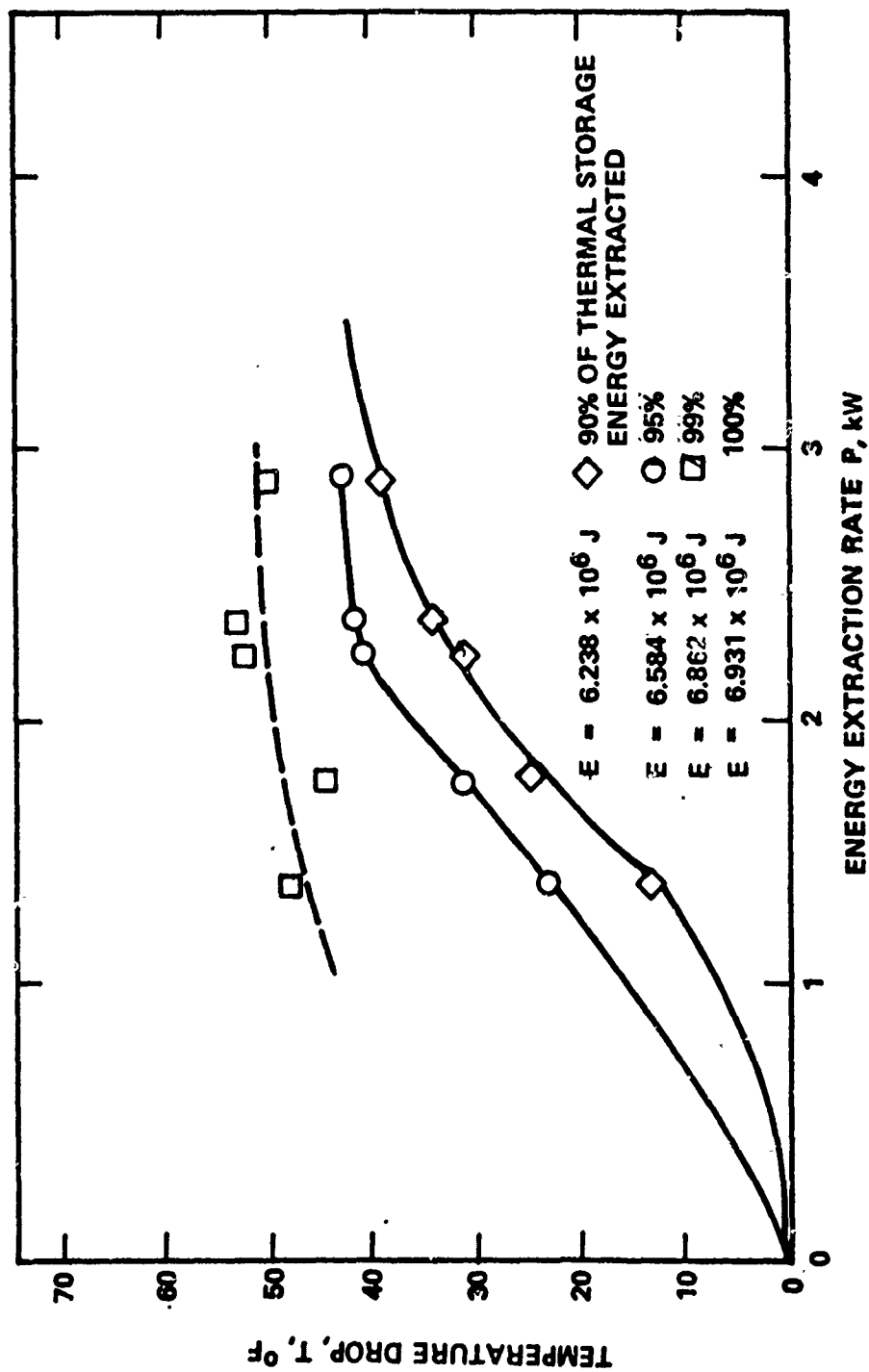


Figure 149. Effect of Energy Release Rate on the Final Temperature of the Secondary Heat Pipe After Thermal Energy Extraction

TABLE XXVI
RADIATION HEAT TRANSFER JOINT AND SECONDARY HEAT PIPE
WITH THERMAL ENERGY STORAGE UNIT

Point	Flow Rate g/sec	Power Transfer kW	Power Extracted kW	Total Power kW	Extraction Time Minutes			Final Temperature Of			Temperature Drop Of		
					90%	95%	99%	90%	95%	99%	90%	95%	99%
1	0.485	1.19	1.70	1.79	63.8	68.6	74.0	1533	1527	1514	25	31	44
2	0.338	0.79	1.31	1.40	82.0	89.2	99.0	1545	1535	1510	13	23	48
3	0.655	2.30	2.52	2.89	43.0	45.5	48.0	1520	1515	1508	38	43	50
4	0.585	1.78	2.11	2.38	50.5	54.2	58.0	1524	1516	1505	34	42	53
5	0.542	1.66	2.05	2.25	52.0	56.0	60.5	1527	1517	1506	31	41	52

in the form of latent heat. The power extracted is the rate of thermal energy extracted from the thermal storage energy material, LiF, at the beginning of the extraction. The third power, total power, is the total energy loss rate from the system by transfer to the radiation heat transfer joint (cooling water) and by losses through the insulation. The total power loss is comprised of the thermal energy released by the thermal energy storage material as well as the sensible energy of the secondary heat pipe material, as the temperature decreases.

7.6 CONCLUSIONS

The testing of the secondary heat pipe with the thermal energy storage unit confirmed the capability of LiF salt to store and release thermal energy in a very predictable process. The test results proved the secondary heat pipe to perform according to the design. The difference of 1.1 percent between the measured thermal energy storage capacity and the design capacity must be considered to be within the measuring and calculating accuracy of the tests.

After the many cycles to which the secondary heat pipe was subjected, neither external mechanical nor structural defects could be detected. The test results remained consistent throughout the tests suggesting that the thermal energy storage unit maintained its operational integrity until the end of the tests. The secondary heat pipe was ready for integration with the primary heat pipe. The testing of the secondary heat pipe also verified the operation of the radiation heat transfer joint.

SECTION VIII

SUBSCALE CAVITY RECEIVER AND HEAT PIPE

8.1 INTRODUCTION

The subscale spherical cavity receiver and heat pipe investigation was designed to verify in a subscale configuration the basic principle of mating a solar collector with a heat pipe. The task was planned for testing a subscale spherical cavity receiver with a subscale heat pipe in an existing solar simulator.

8.2 SYSTEM EVALUATION

The initial plans called for testing of the subscale spherical cavity receiver and heat pipe in the solar simulator or the General Electric Company in Valley Forge, Pennsylvania.

The solar simulator is powered by a 20 kW arc lamp which is placed in a 3-foot diameter reflector. With an included beam divergence angle of about 3 degrees, the total achievable radiation power on a target is 1060 watts.

Based on the beam diameter and divergence angle, the smallest receiver size achievable with an optimum parabolic collector could be calculated. The relation between the receiver diameter and the collector diameter for the conditions shown in Figure 150 are given by

$$D_R/D_C = \sin \theta / \cos(\theta + \phi) \sin \phi \quad (15)$$

where

- D_R = receiver diameter
- D_C = collector diameter
- ϕ = rim angle
- θ = beam divergence half angle

For the receiver to have the smallest diameter so that the total available radiation power can be concentrated on the smallest area which was necessary to simulate the radiation intensity, achievable and desirable in the space system, the denominator of relation 15.

$$I_D = \cos(\theta + \phi) \sin \phi \quad (16)$$

has to be a maximum.

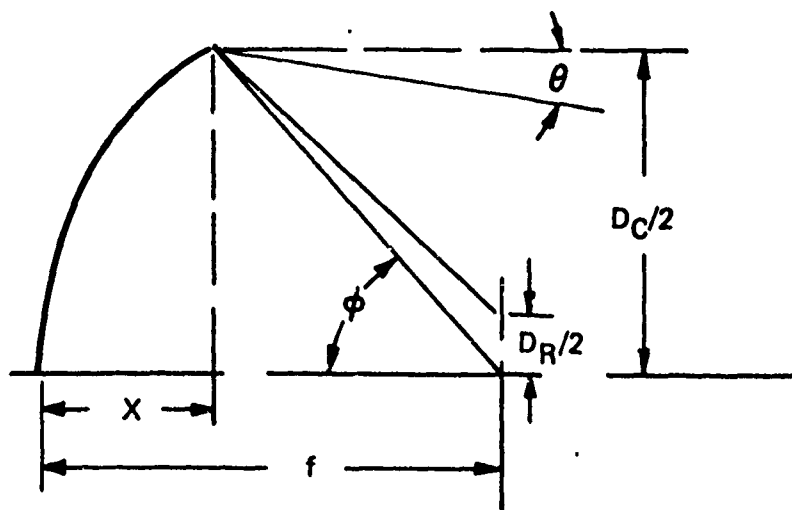


Figure 150. Optical Dimensions for Receiver and Collector Calculations

By differentiation of relation 17 and setting the differential equal to zero the optimum relation between the half angle θ and the rim angle ϕ is found to be

$$\phi = 1/2 \left(\frac{\pi}{2} - \theta \right) \quad (17)$$

For the radiation divergence half angle of one-half of 3 degrees, i.e., 1.5° , the optimum rim angle is found to be

$$\phi = 44.25^\circ$$

When the beam is smaller than the parabolic collector the collector diameter is equal to the beam diameter, i.e., 36 inches. With the collector diameter and the rim angle known, the minimum receiver diameter is found to be

$$D_R = D_C \times \sin 1.5^\circ / \left[\cos (44.25^\circ - 1.5^\circ) \sin 44.25^\circ \right] \quad (18)$$

$$D_R = 1.9354 \text{ inch}$$

For a total radiation power of $P_r = 1060$ watts, the average radiation density on the receiver cannot be more than

$$\dot{q}_R = 55.85 \text{ watt/cm}^2$$

This irradiation would have been the maximum irradiation possible with the General Electric Company solar simulator when employing an optimum collector. Since it was contemplated to size an existing collector which has a 5-foot diameter and a focal length of 66 cm, the minimum receiver diameter would have had to be not smaller than

$$D_R = 1.9805 \text{ inch}$$

For this solar simulator collector combination, the maximum irradiation achievable would have been

$$\dot{q}_R = 53.34 \text{ watt/cm}^2$$

This power density on the receiver would have been only 4.49 percent lower than the irradiation achievable with an optimum collector. Therefore, improving the performances by designing and building a special collector was not contemplated.

For simulating the irradiation on the full scale receiver, an irradiation of about 85 watt/cm^2 was required, as based on the present system calculations. This irradiation can vary by about 10 percent depending on the accuracy with which the final collector can be manufactured and to what tolerances the collector can be oriented in space.

Due to delays in the program and the initiation of the subscale spherical receiver and heat pipe task, a radiation facility became available for testing at Xerox/Electro-Optical Systems. For that facility a radiation source had been developed which could operate at an input power of 50 kW. The component arrangement for testing the subscale spherical receiver and heat pipe in that facility is shown in Figure 151.

When a radiation source is used which can be operated at a total power input of 40 kW, the total radiation power can be at least 4,000 watts.* The spreading angle of the source is 2.7° and at a distance of 39.32 feet the beam diameter is 40.62 inches. Using the parabolic 5 foot collector with a 66 cm focal length the receiver diameter can be 2 inches, having a receiver projected area of 20.253 cm^2 . The average irradiation achievable with this radiation source could thus be 197.5 watt/cm^2 , which would be about 230 percent of the irradiation required for full simulation.

8.3 DESIGN

Since 4,000 watts of radiation power was available and it might have been desirable to exceed the minimum simulation irradiation, the receiver and the heat pipe were designed for a total power transfer of 2 kW.

*Radiation efficiencies of 11.6 percent at 59.8 kW and 12.12 percent at 83.2 kW in the radiation band $\Delta\lambda = 0.45\mu$ to 0.96μ have been measured for that source consistently.

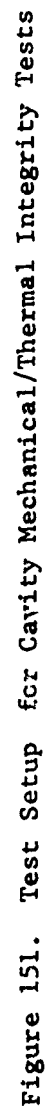
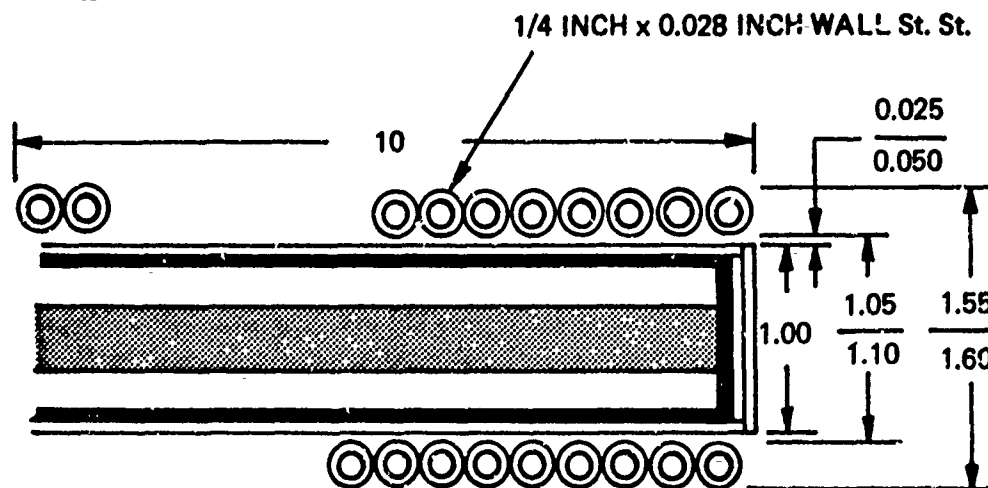


Figure 151. Test Setup for Cavity Mechanical/Thermal Integrity Tests

The condenser was to be cooled by radiation and conduction to a cooling coil surrounding the condenser section of the heat pipe as shown in Figure 152. The total heat transfer for such an arrangement is

$$\dot{Q} = A_C \left\{ \sigma \epsilon (T_{HP}^4 - T_{CC}^4) + k_A (T_{HP} - T_{CC}) / t_A \right\} \quad (19)$$

A_C = condenser area
 σ = Boltzmann's constant
 ϵ = emissivity
 k_A = conductivity of air
 T_{HP} = temperature of heat pipe
 T_{CC} = temperature of cooling unit
 t_A = air gap



For a gap $t_A = 0.050$ inch, the length of the cooling coil was calculated to be

$$L_{CC} = 9.701 \text{ inches}$$

If the gap could be maintained at 0.025 inch, the cooling coil required a length of only

$$L_{CC} = 7.456 \text{ inches}$$

If heat transfer by conduction was disregarded entirely, the cooling coil would have to be

$$L_{CC} = 13.884 \text{ inches}$$

For the desired application, a cooling coil length of 10 inches was selected.

With the major required dimensions of the heat pipe established, the length of the heat pipe was determined as shown in Figure 153.

The heat pipe was designed using the following properties of sodium which was to be the working fluid of the heat pipe at the operating temperature of 1558°F.

	<u>Fluid</u>	<u>Vapor</u>
Surface tension σ , g/sec ²	124	
Thermal conductivity k , watt/cm-°K	0.540	
Latent heat H_{fg} , joules/g	4.4×10^3	
Viscosity μ , g/sec-cm	1.64×10^{-3}	2.245×10^{-4}
Specific gravity ρ , g/cm ³	0.74835	1.95×10^{-4}
Vapor pressure p , dynes/cm ²		6.56×10^5

For a total power transfer of 2 kW, the fluid flow was found to be

$$\dot{W}_S = 2000 / 4.4 \times 10^3 = 0.45 \text{ g/sec.}$$

The pertinent dimensions for the heat pipe design are shown in Figure 154. The important parameters of the heat pipe can be expressed as a function of these dimensions. The diametral wick flow area, A_W is calculated from

$$A_W = r^2 \{2\phi + \sin 2\phi\} \quad (20)$$

The vapor flow area A_V is expressed by

$$A_V = r^2 \{\pi - 2\phi - \sin 2\phi\} \quad (21)$$

$$\text{or } A_V = r^2 \pi - A_W \quad (22)$$

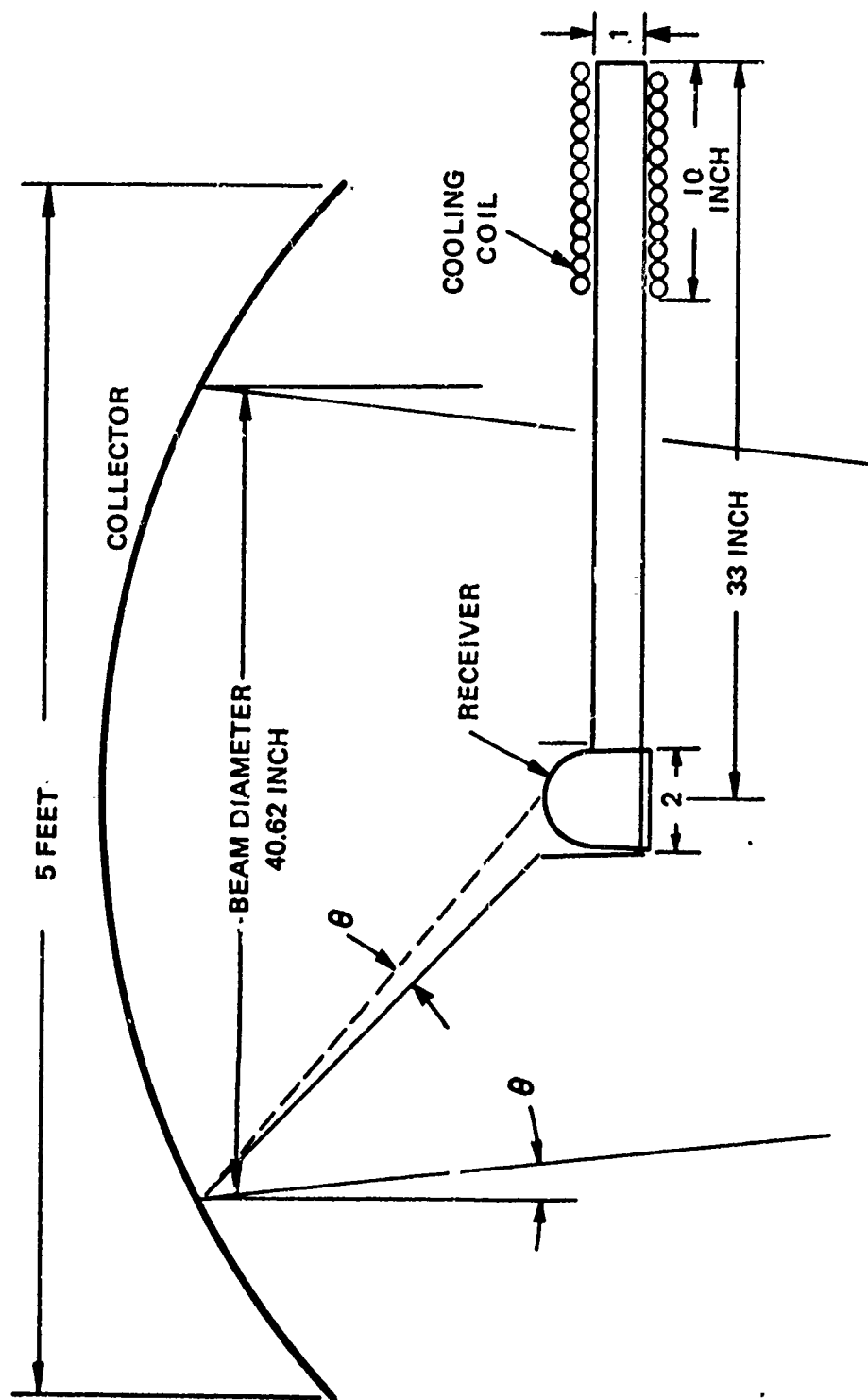


Figure 153. Heat Pipe Dimensions

E0843

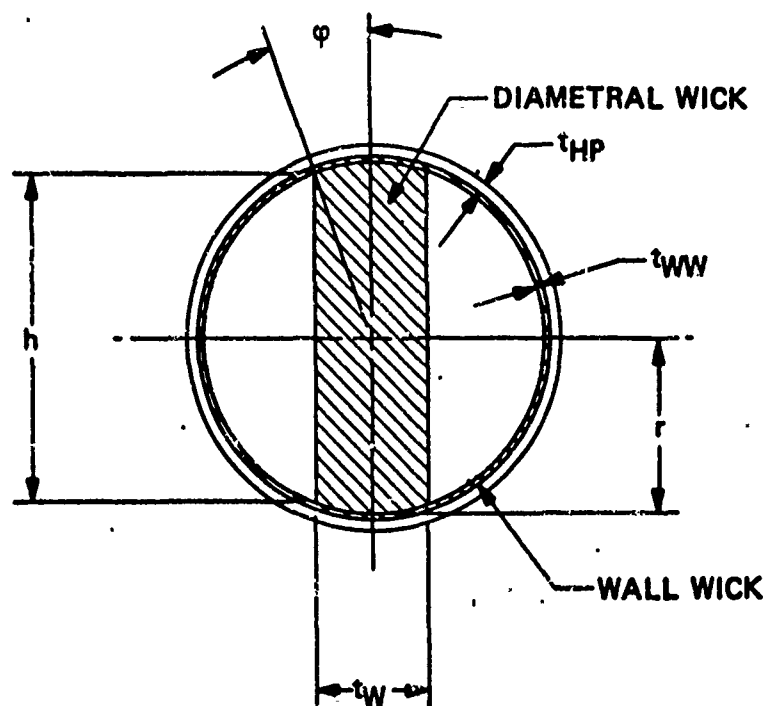


Figure 154. Heat Pipe Design Dimensions

The ratio between the wick flow area and the vapor flow area is

$$\frac{A_W}{A_V} = \frac{2\phi + \sin 2\phi}{\pi - 2\phi - \sin 2\phi} \quad (23)$$

This relation is plotted in Figure 155 for easy reference. The vapor flow surfaces is

$$S = 2r \{ 2 \cos \phi + \pi - 2\phi \} \quad (24)$$

The flow in the wick is expressed by Darcey's law.

$$\dot{V} = \frac{K \Delta p A_W}{\mu L} \quad (25)$$

where

$$\dot{V} = W/\rho f \quad (26)$$

The vapor flow in vapor pass is governed by the flow relation

$$\Delta p_v = f \frac{L}{D_H} \frac{\rho_v v^2}{2g} \quad (27)$$

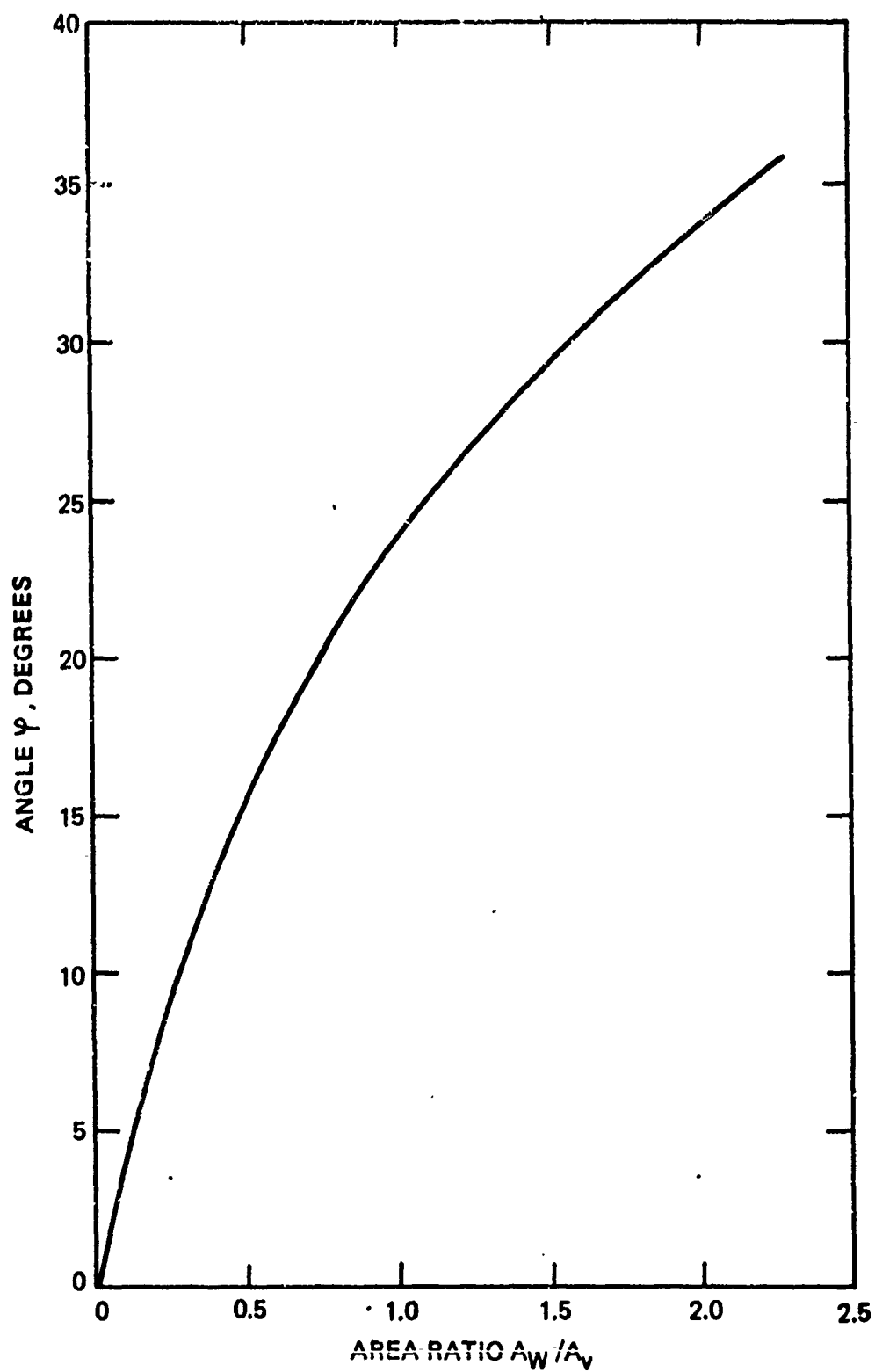


Figure 155. Area Ratio of Wick and Vapor Flow Pass as Function of Angle ϕ

where

$$\begin{aligned}\Delta p_v &= \text{vapor pressure drop} \\ f &= \text{friction factor} \\ L &= \text{flow path length} \\ D_H &= \text{hydraulic diameter} \\ \rho_o &= \text{vapor density}\end{aligned}$$

where the Reynolds number can be expressed by

$$N_{Re} = \frac{4 P}{H_{fg} \mu S} \quad (28)$$

where

$$\begin{aligned}P &= \text{power transfer} \\ H_{fg} &= \text{latent heat of evaporation} \\ \mu &= \text{viscosity} \\ S &= \text{flow path surface}\end{aligned}$$

For an area ratio (A_W/A_V) of 0.5 the pressure drops and the available suction pressure Δp_c are shown in Figure 156. This design appears to be marginal since the available suction pressure is only about 9 percent above the total pressure drop for the optimum mesh size. If the vapor flow area is decreased for the sake of increasing the wick flow area so that the ratio between the wick flow area to the vapor flow area is unity, the wick will have a 26 percent operating margin according to calculations. This design is shown in Figure 157.

Based on the design calculations, a bolting cloth with a mesh of 10 wires per inch and a wire size of 0.0055 inch diameter was selected. The walls of the heat pipe were lined with four layers of this bolting cloth. The total volume of the wick structure in the heat pipe was

$$V_{WT} = 227.6 \text{ cm}^2$$

The wick structure has a 24 percent density so that 76 percent of the wick volume would be soaked with liquid sodium. The liquid sodium volume in the wick at the operating temperature was therefore

$$V_f = 174.54 \text{ cm}^2$$

Many considerations were advanced for filling the heat pipe either with an amount of sodium that would fill the entire wick at the operating temperature without surplus in the heat pipe or that there is sufficient sodium even at room temperature to fill the entire wick without voids. The

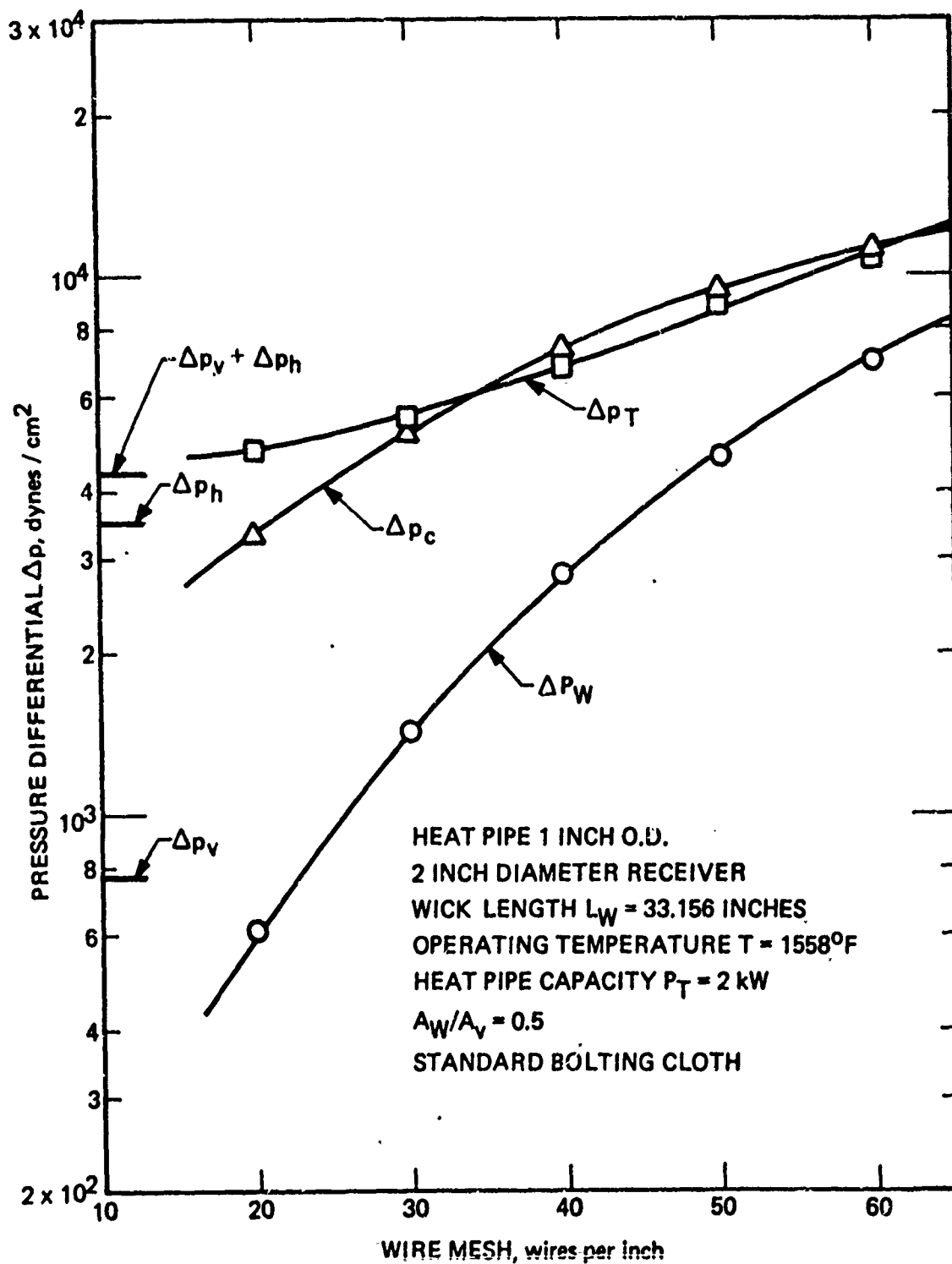


Figure 156. Pressure Drops and Available Pressure for a Heat Pipe Design with a Wick-to-Vapor-Flow Area Ratio of 0.5

50913

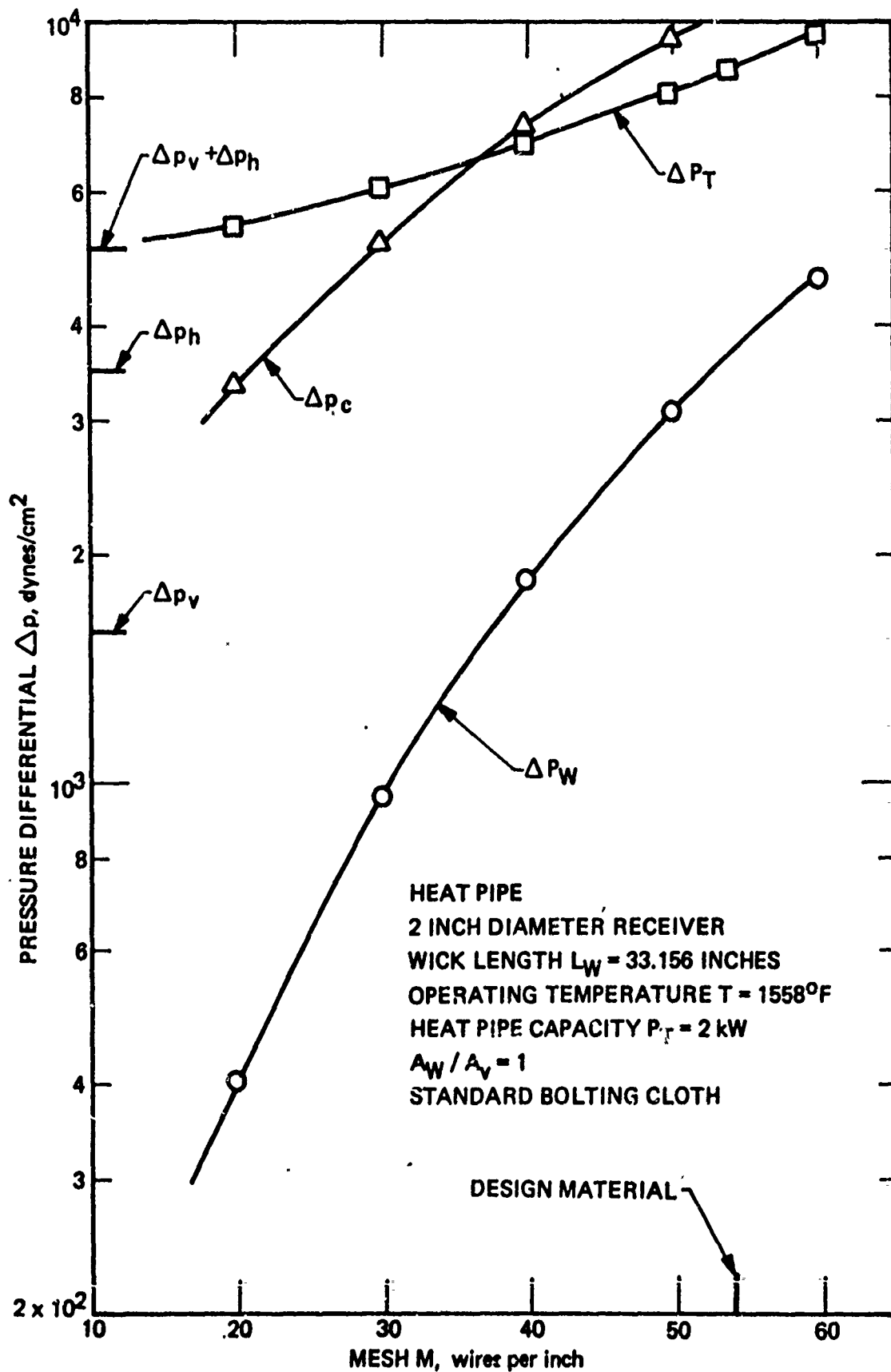


Figure 157. Pressure Drops and Available Pressure for a Heat Pipe Design with a Wick-to-Vapor-Flow Area Ratio of 1

problem is caused by the large change in density of sodium when being heated from room temperature to operating temperature. For this heat pipe design, the approach of filling the heat pipe with the amount of sodium such that the wick would be without voids at the filling temperature of 350°F was taken. It was thought that the amount of sodium that would be displaced from the wick at the operating temperature would not impede the operation of the heat pipe. On the other hand, it was thought that if the heat pipe would be charged with sodium only sufficient to soak the entire wick at the operating temperature, then the wick at the evaporator could possibly be dry during start-up. This naturally could lead to burn out. The heat pipe was therefore to be loaded with 152g of sodium which had the same volume at the filling temperature of 350°F as the free volume of the wick structure.

The receiver was to be a hemisphere with a 2-inch outside diameter enclosed in a radiation shield. Originally, the wall thickness of the receiver was set at $t = 0.062$ inch. During the design it became apparent that there might be an advantage of considering the difference in the thermal loading along the surface of the receiver in specifying the wall thickness. In the center of the receiver, the thermal loading would be maximum while it decreases with the cosine rule towards the edge. It was therefore logical to decrease the wall thickness of the receiver in the center limiting thereby substantially temperature gradients on the receiver surface during operation. Temperature gradients along the receiver surface have to be expected when the backside of the receiver (the evaporator surface) is at a uniform temperature while the frontside (the receiver surface) is exposed to large differences in power input. The final design that evolved for the receiver is shown in Figure 158.

The total power input into the heat pipe was to be about 1,500 watts. It was desirable that the thermal loss from the adiabatic section of the heat pipe would not exceed 20 percent of the total power input at the receiver. Thus, the insulation should be good for a loss of less than 300 watts. The results of simulation calculations are shown in Figure 159 indicating that at the operating temperature of the heat pipe losses of less than 300 watt could be achieved with an insulation thickness of about 0.5 inch. However, in order to achieve faster start-up of the heat pipe which can be accomplished with lower losses from the entire heat pipe, including the condenser section of the heat pipe, it would be attempted to insulate the entire heat pipe for a total heat loss of not more than 300 watts at the operating temperature. The insulation requirement for this case is presented by the upper curve shown in Figure 159. Thus, an insulation thickness of at least 1-inch thick was selected.

8.4 FABRICATION

The receiver was machined from a single piece of Inconel 600. First, the inside of the receiver was rough machined to its approximate dimensions. The final contour was achieved by the Elox process.

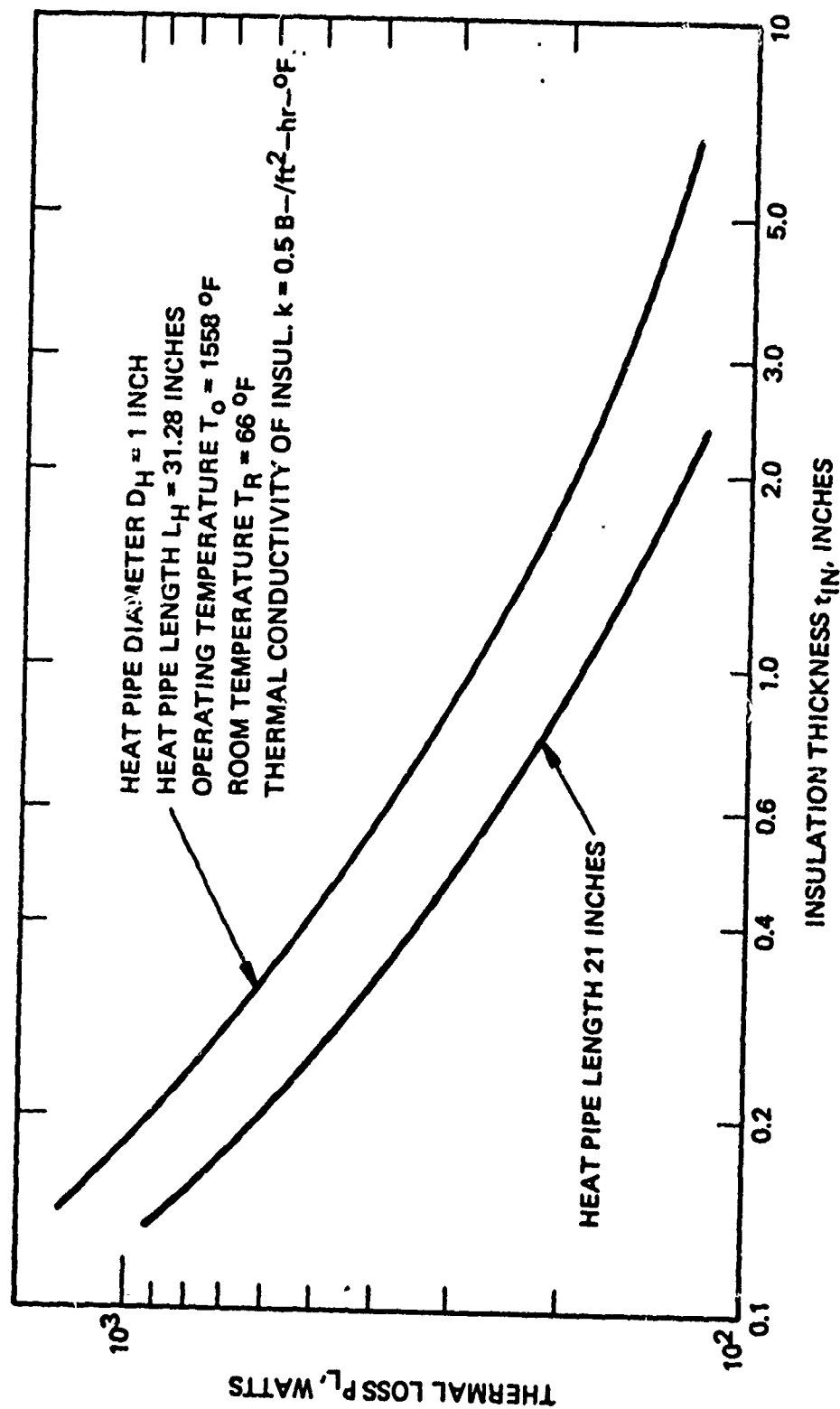


Figure 159. Insulation Requirement for Spherical Receiver Heat Pipe

After final machining the receiver was checked for cracks and imperfections by the Magnaflux process to assure the soundness of the component. For obtaining a uniform surface finish, the receiver surface was then vapor blasted. It was expected that during the initial operation, oxidation of the surface would slowly increase the values of emissivity and absorptivity of the surface. The fully assembled subscale spherical receiver and heat pipe with the heat exchanger are shown in Figures 160 and 161.

Thermocouples were placed along the entire length of the heat pipe and at the back of the cavity as indicated in Figure 162. An auxiliary heater was wound from a calrod unit and placed along the adiabatic section of the heat pipe as shown in Figure 163. Insulation was then installed over the entire heat pipe according to the design calculations.

8.5 FILLING OF HEAT PIPE

For the filling of the subscale cavity heat pipe with the working fluid, sodium, a fill station was assembled which included the sodium supply, pressure gages, a calibrated volume and a vacuum pump. All components which were or would be filled with sodium were traced with heaters and instrumented with thermocouples. The power to the eight heaters could be controlled individually by Variacs, assuring that the desired temperatures could be maintained within the prescribed limits at each point of the system. Argon was used for purging the system. The general setup for charging the heat pipe with sodium is shown in Figures 164 and 165.

Filling of the heat pipe proceeded without difficulty. The heat pipe was weighted prior to and after filling with sodium. The initial weight of the pipe was 2255.4 grams. Fully charged, the weight of the heat pipe was 2404.7 grams. This indicated a sodium weight of 149.3 grams. This was well within the specified weight of 152 ± 10 grams.

8.6 TEST SETUP

After completion of the charging and processing, the subscale cavity heat pipe was installed in the test stand as shown in Figures 166, 167, and 168. A 20-kW irradiation source was built in addition to the 50-kW irradiation source to keep the operating cost to a minimum by using only the least expensive components required for testing. According to the calculations which were based on the latest test results of the radiation source and which became available just prior to testing, radiation efficiencies as high as 12 percent were achieved in the facility. This indicated that a 20-kW source could provide the entire required radiation power for the test of the subscale cavity heat pipe with ease.

11777

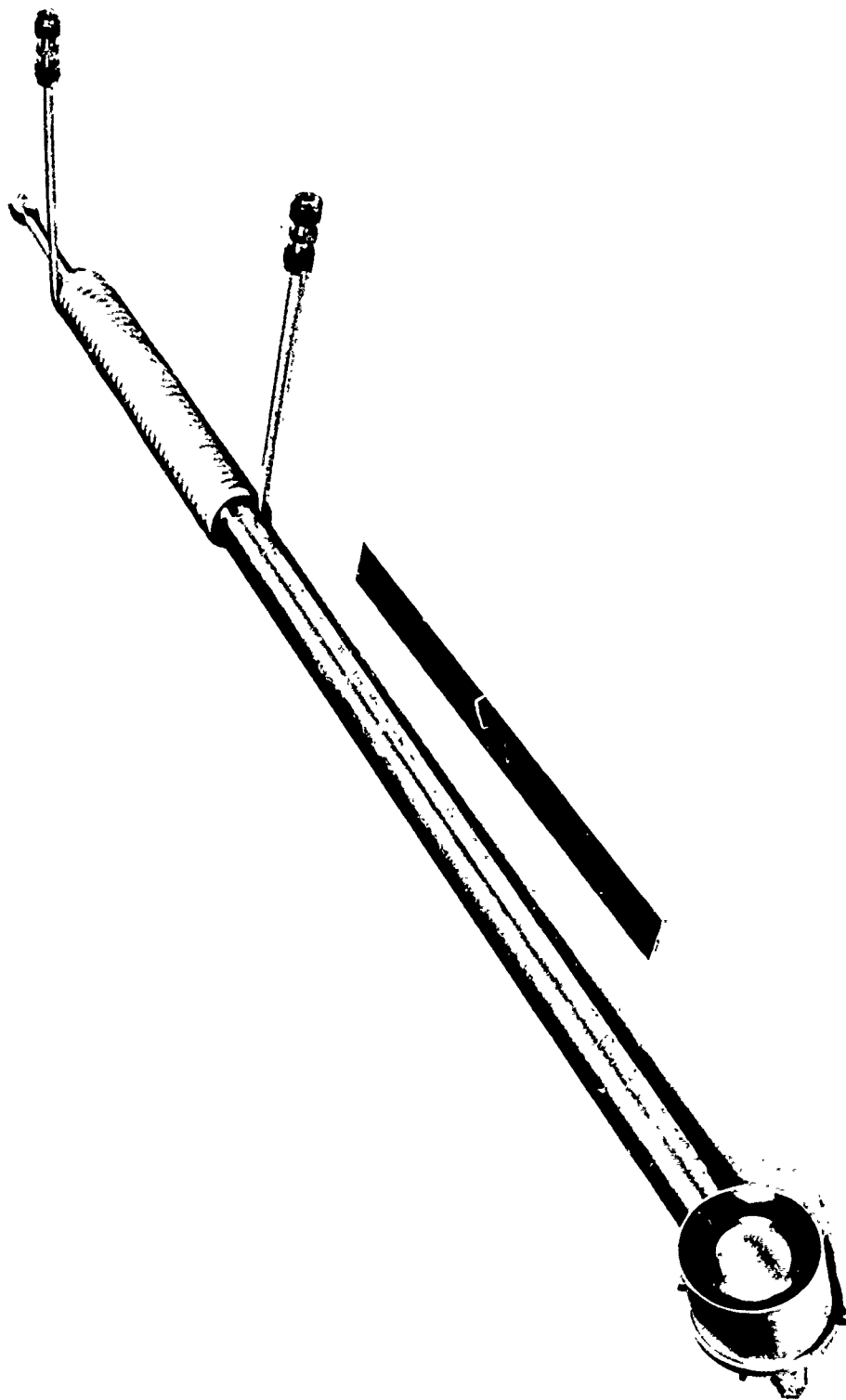


Figure 160. Spherical Receiver/Heat Pipe with Heat Exchanger



Figure 161. Spherical Receiver

117376

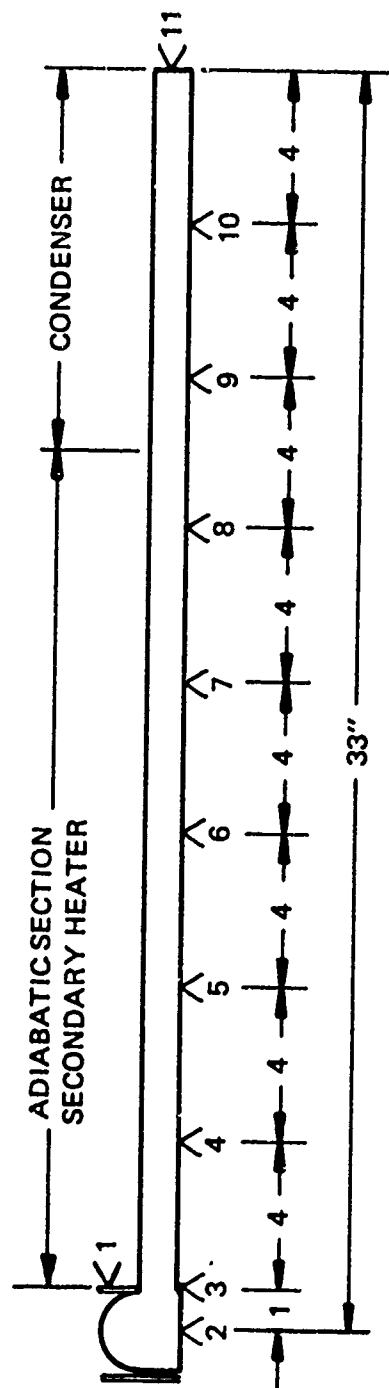


Figure 162. Thermocouple Arrangement for Cavity/Heat Pipe Interface Heat Pipe

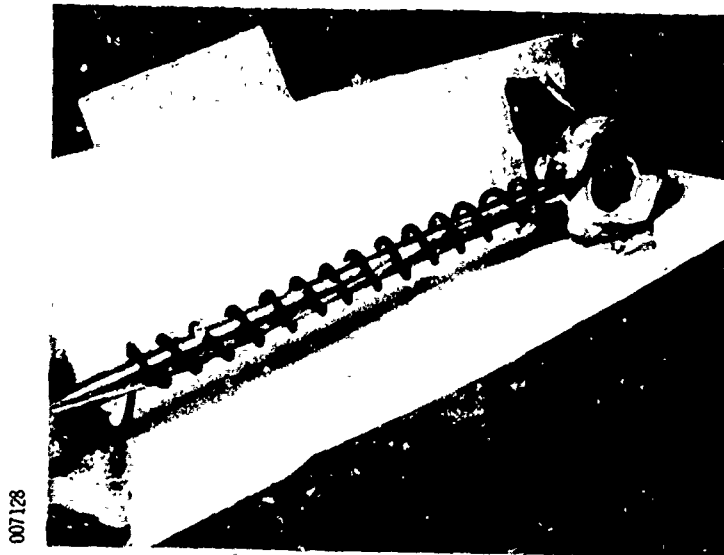


Figure 163. Subscale Cavity Heat Pipe with Auxiliary Heater

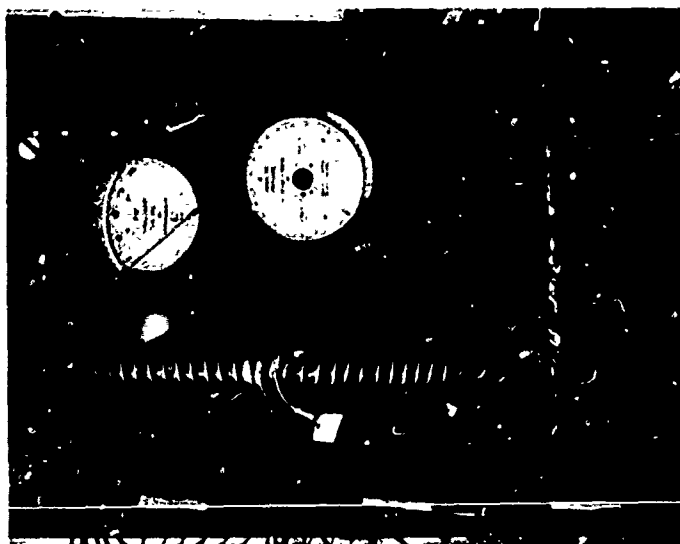


Figure 164. Calibrated Volume and Pressure Gages in Fill Station

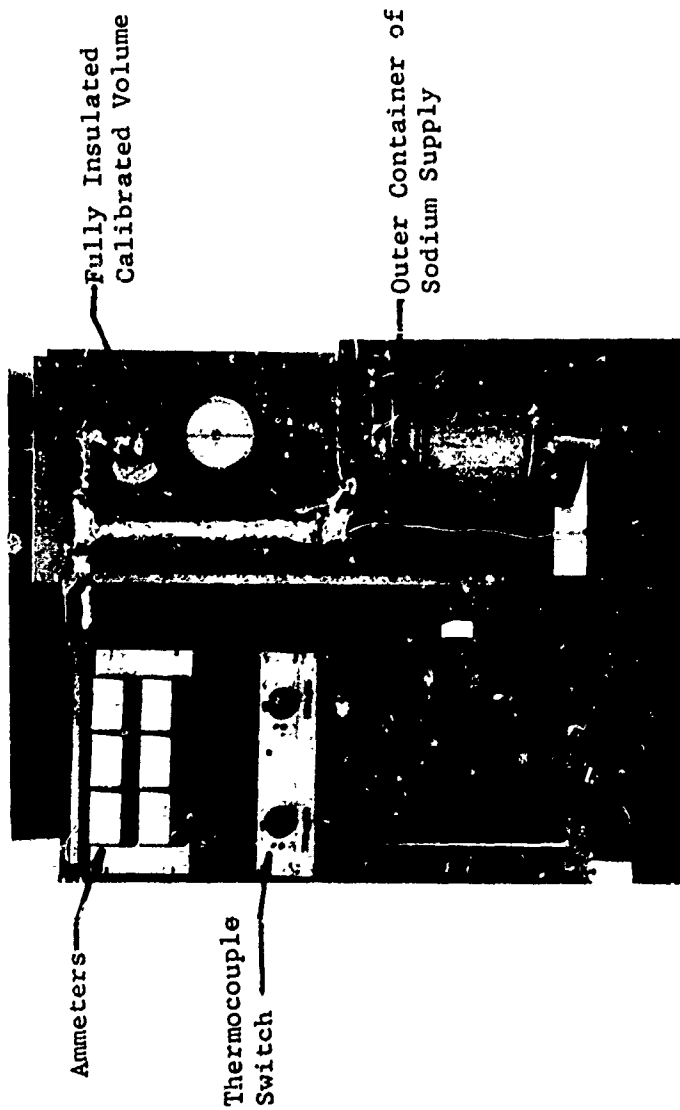


Figure 165. Fill Station

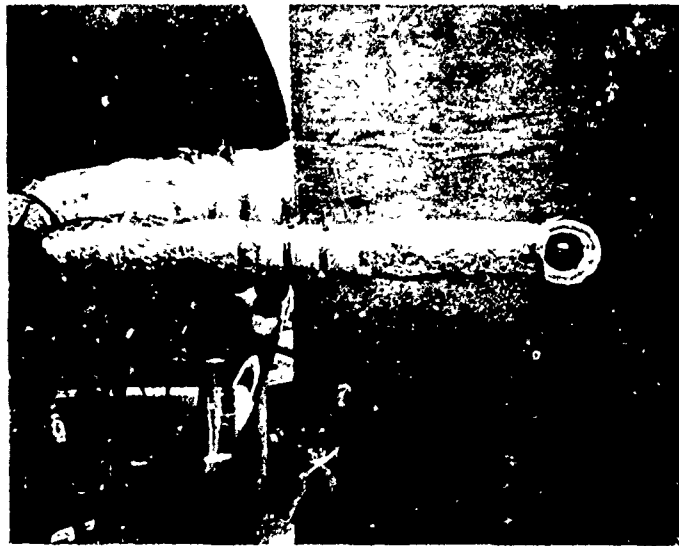


Figure 166. Fully Insulated and Instrumented
Cavity/Heat Pipe

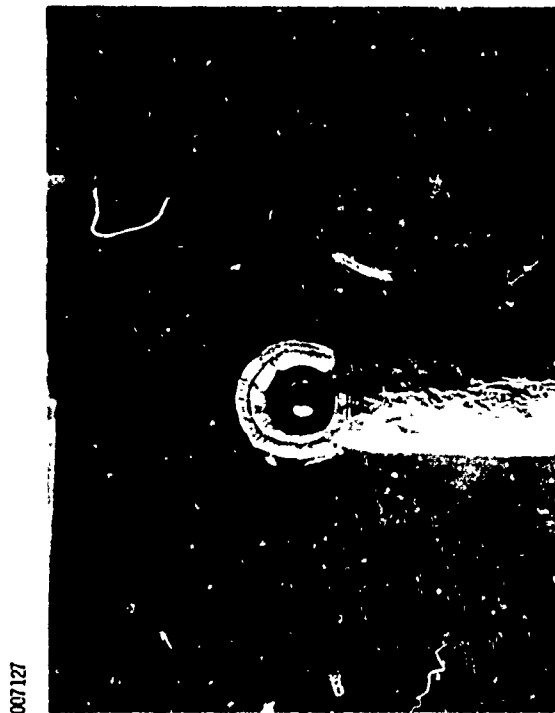
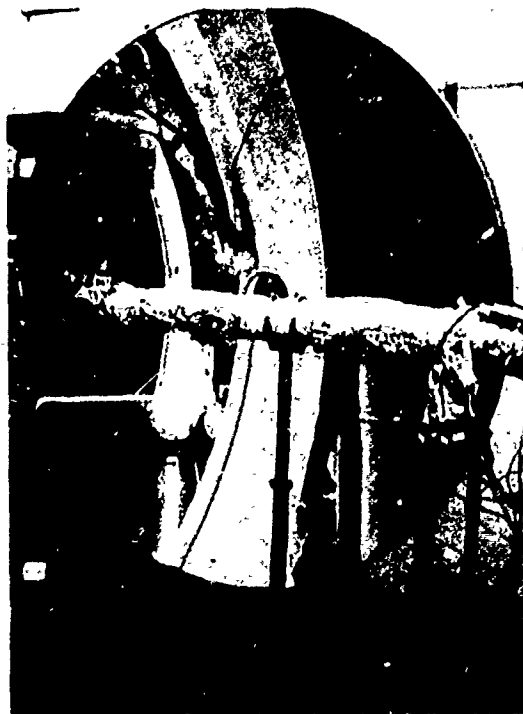


Figure 167. Cavity with Shield and Insulation



007126

Figure 168. Cavity Heat Pipe Test Setup

8.7 TESTING

The experience gained from operating the primary heat pipe, indicated that a full checkout of the heat pipe should be undertaken prior to operating the heat pipe by irradiating the cavity. The initial checkout should establish the capacity of the heat pipe and its transient behavior at full operating temperature. For these tests, the auxiliary heater was used. The heater was also to be employed for bringing the heat pipe to operating temperature prior to exposing the cavity to the irradiation by the radiation source.

In Figures 169 and 170 the temperature distributions of the heat pipe at various input powers are presented as measured by the thermocouples which were shown in Figure 162. The temperature distributions at the lower power input conditions appeared to be consistent with the starting behavior of a high temperature heat pipe, but at the power input of 62.5 watts the temperature distribution exhibited temperature gradients which could not be explained analytically.

When a total power of 1000 watts is transferred through the heat pipe wall and wick at the condenser, the temperature difference between the adiabatic section and the condenser section could not be larger than 21.35°F . Thus, for the conditions experienced at which only a total of 117 watts is applied to the heat pipe, temperature differences of no more than 2°F should have been measured when the heat pipe is fully operational. Temperature gradients along the heat pipe, due to conduction along the heat pipe, could not have been greater than $8.4^{\circ}\text{F}/\text{inch}$ under normal operating conditions.

The analytical results appeared to have pointed to a heat leak in the insulation as the only explanation for the observed temperature gradients. When the outer layer of the insulation was removed, a considerable gap in the insulation joint, at which the thermocouple leads penetrated the insulation, was found. The insulation was replaced and testing of the heat pipe continued. Unfortunately, the apparent fault in the insulation made all the initial test data obsolete and the tests had to be repeated. Since the initial tests were designed to furnish the data for correlating temperature distributions and power losses for the heat pipe, and thus establishing the characteristic of the heat pipe, steady state conditions had to be achieved again prior to taking each data point.

After the improvement in the insulation of the heat pipe, some changes in the operation of the heat pipe were observed which, however, were not substantial. The thermal gradients still persisted, as shown in Figure 171. In Figure 172 the effect of the total power input on the temperatures at the various locations along the heat pipe is shown. All temperatures increased consistently with increasing power input to the auxiliary heater, but the relative temperature differences along the heat pipe remained almost constant. Prior to operating the heat pipe with the radiation source, the cause for this nonuniformity of the temperature distribution

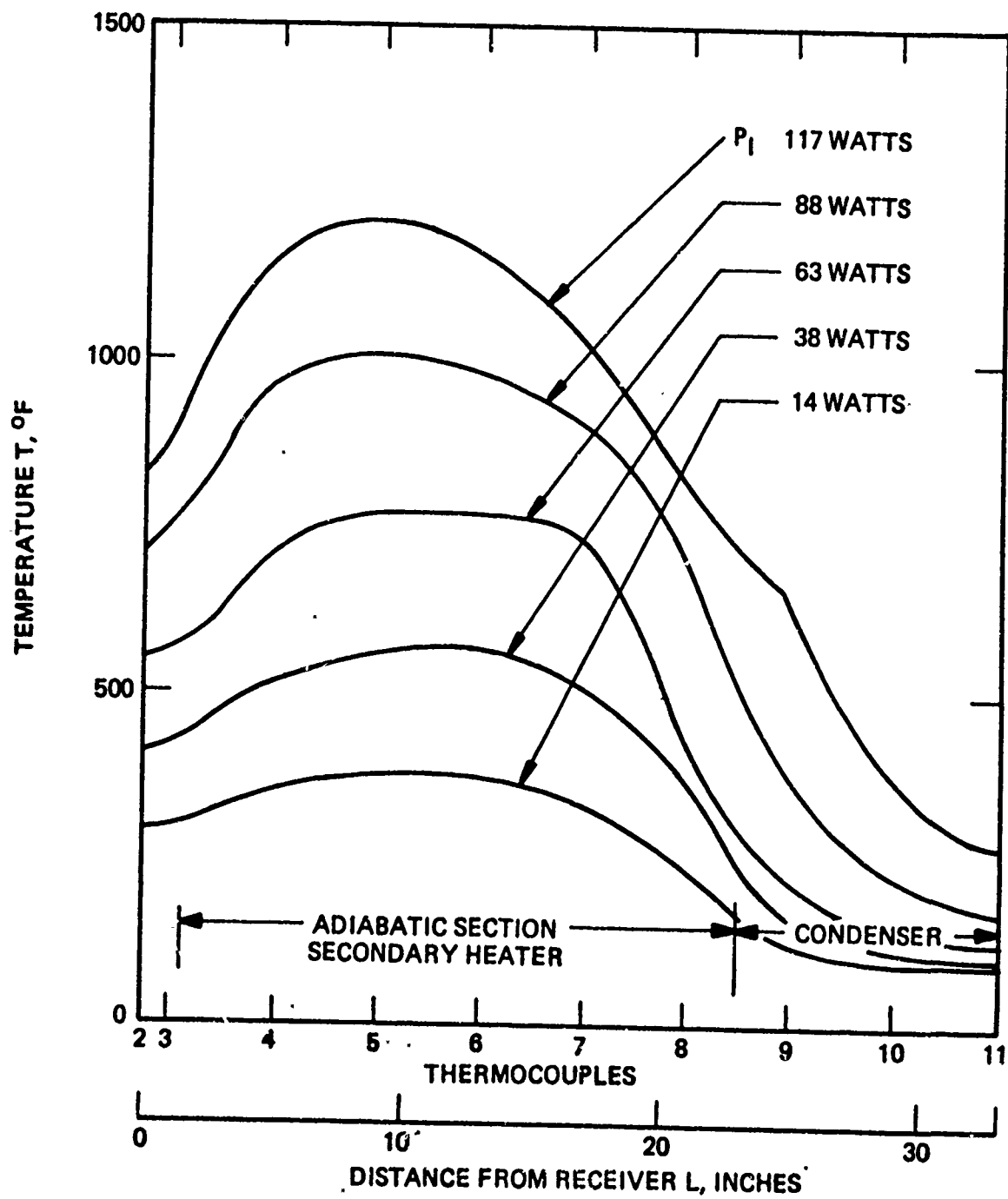


Figure 169. Temperature Distribution Along Subscale Cavity Heat Pipe

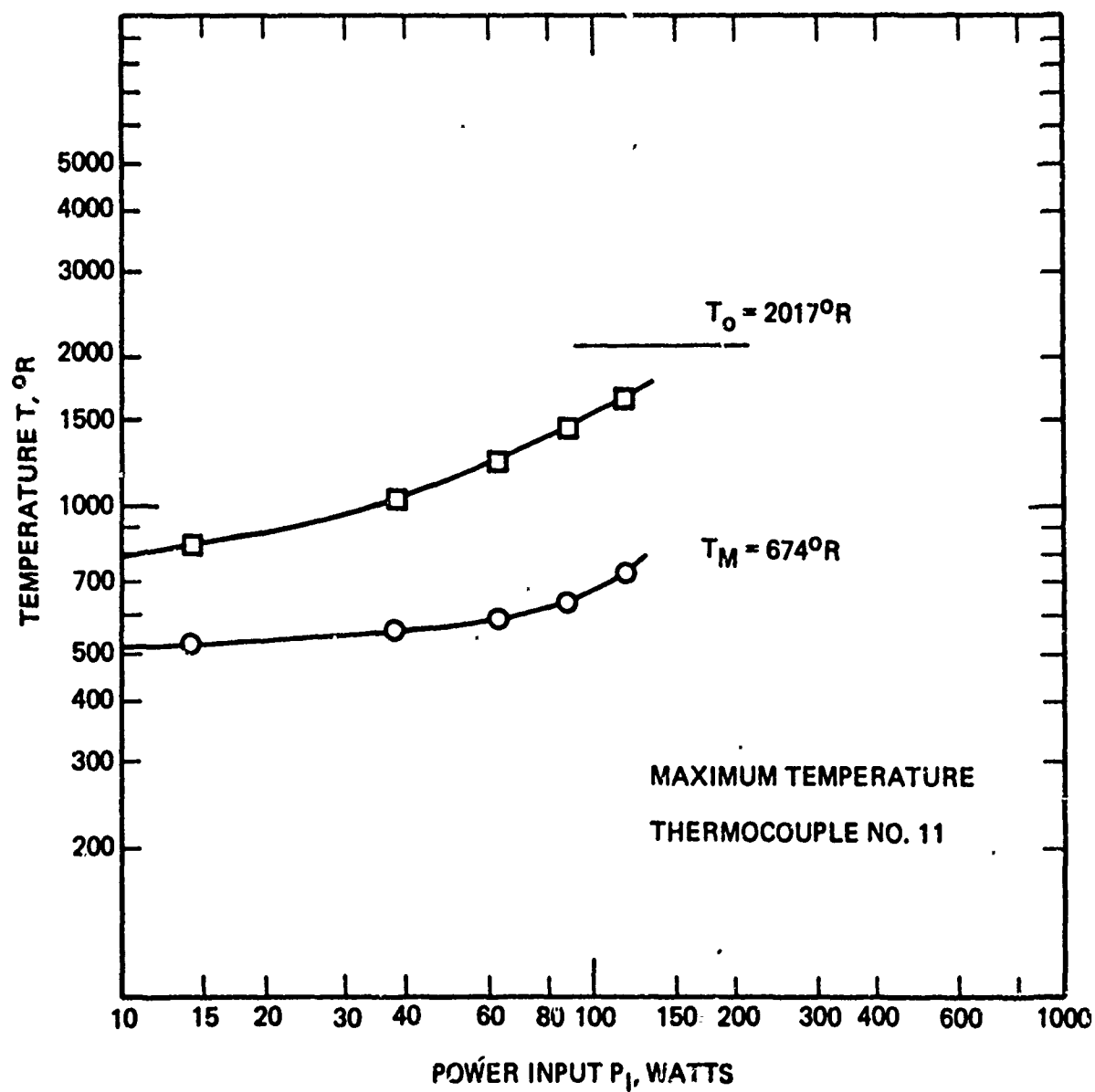


Figure 170. Temperature Distribution Along Subscale Cavity Heat Pipe

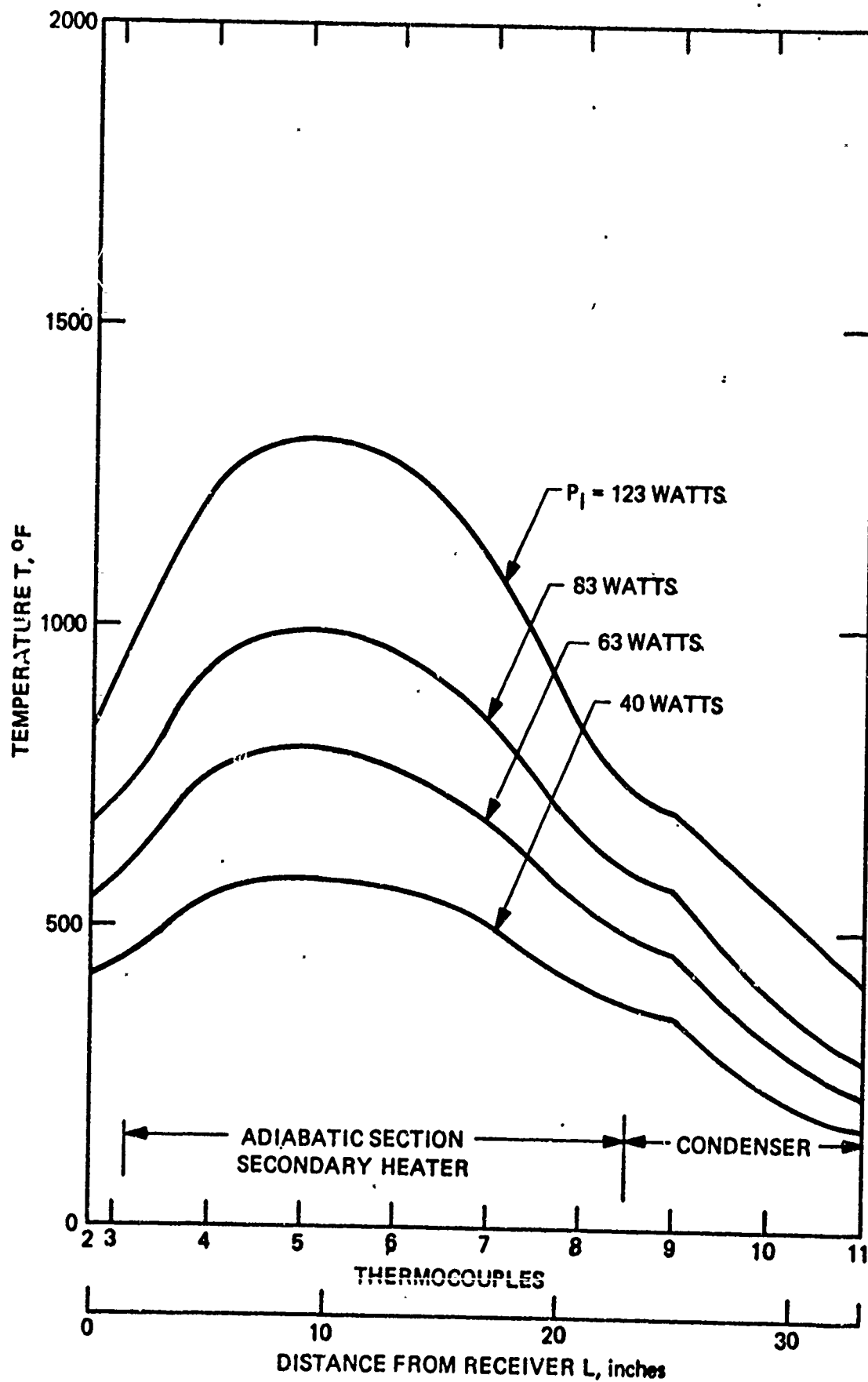


Figure 171. Temperature Distribution Along Cavity Heat Pipe After Improvement of Insulation

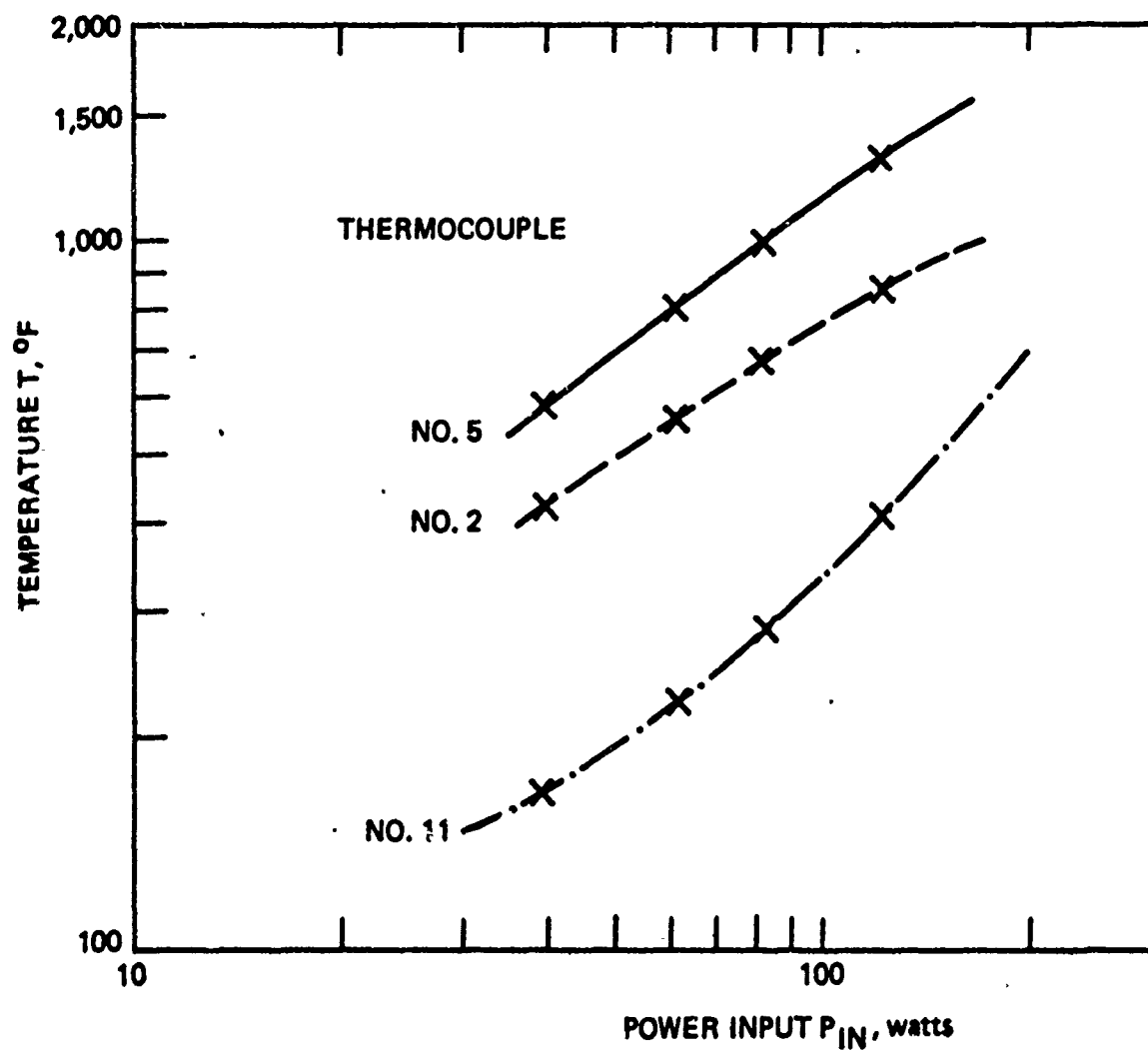


Figure 172. Temperature Distribution Along Subscale Cavity Heat Pipe

along the heat pipe had to be corrected. It had to be expected that with the total power input concentrated on the receiver, which is located near thermocouple #2, the temperature difference between the hottest spot of the heat pipe and the coolest spot would have been even larger.

The measured temperature distributions along the heat pipe could possibly be attributed to the overfill of the heat pipe with sodium which had to be eliminated. A volume was attached to the valve of the fill pipe at the condenser end of the heat pipe. The volume was purged with argon and evacuated. When the heat pipe reached its operating temperature the valve between the heat pipe and the volume was opened. Excess sodium was transferred into the volume. After the relief of the heat pipe, the temperature distribution changed immediately and became very uniform. Steady state temperature distributions at four power inputs were taken which are shown in Figure 173. The data should be compared with the temperature distributions presented in Figures 171 and 172. The correlations between the power input and temperatures along the heat pipe are shown in Figure 174, verifying the consistency of the test data.

With the subscale cavity heat pipe operating uniformly, the first power transfer tests were conducted with power input provided by the auxiliary heater. The extracted power at the condenser section of the heat pipe, was determined from the temperature increase and the flow rate of the cooling air. For measuring the flow rate, a 0.052 inch orifice was built which was calibrated for subsonic flow. This calibration had to be performed quite accurately as the flow rate is a function of the product of the difference and the sum of the upstream and downstream pressures of the orifice. The difference had to be relatively small compared to the absolute pressures because of the adverse combination of a limited available air pressure of only 100 psig and a relatively large pressure drop in the cooling coil. Small errors in the absolute pressures could therefore introduce substantial errors in the pressure factor

$$f_p = \{(p_1 + p_2) \times (p_1 - p_2)\}^{1/2}$$

The calibration data are shown in Figure 175. Pressure measurements between upstream pressure p_1 and downstream pressure p_2 , during tests are shown in Figure 176. The scatter indicated in Figure 176, though relatively small, could have introduced a very large scatter in the determination of the flow rate if the measurements had not been smoothed out.

In Figure 177 the input power supplied by the auxiliary heater, the power losses and the extracted power at the condenser are correlated. Under these conditions the heat pipe operated very consistently and the instrumentation appeared to function well. The scatter of the data is relatively small when considering the large time constant of the system. For improved data each test run would have had to be extended over a 24-hour period which did not seem to be justified as these tests were only designed to check out the heat pipe and the instrumentation.

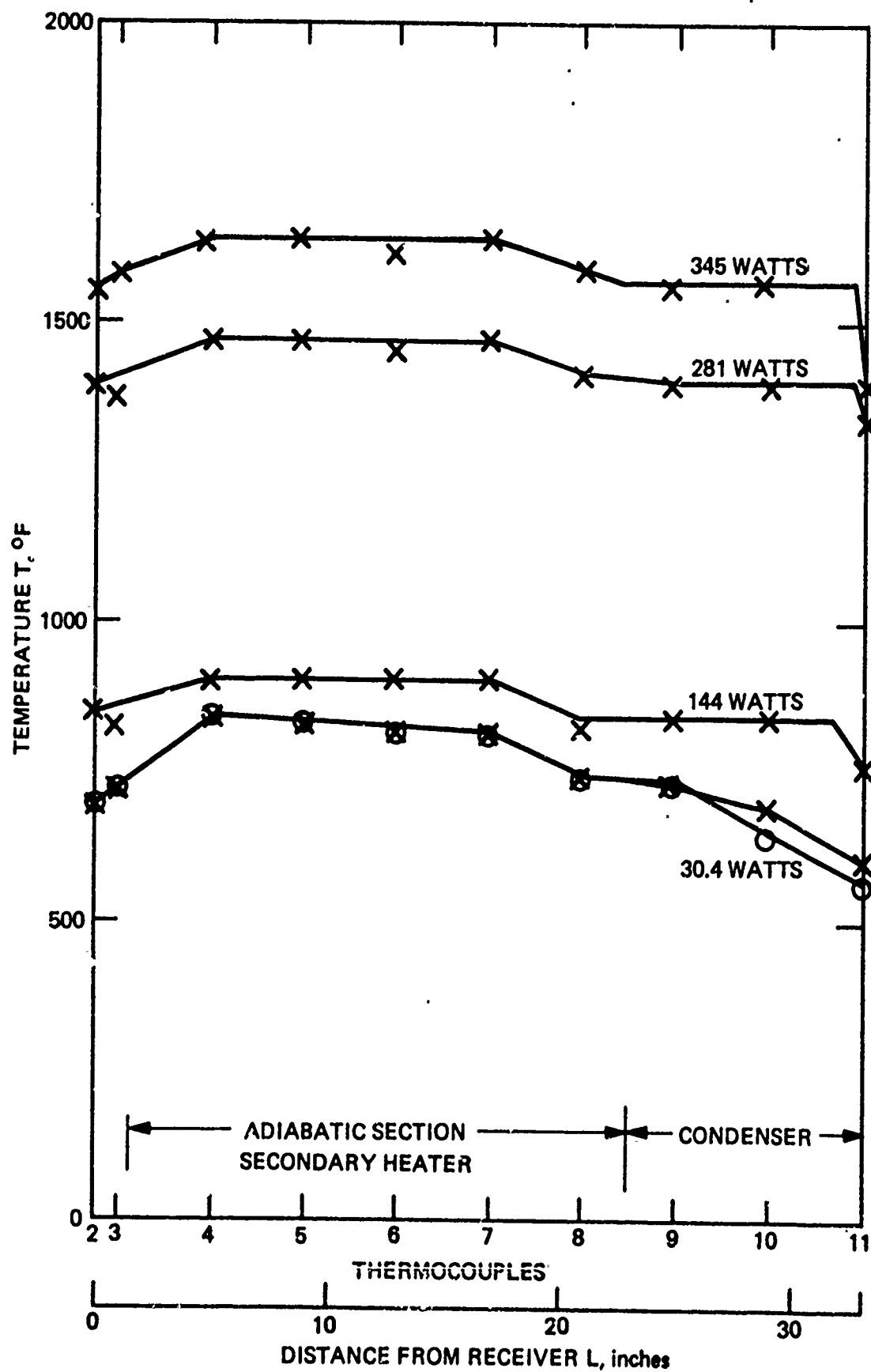


Figure 173. Temperature Distribution at Steady State for Subscale Cavity Heat Pipe

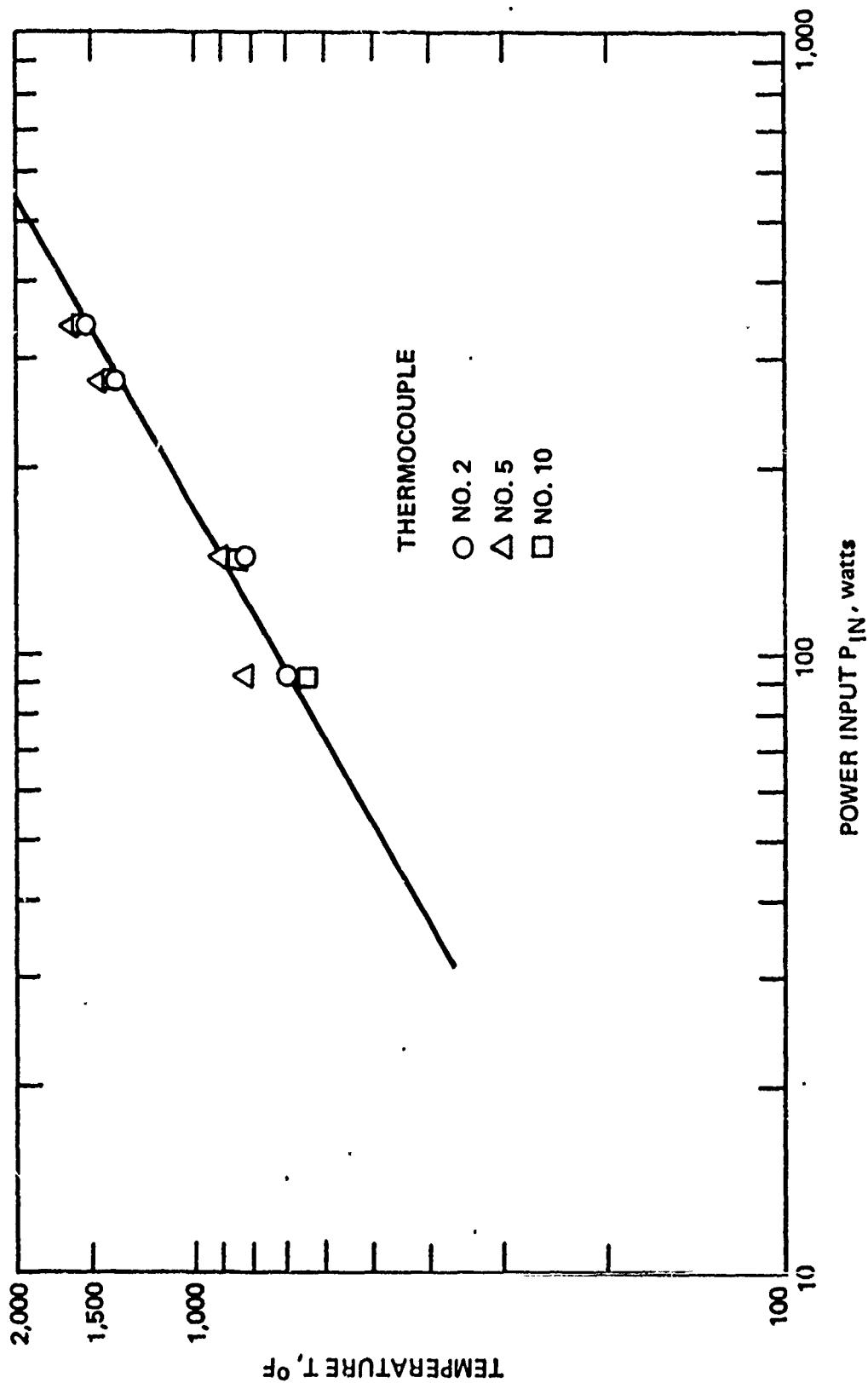


Figure 174. Temperature Distribution Along Subscale Cavity Heat Pipe

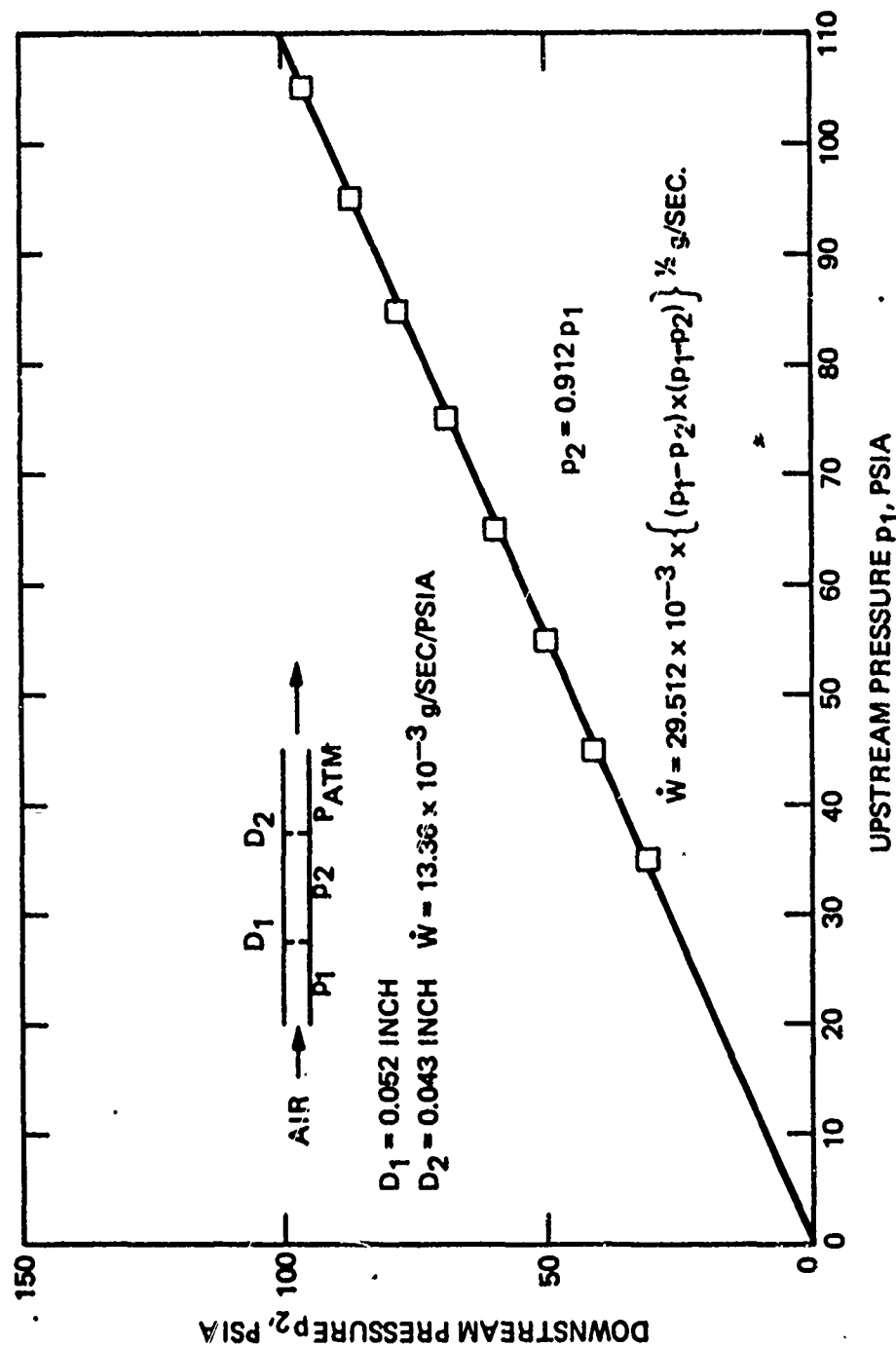


Figure 175. Calibration of Orifice for Subsonic Flow

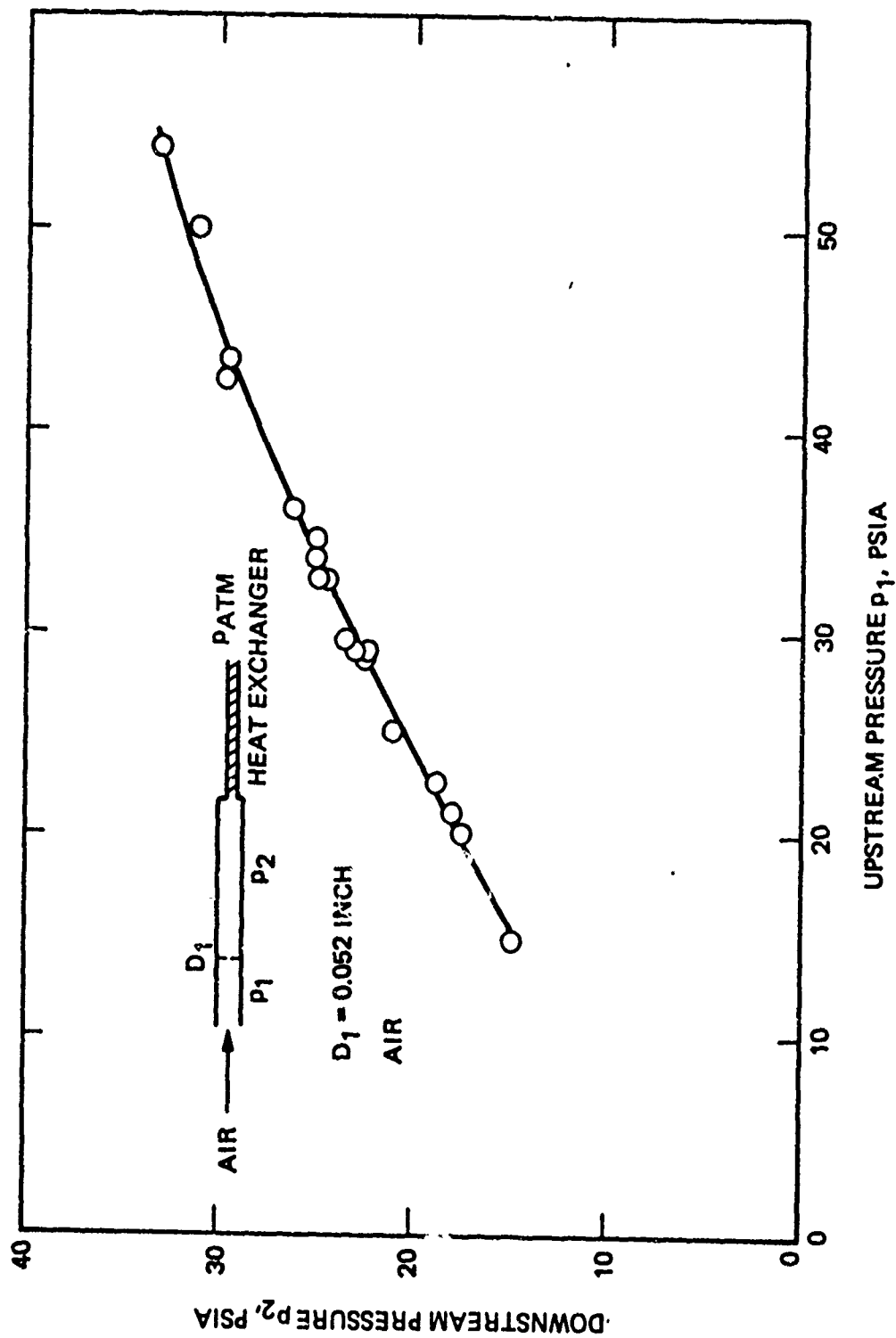


Figure 176. Experimentally Established Correlation Between Upstream Pressure and Downstream Pressure of Measuring Orifice

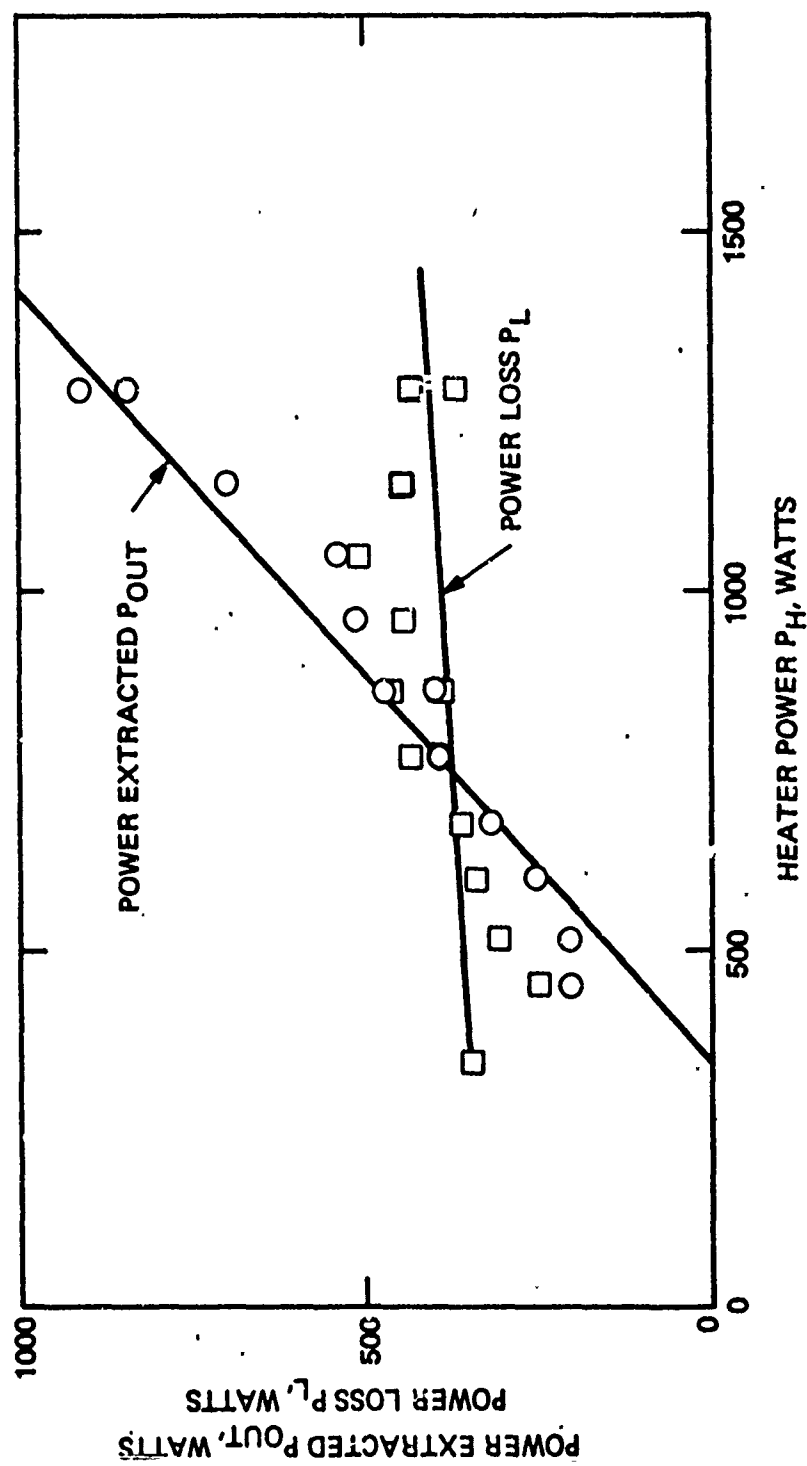


Figure 177. Measured Correlation Between Power Input, Power Losses and Power Extraction at Condenser

After the initial check-out test had been completed with the auxiliary heater, the subscale cavity heat pipe was operated with the radiation source. A radiation loss of 145 watts from the cavity had been calculated. With the cavity insulated the heat pipe was losing 345 watts at the operating temperature. When the cavity was uncovered for testing, the auxiliary heater power had to be raised. Steady state conditions at the operating temperature of 1558°F were achieved with a total power input of 485 watts indicating a loss of 140 watts from the cavity. The auxiliary power was turned off and the radiation source started. A typical temperature distribution with the heat pipe operating entirely with the radiation power impinging on the cavity receiver is shown in Figure 178. The temperature distribution remained flat for all power inputs. In Figure 179 the results of the entire test series are shown.

8.8 CONCLUSION

The design, fabrication, and testing of the subscale cavity receiver with the heat pipe produced a considerable amount of valuable information which was later useful in the design, fabrication, and testing of the second primary heat pipe. During the initial testing of the subscale heat pipe with the auxiliary heater, the detrimental effect of surplus sodium on heat pipe operation was dramatically established. Any sodium which is not contained in the wick during power transfer apparently blocks the heat transfer at the condenser which leads to large temperature differentials along the heat pipe.

The cavity was exposed to radiation heat loads which were close to those for which the cavity of the space system will be designed. The cavity and the heat pipe operated consistently up to an apparent radiation power input of 1685 watts. For the projected receiver area of 20.258 cm², the average power density was therefore 83.18 watt/cm². For these conditions, the radiation power of the radiation source was apparently only 8.85 percent. This efficiency appears to be quite low. It is therefore possible that the actual radiation power was higher and that a power density of 89.125 watt/cm² as seen by the cavity in the solar collector system was exceeded by a considerable margin.

The subscale cavity with the heat pipe established that the concept of collecting solar radiation energy with a parabolic collector and focusing it on a receiver surface, which is cooled by the evaporator of a heat pipe which conducts the thermal energy to a condenser, is viable as a power system for thermal power.

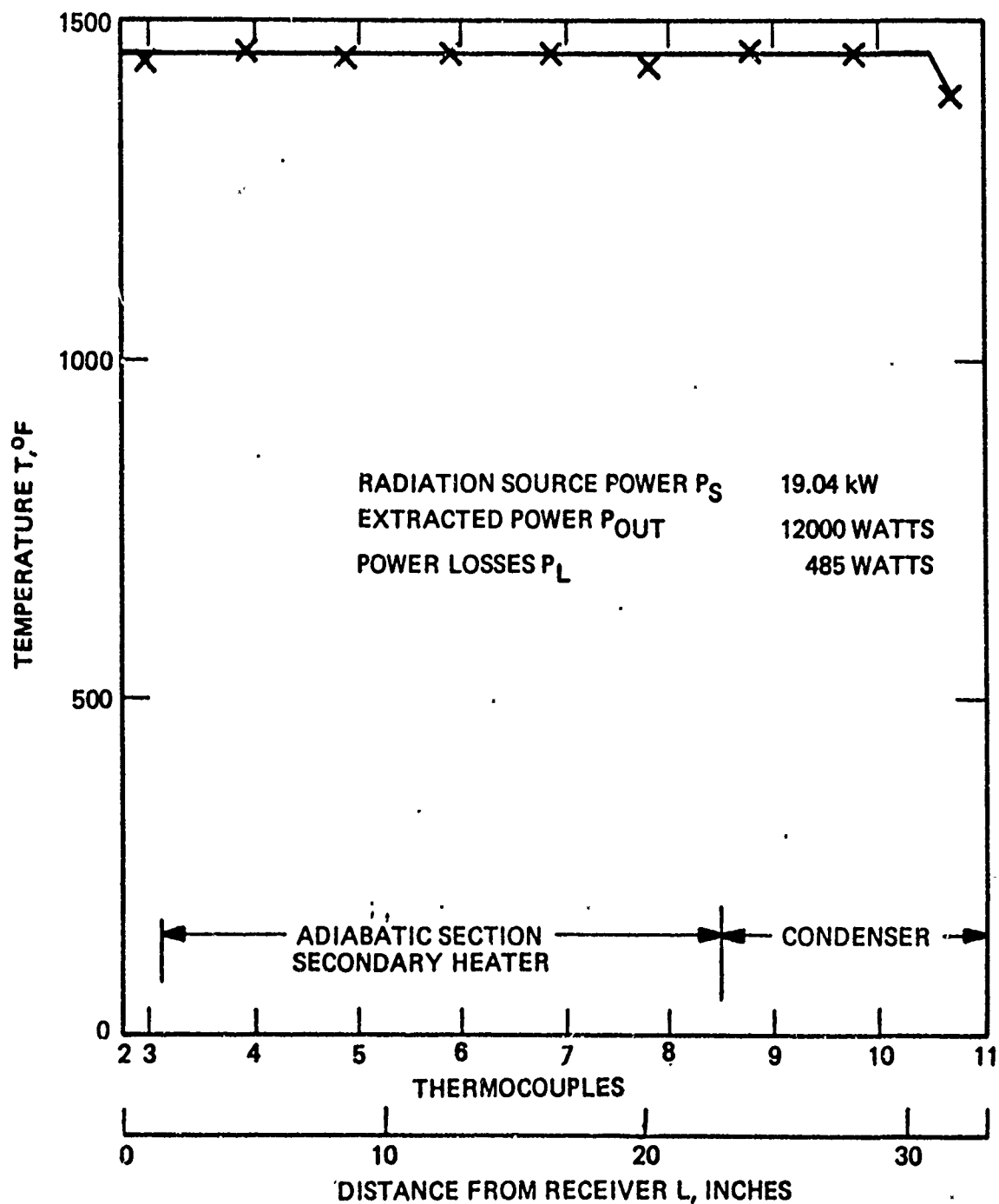


Figure 178. Temperature Distribution Along Cavity Heat Pipe During Radiation Test

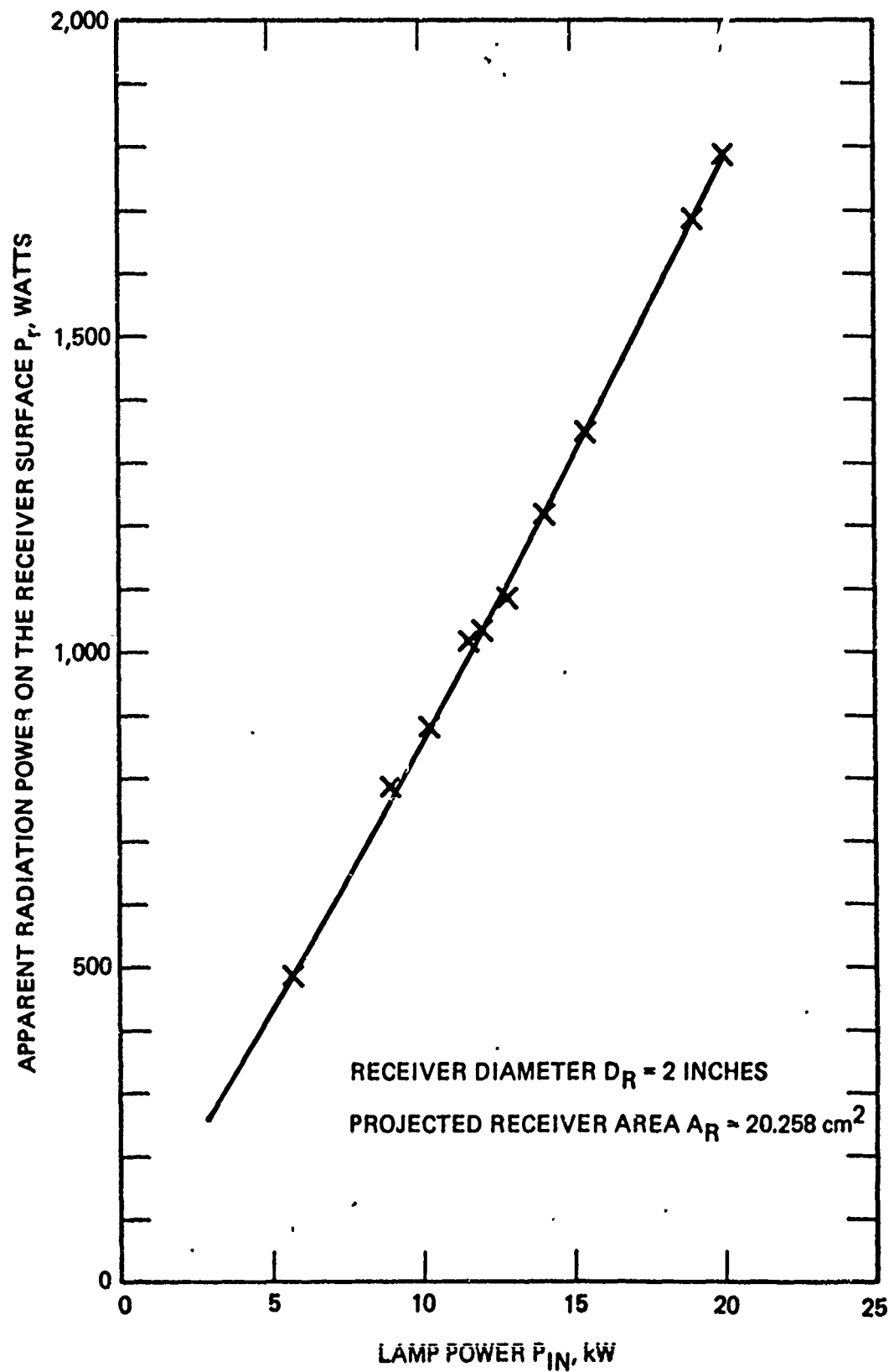


Figure 179. Apparent Radiation Power on the Cavity Receiver as Function of Power Input into the Radiation Source.

50899

SECTION IX

EXPERIMENTAL WICK STUDY

9.1 INTRODUCTION

The wick study was conceived for generating data for the design of the diametrical wick of the primary heat pipe. Test data generated with the first primary heat pipe and an analysis of the as-built wick indicated that the effect of several important parameters of the wick were not well understood despite the fact that they strongly effect the power transfer capability of the primary heat pipe. The most important parameter appeared to be the permeability of the wick material in the as-built structure of the wick. The analysis indicated that the permeability could not only be a function of the mesh and the wire size of the wire cloth, but that the density to which the wick material has been compressed must also have a major effect. A small program for evaluating the diametral wick permeability experimentally was laid out in support of the redesign of the primary heat pipe.

9.2 EXPERIMENTAL SETUP

A fixture was designed by which the effect of compressing the wick could be tested. A diametral wick, built-up of layers of bolting cloth, could be placed into a cavity which was about 21 inches long and 1.5 inch wide. The height of the cavity, which would be equal to the diametral wick thickness, could be adjusted by the use of shims. The largest height was 0.75 inch. Layers of the wick material were placed into the cavity so that the uncompressed height was equal to the 0.75 inch. The non-compressed thickness of a wick was defined by the relation

$$t_w = 2 \times N \times d$$

where

$$t_w = \text{diametral wick thickness}$$

$$N = \text{number of layers of bolting cloth}$$

$$d = \text{wire diameter}$$

The permeability of the wick was determined by the pressure drop across the 21 inch long wick and the water flow rate. Variations in the wick configuration were obtained by either compressing the wick material by the addition of a shim or by adding or removing layers of wick material and adding a shim. Tests were conducted with screen material varying in

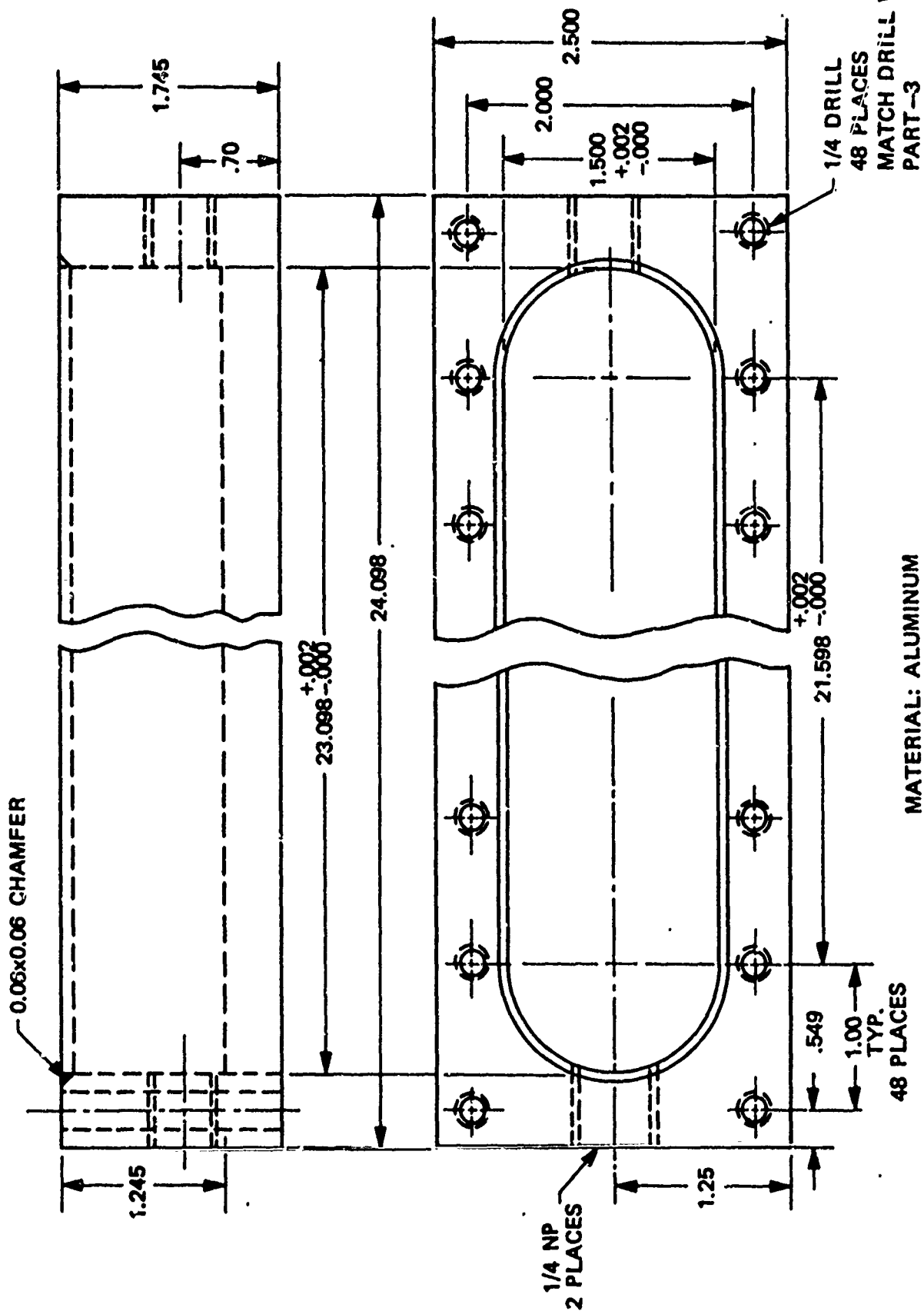
mesh size and wire diameter. The wick test fixture is shown in Figures 180 through 183. The test fixture and representative diametral wicks are shown in Figure 183. The test fixture comprised the main body, the insert and the lid. The wick, consisting of several layers of bolting cloth, was folded to a width of 1.5 inches. A representative wick, made of 62 mesh bolting cloth and having a wire size of 0.0045 inch diameter, is shown below the main body while a wick made of bolting cloth of 24 mesh with a wire diameter of 0.075 inch is shown below it. The main body is closed with the insert which seals against the main body with an "o" ring. The insert has Swagelok fittings at both ends to permit installing pressure measuring devices. Below the insert are shown the three shims which could compress the wick to three packing factors. At the bottom is the lid which holds the insert and shims in place. The flow test set up is presented schematically in Figure 184 and the laboratory set up is shown in Figure 185.

At the low flow rates, which are representative of the flow condition in the wick of the primary heat pipe, the pressure differential between the inlet and outlet of the wick were measured by the level difference of the water in the glass tubes which are placed into the Swagelok fittings. At high flow rates and large pressure drops across the wick, the pressure differential was measured with a pressure differential meter.

Low flow rates were determined by weighing the amount of water flowing during a measured length of time. High flow rates were measured by the pressure differential across a calibrated sharp orifice.

Wicks were tested at low and high flow rates though the data required were only for laminar flow conditions. Testing at high flow rates was performed to determine the general behavior of wicks made of bolting cloth. In Figure 186 the results of tests performed with a wick made out of 24 mesh bolting cloth having a wire diameter of 0.0075 inch are shown. In this figure, the laminar as well as the turbulent flow tests are shown. In the turbulent flow regime the flow rate per unit flow area is decreased by about 34 percent when the wick material has been compressed by 75 percent.

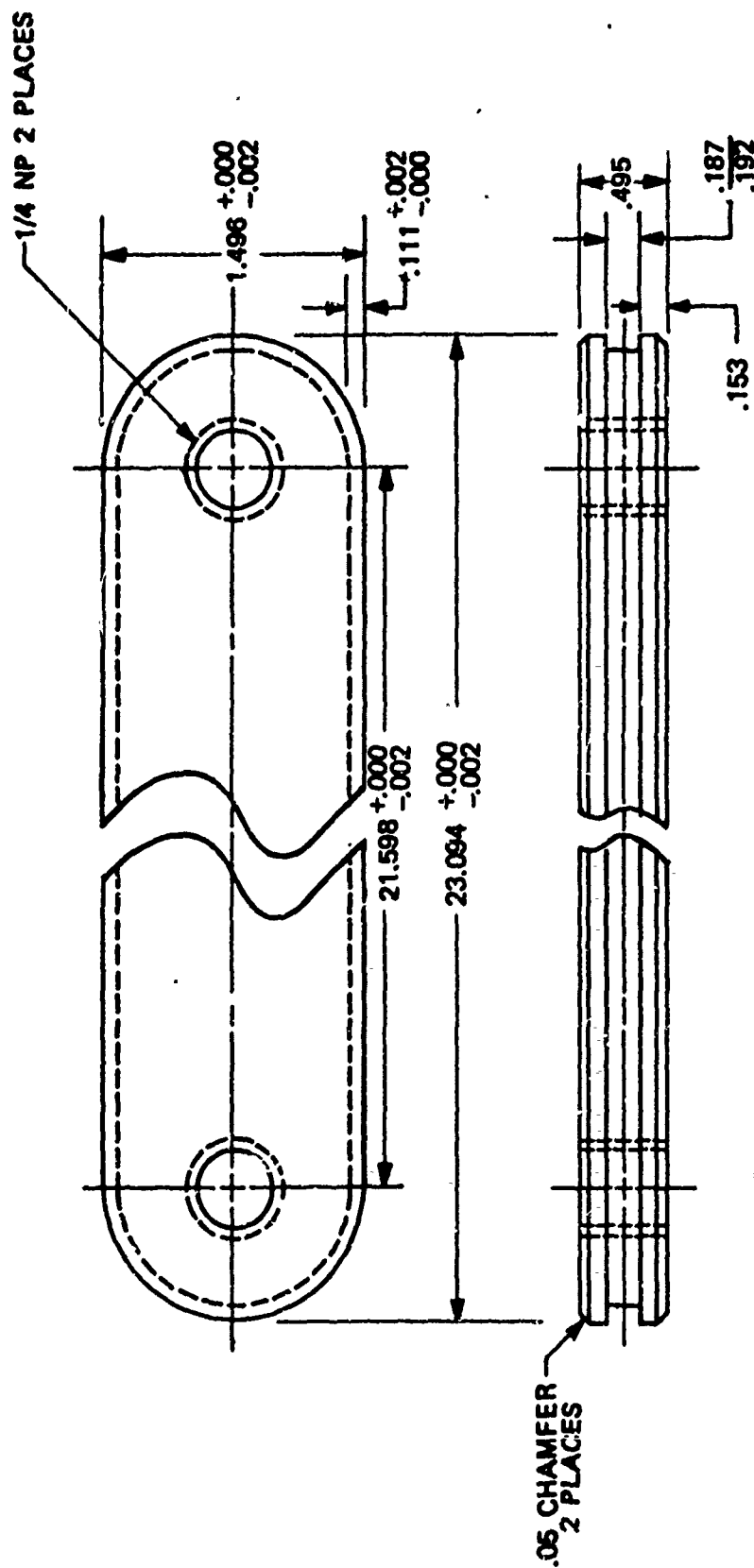
Turbulent Flow $\Delta P = 10 \text{ psi}$				
<u>Shim</u>	<u>Flow Rate</u> <u>lb/sec</u>	<u>Flow Area</u> <u>inch²</u>	<u>\dot{W}/A</u> <u>lb/sec-in²</u>	<u>$\dot{W}/A_1 / \dot{W}/A_2$</u>
0	0.65	1.5 x 0.75	0.5778	1
0.1875	0.32	1.5 x 0.5625	0.3793	0.66



MATERIAL: ALUMINUM

Figure 180. Wick Study Fixture

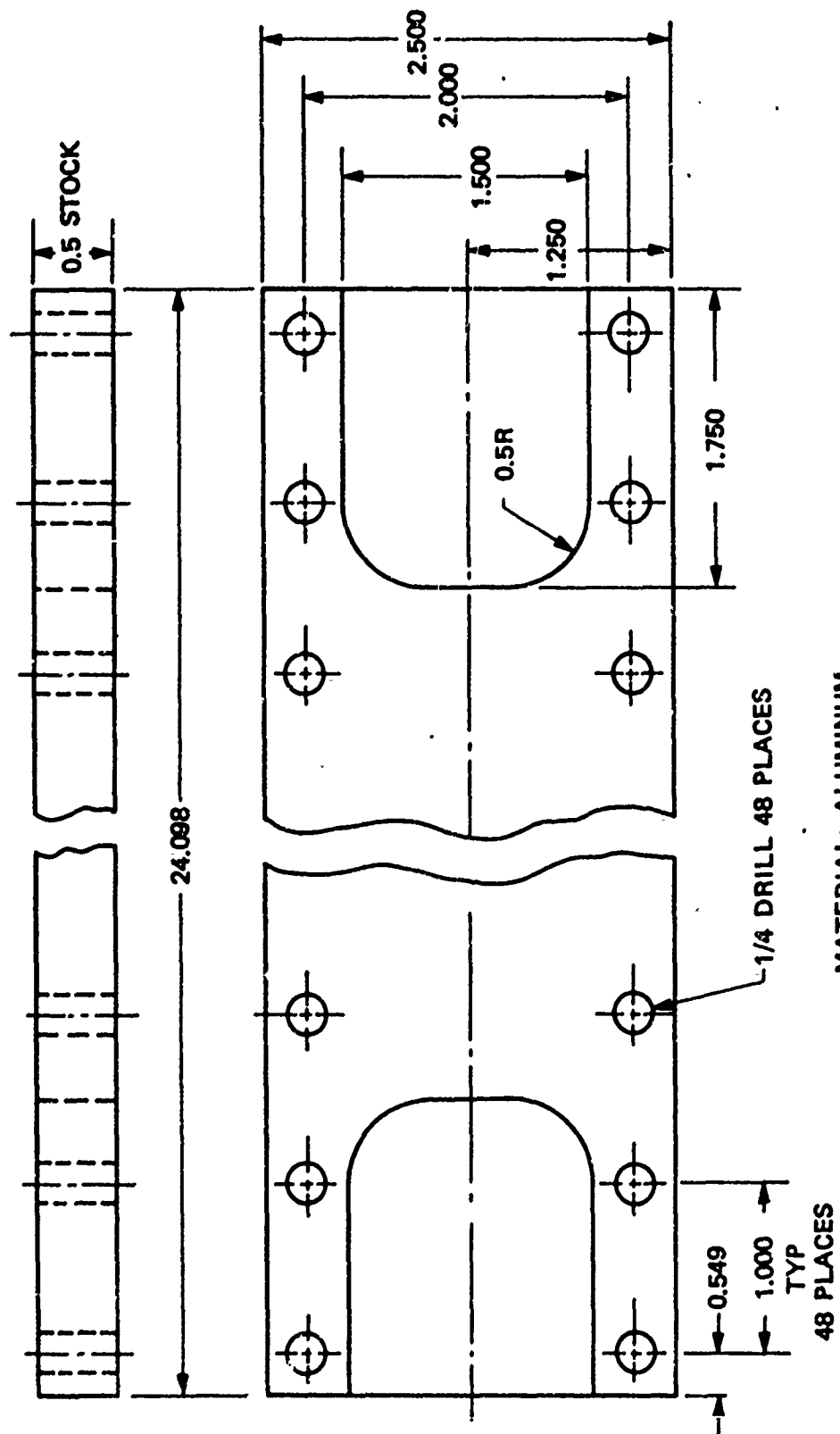
50862



MATERIAL: ALUMINUM
"O" RING 2 - 281

Part 2 of 3

Figure 181. Wick Study Fixture



MATERIAL: ALUMINUM

Part 3 of 3

Figure 182. Wick Study Fixture

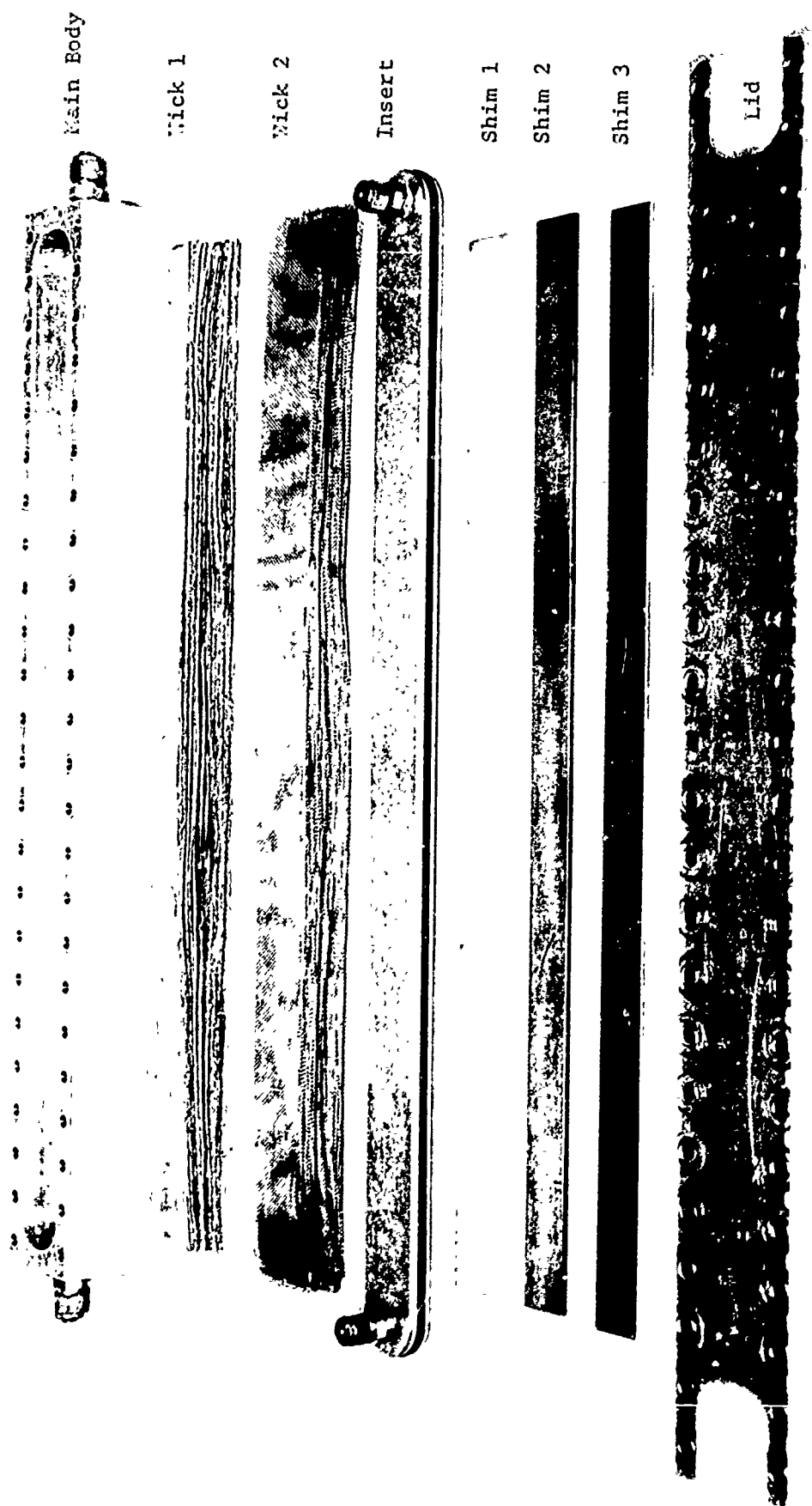


Figure 183. Wick Study Test Fixture

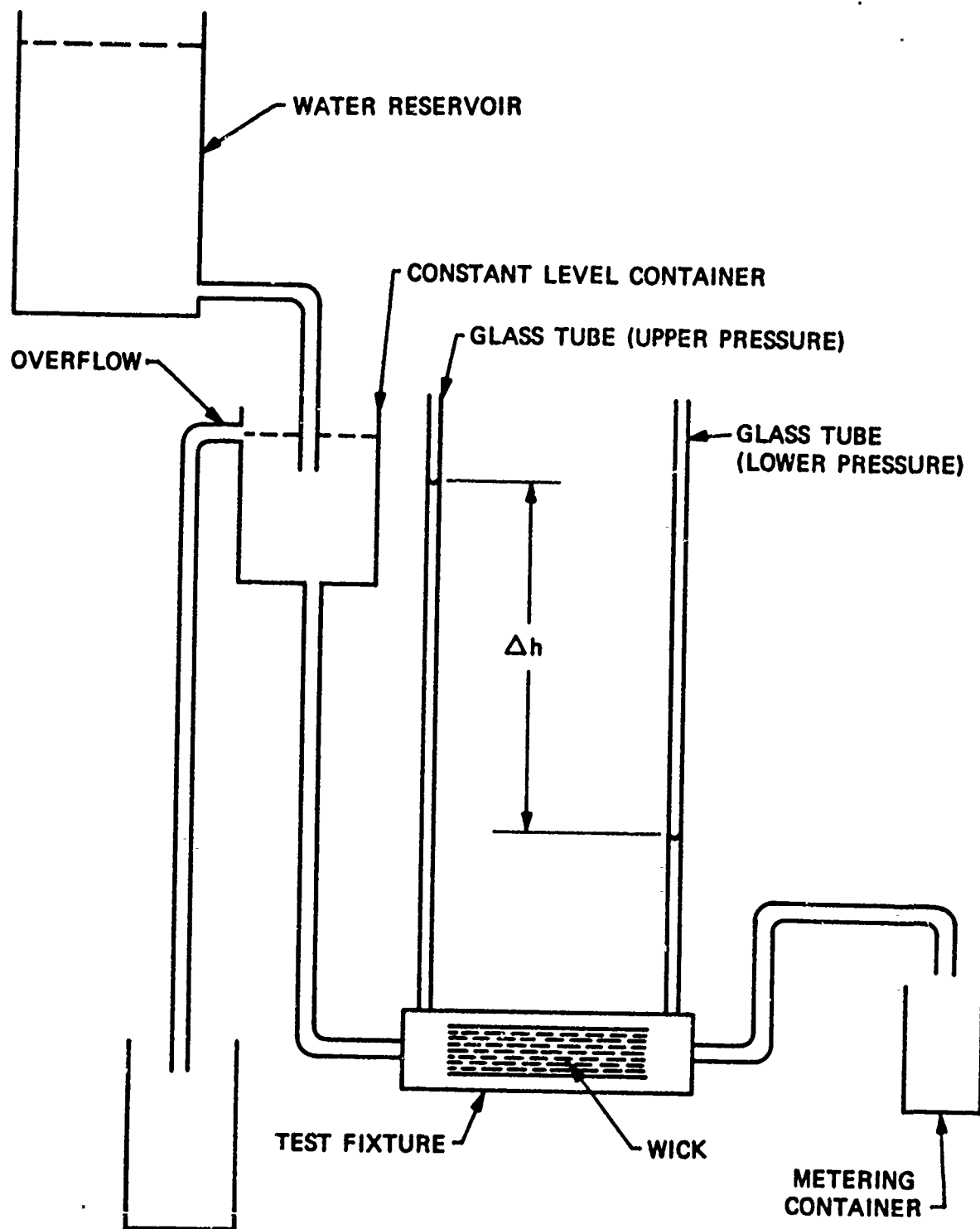


Figure 184. Wick Study Setup Schematic

006831

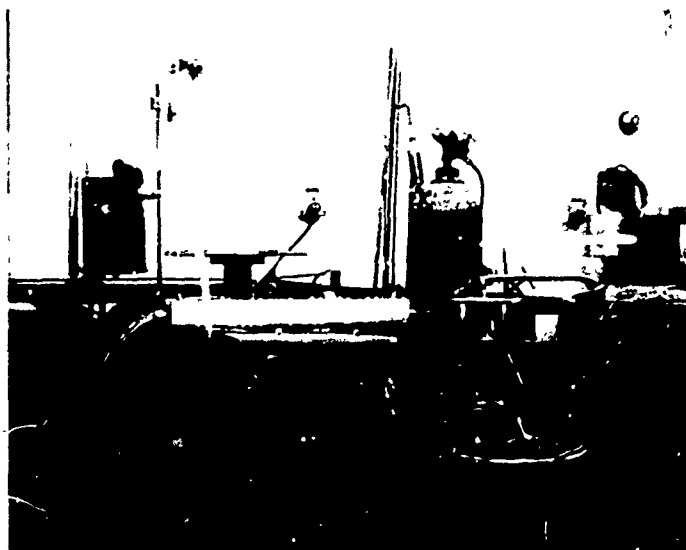


Figure 185. Laboratory Setup for Wick Study

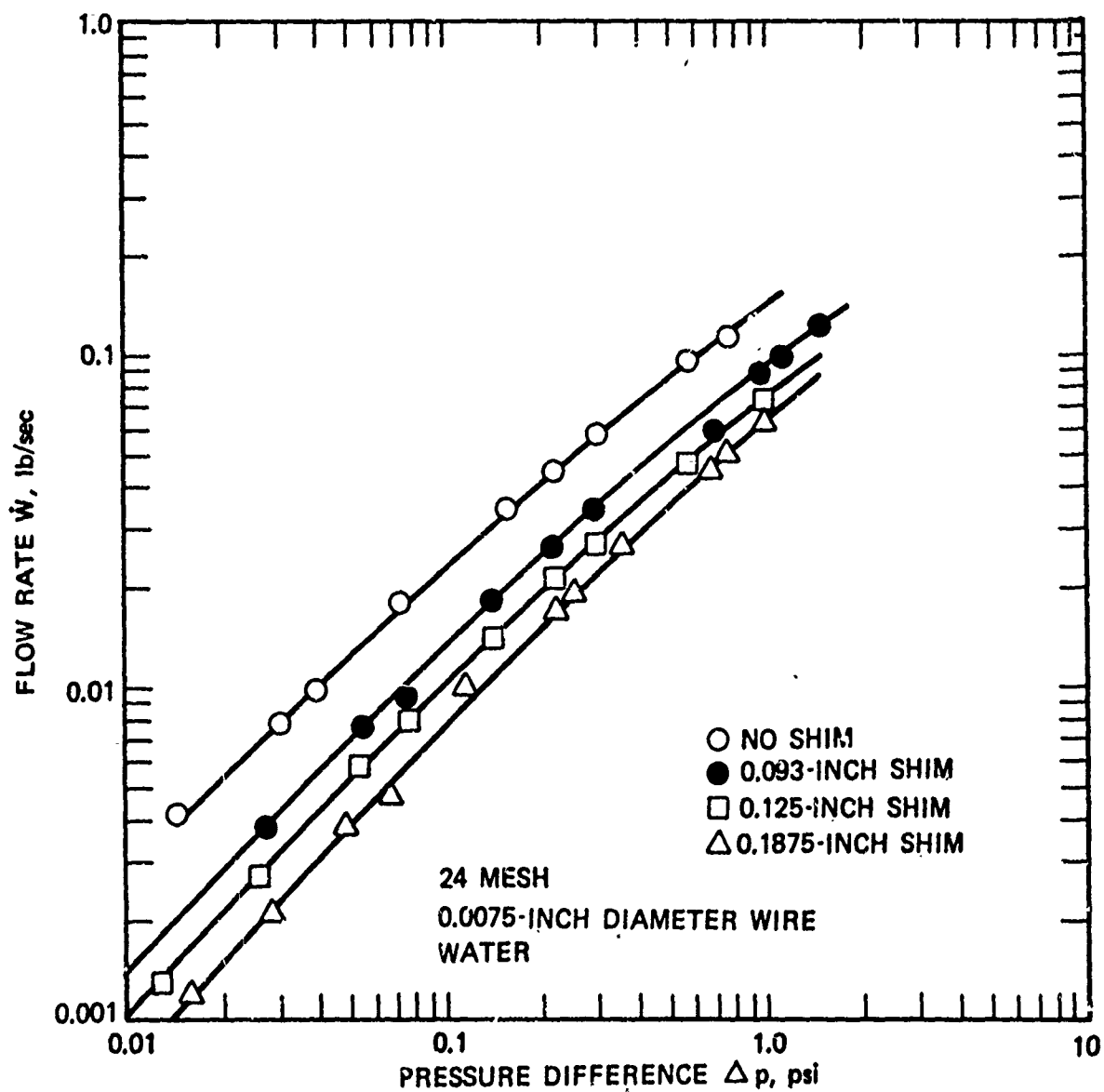


Figure 186. Correlations Between Pressure Difference and Flow Rate

However, in the laminar flow regime as shown in Figure 186, the flow rate is decreased by 61 percent due to the compaction of the wick material.

Laminar Flow $\Delta p = 0.03$ psi

<u>Shim</u>	<u>Flow Rate</u> <u>lb/sec</u>	<u>Flow Area</u> <u>inch²</u>	<u>$(\dot{W}/A)_2$</u> <u>lb/m-m²</u>	<u>$(\dot{W}/A)_1/(\dot{W}/A)_2$</u>
0	0.0082	1.5 x 0.75	0.00729	1
0.1875	0.0023	1.5 x 0.5625	0.00273	0.374

In the laminar flow regime, this means that the permeability of the diametral wick was only 37 percent of the permeability of the non-compressed wick material. This decrease in permeability was even larger than had been predicted.

To investigate the interrelation between mesh size and decrease of permeability due to compression of the diametral wick, the wick test was conducted with bolting cloth of three different meshes. Mesh 24 with a wire diameter of 0.0075 inch, Mesh 40 with a wire diameter of 0.0065 inch, and Mesh 62 with a wire diameter of 0.0045 inch. The working fluid for all tests remained water. The results of the entire test series is presented in Figures 187, 188 and 189.

In Figure 190 the measured pressure drops for the three bolting cloths are cross plotted for a single flow rate. The results confirmed the drastic reduction in the permeability with increasing compression of the wick material which is expressed by the decrease of the packing factor. With a packing factor of 0.75, the projected wick area is only 25 percent smaller and thus the pressure drop across the wick would be calculated to be only 33.33 percent larger if the greater density of the wick is not taken into account. For a mesh of 38 wire per inch of standard bolting cloth, the pressure drop has, however, been increased by a factor of 4.29, i.e., the pressure drop is 429 percent of the pressure drop associated with the uncompressed wick and not just 133 percent. Thus, the pressure drop is 3.22 times higher than based on area change only.

In Figure 191, a comparison is made between the permeability K_M which was experimentally determined and the permeability which was calculated by the relation presented in Reference 18 (K_1). At 38 mesh, the measured permeability is 3.25 times higher than the permeability predicted by a relation for K_1 . This means that a wick constructed of bolting cloth with a 38 mesh has almost a permeability as calculated by K_1 if it is compressed to a packing factor of 0.75.

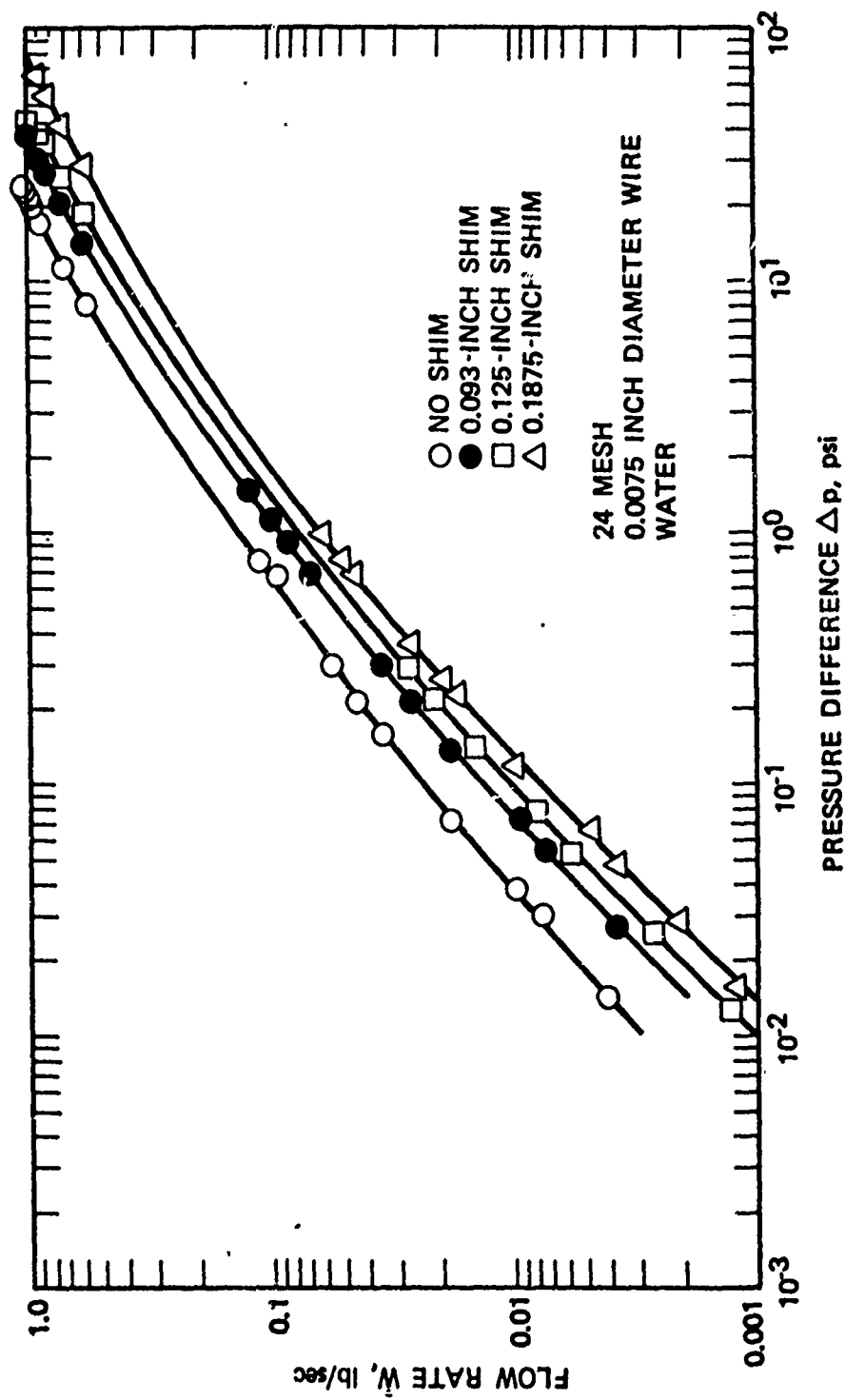


Figure 187. Correlations Between Pressure Difference and Flow Rate

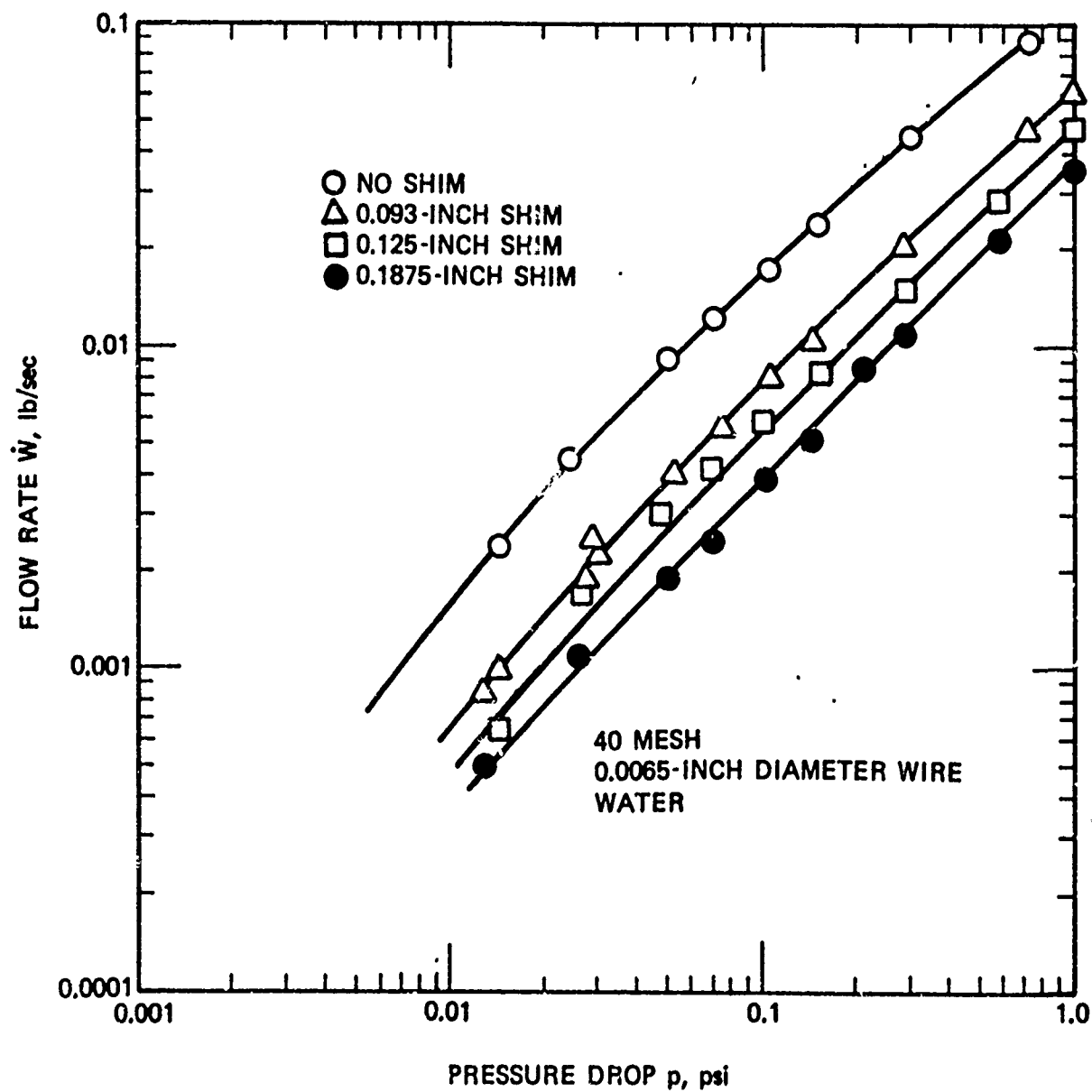


Figure 188. Correlations Between Pressure Drop and Flow Rate Through Wick Structure

50866

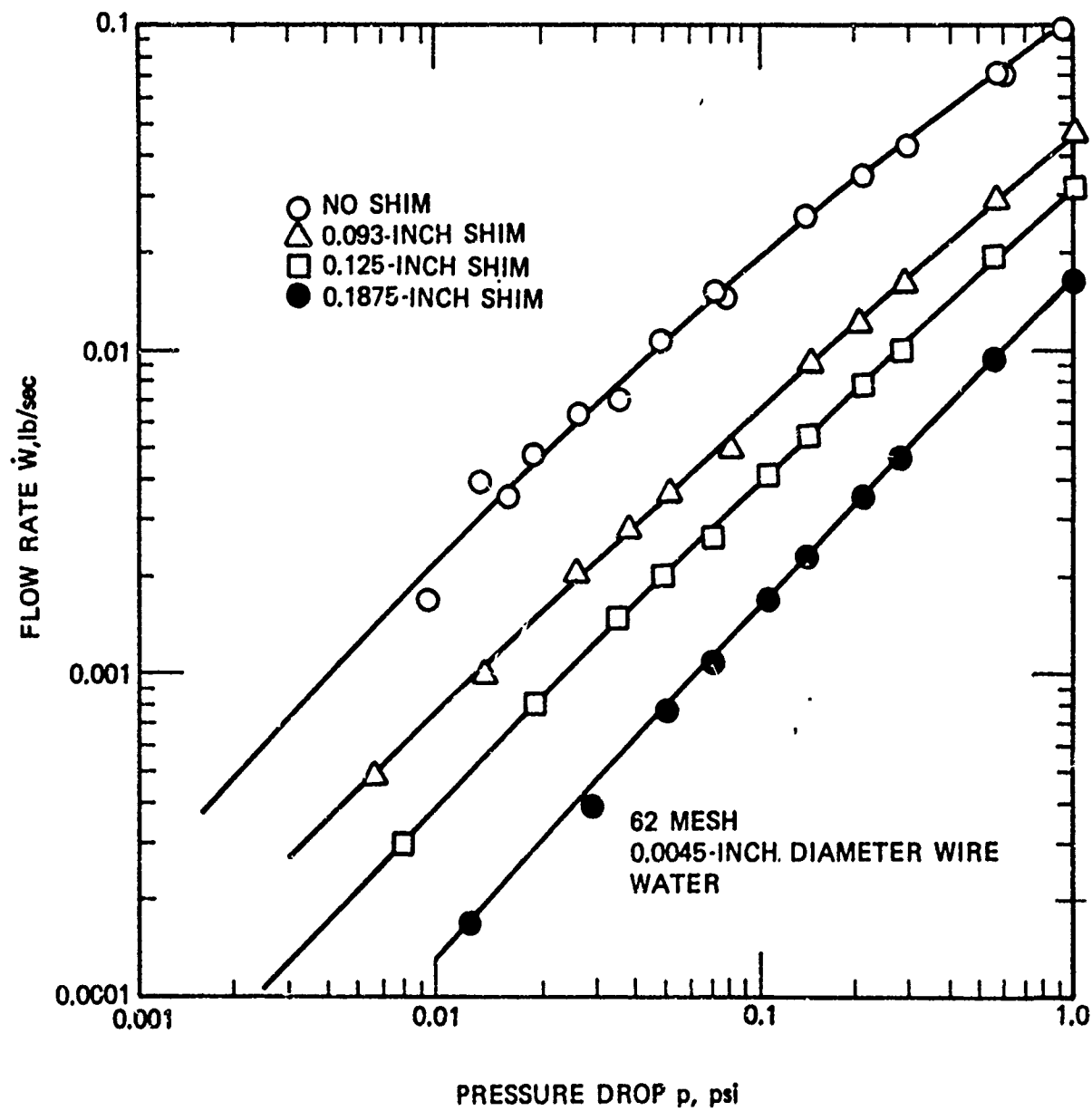


Figure 189. Correlations Between Pressure Drop and Flow Rate Through Wick Structure

50867

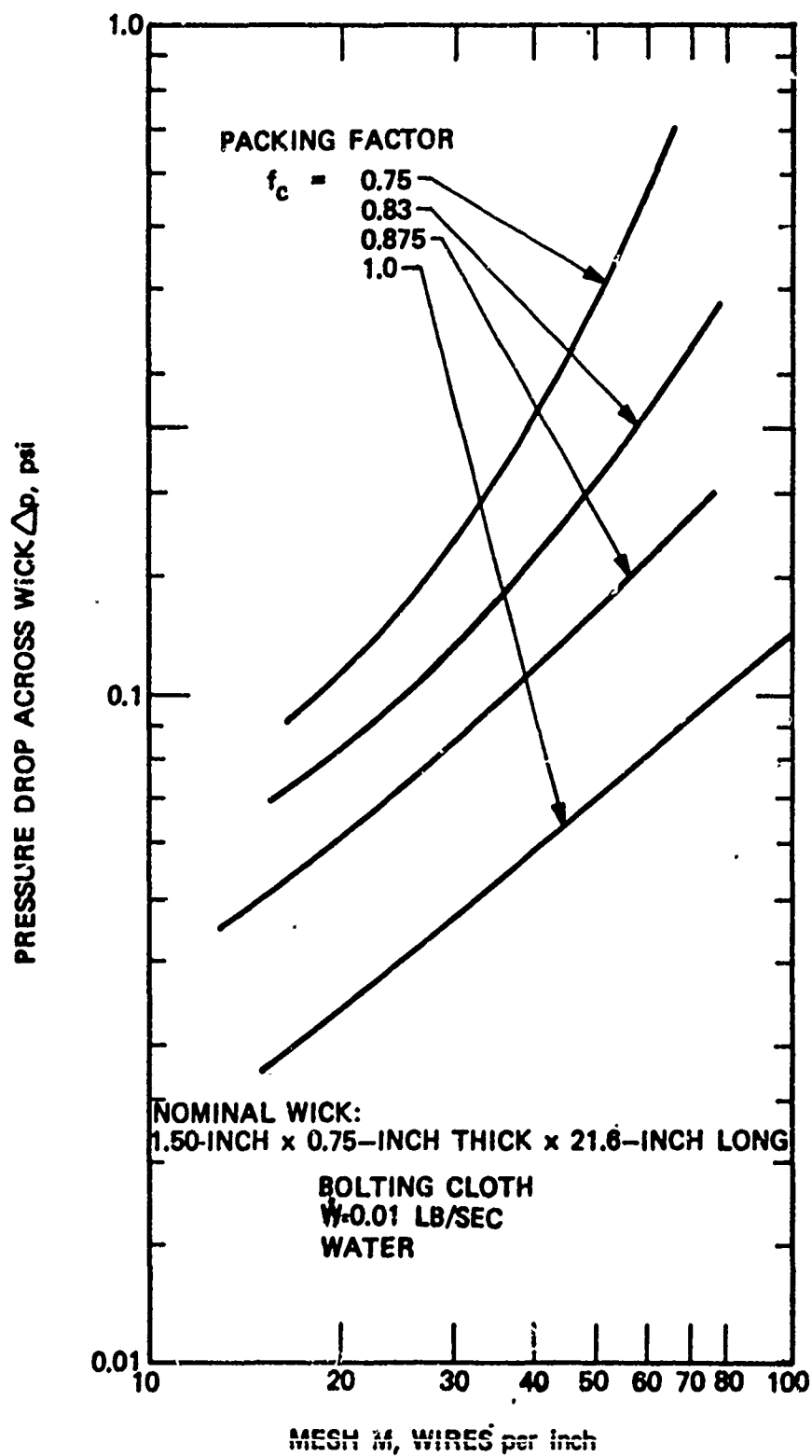


Figure 190. Pressure Drop Across a Wick Structure

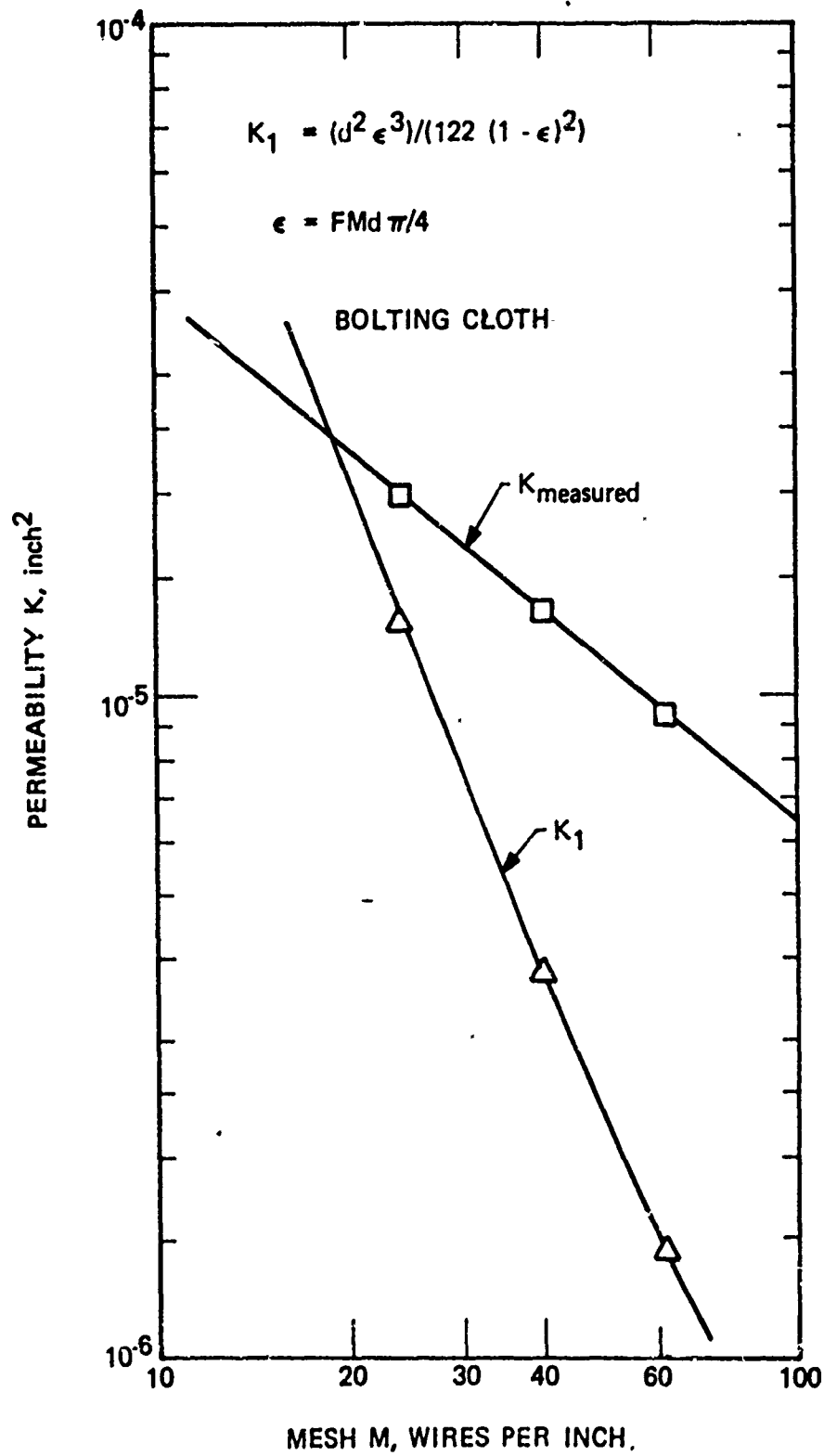


Figure 191. Permeability K for Standard Bolting Cloth

In Figure 192, which was already shown in Volume II of this report, calculations based on the permeability evaluated with the relation for K_1 were presented. The wick test data established that the permeability calculations should have given the correct value for the as-built wick of the first primary heat pipe because of the compensating effect. Since the primary heat pipe was operated in 1-g gravitational field, the correction for full vapor pressure drop and full heat pipe elevation are applicable. A flow factor of 0.096 dyn was required for transferring 6 kW through the 15 ft long heat pipe. Apparently, only 5.7×10^2 dynes were available. Thus, the capacity of the heat pipe should have been 3.5 kW. This value is not very far off the apparently 3 kW power capacity.

9.3 CONCLUSION

The wick study shed considerable light on the observed behavior of the first primary heat pipe and provided confidence that the measured power transfer limit could be explained. The wick study furnished the needed experimental data for the design of the second primary heat pipe and for the heat pipe which was used for testing the subscale cavity. It should still be attempted to find a better agreement between the analytical results and the experimental data.

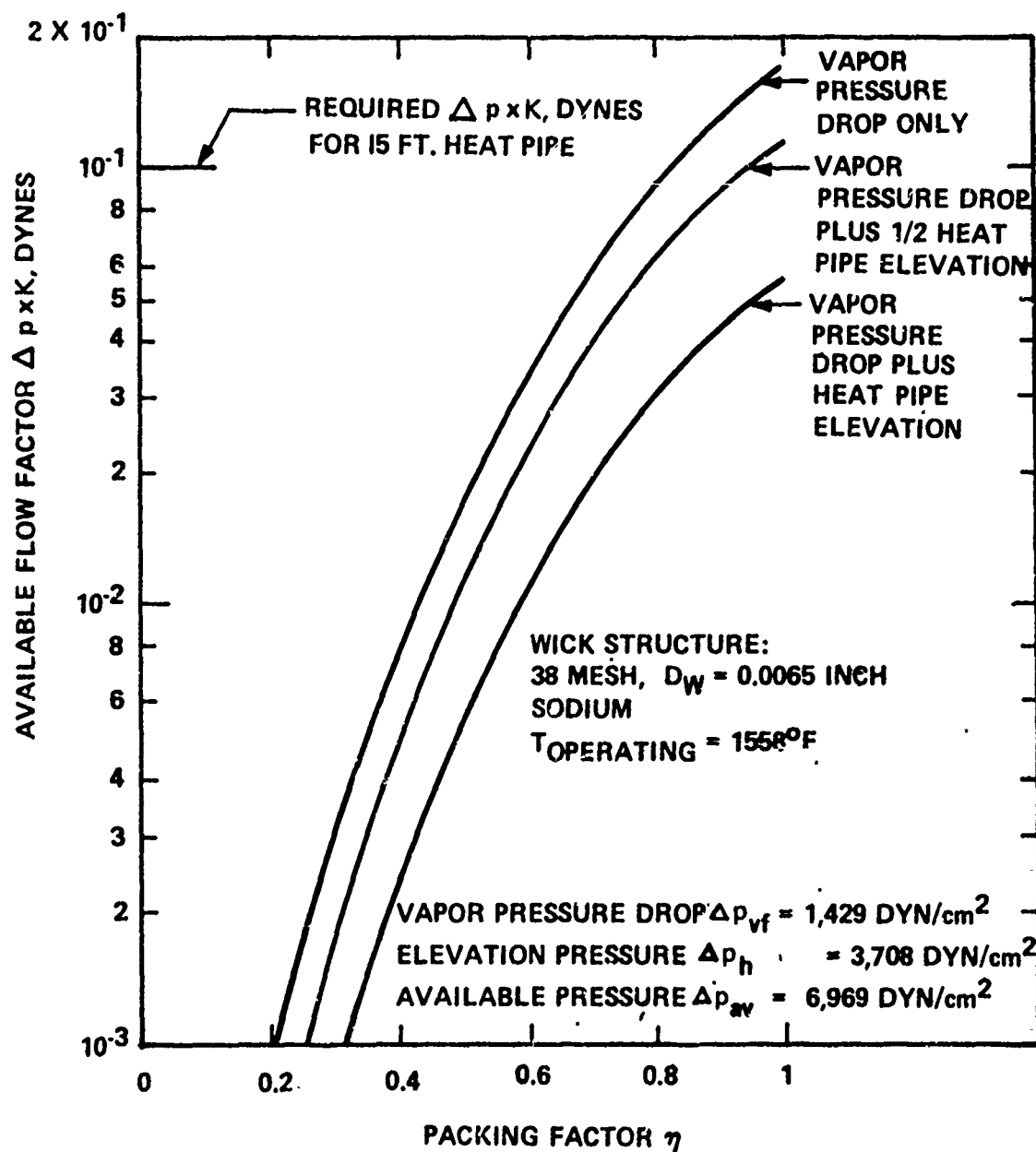


Figure 192. Available Flow Factor $\Delta p \times K$ as a Function of the Packing Factor

REFERENCES

1. "Thermal Train Subsystem for the Solar Collector Thermal Power System," TRW Proposal 21197.000; July 1971.
2. B. D. Marcus, TRW Systems Report 13111-6021-RO-00, "Theory and Design of Variable Conductance Heat Pipes, Research Report No. 1," April 1971.
3. R. E. Cleary, et al., "Determination of the Emissivity of Materials, Final Report," Pratt and Whitney Aircraft Report PWA-3278; 30 June 1968.
4. W. D. DeWitt, et al., "Multi-Foil Type Thermal Insulation" (Union Carbide); Third International Society of Energy Conversion Engineering Conference, 1968 Record.
5. M. L. Paquin, "Multi-Foil Thermal Insulation Development Program" (Thermo Electron Corporation); Fourth International Society of Energy Conversion Engineering Conference, 1969 Record.
6. "Silicon Germanium Thermoelectric Materials and Module Development Program," AEC Research and Development Program, ALO (2510)-8, Category UC33 TID 4500, October 1 to December 31, 1969.
7. J. N. Pike and I. R. Ladd, "Fibrous Zirconia for High Temperature Heat Shielding and Thermal Insulation," Union Carbide Report UCRL-507, August 1968.
8. L. W. Carlson, "Spacecraft Rocket Engine Chamber Insulation Materials," Rocketdyne Report R 7548, 31 July 1968.
9. J. W. Ramsey, C. B. Petersen, and R. N. Schmidt; "Solar Heat Source Feasibility Study," Honeywell Systems and Research Division Report AFML-TR-70-294, January 1971.
10. J. B. Dunlay, "The Development of Foil Thermal Insulation for High Temperature Heat Source," (Thermo Electric Co.) Sponsored under AEC Contract AT930-1)-3634, 1968.
11. B. H. Hamling, A. W. Neumann, and W. H. Drescher (Union Carbide), "Ceramic Fibers and Textiles from Organic Precursors"; American Chemical Society Meeting, 8 September 1968.
12. J. B. Dunlay, et al., "Vacuum Foil-Type Thermal Insulation for Radioisotope Power Systems-Phase 1 Final Report", (Thermo Electron Corp.); AEC R & D Report TE No. 4059-67-68 ALO 3634-6, Category UC-33; August 1967.

13. Tipton, C. R., Ed., Reactor Handbook Vol. I, Interscience Publishers, Inc., New York, 1960.
14. International Critical Tables Vol. III, Washburn, E. W., Ed., McGraw-Hill Book Company, Inc., New York, 1928.
15. Lumsden, J., "Thermodynamics of Molten Salt Mixtures," Academic Press, London, 1966.
16. TRW Final Report, "Brayton Cycle Cavity Receiver Design Study," NASA CR-54752, 1965.
17. Knapp, W. J., Jour. Am. Ceram. Soc. 26, 1943.
18. JANAF Interim Thermochemical Tables, (Sept. 30, 1962). The Dow Chemical Company, Midland, Michigan.
19. W. D. Weatherford, Jr., et al., "Properties of Inorganic Energy - Conversion and Heat-Transfer Fluids for Space Applications," WADD TR 61-96, Nov. 1961.
20. C. T. Ewig, et al., - Journal of Chemical and Engineering Data 11, pg. 468, 1966.
21. J. W. Taylor, The Surface Tension of Liquid Metals and Alloys, A.E.R.E. M/TN 24, A.E.R.E. Harwell, 1954.
22. Huntington Alloy Catalog, Inconel Alloy 600.
23. Cambridge Wire Cloth Catalog, Cambridge Wire Cloth Company, Cambridge, Maryland, 1969.